Defect engineering of ultra-thin layered molybdenum disulfide towards novel memristive and optoelectronic applications

Dissertation by
Jakub Piotr Jadwiszczak, B.A. (Mod)

Ph.D. in Physics

SCHOOL OF PHYSICS
Trinity College, the University of Dublin

2019
Dublin, Ireland

© 2019

Jakub Piotr Jadwiszczak, B.A. (Mod)
ORCID: 0000-0002-9518-9402

All rights reserved

"Not long ago, I expressed the view that the lack of general education and of thorough training in chemistry was one of the reasons of the causes of the deterioration of chemical research in Germany (. . .). Will anyone to whom my worries seem exaggerated please read, if he can, a recent memoir by a Herr van't Hoff on *The Arrangement of Atoms in Space*, a document crammed to the hilt with the outpouring of childish fantasy (. . .). This Dr. J. H. van't Hoff, employed by the Veterinary College at Utrecht, has, so it seems, no taste for accurate chemical research. He finds it more convenient to mount his Pegasus (evidently taken from the stables of the Veterinary College) and to announce how, on his bold flight to Mount Parnassus, he saw the atoms arranged in space."

Prof. Hermann Kolbe,
1877

I have read and I understand the plagiarism provisions in the General Regulations of the University Calendar for the current year, found at `http://www.tcd.ie/calendar`.

Signed:

I have also completed the Online Tutorial on avoiding plagiarism “Ready Steady Write", located at `http://tcd-ie.libguides.com/plagiarism/ready-steady-write`.

Signed:

November 2019, Trinity College Dublin.

I declare that this thesis has not been submitted as an exercise for a degree at this or any other university and that it details entirely my own work. Due acknowledgements and references are given to the work of others where appropriate.

I agree to deposit this thesis in the University’s open access institutional repository or allow the library to do so on my behalf, subject to Irish Copyright Legislation and Trinity College Library conditions of use and acknowledgement.

Jakub Jadwiszczak

Acknowledgements

Ever since I joined his group, my supervisor Professor Hongzhou Zhang has proven to be the most insightful, inspiring and patient mentor that any student could ask for. I am truly grateful to have worked alongside a scientist of his talent and devotion.

I have also been fortunate to be part of a fantastic research group, where knowledge and skills are cherished and passed onto new members. I would like to thank Prof. Yangbo Zhou and Dr. Danny Fox for their enduring support in and out of the lab. Darragh Keane for all the hours we put in together in the lab. Dr. Pierce Maguire for his experience and level-headed approach. Dr. Robbie O'Connell for assistance with all technical issues. Abbas Khalid for always providing the bigger picture. Gen Li, as well as all of our summer and undergrad students over the years, for giving me ample opportunities to develop my own skills as a mentor.

No scientific work would ever proceed smoothly without the assistance of technical staff. I owe so much to Clive Downing, Dermot Daly, Dr. Eoin McCarthy, Dr. Allen Bellew, Julia Kremer, Neal O'Hara, Dr. Megan Cavanan and others, who over the years have kept me from destroying equipment and gave crucial advice when it comes to experimental work.

My friends have been the persistent source of strength throughout the last four years. In them, I have found understanding (it helps that they're all also PhD students!) and comfort when things weren't going to plan. So here, I'd like to thank the future doctors: Daniel Kelly, Conor Cullen, JB Boland and Jeff McHugh.

Science is a collaborative effort, and I have learned an unbelievable amount from people with whom I've worked formally throughout the last few years. The list is quite long, but each of them deserves recognition (and is also mentioned at each point in the thesis, where their contribution was major): Conor Cullen, Dr. Niall McEvoy, Prof. Georg Duesberg, Dr. Aleksey Shmeliov, Prof. Valeria Nicolosi, Dr. John Gough, Prof. Louise Bradley, Prof. James Lunney, Dr. Colin O'Callaghan, Ian O'Reilly, Eamonn Weitz, Prof. Mauro Ferreira, Prof. Cormac McGuinness and Prof. John Boland.

My time spent in Peking University in China was very special and I'd like to acknowledge everyone who made it possible: Prof. Zhi-Min Liao for hosting me in his group, Dr. Rui Zhu for sorting out the accommodation, Prof. Yangbo Zhou for financing the trip and the research, Dr. Jun Xu for facilitating the microscopy

experiments, Hua-Ding Song for helping with the cryostat and device fabrication, Rongrong Li for guiding me around and Mingqiang Li for being a great companion in and out of the lab.

I'd like to acknowledge the members of the IQST/NINT lab headed by Prof. Paul Barclay at the University of Calgary, Canada, for inspiring me during my final year undergraduate project to pursue a PhD in physics.

My wife Marta for putting up with me for the last four years... I know it wasn't easy at times, but we made it through to the other side - and also managed to get married in the thick of it! I love you forever.

Finally, I would like to thank my parents, Mirosław & Edyta, for always being there for me and supporting my education at all costs. I am forever indebted to you for your sacrifices.

List of publications

Journal Articles

1. *On the nature of resistance states in the monolayer MoS_2 memtransistor*, **Jadwiszczak, J.** and Zhou, Y. and Song, H.-D. and Cullen, C. P. and McCarthy, E.K. and Maguire, P. and Keane, D. and McEvoy, N. and Zhu, R. and Xu, J. and Duesberg, G. S. and Liao, Z.-M. and Boland, J. J. and Zhang, H., **in preparation**, 2019. - discussed in **Chapter 10**.

2. *Plasma treatment of layered semiconductors for electronic device applications (review article)*,
Jadwiszczak J. and Stanford, M. and Bolshakov, P. and Guo, J. and Zhou, Y. and Young, C.D. and Tour, J. M. and Zhang, H., **in preparation**, 2019.

3. *Effect of localized ion irradiation on the performance of monolayer MoS_2 FETs*,
Jadwiszczak, J. and Maguire, P. and Cullen, C. P. and Duesberg, G. S. and Zhang, H., **under review**, 2019. - discussed in **Chapter 8**.

4. *Neuromorphic MoS_2 memtransistors fabricated by localised helium ion beam irradiation*, **Jadwiszczak, J.** and Keane, D. and Maguire, P. and Cullen, C. P. and Zhou, Y. and Song, H.-D. and Downing, C. and Fox, D. S. and McEvoy, N. and Zhu, R. and Xu, J. and Duesberg, G. S. and Liao, Z.-M. and Boland, J. J. and Zhang, H., **under review**, 2019. - discussed in **Chapter 9**.

5. *Defect-moderated oxidative etching of MoS_2*,
Maguire, P. and **Jadwiszczak, J.** and O'Brien, M. and Keane, D. and Duesberg, G. S. and McEvoy, N. and Zhang, H., **Journal of Applied Physics**, 126, 164301, 2019.

6. *Suppression of the Shear Raman Mode in Defective Bilayer MoS_2*, Maguire, P. and Downing, C. and **Jadwiszczak, J.** and O'Brien, M. and Keane, D. and McManus, J. B. and Duesberg, G. S. and Nicolosi, V. and McEvoy, N. and Zhang, H., **Journal of Applied Physics**, 125, 064305, 2019.

7. *Photoresponsivity enhancement in monolayer MoS_2 by rapid O_2:Ar plasma treatment*,
Jadwiszczak, J. and Li, G. and Cullen, C.P. and Wang, J.J.and Maguire,

P. and Duesberg, G.S. and Lunney, J. G. and Zhang, H., **Applied Physics Letters**, 114, 091103, 2019. - discussed in **Chapter 7**.

8. *Defect sizing, separation, and substrate effects in ion-irradiated monolayer two-dimensional materials*,
   Maguire, P. and Fox, D. S. and Zhou, Y. and Wang, Q. and O'Brien, M. and **Jadwiszczak, J.** and Cullen, C. P and McManus, J. and Bateman, S. and McEvoy, N.and Duesberg, G.S. and Zhang, H., **Physical Review B**, 98, 13, 134109, 2018.

9. *Low-temperature electrical conduction of plasma-treated bilayer MoS_2*,
   Jadwiszczak, J. and Zhou, Y. and Zhang, H., **MRS Communications**, 1-7, 2018. - discussed in **Chapter 6**.

10. *Oxide-mediated recovery of field-effect mobility in plasma-treated MoS_2*,
    Jadwiszczak, J. and O'Callaghan, C. and Zhou, Y. and Fox, D. S and Weitz, E. and Keane, D. and Cullen, C. P and O'Reilly, I. and Downing, C. and Shmeliov, A. and Maguire, P. and Gough, J. J. and McGuinness, C. and Ferreira, M. S. and Bradley, A. L. and Boland, J. J. and Duesberg, G. S. and Nicolosi, V. and Zhang, H., **Science Advances**, 4, 3, eaao5031, 2018. - discussed in **Chapter 5**.

11. *Programmable graphene doping via electron beam irradiation*,
    Zhou, Y. and **Jadwiszczak, J.** and Keane, D. and Chen, Y. and Yu, D. and Zhang, H., **Nanoscale**, 9, 25, 8657–8664, 2017.

12. *Precise milling of nano-gap chains in graphene with a focused helium ion beam*,
    Zhou, Y. and Maguire, P. and **Jadwiszczak, J.** and Muruganathan, M. and Mizuta, H. and Zhang, H., **Nanotechnology**, 27, 32, 325302, 2016.

Talks & Conferences

1. *Neuromorphic MoS_2 memtransistors fabricated by localised helium ion beam irradiation* (poster),
   Jadwiszczak, J., **Microscience Microscopy Congress 2019 (mmc2019)**, Manchester, UK, July, 2019.

2. *Defect engineering of 2D molybdenum disulfide towards novel memristive and optoelectronic applications* (invited seminar),

Jadwiszczak, J., **Massachusetts Institute of Technology**, Cambridge, MA., USA, May, 2019.

3. *Defect engineering of 2D molybdenum disulfide towards novel memristive and optoelectronic applications* (invited seminar),
Jadwiszczak, J., **Cornell University**, Ithaca, NY., USA, May, 2019.

4. *Defect engineering of ultra-thin molybdenum disulfide towards novel memristive and optoelectronic applications* (invited seminar),
Jadwiszczak, J., **Columbia University**, New York City, NY., USA, April, 2019.

5. *Single-layer neuromorphic MoS_2 memtransistors fabricated by helium ion beam irradiation* (contributed talk),
Jadwiszczak, J., **Materials Research Society Spring Meeting**, Phoenix, AZ., USA, April, 2019.

6. *Neuromorphic MoS_2 memtransistors fabricated by localised helium ion beam irradiation* (contributed talk),
Jadwiszczak, J., **21st International Conference on Microscopy of Semiconducting Materials**, University of Cambridge, UK, April, 2019.

7. *Single-layer neuromorphic MoS_2 memtransistors fabricated by helium ion beam irradiation* (contributed talk),
Jadwiszczak, J., **The Second International Meeting of the PicoFIB Network**, University College London, UK, February, 2019.

8. *Modifying electronic properties of 2D MoS_2 by defect engineering in the helium ion microscope* (invited seminar),
Jadwiszczak, J., **Nanchang University**, Jiangxi, China, July, 2018.

9. *Oxide-mediated self-limiting recovery of field-effect mobility in plasma-treated MoS_2* (contributed talk),
Jadwiszczak, J., **Materials Research Society Fall Meeting**, Boston, MA., USA, November, 2017.

10. *47^{th} IFF Spring School on Memristive Phenomena - From Fundamental Physics to Neuromorphic Computing* (workshop conference),
Jadwiszczak, J., **Forschungszentrum Jülich**, Jülich, Germany, March, 2016.

11. *Site-specific modification of MoS_2 with helium ion beam towards memristive defect networks* (poster),
Jadwiszczak, J., **Nanoweek Ireland**, University of Limerick, Ireland, September, 2015.

Abstract

Defect engineering of ultra-thin layered molybdenum disulfide towards novel memristive and optoelectronic applications

Jakub Jadwiszczak

In the ever-evolving field of nanoelectronics, new paradigms are constantly sought-after to improve the performance of next-generation circuit components. In the last decade, two-dimensional (2D) semiconductors have emerged as promising candidates to usher in a new age of low-power devices. The family of transition metal dichalcogenides, such as molybdenum disulfide (MoS_2), offers a unique versatility of physical properties (flexibility, transparency, charge carrier confinement) and integrates easily with existing silicon-based fabrication processes. To a large extent, the implementation of potential applications is governed by the properties of the material systems. The ability to manipulate these properties on the nanoscale is a central theme of this dissertation, with a particular focus on modulating the electrical properties of devices based on 2D MoS_2 by the purposeful introduction of defects. Two main avenues were pursued in this thesis to study the modulation of the electronic and optoelectronic properties of ultra-thin MoS_2 - *plasma treatment* and *helium ion beam irradiation*. Both techniques were established as viable methods for activating novel functionalities in low-dimensional materials; despite residing on the opposite ends of the spectra of fabrication scalability, cost, time efficiency, site-specificity and dose control.

Plasma processing allows for wafer-scale, fast and cost-efficient surface doping of on-substrate MoS_2 samples. Time-controlled exposures to a mixture of O_2:Ar (1:3) plasma resulted in a dose-dependent recovery of electron mobility in MoS_2 field effect transistors - studied as a function of material thickness from 1 to 10 layers. Detailed spectroscopic and microscopic characterisation revealed the role played by a sub-stoichiometric phase of surface-bound MoO_x in electrostatically screening the underlying MoS_2 transistor channel; thus boosting the carrier mobility in highly-defective MoS_2 devices. Robust simulations confirmed the beneficial role of the highly conductive oxide phase on the transistor channel conductance.

This study of the dose and layer number dependence was extended to low-temperature (80 K) electrical characterisation of bilayer MoS_2 as a function of increasing plasma

processing time. The Efros–Shklovskii hopping regime of the untreated sample was seen to transition to a mixed thermally-activated regime at high temperatures upon plasma treatment. Another crossover was observed in the defective system, below 181 K, to a strongly short-range Arrhenius regime due to a critical defect density achieved by the continuing plasma treatment. Investigation of the temperature-dependent emission current revealed a significant lowering of the effective Schottky barrier height for the bilayer MoS_2 channel with plasma treatment. Meanwhile, it was demonstrated that the photoresponsivity of synthetic MoS_2 monolayer phototransistors can be enhanced ten-fold by the introduction of these surface-bound molybdenum oxides by rapid plasma exposures (2 seconds). The effect of the mobility and photoresponsivity enhancement was found to depend on the laser power and was more prominent at powers exceeding several μWatts.

Helium ion beam irradiation is a site-specific method for the dose-controlled sputtering of material down to nanometre-scale regions in layered semiconductors. Previous work has demonstrated that it is a practical method for the introduction of sulfur vacancies in MoS_2. This also leads to a dose-mediated resistivity tuning in the material by several orders of magnitude. In this thesis, it was demonstrated that by tuning the irradiation strategy and localising the damage to specific sites, the electronic characteristics of on-dielectric MoS_2 field effect transistors can be well-controlled. The effects of irradiating a monolayer MoS_2 device with the helium ion beam as a function of increasing exposure area were examined. Increased irradiation areas resulted in poorer on/off ratios for the transistor, a severe deterioration of carrier mobility and an increased hole-branch conduction due to the saturation of vacancy sites by atmospheric p-type dopants.

Building on this knowledge, a hybrid MoS_2 device known as the *memtransistor* was fabricated by confining MoS_2 channel-bisecting irradiations to quasi-one dimensional line scans. These highly site-specific irradiations create charged defects in the MoS_2 lattice. The reversible drift of these locally-seeded defects in the applied electric field modulates the resistance of the semiconducting channel, enabling versatile memristive functionality on the nanoscale. These devices can reliably retain their resistance ratios and set/reset biases for up to 1180 switching cycles, while a range of optimal voltage ramping speeds was also investigated. Long-term potentiation and depression with sharp habituation that is demanded by future neuromorphic architectures was demonstrated in these devices.

The fabricated memtransistor devices were characterised through spectroscopic and

microscopic methods to determine the nature of the resistive switching. The property of device asymmetry was found to play a key role in the emergence of bipolar memristive behaviour exhibited by the devices. The proposed physical mechanism for the switching relies on the cyclical shrinkage and extension of the asymmetric sulfur vacancy distribution introduced into the MoS_2 channel by the He^+ ion beam. The individual device resistance states were probed and characterised by means of cryogenic charge transport down to 1.5 K. These experiments uncovered the impact of sulfur vacancy drift on the device operation; parametrised by large differences in the gate threshold voltage, electron mobility scaling with temperature, the electron localisation lengths, the amplitude of 1/f noise and the current density saturation between the two resistance states. Moreover, an early onset metal-insulator transition was observed in the low resistance sate, as mediated by the reversible doping brought about by the bi-directional drift of sulfur vacancies. This method of inducing resistive switching in monolayer MoS_2 thus also demonstrates the utility of field-controllable dopant drift in facilitating exotic physical phenomena in 2D materials.

The work described herein establishes the feasibility of ion irradiation for the controllable fabrication of 2D memristive devices, with promising key performance parameters such as low power consumption. The applicability of these devices for synaptic emulation may thus address the demands of future neuromorphic hardware architectures.

Keywords: Two-dimensional layered materials, molybdenum disulfide, field effect transistors, defect engineering, plasma etching, electron beam lithography, van der Waals materials, electron mobility, cryogenic charge transport, phase transition, semiconductor doping, point defects, memristors, resistive switches, helium ion microscope, ion beam engineering, photoresponsivity, neuromorphic.

Table of Contents

Acknowledgements v
Abstract xi
Table of Contents xv
List of Illustrations xvii
List of Tables xxiii
Chapter I: Overview 1
1.1 Motivation and wider context 1
1.2 Outline of the thesis 3
Chapter II: Fundamentals in 2D MoS_2 and its devices 7
2.1 Layered semiconducting TMDs 7
2.2 Condensed matter phenomena in MoS_2 9
2.3 TMD MOSFETs 17
2.4 Memristors 26
Chapter III: MoS_2 modification and functionalisation 39
3.1 Plasma functionalisation 39
3.2 Helium ion beam irradiation 50
Chapter IV: Device fabrication and characterisation techniques 61
4.1 Material synthesis and device fabrication 61
4.2 Material modification 74
4.3 Characterisation methods 79
Chapter V: Oxide-mediated recovery of field-effect mobility in plasma-treated MoS_2 103
5.1 Recovery of μ_{fe} in plasma-treated MoS_2 104
5.2 MoS_2 surface modification by oxygen insertion 108
5.3 Spectroscopic analyses of the surface-bound oxide 111
5.4 Nanoscale effects of plasma etching at recovery time 116
5.5 Dependence of the mobility recovery on MoS_2 layer number 122
5.6 Resistive network modelling of conductivity over time 128
5.7 Conclusions and outlook 131
Chapter VI: Low-temperature electrical conduction in plasma-treated bilayer MoS_2 133
6.1 Effects of plasma treatment on the temperature-graded FET characteristics 133
6.2 Impact of plasma-created defects on the temperature-dependent electrical conductance of MoS_2 136
6.3 Plasma-mediated modulation of device emission current and the Schottky barrier height 137
6.4 Evolution of the temperature-dependent conduction mechanisms with increasing plasma exposure time 140

6.5 Conclusions and outlook . . . 142
Chapter VII: Photoresponsivity enhancement in monolayer MoS_2 by rapid O_2:Ar plasma treatment . . . 143
7.1 The effect of illumination on the output characteristics of plasma-modified devices . . . 144
7.2 Effects on the transfer characteristics and μ_{fe} . . . 146
7.3 Photoresponsivity and temporal characteristics after plasma treatment 147
7.4 Spectroscopic characterisation of the surface and proposed R_{ph} enhancement mechanism . . . 151
7.5 Conclusions and outlook . . . 153
Chapter VIII: Effect of varying the irradiation area on the conductance of monolayer MoS_2 . . . 155
8.1 Device fabrication and experimental design . . . 155
8.2 Electrical performance as a function of I_R . . . 159
8.3 Effect of irradiating the MoS_2/electrode interface . . . 162
8.4 SRIM simulation of interface damage . . . 164
8.5 Correlating I_R, grain boundaries and interface damage with electrical performance . . . 165
8.6 Conclusions . . . 178
Chapter IX: Neuromorphic MoS_2 memtransistors fabricated by localised helium ion beam irradiation . . . 181
9.1 Memtransistor fabrication with the helium ion microscope . . . 182
9.2 Resistive switching in He^+-irradiated MoS_2 . . . 188
9.3 Performance metrics of the HIM-enabled MoS_2 memtransistor . . . 193
9.4 Remark on the definition of set voltage . . . 198
9.5 Neuromorphic memtransistor performance . . . 200
9.6 Spectroscopic studies . . . 206
9.7 Considerations of asymmetry . . . 213
9.8 *In-situ* TEM biasing . . . 216
9.9 Conclusions and outlook . . . 218
Chapter X: On the nature of resistance states in the MoS_2 memtransistor . . . 221
10.1 Effect of asymmetric irradiations on device performance . . . 221
10.2 Effects of crystal orientation . . . 231
10.3 Proposed switching mechanism . . . 233
10.4 Low temperature electrical characterisation of the MoS_2 memtransistor 235
10.5 Electron mobility scaling with temperature . . . 238
10.6 Conductance mechanisms in the two resistance states . . . 241
10.7 1/f noise and carrier velocity saturation in LRS and HRS . . . 244
10.8 Conclusions and outlook . . . 251
Chapter XI: Conclusions and future work . . . 253
References . . . 261
Appendix A: Typical electron beam lithography recipe . . . 289
Appendix B: *Thickogram* calculation of MoO_3 on MoS_2 . . . 291
Appendix C: Simulation of conductive networks . . . 293
Appendix D: Defining the current polarity in our memtransistors . . . 297

List of Illustrations

Number *Page*

2.1 **Crystal and electronic band structures of MoS_2.** . . . 8
2.2 **Metal-insulator transition in monolayer MoS_2.** . . . 10
2.3 **MIT crossovers and hopping transport reported in MoS_2.** . . . 12
2.4 **Pink noise in MoS_2.** . . . 14
2.5 **Drift velocity saturation in ultra-thin layered semiconductors.** . . . 16
2.6 **Visualising the charge confinement in a single-layer TMD channel.** . . . 19
2.7 **Diagram conceptualising the working principles of a 2D FET.** . . . 20
2.8 **Metal-van der Waals semiconductor contact geometries and associated band diagrams of the junctions.** . . . 26
2.9 **The four fundamental two-terminal circuit elements.** . . . 27
2.10 **The first resistive switch.** . . . 29
2.11 **Hardware implementation of memristors.** . . . 30
2.12 **Memristive synapses and neuromorphic behaviour.** . . . 32
2.13 ***I–V* characteristics of MoS_2 resistive switches.** . . . 33
2.14 **More properties of the grain boundary-activated MoS_2 memristive switch.** . . . 34
2.15 **Characteristics of the polycrystalline MoS_2 memtransistor.** . . . 35
2.16 **2D memristive devices.** . . . 37
3.1 **Overview of plasma generation and species used for the modification of layered semiconductors.** . . . 42
3.2 **Etching of layered semiconductors with plasma.** . . . 44
3.3 **p-type doping of TMDs with plasma.** . . . 47
3.4 **n-type doping of TMDs with plasma.** . . . 49
3.5 **The helium ion microscope.** . . . 51
3.6 **Beam-sample interaction.** . . . 53
3.7 **Scattering cross-section.** . . . 55
3.8 **Nanopatterning of MoS_2 with the helium ion beam.** . . . 56
3.9 **Electrical tuning of MoS_2 with the helium ion beam.** . . . 57
3.10 **Percolating path formation along defect edges in He^+-irradiated WSe_2 as a function of dose.** . . . 58
4.1 **Molybdenum trioxide CVD precursor.** . . . 62
4.2 **CVD growth of MoS_2 in the Duesberg lab.** . . . 63

4.3 **Characterisation of as-grown MoS_2 samples.** . . . 64
4.4 **Mechanical exfoliation of MoS_2 flakes.** . . . 66
4.5 **Optical contrast of exfoliated MoS_2 flakes.** . . . 67
4.6 **Process flow chart of electron beam lithography.** . . . 69
4.7 **Work flow of multiple channel fabrication on monolayer CVD MoS_2.** . . . 70
4.8 **Optical lithography of MoS_2 samples.** . . . 72
4.9 **Polymer stamp transfer process.** . . . 74
4.10 **Cross section of the plasma cleaner and ion energy dependence on gas pressure.** 75
4.11 **Evaluation of the He^+ probe size before memtransistor fabrication.** . . . 76
4.12 **Distribution of measured beam current prior to pattern irradiation.** . . . 77
4.13 **Irradiation geometry and resulting pattern.** . . . 78
4.14 **Asymmetric dose delivery.** . . . 79
4.15 **Atomic force microscopy.** . . . 80
4.16 **Scanning electron microscopy.** . . . 83
4.17 **(Scanning) Transmission electron microscopy.** . . . 85
4.18 **Raman scattering.** . . . 88
4.19 **Raman modes of MoS_2.** . . . 89
4.20 **Photoluminescence spectroscopy of MoS_2.** . . . 91
4.21 **Energy dispersive X-ray spectroscopy.** . . . 92
4.22 **Electron energy loss spectroscopy.** . . . 94
4.23 **X-ray photoelectron spectroscopy.** . . . 96
4.24 **Electrical characterisation in the SEM.** . . . 98
4.25 **SEM cryo-stage.** . . . 99
4.26 **Experimental set-up for cryogenic charge transport experiments.** . . . 101
5.1 **Outline of device geometry and stability.** . . . 104
5.2 **Electrical characterisation of the 4L device.** . . . 105
5.3 **Effects of pure argon plasma.** . . . 107
5.4 **Surface morphology of plasma-treated MoS_2.** . . . 109
5.5 **Topography and optical contrast variation of the same 4L MoS_2 flake.** . . . 110
5.6 **Spectroscopic signatures of oxidised MoS_2.** . . . 112
5.7 **Shifts of XPS spectra and evidence for S-O bonding.** . . . 114
5.8 **PL signatures of oxidised 1L MoS_2.** . . . 115
5.9 **Nanoscale effects of plasma treatment on MoS_2.** . . . 116
5.10 **`QSTEM` simulations of stripped bilayer MoS_2.** . . . 117
5.11 **HRTEM images of plasma-treated MoS_2.** . . . 118
5.12 **ACSTEM images of plasma-treated MoS_2.** . . . 118

5.13 **Void dimension statistics from ACSTEM images of plasma-treated bilayer MoS_2.** 119
5.14 **Nanoscale spectroscopies.** 120
5.15 **Volatility of the oxide and the rate of conversion.** 122
5.16 **Evolution of *I-V* sweeps with plasma time for devices of particular layer number.** 123
5.17 **Evolution of gate sweeps with plasma time for devices of particular layer number.** 123
5.18 **Extracted field-effect mobilities corresponding to devices of particular layer number.** 124
5.19 **Full data set of subthreshold swings derived for samples of all thicknesses over plasma exposure time.** 124
5.20 **Effect of layer number on the mobility recovery.** 126
5.21 **Resistive network simulation of oxidised MoS_2.** 130
6.1 **Temperature-dependent output and transfer characteristics of bilayer MoS_2 with increasing plasma treatment.** 134
6.2 **Temperature-dependent conductance scaling with increasing plasma treatment.** 136
6.3 **Richardson plots and Schottky barrier height extractions with increasing plasma treatment.** 138
6.4 **Zabrodskii analysis as a function of increasing plasma exposure.** 140
7.1 **Output characteristics comparison between untreated and treated samples under laser illumination.** 145
7.2 **Transfer characteristics, mobility and photocurrent scaling with power comparisons between untreated and treated samples under laser illumination.** . . 146
7.3 **Photoresponsivity and temporal response of the MoS_2 phototransistor.** 149
7.4 **Spectroscopic characterisation of plasma-treated CVD MoS_2 samples.** 151
7.5 **Proposed mechanism of charge trapping responsible for the observed photoresponsivity enhancement.** 152
8.1 **Low-bias output characteristics of fabricated monolayer CVD MoS_2 FETs.** . . 156
8.2 **Transfer characteristics of fabricated monolayer CVD MoS_2 FETs.** 157
8.3 **Examples of irradiated devices.** 159
8.4 **Effect of irradiating the device at I_R = 0.07.** 159
8.5 **Electrical characteristics as a function of increasing I_R.** 161
8.6 **SEM images of example devices where one of the electrode/MoS_2 interfaces was irradiated.** 163
8.7 **Three sets of *I-V* and output curves corresponding to the low, medium and high I_R regimes.** 164
8.8 **SRIM simulation of the vacancy yield generated as the He^+ beam penetrates the device.** 165

8.9 **Three SEM images of the same as-made MoS_2 FET device.** 166
8.10 **Electrical characterisation of the three channels on the device in Fig. 8.9.** . . . 167
8.11 **Examples of strained MoS_2 CVD growth achieved by restricting sulfur gas supply, compared with our CVD flakes.** 168
8.12 **Examples of hysteretic *I-V* curves in two devices after He^+ ion irradiation.** . . 169
8.13 **A series of gate curves for each tested device with changing I_R.** 170
8.14 **Extraction of threshold biases from gate curves before and after helium ion beam irradiation.** 171
8.15 **Distributions of extracted parameters from any hysteretic *I-V* curves in the data set as a function of irradiation-to-channel ratio.** 172
8.16 **Heat map of Pearson's r coefficients between variables.** 175
8.17 **Box plots of certain device parameters, categorised by grouping for the t-test.** . 177
9.1 **Device fabrication and characterisation of the irradiated region.** 182
9.2 **SEM and HIM images of irradiated devices.** 183
9.3 **Plan-view TEM images of ion beam cuts performed on suspended MoS_2 at doses of 0.16 and 1.6 pC μm^{-1}, and a cross-sectional TEM image of the fissure region after a FIB lift-out.** 184
9.4 **Dependence of hydrocarbon BID mound height on the delivered ion dose.** . . 186
9.5 **AFM of a device irradiated at the memristive dose.** 186
9.6 **Sketch of simulated dose delivery.** 187
9.7 **Typical *I-V* and gate curves of non-irradiated CVD devices.** 188
9.8 **Gate-tunable resistive switching in the helium ion beam-fabricated memtransistor.** 189
9.9 **Example of switching on another 1L CVD device.** 191
9.10 **Switching behaviour in mechanically-exfoliated bilayer MoS_2.** 192
9.11 **Examples of resistive switching on mechanically-exfoliated samples of different layer number.** 192
9.12 **Consecutive switching cycles of a monolayer CVD memtransistor device.** . . . 193
9.13 **Cycling endurance and stability of resistance states.** 194
9.14 **V_{set} & V_{reset} stability, and a simplified circuit diagram of the device.** 196
9.15 **Lissajous figure of the memtransistor at high s_r.** 197
9.16 **Fits to the SCLC and TLC models in HRS.** 200
9.17 **Neuromorphic memtransistor performance, cross-terminal conductance modulation and pulsed input response.** 202
9.18 **Higher impulse response, retention characteristics at different read biases and binary switching characteristics.** 203

9.19 **Representative sketch outlining the device geometry.** . . . 205
9.20 **Raman and PL spectroscopic characterisation of the memtransistor in different resistance states.** . . . 207
9.21 **Raman and PL spectra averaged from each side of the fissure on the switched device.** . . . 208
9.22 **Additional Raman maps and normalised PL spectra.** . . . 209
9.23 **Raman and PL spectroscopic characterisation of helium ion fissures created at doses of 0.2 pC μm^{-1} and 2 pC μm^{-1}.** . . . 211
9.24 **PL line profiles of fissure regions at different ion doses and emission energies.** . . 212
9.25 **Effects of asymmetric irradiations on initial resistance state setting.** . . . 214
9.26 **Irradiations of suspended MoS_2 for *in-situ* biasing in the TEM.** . . . 216
9.27 **Effects of biasing the sample *in-situ* in the TEM.** . . . 217
10.1 **TEM images of asymmetric HIM irradiations on MoS_2 as a function of stage tilt, Θ.** . . . 224
10.2 **Images of a memtransistor device irradiated at 50°.** . . . 225
10.3 **Schematics of the asymmetrically-irradiated memtransistor device and HRTEM image of the fissure.** . . . 226
10.4 **Electrical characteristics of MoS_2 memtransistors relative to the asymmetry of the ion beam-created fissure.** . . . 227
10.5 **Evidence of asymmetric defect migration taken in the SEM.** . . . 230
10.6 **Effects of crystal orientation during irradiation.** . . . 232
10.7 **Switching mechanism basis.** . . . 234
10.8 **Switching between states.** . . . 235
10.9 **Temperature-dependent output and transfer characteristics of the monolayer MoS_2 memtransistor in the high and low resistance states.** . . . 236
10.10 **Impact of device resistance states on electron transport.** . . . 238
10.11 **Electron mobility scaling with temperature, before and after irradiation at different gate biases.** . . . 240
10.12 **Conductance mechanisms, carrier localisation lengths and carrier injection barrier heights in the two resistance states.** . . . 243
10.13 **1/f noise in the temporal traces of current in each resistance state.** . . . 246
10.14 **Pink noise spectra and the current density saturation response of the memtransistor states at different carrier concentrations.** . . . 247
10.15 **Low-field current density saturation as a function of temperature in the two resistance states at different carrier concentrations.** . . . 250
11.1 **Large-scale device fabrication.** . . . 257

1 **Plot of the concentration of the three phases in the simulation as they change with iteration number.** 294
2 **Trial and error plots for different combinations of conductances between the 3 phases $C1$, $C2$ and $C3$.** 294
3 **Example conductance plots and associated phase concentration charts generated for the cases of networks where sites are not destroyed and where all sites eventually are destroyed.** 295
4 **Defining the current polarity in the MoS_2 memtransistor.** 297

List of Tables

Number *Page*

5.1 **XPS peak shifts with exposure time relative to the C 1s core line.** 115

6.1 **Summary of extracted a exponents in each temperature regime for every plasma treatment time.** 141

8.1 **Summary of exposure parameters used to make patterns for different I_R exposures.** 157

8.2 **Summary of different device qualifiers extracted for statistical analyses.** . . . 173

9.1 **Summary of ion BID heights on different samples mapped with AFM.** 187

9.2 **A summary of various performance parameters from relevant MoS_2 memory devices in the literature.** 198

9.3 **Summary of spectral fitting parameters.** 209

10.1 **Asymmetric irradiation parameters for TEM imaging.** 222

10.2 **Asymmetric irradiation parameters employed for electrical testing.** 225

Acronyms

1L single-layer. 8, 64

2D two-dimensional. 1–4, 7, 11, 16, 18–20, 22–26, 30, 33, 34, 36, 37, 39–43, 46, 48, 50, 55, 56, 58, 59, 61, 65, 74, 83, 86, 88, 103, 108, 113, 116, 120, 122, 124, 127, 129–131, 133, 135–137, 141–143, 150, 181, 185, 198–200, 218, 237, 243, 249, 250, 253, 256, 257

ACSTEM aberration-corrected scanning transmission electron microscopy. 44, 45, 49, 50, 86, 94, 113, 116–121, 125, 127, 131

AFM atomic force microscopy. 34, 43–45, 66–68, 79–81, 108–110, 153, 168, 185–187

BID beam-induced deposition. 184–187

CAD computer-aided design. 70

CMOS complementary metal-oxide-semiconductor. 1, 32

CNF carrier number fluctuation. 13, 14, 247, 248

CRANN Centre for Research on Adaptive Nanostructures and Nanodevices. 67, 81, 84, 89, 97, 144, 290

CVD chemical vapour deposition. 12, 14–16, 34, 37, 45, 48, 62, 63, 69, 70, 143–146, 151, 153, 155–157, 166, 168, 178, 182, 183, 186, 188–190, 193–195, 203, 206, 210, 211, 213, 216, 218, 222, 224, 229–231, 237, 240, 241, 251

DFT density functional theory. 46

EBL electron beam lithography. 68, 70–72, 97, 133, 144, 155, 182, 218, 254, 258, 289

EDX energy-dispersive X-ray spectroscopy. 84, 92–94, 111–113, 119–122, 182, 217, 218

EELS electron energy loss spectroscopy. 93, 94, 119, 120

ES Efros–Shklovskii. 12, 133, 140–142, 254

ET Everhart-Thornley. 82, 83

FET field effect transistor. 4, 5, 13–23, 34, 35, 37, 40, 45–50, 57–59, 76–78, 103, 106, 108, 122, 123, 126, 127, 131, 133, 135–137, 139, 141–148, 150, 152, 153, 155–157, 159, 161–163, 165, 166, 168, 175, 177–179, 182, 188, 189, 213, 215, 229, 237, 239, 243, 244, 246, 248, 251, 253, 254, 256, 258, 297

FFT fast Fourier transform. 182, 183, 222–224

FIB focused ion beam. 51, 184

FWHM full-width-at-half-maximum. 75, 89, 91, 111, 114, 115, 151, 162

GB grain boundary. 15, 33–37, 165–168, 171–173, 175, 177, 178, 181, 198, 199, 229, 256

GFIS gas field ion source. 51

HIM helium ion microscope. 3, 51, 52, 76–78, 181–183, 185, 216, 217, 222, 224, 236, 257, 258

HRS high resistance state. 33–35, 189, 190, 192, 193, 195, 196, 198–205, 207–210, 213–215, 228, 231, 233–251, 258

HRTEM high-resolution transmission electron microscopy. 56, 117, 118, 136, 137, 222, 225, 226

IMFP inelastic mean free path. 96, 291

IPA propan-2-ol. 62, 65, 73, 133, 144, 185, 216, 289, 290

LPE liquid phase exfoliation. 62, 65

LRS low resistance state. 33–36, 189–193, 195, 198–205, 207–210, 213–215, 221, 227, 228, 231, 233–251, 258, 298

LTD long term depression. 32, 35, 36, 201–203

LTP long term potentiation. 32, 35, 36, 201–203

MIT metal-insulator transition. 11, 12, 237–239

MOSFET metal-oxide-semiconductor field effect transistor. 17, 18, 46, 135

NA numerical aperture. 144, 206

NDR negative differential resistance. 29, 33, 191–193

NNH nearest-neighbour hopping. 12, 58, 141

PL photoluminescence. 34, 50, 64, 67, 90, 91, 95, 111–113, 115, 142–144, 151–153, 206–214, 233

PMMA poly(methyl methacrylate). 49, 69, 70, 72–74, 133, 144, 216, 222, 289

RMS root mean square. 45, 109, 187

rpm revolutions per minute. 71, 289

RTN random telegraph noise. 15, 246

SCLC space-charge limited current. 198–200

SE secondary electron. 75, 82, 83, 98, 109, 152, 182, 183, 229

SEM scanning electron microscopy. 52, 64, 72, 78, 81–84, 92, 98–100, 109, 110, 120–122, 133, 134, 152, 158, 159, 162, 166, 168, 182, 183, 185, 186, 208, 225, 229, 230, 233, 289

SMU source measure unit. 100, 101, 133, 144, 193, 298

SRIM stopping range of ions in matter. 164, 165, 256

STEM scanning transmission electron microscopy. 56, 58, 85, 86, 120

TEM transmission electron microscopy. 55, 56, 62, 72, 74, 84–86, 92–94, 121, 122, 131, 182–185, 187, 213, 216–218, 222, 224, 232

TLC trap limited current. 198–200

TMD transition metal dichalcogenide. 1, 2, 4, 7–9, 15, 18, 19, 22–24, 26, 36, 39, 40, 42, 43, 45, 46, 48, 50, 55, 64, 72, 73, 97, 131, 140, 147, 156, 179, 181, 192, 255

UHV ultra-high vacuum. 40, 51, 82, 94, 120–122, 131

UV ultraviolet. 39, 43, 71

VCM valence change memory. 30

VRH variable-range hopping. 12, 13, 58, 140, 241, 244

XPS X-ray photoelectron spectroscopy. 48–50, 64, 94–97, 111–114, 253

Chapter 1

Overview

1.1 Motivation and wider context

Since the invention of the germanium transistor by Bardeen, Brattain and Shockley in 1947 [1], the semiconductor industry has striven for progress in on-chip circuit technologies that underpin our daily lives. The modern age of electronics is rapidly approaching a paradigm shift, as Moore's Law begins to falter beyond the 10-nm node regime [2]. The International Roadmap for Semiconductor Technology has recently been replaced by the International Roadmap for Devices and Systems [3], reflecting the change in focus with regard to new integrated circuit design and implementations of nanotechnology in everyday devices. As the Internet of Things and neural network computing come to the fore of scientific research worldwide, efforts have shifted to multidisciplinary approaches combining various areas of physics, chemistry, engineering and biology.

Spearheading this movement in the field of nanoscience is the area of two-dimensional (2D) materials, where recently-discovered allotropes of well-known chemical compounds have proven to exhibit extraordinary properties when studied on the nanoscale. Graphene, the prototypical 2D material, has attracted tremendous interest since its discovery in 2004 [4]. Owing to its superlative physical properties such as high carrier mobility [5], minimum electrical conductivity [6], mechanical strength [7] and thermal conductivity [8], it has garnered much institutional funding [9] and scrutiny from both experts and the public. In recent years, doubts have been cast as to the fruition of graphene-related research [10] when it comes to everyday applications. Long-heralded as the successor to silicon-based technology, graphene faces considerable challenges. Notably, the fact that it does not possess a band gap limits its ubiquitous use in radio frequency amplifiers and complementary metal-oxide-semiconductor (CMOS)-like logic [11, 12]. In addition, the isolation of high crystal quality large-area graphene is currently a far cry from the industry-standard Czochralski process.

Researchers have begun to migrate beyond planar carbon in search of low-dimensional materials that could prove useful in new generation flexible electronics, photodetectors, light emitting diodes and tunnelling transistors. Transition metal dichalco-

genide (TMD) compounds are a family of layered inorganic crystals, whose versatile physical properties are complementary to that of graphene. When considering electron-rich systems in two dimensions, non-trivial physical behaviour also emerges for these crystalline solids. The advent of 2D van der Waals crystals has hence led to a boom in fundamental solid-state physics research, where decade-old theories that were thought to be experimentally unverifiable have found confirmation through work done in van der Waals heterostructures [13]. The ability to manipulate these properties on the nanoscale is a central theme of this thesis, with particular focus on the electrical properties and devices which could be fabricated using TMDs.

In recent years, monolayer molybdenum disulfide (MoS_2) has come to rival graphene in research interest and device application since the demonstrations of single layer semiconducting devices in 2010-2011 [14, 15, 16, 17]. It thus naturally became the focus of fruitful research for many groups working on nanoscale devices. Although the issues plaguing pristine MoS_2 flakes are far from solved (contact resistance, yield of fabrication, grain boundaries, high concentration of unwanted impurities, etc.), many groups have begun to look into intentionally-defective MoS_2 as a platform for unconventional physics and devices. At the same time, research into nonlinear electronics which began in the 1960s with devices such as the Esaki diode and the Josephson junction [18], is experiencing a renaissance period with the discovery of *resistive switches* which mimic the physical behaviour of a device known as a *memristor*. Leon Chua, then of Purdue University, set out to axiomatically define the basic characteristics of nonlinear circuit elements in the 1970s. Based on symmetry considerations that linked the basic physical quantities governing passive circuit elements (voltage, current, charge, flux) he argued for the existence of an undiscovered circuit element whose charge depends on the history of the magnetic flux that has passed through it [19]. He henceforth defined a memristor, or *memory resistor*, as a nonlinear circuit element whose resistance depends on the history of the electric current that has flown through it.

In May 2008, a group from HP Labs led by R. Stanley Williams reported in *Nature* the discovery of the first monolithic memristor [20]. This was a stack of TiO_2 sandwiched between Pt electrodes, whose operation depended on the drift of charged oxygen vacancies between the electrodes. The changing concentration of vacancies varied the resistance of the material in a reversible manner, allowing the formation of a pinched hysteresis loop in the *I-V* curve of the resistor - a fingerprint of memristive functionality. The research area exploded in interest, with thousands

of publications on resistive switches emerging in the last decade. Mainly based on oxide semiconductors, these devices can imitate the functionality of synaptic junctions in the brain; which leads to promising applications in future hardware artificial intelligence and bio-realistic circuits. This potential inclusion of both logic and memory in the same device could bring about a new dawn of electronics, where information no longer has to be processed away from the area in which it is stored - as is the case in our computers and smartphones today. The advancements of this scheme, also known as the *non-von Neumann paradigm*, would lead to more energy-efficient and data-intensive computing.

Researchers have been trying to combine the superlative properties of 2D materials, e.g. low power consumption, flexibility, transparency, etc., with the functionality of a memristor. Thus far, this has required the fabrication of vertical van der Waals stacks to mediate conductive filament formation through 2D layers, or careful lithography over vacancy-rich grain boundaries in large-area films grown in specific conditions.

Soon after the first experimental demonstration of the resistive switch, and other more complex architectures implementing memristive devices, it was noticed that the drift of ionic species which allows for the alteration of material resistance closely resembles the electrical resistance modulation of synaptic axons in the brain. A *synapse* is a biological junction in the structure of a nerve cell (*neuron*) which allows for the passing of electrical signals between different cells. It is effectively a two-terminal device whose conductance can be incrementally changed by the electrical charge which has passed through it. Its input conducting wire, the *axon*, carries bio-electrical impulses known as *action potentials* into the synapse. The current model for memory consolidation, known as *Hebbian learning*, relies on groups of neurons consolidating into *engrams* after habituating to a given set of electrical impulses by changing the electrical resistance of the synaptic junction [21]. This synaptic *plasticity* is considered an important factor for the efficacy of learning in the brain.

1.2 Outline of the thesis

In this thesis, we will explore and demonstrate the site-specific and layer thickness-independent method of introducing memristive functionality into 2D semiconductors in the post-metallisation stage using a helium ion microscope (HIM). Hence, we set out the central research question:

"Can we activate novel electronic functionalities in 2D MoS_2 through the intentional introduction of defects and impurities?"

We will discuss two experimental approaches for introducing defects into molybdenum disulfide: **plasma treatment** and **helium ion beam irradiation**.

The former is an easy and cheap method for the global modification of the properties of hundreds of MoS_2 flakes at once by surface doping. A literature review of this approach, utilising different plasma species, will provide detailed context on the experiments described herein. Several characterisation techniques have been availed of in order to figure out what happens to the ultra-thin molybdenite samples when exposed to the oxygen:argon plasma mixture for differing lengths of time. A brief overview of these techniques will be given in order to inform the subsequent analysis. Transistor device fabrication will also be rightly discussed in detail, as the MoS_2 field effect transistor (FET) channel serves as the main platform of study in this thesis.

The latter is a more specialised and highly localised method of modifying materials on the nanoscale. A deeper introduction into beam-sample interaction will hence be required. As the fabricated device is a resistive switch by definition, an overview of memristor science will be needed to contextualise the experimental achievements of our study. The cryogenic charge transport measurements which reveal the functionality of the so-called MoS_2 *memtransistor* will be discussed against the backdrop of well-established condensed matter physics.

The dissertation chapters will explore the following topics:

1. *Fundamentals in 2D MoS_2 and its devices* - a literature review will provide context for the materials and devices investigated in this work.

2. *MoS_2 modification and functionalisation* - we will overview the mechanisms of plasma-mediated doping of TMDs and the tuning of the properties of 2D materials with the helium ion beam.

3. *Characterisation techniques* - this section will be dedicated to describing the process of material growth (or exfoliation), the device fabrication and modification methods, and the experimental techniques employed in this work to characterise our modified materials.

4. *Oxide-mediated recovery of field-effect mobility in plasma-treated MoS_2* - in this chapter we will describe the tuning of the electrical properties of exfoliated MoS_2 by surface doping with O_2:Ar (1:3) plasma. We will outline a model for the surface inclusion of sub-stoichiometric oxides which tune the carrier mobility of MoS_2 FETs as a function of MoS_2 layer number. This will also include simulations of resistor networks and detailed microscopic and spectroscopic studies of the modified MoS_2 devices.

5. *Low-temperature electrical conductance of plasma-treated MoS_2* - we will build on our layer-dependent model from the previous chapter to study the transport mechanisms in highly-defective bilayer MoS_2 at liquid nitrogen temperatures.

6. *Photoresponsivity enhancement in monolayer MoS_2 by rapid O_2:Ar plasma treatment* - a low-dose variant of our plasma approach for functionalising MoS_2 will be applied to synthetic monolayer samples. We will study the beneficial effect of this surface oxide inclusion on the optoelectronic properties of our monolayer FET devices.

7. *Effect of varying the irradiation area on the conductance of monolayer MoS_2* - a systematic study will introduce us to the effects of increasing the He^+ ion beam-irradiated area on synthetic monolayer MoS_2 FETs, with statistical tests evaluating the role of grain boundaries on the electrical transport properties in our starting material.

8. *Neuromorphic MoS_2 memtransistors fabricated by localised helium ion beam irradiation* - a special case of linear high-dose He^+ ion delivery, bisecting the MoS_2 FET channel, will prove to initiate gate-tunable resistive switching in monolayer and multilayer MoS_2 samples. We will evaluate our devices against the typical performance benchmarks, and study the effects of this irradiation with microscopy and spectroscopy to unveil the role of sulfur vacancies in mediating the observed memristive behaviour.

9. *On the nature of resistance states in the MoS_2 memtransistor* - the final results chapter will consider the role of asymmetry in our irradiated devices and will outline a proposed mechanism for the observed resistive switching. In addition, cryogenic charge transport measurements will inform the physical differences between resistance states observed in the same device.

10. *Conclusions & future work* - we will conclude with remarks on the achievements of this doctoral thesis and what future work they might fuel in the field of low-dimensional devices.

Chapter 2

Fundamentals in 2D MoS_2 and its devices

> "its purposes how dark, yet have we ever sought to produce these thin Sheets innumerable, to spread a given Volume as close to pure Surface as possible, whilst on route discovering various new forms, the Leyden Pile, decks of Playing-Cards, Contrivances which, like the Lever or Pulley, quite multiply the apparent forces, often unto disproportionate results."
>
> - Thomas Pynchon, *Mason & Dixon*, 1997.

In this chapter, we will first briefly concern ourselves with the main material system which is the focus of this thesis - 2D MoS_2. We will overview its crystal and electronic band structures, its fundamental charge transport properties and its usage as a channel in field-effect transistors. We will then review the concept of a memristor and the applications of memristive nano-devices to neuromorphic emulation. This will allow us to contextualise the recent emergence of memristive phenomena in 2D layered semiconductors.

2.1 Layered semiconducting TMDs

In the wake of the graphene boom after 2004, researchers had turned to exfoliating other known van der Waals materials down to single molecular layers using adhesive tape. The Manchester group had shown as early as 2005 that crystal monolayers of $NbSe_2$ and MoS_2 can be produced in the same way as graphene [22]. These two materials are members of the class of transition metal dichalcogenides - inorganic compounds with the general chemical formula $\mathbf{MX}_2$, where **M** denotes a transition metal and **X** is a chalcogen atom (group 16 of the periodic table). TMDs form layered

crystal structures through weak van der Waals bonds between the adjacent layers. A monolayer TMD is three atoms-thin (< 1 nm) and can have electronic properties drastically different from its bulk counterpart, e.g. a direct band gap in single-layer (1L) MoS_2, but indirect in the bulk. A whole zoo of stable molecular arrangements of these monolayer compounds has been predicted to exist computationally [23], though many are difficult to exfoliate from the bulk. Approaches such as liquid phase exfoliation [24, 25] have advanced the production yield of low-dimensional crystals. Synthetic methods of monolayer growth have also been developed over the last 10 years, as well as methods of combining various TMDs together to form vertical and lateral *heterostructures* [26]. Importantly, many representatives of the TMD family are semiconductors, with band gaps of the order of 1-2 eV. One such material - MoS_2 - is the focus of this dissertation.

Molybdenum disulfide, or *molybdenite* in its mineral form, had been studied by the renowned chemist Linus Pauling as far back as 1923 [27]. This relatively common inorganic compound is widely used as a lubricant in the automotive industry, and has long served as an ore for molybdenum metal. The material structure is characterised by S-Mo-S covalent bonds forming the basic units of a molecular layer. These layers then stack vertically in various arrangements, forming bulk molybdenite through interlayer van der Waals bonding. Various *polytypes* (stacking orders) have been identified, including 2H, 3R, 1T and 1T′ (**Figs. 2.1(a,b)**).

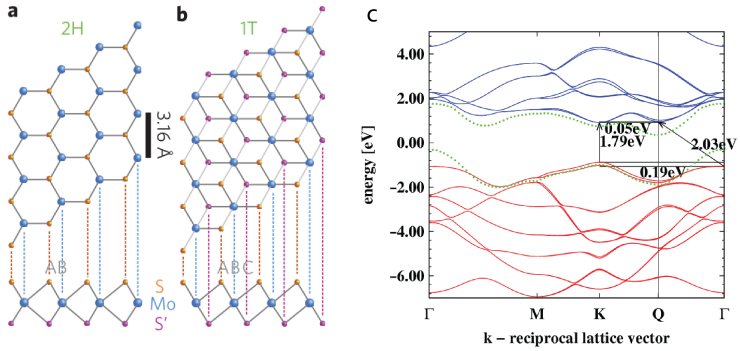

Figure 2.1: The structure of **(a)** 2H-MoS_2 and **(b)** 1T-MoS_2 polytypes [28]. **(c)** The electronic band structure of monolayer 2H-MoS_2 [29].

For the most common polytype, the semiconducting 2H-MoS_2, when viewed along the [0001] direction, the Mo and S atomic columns form a hexagonal lattice, reminiscent of graphene sheets. The unit cell parameters are defined by the following primitive vectors [30]:

$$\vec{a} = (a, 0, 0), \quad \vec{b} = \left(\frac{a}{2}, \frac{\sqrt{3}a}{2}, 0\right), \quad \vec{c} = (0, 0, c) \tag{2.1}$$

where a = 3.15 Å and c = 12.3 Å [31]. This results in a trigonal prismatic coordination for the Mo^{4+} centre and the six surrounding sulfide ligands. Note; $\vec{a}$ and $\vec{b}$ are in-plane, while $\vec{c}$ is out-of-plane and is the height of the conventional 2H unit cell, rather than the physical thickness of a monolayer.

The electronic band structure of single-layer 2H-MoS_2 (**Fig. 2.1(c)**) reflects its semiconducting character, with the Fermi level located in between the conduction and valence bands [29]. The direct band gap is located at the $\mathcal{K}$ point of the Brillouin zone, and has been reported to be anywhere between 1.79 - 1.85 eV in energy; while the effective mass of electrons is (unusually) higher than that of holes. The shape of the conduction bands is largely governed by the hybridisation of the S 3p and Mo 4d orbitals; which is also sensitive to the introduction of further molecular layers, resulting in a direct-to-indirect gap shift for multi-layer MoS_2. As there are no dangling bonds on the basal plane, many TMD crystals are stable in atmosphere unless considerable defects are present on the surface to provide chemically-active sites.

2.2 Condensed matter phenomena in MoS_2

To understand the effects of ion modification on the electronic properties of MoS_2, let us first briefly contextualise the background of relevant condensed matter phenomena in monolayer MoS_2, especially those observed at low (liquid helium) temperatures. These phenomena, including the metal-insulator transition, carrier transport mechanisms, 1/f noise and current density saturation, provide abundant information for us to understand the defect-mediated electronic processes.

2.2.1 Metal-insulator phase transition and transport mechanisms

In 2013, Radisavljevic and Kis studied the cryogenic charge transport in back and top-gated exfoliated monolayer MoS_2 (**Fig. 2.2**) [32]. For the back-gated device, they observed standard semiconductor-like electron mobility scaling with decreasing temperature. This dependence was characterised by a drop in mobility above ~ 200 K as $\mu \sim T^{-\gamma}$, with $\gamma \approx 1.4$, due to electron-phonon scattering which dominates at high temperatures, and a drop in mobility below ~ 200 K due to scattering from charged impurities. The electrical conductance, G, was observed to follow

Arrhenius-like activated behaviour with temperature, with the conductance dropping at low temperatures, even at very high gate biases.

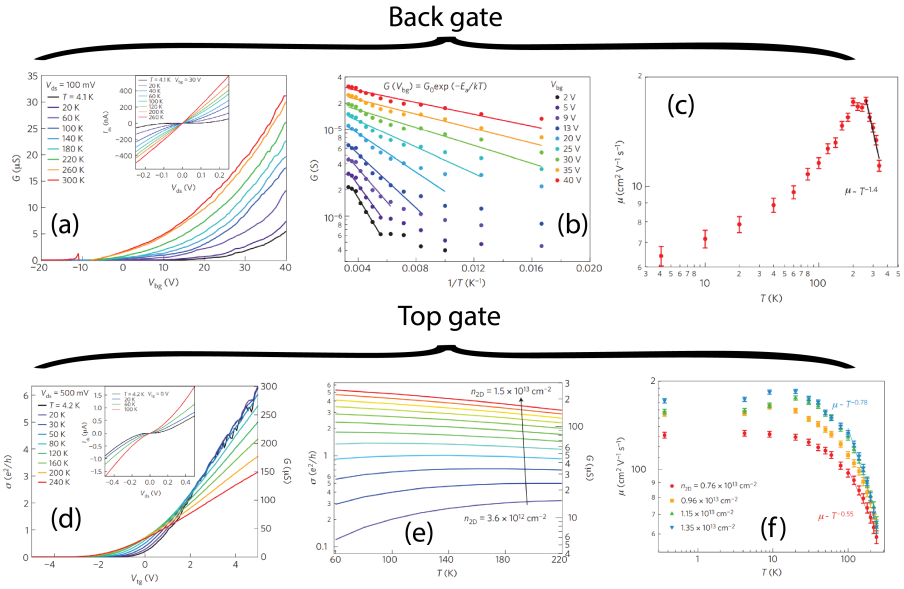

Figure 2.2: **Metal-insulator transition in monolayer MoS_2.** **(a)** Conductance, G, as a function of back-gate bias, V_{bg}, for a single-gate monolayer MoS_2 device acquired at different temperatures. The inset shows double sweeps of I_{ds}–V_{ds} characteristics for several temperatures at V_{bg} = 30 V with negligible hysteresis for all temperatures. **(b)** Arrhenius plot of G for different values of V_{bg}. Solid lines are linear fits to the data showing activated behaviour for limited regions of T and V_{bg} (charge density). **(c)** The dependence of μ on T shows a pronounced low-temperature regime consistent with transport dominated by scattering from charged impurities. Above ~ 200 K, μ is limited by phonon scattering and follows a $\mu \sim T^{-1.4}$ dependence. Error bars are estimated on the basis of uncertainties in determining the voltage drop across the channel. **(d)** G and σ for different values of the top gate bias, V_{tg} and T. For low values of V_{tg}, σ decreases with T. Above V_{tg} ~ 1–2 V, monolayer MoS_2 enters a metallic state, with increasing σ as T is decreased. The inset shows double I_{ds}–V_{ds} sweeps. **(e)** T-dependence of σ for different values of n_{2D}. **(f)** μ is practically independent of T under 30 K, indicating screening of charged impurities due to deposition of the top-gate dielectric. Above ~ 100 K, μ decreases owing to phonon scattering and follows a $T^{-\gamma}$ dependence with γ = 0.55–0.78. The strongly reduced value of the exponent γ with respect to the single-gated device (γ = 1.4) is indicative of phonon mode quenching. Error bars are estimated on the basis of uncertainties in determining the voltage drop across the channel. All figures and captions adapted from [32].

The two-dimensional carrier concentration, n_{2D}, is calculated using a parallel plate capacitor model:

$$n_{2D} = \frac{C_{ox} \cdot \Delta V_g}{e} \tag{2.2}$$

where the gate oxide capacitance is $C_{ox} = \frac{\varepsilon_0 \varepsilon_{ox}}{d_{ox}}$, the permittivity of free space $\varepsilon_0 = 8.85 \cdot 10^{-12}$ F m^{-1}, the electronic charge $e = 1.6 \cdot 10^{-19}$ C, $\Delta V_g = V_g - V_{th}$, d_{ox}

is the oxide thickness, V_g is the gate voltage and V_{th} is the threshold gate voltage. The quantum capacitance of the channel ought to be treated in series with the gate oxide capacitance above some critical gate voltage. As the quantum capacitance is a function of the valley degeneracy of the given material system and also of its effective electron mass (parameters that may not be known accurately, especially in heavily defective systems), these additional considerations are often not incorporated into experimental results, making the absolute values of n_{2D} which are extracted somewhat inaccurate [33]. The parallel capacitor model tends to overestimate the 2D carrier concentration by $\sim 30\%$ at $n_{2D} \sim 10^{12}$ cm^{-2}, but only by about 2.5% at $n_{2D} \sim 10^{13}$ cm^{-2} [34], and is thus often used in studies of 2D materials gated into saturation.

Digression aside, when monolayer MoS_2 is encapsulated in high-κ HfO_2, a crossover of conductance regimes is observed above a certain carrier concentration. Both the device conductance and electron mobility are seen to increase with decreasing temperature, indicating metallic-like behaviour in the device at low temperatures. A so-called *metal-insulator transition* above a charge density $\sim 10^{13}$ cm^{-2}, as mediated by the increasing gate bias, was hence reported and proposed to arise from electron-electron correlation effects and weak localisation in this high n_{2D} regime. Below the critical gate voltage necessary to induce the metal-insulator transition (MIT), the device retains its insulator (semiconductor) nature until enough electrons are present in the channel so that the *Ioffe-Regel criterion* [35] of a strongly-interacting regime is reached, i.e. $k_F \cdot l_e >> 1$, where the respective Fermi wave vector and elastic mean free path of the carriers are defined as:

$$k_F = \sqrt{2\pi n_{2D}} \quad \text{and} \quad l_e = \frac{\hbar k_F \sigma}{n_{2D} e^2} \tag{2.3}$$

where $\hbar$ is the reduced Planck constant, σ is the conductivity and e is the electronic charge.

A similar crossover and mobility scaling were also observed in hexagonal boron nitride-encapsulated multilayer MoS_2 [36], unencapsulated exfoliated monolayer [37] and multilayer MoS_2 [38], and polymorphic 1T/2H-MoS_2 [39, 40] (**Fig. 2.3(a-b)**). Interestingly, the approach to the transition is asymmetric in temperature scaling from the metallic and insulating sides, due to differing dielectric screening environments. This asymmetry is weakened, however, in the monolayer regime where the MIT is thought to be disorder-driven [38].

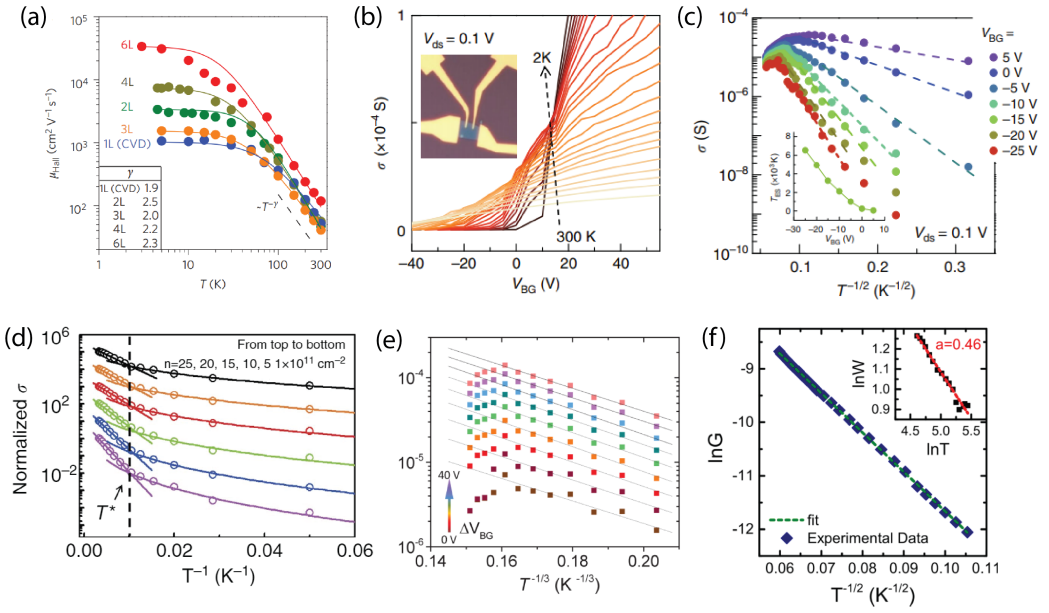

Figure 2.3: **MIT crossovers and hopping transport reported in MoS_2.** **(a)** Electron mobility scaling with temperature in encapsulated MoS_2 of various layer number [36]. **(b)** MIT crossover observed in back-gated few-layer MoS_2. [38] **(c)** ES hopping behaviour fitted to the sample in **(b)** [38]. **(d)** NNH mechanism fits to monolayer MoS_2 [41]. **(e)** VRH mechanism fits to single-layer CVD MoS_2 [42]. **(f)** Plot showing good fits to ES hopping in polymorphic MoS_2. Inset: Zabrodskii analysis plot. [39]. μ; electron mobility, T; temperature, σ; conductivity, G; conductance.

Evidence for various charge transport mechanisms in MoS_2 has emerged in recent years, including the nearest-neighbour hopping (NNH) ($\sim T^{-1}$), the variable-range hopping (VRH) ($\sim T^{-1/3}$) and the Efros–Shklovskii (ES) ($\sim T^{-1/2}$) regimes (**Fig. 2.3(c-f)**). These mechanisms have long been studied in the case of lightly-doped and disordered semiconductors. Briefly, the hopping of carriers between defective sites is effectively described by the probability of carrier tunnelling between sites separated by some distance in the crystal lattice - subject to parameters such as the localisation length and energy [43]. An analysis of empirical data, originally proposed by Zabrodskii [44], allows for the extraction of the parameter W:

$$W = -\frac{\partial \ln \rho}{\partial \ln T} \tag{2.4}$$

where ρ is the device resistivity and T is the measured temperature. Thus, the conduction mechanism can be determined from the slope of the plot of $\ln(W)$ versus $\ln(T)$, due to the exponential dependence of conductivity on the temperature and the device dimensionality [39, 40, 45]. Reports on chemical vapour deposition (CVD)

monolayers of MoS_2, in particular, point to a modified trap-mediated VRH mechanism, due to the increased concentration of sulfur vacancies relative to exfoliated crystals [41, 42].

2.2.2 1/f noise spectroscopy

1/f noise spectroscopy, also known as *pink* or *flicker* noise in electronics, is a meaningful auxiliary experimental technique for the study of the role of carrier localisation (and hence the transport mechanism) in semiconducting devices. We will avail of this technique when studying temperature-dependent current traces across helium ion beam-created "synthetic boundaries" in MoS_2 in the last chapter of this thesis. The presence of short range disorder (e.g. defects, vacancies) in crystalline materials leads to carrier trapping and de-trapping as charge is transported across the FET channel. This naturally causes a temporal fluctuation in the recorded current across the channel terminals. The power spectral density of the frequencies (f) composing the raw signal is of the form:

$$S_I(f) \propto \frac{1}{f^{\beta}} \tag{2.5}$$

where the exponent β is usually close to 1. Whereas the commonly-known phenomenon of *white noise* has equal intensity at different frequencies, the intensity of 1/f noise falls off every time the frequency is doubled (for each octave). Thus, low-frequency 1/f spectroscopy allows for the probing of physical phenomena happening at $\sim$ 0.01 - 10 Hz.

These time-domain current fluctuations are thought to arise from the variation of the carrier mobility as carriers traverse the channel and undergo scattering, as well as the carrier number fluctuation (CNF) relating to the available charge concentration in the conductor. Thus, the amplitude of 1/f noise will vary in MoS_2 channels when the device is gated (**Fig. 2.4(a-b)**), as the different stages of the field effect change the number of available carriers in the channel [46, 47], as well as at different drain-source biases due to differing carrier injection at the contacts [48].

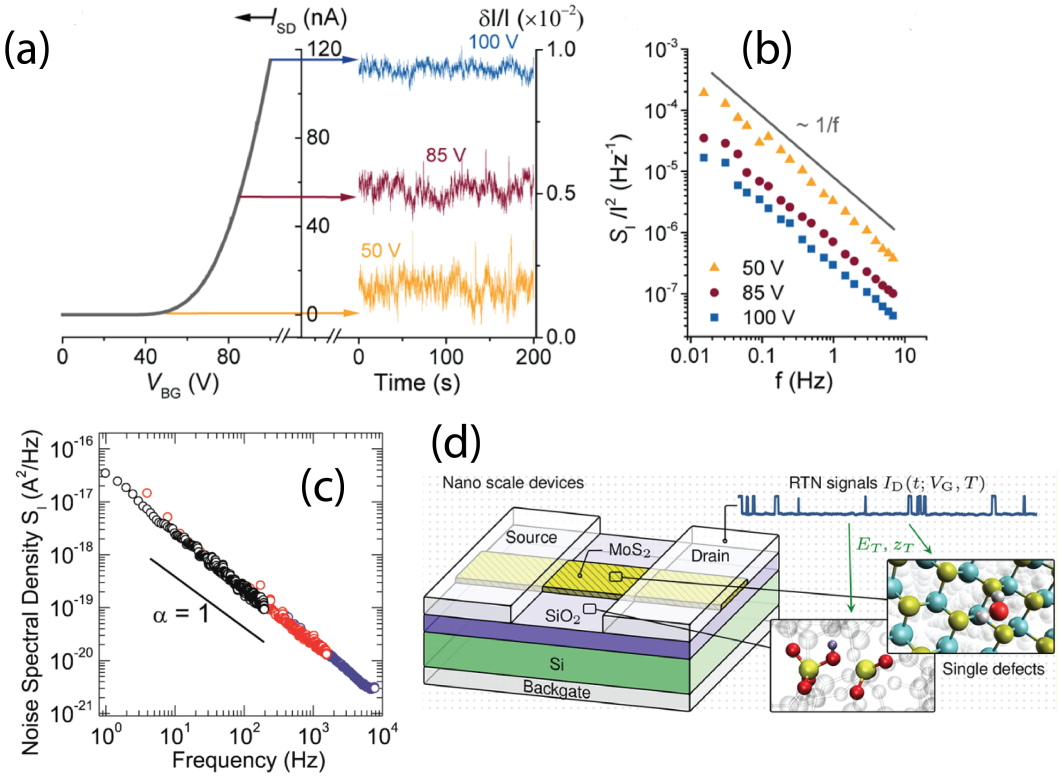

Figure 2.4: **Pink noise in MoS_2.** **(a)** Transfer characteristics (left) of a grain boundary-containing region of a monolayer CVD MoS_2 device, with the corresponding time series of current fluctuations at three gate voltages shown on the right [42]. **(b)** Normalised power spectral density S_I/I^2 as a function of frequency at V_g = 50, 85, and 100 V obtained from **(a)** [42]. **(c)** Noise spectral density (S_I) as a function of frequency at V_g = 20 V and V_{ds} = 0.2 V, showing $1/f^{\beta}$ behaviour with β = 1.07 ± 0.01 in monolayer CVD MoS_2. The black line shows ideal $1/f$ behaviour [46]. **(d)** Time series of drain-source current showing RTN spikes due to single defects in MoS_2 FET channels [49]. I, I_{SD}, I_D; drain-source current, T; temperature, t; time.

Sangwan *et al.* [46] have shown that the measured low-frequency 1/f noise in pristine monolayer MoS_2 can be explained by the *Hooge model* (**Fig. 2.4(c)**), depending on the device environment (pressure level, adsorbates, etc.). The Hooge empirical law is expressed as:

$$S_I = \frac{AI^{\gamma}}{f^{\beta}} \tag{2.6}$$

where S_I is the current power spectral density, I is the mean device current, f is the frequency and A is the noise amplitude. The exponents β and γ are ideally close to 1 and 2, respectively. Studies of passivated MoS_2 devices, however, showed strong deviation from the Hooge formalism, with CNF arising from substrate-related de-trapping being the likely candidate to explain current noise in these non-bulk

transistors [50]. Hsieh *et al.*, in turn, studied the dependence of 1/f noise on the presence of grain boundaries in monolayer CVD MoS_2. Unsurprisingly, they found that as carriers traversed grain boundary (GB) regions in MoS_2, the amplitude of pink noise was orders of magnitude higher than in pristine single-grain regions of the same sample, across a range of temperatures [42]. A modified McWorther model, which is often used to consider the role of traps at the channel-dielectric interface [51], helped to explain the dependence of this amplitude on the increased trap density in the GB region. The electrical conductance and mobility across GBs in MoS_2 [52] depends on the orientation angle of the boundary relative to the contacts [53]. This suggests that the underlying transport mechanism in each case stems from strong localisation effects at GBs in one extreme, and the presence of extended metallic mid-gap states [54] in the other extreme. Such states have been previously observed in monolayer TMDs with spectroscopic techniques [55, 56]. In addition, noise measurements on ultra-scaled (65×50 nm) MoS_2 FETs (**Fig. 2.4(d)**) with a very low defect concentration ($< 10^{12}$ cm^{-2}), elucidated the origin of random telegraph noise (RTN) spikes in the recorded non-stationary drain-source current signal [49]. The charge capture and emission times were extracted for single vacancy traps, while adsorbate-born noise spikes could be distinguished from those originating in gate oxide traps.

2.2.3 Current density and carrier velocity saturation

As carriers traverse the FET channel, they do so with a transit frequency often defined as:

$$f_T = \frac{v_d}{2\pi L} \tag{2.7}$$

where v_d is their drift velocity and L is the carrier transit length (device channel length) [57, 58]. Due to scattering from phonons, v_d approaches a saturation value (v_{sat}) when the lateral electric field applied across the channel begins to exceed 1 V μm^{-1} [59]. In the Caughey-Thomas model [60], v_{sat} is related to v_d through the carrier mobility (μ) and the applied electric field (F):

$$v_d(F) = \frac{\mu F}{\left[1 + \left(\frac{\mu F}{v_{\text{sat}}}\right)^{\gamma}\right]^{1/\gamma}} \tag{2.8}$$

where γ is a fitting exponent that governs how rapidly the low-field linear regime turns over to the high-field saturation regime [61]. Though self-heating effects are

often not included in the model, it accurately describes the reduction in carrier velocity both with increasing F and increasing n_{2D} in the FET channel [62]. This velocity saturation effect ultimately limits the clock rate of the transistor and controls the charge transport across the FET channel in the high-field regime. In monolayer CVD MoS_2, experimentally-verified v_{sat} can be as high as $\sim 3.4 \cdot 10^6$ cm s^{-1} [63]. Fits to the model at different temperatures are presented in **Figs. 2.5(a-c)**

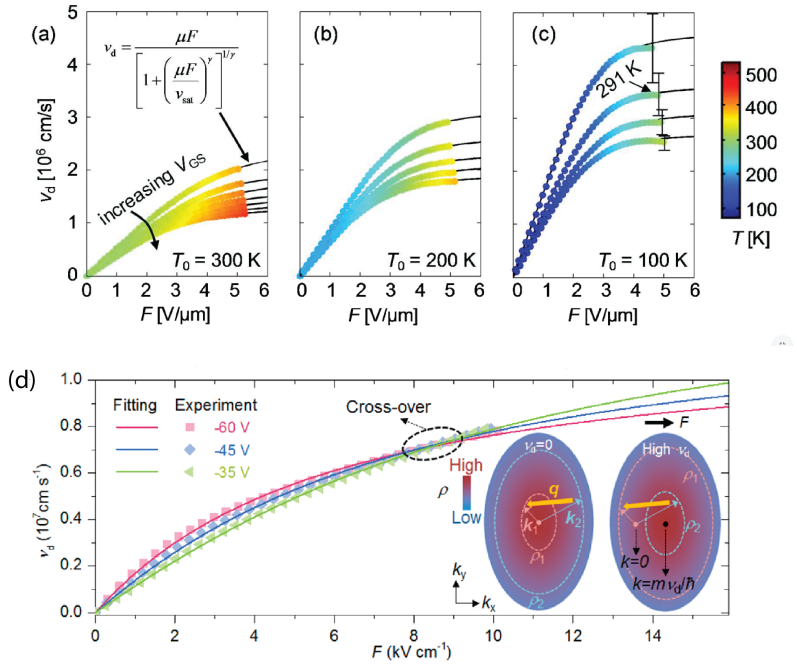

Figure 2.5: **Drift velocity saturation in ultra-thin layered semiconductors.** Extracted velocity-field relationships in MoS_2 FETs at **(a)** T_0 = 300 K, ambient, **(b)** T_0 = 200 K, ambient, and **(c)** T_0 = 100 K, ambient. Symbols are data points, with colours indicative of device operating T and black lines are empirical fits using the Caughey-Thomas equation. The device self-heats by ΔT up to $\sim$ 200 K at lateral fields in the velocity saturation regime. v_d and hence v_{sat} increase at lower T_0, as expected. **(a-c)** adapted from [63]. **(d)** Theoretical fittings of v_d at 80 K in black phosphorus FETs. Inset shows the illustration of the drifted Fermi-Dirac distribution model at vanishing and high drift velocity; adapted from [64]. V_{GS}; gate-source bias, ρ; carrier population, m; effective mass, $\hbar$; reduced Planck constant, F; electric field magnitude, T; temperature, k, q; reciprocal space vectors, μ; carrier mobility.

The reason why we want to consider v_{sat} (and by extension the current density saturation, $J_{sat} = v_d \cdot e \cdot n$, where e is the electronic charge and n is the carrier density) at all in this work, is that the onset of saturation for a given F also depends on the concentration of impurities in the 2D FET channel. v_d is heavily dominated by electron-impurity and electron-phonon scattering in the high-field regime for an n-type transistor like MoS_2. A crossover exists between the scattering regimes that govern the physics of the low-field and high-field scenarios, when one has

the ability to tune both the carrier density and the lateral field. At low fields, v_d scales linearly with F, according to the mobility-proportional model also observed in black phosphorus [64] and graphene [61]; in line with the classical Drude model for scattering from long- and short-range impurities in the crystal lattice. As the carrier density increases (through gating, for example), the enhanced screening of the impurity potentials by the field effect now enveloping the channel leads to higher mobilities and drift velocities.

As illustrated in the k-space diagram in the inset of **Fig. 2.5(d)**, at low v_d the carrier population (ρ) with low crystal momentum values is high, as governed by the Fermi-Dirac distribution. Note that this diagram is for black phosphorus and is thus anisotropic along k_x and k_y due to its crystal structure. As the velocity is increased at low fields, the carriers move and are scattered by phonons with momentum $q = k_2 - k_1$, whose energy is absorbed by the charge carrier. The situation is reversed in the high-field regime. ρ is higher for larger values of k. Carriers with higher energy are more likely to transfer that energy into creating a phonon, thus leading to an overall gain in the phonon emission. This roughly scales as $\sim v_d^{2-4}$ and linearly with the effective mass (m) and the dopant concentration (n) [64], increasing the phonon population at high fields. The excess energy gained by electrons due to the high electric field will then be used to produce a larger phonon population, whose concentration will increase the rate of scattering for electrons in the crystal, ultimately saturating the drift velocity to v_{sat}.

Thus, electron-impurity scattering is the governing mechanism for transport in the low-field regime [64]. Since phonon gain will increase with rising n, we can thus expect the saturation of v_d to be much more rapid in MoS_2 samples containing a lot of defects and impurities. In the limit where the dopant concentration difference between samples is not high ($n_{2D} \sim 10^{11}$-10^{12} cm^{-2}), studying the current density saturation behaviour of the devices at high lateral fields can reveal to us the differing dynamics of charge transport across the FET channel. This idea will be explored experimentally as a function of temperature in the last chapter of this dissertation.

2.3 TMD MOSFETs

The metal-oxide-semiconductor field effect transistor (MOSFET) is the main experimental platform of choice for this thesis. Therefore, we need to overview the working principles of these devices, their figures of merit and potential shortcom-

ings, in order to have a good idea of how the modification of the MoS_2 FET channel affects the electrical properties of the material.

2.3.1 Basic principles of 2D MOSFETs

Semiconductors have long been utilised as materials in MOSFET channels. The carrier density of the channel can be modulated through the application of a *gate* voltage, V_g through a *gate dielectric*. Much like in the case of a capacitor, by charging one plate on the side of an insulating spacer, we can induce an opposite charge on the plate on the other side of the dielectric. A high enough voltage will produce an *inversion layer* in the semiconducting channel immediately adjacent to the other side of the gate dielectric, allowing enhanced current to flow between the biased *source* and *drain* regions contacting the channel.

The performance of FETs fabricated from bulk materials is hampered by what are known as *short channel effects*. An extremely short channel length results in considerable leakage current between the source and drain terminals in the OFF state, meaning that considerable static power is generated as heat when the FET is OFF [65]. Typical FETs based on 2D layered materials consist of three terminals in electrical contact with what is essentially a system that confines charge carriers in two dimensions. This allows the gate field to act uniformly on all charge carriers in the channel, which in theory should lead to an almost-ideal functionality of the transistor. As seen in **Fig. 2.6**, the molecularly-thin channel of a TMD FET allows for the precise electrostatic control on charge carriers sandwiched between the gate dielectric and the substrate. In addition, the lack of dangling bonds on the surface of TMDs creates less interfacial charge traps that contribute to mobile carrier wave function scattering in the channel [66]. The substrate itself can also act as a gate oxide with a given relative permittivity (e.g. ε_r = 3.9 for SiO_2). Its increased thickness leads to a less-than-ideal scenario where the so-called *back-gate* bias needs to be operated in the range of tens of volts to invert the channel, but for research and development purposes this suffices.

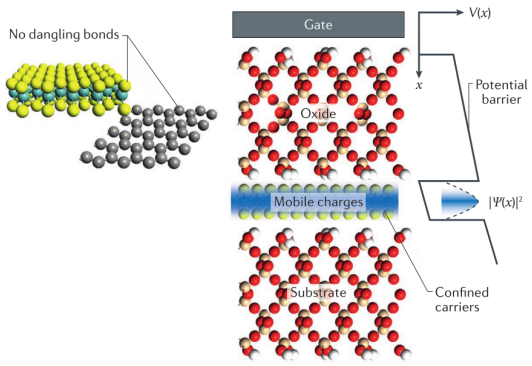

Figure 2.6: Illustration visualising the charge confinement in a single-layer TMD channel encapsulated by a top gate oxide on a substrate (adapted from [67]). Leakage current ought to be minimal at a gate voltage that turns the channel off. $V(x)$ is the electric potential along the x direction defined on the axes.

Fig. 2.7 demonstrates the operating principles of a FET utilising a 2D channel. Panel **a** shows a cross-sectional schematic of an encapsulated FET device. Panel **b** demonstrates the associated energy band alignment between the gate electrodes, gate oxides and the semiconducting channel near the source. The band offsets are parametrised along the z direction by the following quantities: $q\phi_B$ is the energetic Schottky barrier height which exists between the gate metal and the gate dielectric, with qV_i representing the voltage drop inside the dielectric itself. ΔE_c represents the conduction band offset. The quasi-Fermi level of the source electrode E_{Fs}, marked by the dotted line, can be tuned by the gate voltage, V_{g}. This effectively populates a distribution of active carrier modes in the channel, $f(k_x, k_y)$, where k_x, k_y are the perpendicular reciprocal space vectors.

Panel **c** visualises this electron population in the channel as a function of V_{g} at different stages of transistor operation. The semi-logarithmic transfer curve on the bottom of the diagram marks three distinct operation points for the FET. The first from the left highlights the subthreshold region of the device, just before the transistor is turned on. The associated k-space population of electronic states in the channel is limited at this point. As the gate bias is swept past the threshold voltage (V_{T} on the plot), and into the linear region of the FET, k_x and k_y begin to occupy more states until the saturation region is reached in the top diagram, indicating full channel occupation of allowed electron propagation.

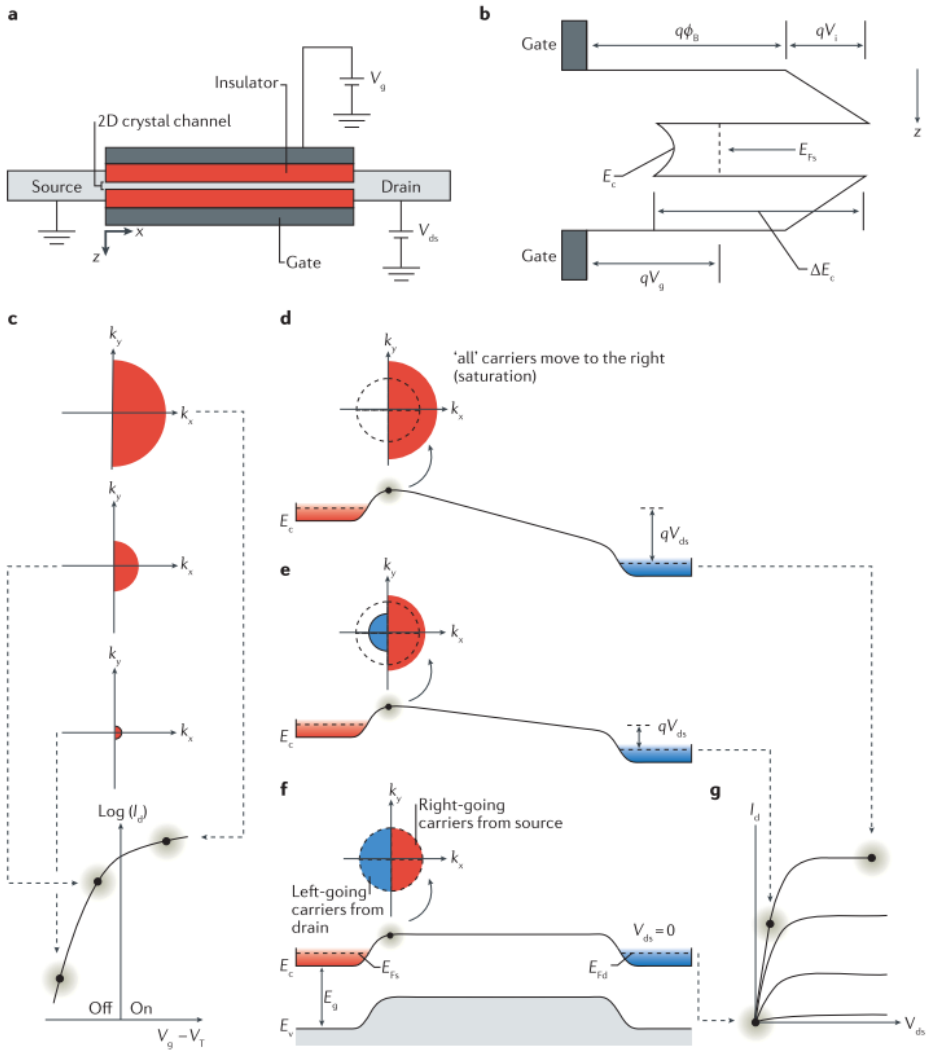

Figure 2.7: Diagram conceptualising the working principles of a 2D FET [65].

Panels **d**, **e** and **f** map onto various regions of the output characteristics (the I_{ds} vs V_{ds} plot), illustrating the band offsets between the source and drain electrodes across the channel at different values of the drain-source bias, V_{ds}. At no applied external bias (**f**), the quasi-Fermi levels are equalised and an equal amount of charges moves in both directions, visualised by the blue and red semi-circles occupying the same area of k-space. As bands are offset by applying a larger and larger V_{ds} through **e** and **d**, the concentration of right-moving red carriers begins to dominate over the left-moving blue carriers, as it becomes energetically favourable for charges to move from source to drain. Eventually all carriers move to the right denoting saturation of the channel. Note that the area of occupied k-space remains constant at a given

gate voltage, just the direction of occupation is shifted subject to the polarity of the applied drain-source bias.

Reaching saturation has several consequences for modern electronics. In a process termed *fan-out*, the saturated I_{ds} of one FET is used as the input at the gate of another in an integrated circuit [65]. If saturation is not reached for a given FET and fan-out fails, the gain of the circuit is substantially reduced. Hence, tunability of the channel by the gate and reduction of static power and leakage must be balanced finely for atomically-thin materials to be employed in future-generation integrated electronics.

2.3.2 Figures of merit

Certain figures of merit, such as the field-effect mobility (μ_{fe}), ON/OFF ratio $\left(\frac{I_{on}}{I_{off}}\right)$ and subthreshold swing (S_{sub}) are often used to categorise the performance of these nanoscale devices; in line with semiconductor device physics formalised in the mid-twentieth century. The field-effect mobility refers to carrier mobility determined using a two-probe measurement, rather than a four-probe Hall effect measurement. μ_{fe} can be evaluated in the linear (ohmic) region of the *transfer curve* (I_{ds} vs V_g) of the transistor, or in the *saturation region*, i.e. where the channel is fully inverted. Extracted values of μ_{fe} from these two regions will differ due to the *pinch-off* condition which can occur at high drain-source biases in FETs; where the I_{ds} dependence on V_g becomes non-linear [58]. A critical perspective on the extraction and reporting of mobility values of FETs can be found in a recent article by Choi *et al.* [68]. Throughout this thesis, we will often consider the field-effect mobility as extracted from the linear region, i.e.:

$$\mu_{fe} = \frac{L}{V_{ds} C_{ox} W} \cdot \left.\frac{\partial I_{ds}}{\partial V_g}\right|_{V_g^{linear}} \tag{2.9}$$

where C_{ox} is the back-gate oxide capacitance (11.5 nF cm^{-2} for 285 nm SiO_2), L and W are the length and width of the FET channel, V_{ds} is the drain-source bias (1 V or less) and the *transconductance* is evaluated at a constant gate bias in the ohmic region (for standard MoS_2 devices this is usually around V_g = 0 V) [17].

The transconductance, $g_m = \frac{\partial I_{ds}}{\partial V_g}$, is the derivative of the output current with respect to the gate bias, i.e. it tracks how sensitive the transistor output is to changes in the applied gate field. If we fit a line to the linear region of the transfer curve on a $\log(I_{ds})$ vs V_g plot, we can obtain the *subthreshold slope*. If we take the reciprocal of

this quantity, we can talk about another common figure of merit for the functionality of a transistor - the *subthreshold swing*. Usually expressed in units of mV dec^{-1}, it effectively describes by how many orders of magnitude (decades) the output current is modulated through small changes of the gate bias; in particular those around the *threshold bias*, V_{th}:

$$S_{sub} = \ln(10) \cdot \left. \frac{\partial V_g}{\partial \log(I_{ds})} \right|_{V_g \approx V_{th}} \tag{2.10}$$

where all the variables have their usual meaning. A smaller S_{sub} corresponds to a steeper transition into the linear region beyond V_{th}, and indicates a more efficient device performance and lower power consumption to achieve switching [58]. In 2D nano-devices, due to the lack of dangling bonds and the reduced interfacial states at the surface, the S_{sub} is relatively low compared to bulk semiconductors and ought to approach the theoretical "Boltzmann limit" of 60 mV dec^{-1} for non-tunnelling devices. For tunnelling FETs, the Boltzmann limit can be breached only by filtering through electrons of a certain energy range [65].

The above-mentioned threshold bias, V_{th}, is the minimum gate voltage necessary to create a conducting path between the source and drain electrodes in a FET channel. Explicitly, this is a function of the oxide thickness and the charge which is induced in the channel by the field effect. As the Fermi level is shifted towards the conduction/valence bands with the presence of impurities and dopants, the V_{th} of TMDs is sensitive to their environment, i.e. the presence of electron acceptors/donors on the FET channel surface [69, 70], as well as the history of electrical testing which the device has undergone [71, 72]. We note that MoS_2 FETs are classified under *depletion mode* (normally on) n-type devices, as the V_g needed to turn on the channel is less than 0 V [73].

High carrier mobility is a key parameter needed to achieve fast device operation. As FETs are mainly used for switching purposes in electronic circuits, the associated oscillation frequency (otherwise known as *clock rate*) of this switch will depend greatly on the timely ability of charge carriers to move from source to drain electrodes. TMDs have demonstrated moderate mobilities so far, with HfO_2-encapsulated top-gated MoS_2 devices reaching μ_{fe} values of several hundreds of cm^2 V^{-1} s^{-1} at room temperature [74]. Mobility engineering in 2D materials is becoming a key research interest, as groups strive to reduce charge scattering with hexagonal boron nitride encapsulation [75], and modulation with angularly-mismatched van der Waals stacking of heterostructures [76]. μ_{fe} in low-dimensional MoS_2 is greatly affected by the chemical state of the two planar interfaces in the 2D flake. The nature

of the surface termination largely contributes to carrier scattering and electrostatic control over the channel provided by the gate. The large discrepancy often observed in the quality of devices measured in vacuum versus those studied in the ambient is a direct consequence of this. Unencapsulated MoS_2 tested in air exhibits a large shift of V_{th} towards positive gate biases, indicating p-type doping from oxygen-containing adsorbates which consequently reduce mobilities [37, 46, 77].

Several schemes of gating have come to the fore, with various dielectrics such as ionic gels [78], [79, 80], organic polymers [81] and high-κ transition metal oxides [17, 32] being studied. These materials reduce scattering and preserve the room temperature mobility of MoS_2 without sacrificing device tunability and channel control. On the other hand, polishing of substrates on which the flake is deposited [82], as well as direct deposition on boron nitride [83], have been shown to improve the mobility substantially. A challenge remains, however, in controlling the intrinsic doping levels in MoS_2 in order to easily achieve p-type or ambipolar gate characteristics. A considerable amount of research has gone into the fabrication, study and improvement of the performance of MoS_2 FETs since the prototypical demonstration by Radisavljevic *et al.* in 2011 [17]. Their mechanically-exfoliated monolayer device incorporated a 30 nm-thick HfO_2 top gate dielectric which allowed for an ON/OFF ratio of 10^8 at room temperature, femtoampere off-currents and a high degree of electrostatic control reflected by a close-to-ideal S_{sub} of 74 mV dec^{-1}. Further fundamental studies have shown that MoS_2 FETs only suffer electrical breakdown beyond large current densities of $5 \cdot 10^7$ A cm^{-2} (50 times that of copper) [84], possess a layer-dependent carrier mobility [82] and can be operated in the gigahertz frequency range [85], rendering them competitive against current switching technologies. Importantly, as MoS_2 has a medium-range band gap it can satisfy the ever-present conundrum of semiconducting switching devices, i.e. balancing low off-state current with relatively high carrier mobility in the on-state [86]. The introduction of foreign species into the material is one way of tuning all of the above-mentioned parameters in MoS_2 devices. In this thesis, we will study the effects of introducing impurities into MoS_2 by the exposure to oxygen-containing plasma, and the effects of creating atomic vacancies with the helium ion beam.

2.3.3 Effects of the contact interface

A metal-semiconductor junction, typical of that formed between a low-dimensional TMD and a metal electrode, is classified either as a *Schottky barrier* or an *ohmic contact*. A typical n-type 2D FET such as MoS_2, coupled to source and drain

electrodes, effectively consists of two Schottky diodes connected anti-serially. The contact which is in reverse bias will register a large voltage drop and governs the functionality of the device [87]. In the case of a reverse-biased diode (meaning current injection from the metal into the semiconductor), different mechanisms exist for charge carriers to be transported across the barrier [88]:

a) *Thermionic emission* - occurs when an electron in the metal has managed to diffuse or drift through the depletion region and can move into the semiconductor, provided available Bloch states exist in the material. A 2D emission current density (at $qV >> k_BT$) over the barrier has the form:

$$J = A^*T^\alpha \exp\left(\frac{-q\Phi_B}{k_BT}\right) \tag{2.11}$$

where A^* is the 2D Richardson constant, T is the temperature, α is a dimensionality constant equal to $\frac{3}{2}$, q is the Coulombic charge, k_B is the Boltzmann constant and Φ_B is the Schottky barrier height.

b) *Field emission (tunnelling)* - electrons lacking energy to emit over the barrier can tunnel across the interface at an energy close to the Fermi energy of the semiconductor. An increase in temperature narrows the tunnelling barrier and leads to a dominant contribution from thermionic emission over the barrier, and the tunnelling contribution to the total current becomes negligible. The tunnelling current is of the form [89]:

$$J \propto \exp\left(\frac{qV}{E_0}\right) \tag{2.12}$$

where V is the applied bias and E_0 depends on the effective electron mass, the semiconductor permittivity and the donor concentration.

Charge injection from the electrode into the 2D semiconductor (at moderate doping levels) is mostly governed by thermionic emission over the Schottky barrier and the persistent van der Waals barrier that exists at the interface. *Metal-induced gap states* [90] present at this interface can result in a phenomenon known as *Fermi level pinning*, whereby energy bands of the TMD “bend" to accommodate the chemical environment of the interfacial atoms [91]. A consequence of this is the formation of undesirable Schottky barriers which are independent of the work functions of the materials used (in discord with the empirical work function-matching *Mott Rule* usually used to gauge the choice of contact metal for a given material). The height

of this Schottky barrier can be extracted directly from empirical measurements, by allowing V_g to tune the conduction band in the semiconductor so that it becomes level with the energy barrier (E_A) needed for emission from the metal. At this point, the linear relationship between the activation energy, E_A, and V_g breaks down as field emission (tunnelling) begins to contribute to charge injection across the barrier. Thus, low-temperature electrical measurements can reveal the physical nature of the interface in the simplest two-probe device geometry.

Achieving low contact resistance (R_c) is pivotal for the desired implementation of 2D semiconductors in future switching electronics, as high drive currents are needed to discern between ON and OFF states. Van der Waals materials such as MoS_2 or WS_2 have relatively pristine surfaces, with little dangling bonds available to form chemical bonds with adsorbed atoms. This differs considerably from non-van der Waals semiconductors, where unsaturated surface states are readily available for covalent bonding (**Fig. 2.8.(a)**). In the case of 2D flakes, one way to form covalent bonds to the device channel is to deposit electrodes in an edge-contacted geometry that forms a seamless planar junction between the metal and the semiconductor [92]. However, as this type of metallisation is difficult to achieve experimentally, most devices tested in the literature rely on top contacts, where the film is deposited on the basal crystal plane; (001) for hexagonal systems. This in turn leads to an increased sheet resistance as an additional van der Waals barrier is now present between the metal and the semiconductor, inhibiting charge injection into the channel (**Fig. 2.8.(b)**).

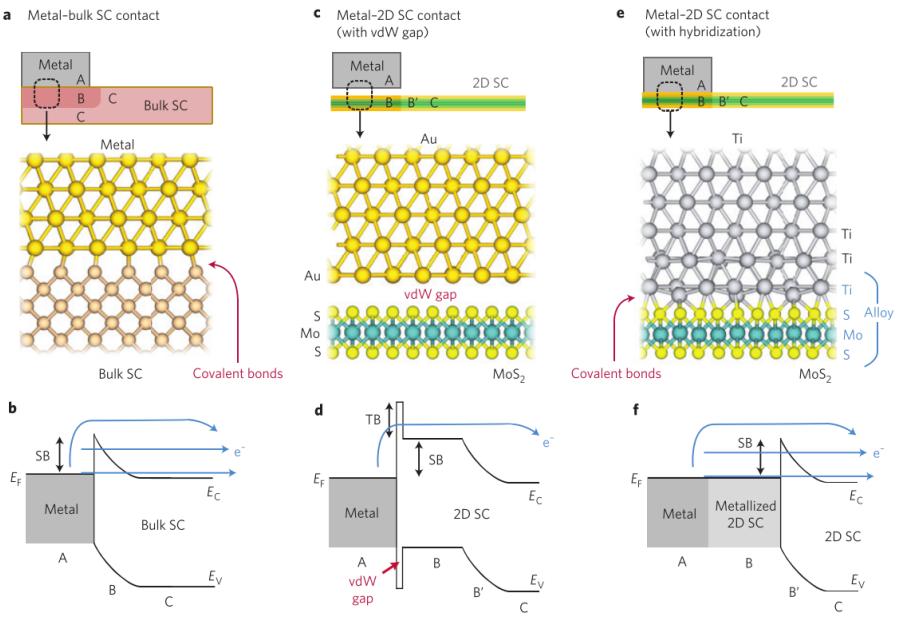

Figure 2.8: Metal-van der Waals semiconductor contact geometries and associated band diagrams of the junctions. SB is the Schottky barrier, TB is the tunneling barrier, SC is the semiconductor, E_C is the bottom of the conduction band, E_V is the top of the valence band and e^- are electrons. [87].

In reality, some impurities or oxide centres will exist at the interface and contribute to band bending towards the metal's Fermi level. As the TMD will not readily form chemical bonds with the deposited metal of the electrode, it may be the case that the film is easily delaminated from the flake during experimental handling and measurement, effectively opening the circuit. A thin *adhesion layer* producing a smaller lattice mismatch is therefore deposited before putting down the electrode metal. This intermediary layer, which effectively forms an alloy with the 2D material channel (**Fig. 2.8.(c)**), diminishes the effect of serial R_c. Transition metals such as titanium, molybdenum and tungsten have been shown to reduce R_c as they form hybrid orbitals with sulfur at the MoS_2 interface. Non-localised gap states are formed in the material, contributing a metallic-like character to its band structure, lowering the sheet resistance of the material underneath the electrode [87].

2.4 Memristors

2.4.1 History and basic functionality

The term *memristor* is a portmanteau of "memory" and "resistor". In his seminal 1971 paper [19], Leon Chua described *a new two-terminal circuit element characterised by a relationship between the charge*:

$$q(t) \equiv \int_{-\infty}^{t} i(\tau)\,\mathrm{d}\tau \tag{2.13}$$

and the flux-linkage:

$$\varphi(t) \equiv \int_{-\infty}^{t} v(\tau)\,\mathrm{d}\tau \tag{2.14}$$

In the above two integrals, where t and τ are time, the four central physical quantities governing the behaviour of two-terminal circuit elements are present:

1. v - the voltage, or the potential difference across the terminals of the device.
2. i - the electric current flowing through the device when a potential difference is present.
3. q - the electric charge in the device.
4. φ - the *flux linkage*. This property of a two-terminal element links the induced electromotive force to the magnetic field-producing current passing through an element by *Faraday's law of induction*.

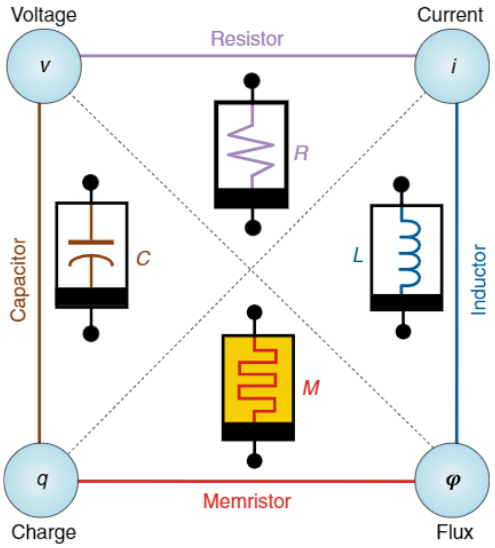

Figure 2.9: **The four fundamental two-terminal circuit elements.** The resistor is defined by a relationship between voltage (v) and current (i); the inductor by a relationship between flux (φ) and current (i); the capacitor by a relationship between charge (q) and voltage (v); and the memristor by a relationship between flux (φ) and charge (q). R; resistance, C; capacitance, L; inductance, M; memristance. Adapted from [18].

At the time of Chua's paper, the six possible relationships between these four quantities have not all been defined through working circuit elements. In **Fig. 2.9** we can see how q and v have been linked through the functionality of a capacitor, v and i in that of a resistor, and i and φ in the inductor. However, no links existed between φ and q. For the sake of completeness, Chua argued that a device must exist so that the voltage across a memristor (and hence its resistance) must depend on the change in the flux linkage as dictated by a moving charge distribution. He built representative circuits using a combination of off-the-shelf components and formalised the concept of a *memristance* in the below relationships:

$$v(t) = M[q(t)]i(t) \tag{2.15}$$

where the memristance M of a voltage-controlled memristor is defined as:

$$M(q) \equiv \frac{\mathrm{d}\varphi(q)}{\mathrm{d}q} \tag{2.16}$$

and

$$i(t) = W[\varphi(t)]v(t) \tag{2.17}$$

where the *memductance* W of a current-controlled memristor is defined as:

$$W(\varphi) \equiv \frac{\mathrm{d}q(\varphi)}{\mathrm{d}\varphi} \tag{2.18}$$

These theoretical devices are distinguished by a few key characteristics, namely:

- the instantaneous memristance at time t_0 depends on the time integral of the current from $t = -\infty$ to $t = t_0$. This means the resistance of the device depends on the entire history of the current that has flown through it.
- the hysteresis loop traced out in a typical *I-V* curve is pinched at the origin, i.e. there is no current flowing through the device when the applied bias is zero.
- The frequency with which the signal is sampled tunes the degree of hysteresis in the memristor. In the limit of applying a very high AC voltage frequency, memristor functionality becomes that of a typical time-invariant ohmic resistor [93] - the hysteresis loop collapses.

The memristor concept was refined to be dependent on various iterations of so-called *state variables* inherent to devices over the next decades but remained a theoretical circuit element until 2008, when it was “found" by Strukov *et al.* [20]. Their TiO_2 matrix sandwiched between Pt electrodes exhibited highly nonlinear *I-V* characteristics, including negative differential resistance (NDR), a frequency-dependent *I-V* hysteresis loop, and resistance states which differed by a factor of up to 380 (**Fig. 2.10**).

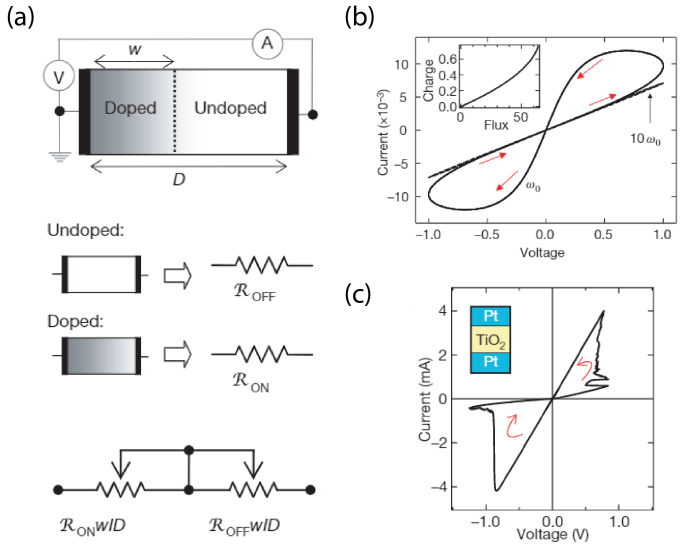

Figure 2.10: **The first resistive switch.** **(a)** Diagrams of the structure and functionality of the contacted TiO_2 stack, showing how the extension of the oxygen vacancy-doped region, w, changes the resistance of the device ($\mathcal{R}$) across its length, D. **(b)** Frequency-dependent closing of the hysteretic loop in the *I-V* characteristics of the device. Note the zero-bias pinching in the loop. **(c)** Typical highly nonlinear output characteristics of the device when swept between ± 1 V. Figures adapted from [20].

Although this type of device qualitatively imitates the behaviour of a memristor, it is not a true ideal memristive system. Notice that the above-presented functionality would remain identical in a universe where magnetism did not exist. This fundamental controversy has led to many researchers arguing for nomenclature changes [94], while engineers in particular continue to use the misnomer *memristor* when talking about these devices. For the sake of accuracy, in this thesis we will stick to the concept of a *resistive switch* when describing these devices, although they fall under the larger umbrella of *memristive* systems as they exhibit a lot of their predicted properties.

2.4.2 Developments and neuromorphic properties

The field quickly bloomed as groups began to discover similar behaviour in other solid-state oxide materials such as ZnO, HfO_2 or $SrTiO_3$ [95]. More complex switching phenomena and distinctions between *bipolar* and *unipolar* devices emerged. These qualifiers depend on whether the applied bias polarity needs to be reversed in order to switch resistance states. In addition, the switching mechanisms began to be categorised into respective classes such as: *electrostatic*, *phase-change*, *electrochemical metallisation* and *valence change* memories. We will concern ourselves mostly with valence change resistive memories in this thesis, as they are relevant to semiconducting 2D MoS_2 devices. For an overview of other switching mechanisms and material classes we refer to the extensive review article by Waser *et al.* [96].

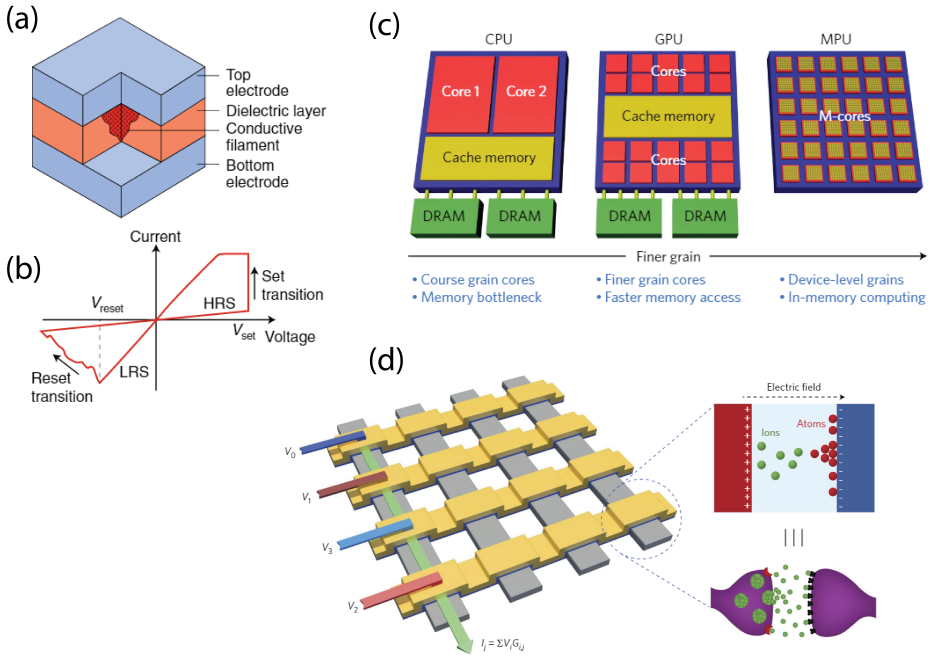

Figure 2.11: **(a)** Sketch of the typical structure of a resistive switching component. **(b)** Representative *I-V* characteristics of a resistive switch, highlighting the transitions between HRS and LRS at the set and reset biases, V_{set} and V_{reset}. **(c)** Possible evolution of the computing system. **(d)** Hardware implementation of artificial neural networks in a memristor crossbar array. **(a)**, **(b)** adapted from [97]; **(c)**, **(d)** adapted from [98]. GPU; graphics processing unit, CPU; central processing unit, DRAM; dynamic random access memory, MPU; memory processing unit.

Valence change memory (VCM) is mediated by the migration of ions and is often described in terms of the motion of the corresponding atomic vacancies. The resulting change in the local stoichiometry varies the oxidation state of the metal coordination centre, thus changing the electrical conductivity. This is effectively a

chemical reduction or oxidation reaction, depending on the polarity of the applied voltage impulse. These nanoionic or *ionotronic* (ion electronics) systems are usually relatively large devices (**Fig. 2.11(a)**) whose functionality can be probed with many characterisation techniques; including various spectroscopies, microscopies and electrical testing. Strategies and best practices for non-destructive characterisation are being constantly improved, with switching mechanisms now being observable on the atomic scale with elemental analysis capabilities [99]. A key feature of memristive systems is the *non-volatile* nature of the resistance states induced by the set and reset transitions (**Fig. 2.11(b)**). This means that when external power is cut from the device, the resistance state will remain as last accessed upon the next time power is provided for readout. This feature makes resistive random access memory an attractive alternative to charge storage-based technologies of today. The future of electronics based on these memristive systems points towards in-memory computing [97] and non-von Nuemann architectures where the proposed *memory processing units* (**Fig. 2.11(c)**) replace current cores and cache memories as the grain size of components is continually down-scaled [98]. This will allow for the processing and accessing of information to happen in the same area of the chip, substantially reducing the time necessary to send signals to the cache memory and back to the processing unit. Crossbar arrays can also be fabricated (**Fig. 2.11(d)**), allowing for the implementation of large-scale structures that could avail of the non-volatile nature of resistive memory to carry out processes such as analogue image recognition and pattern classification [100] and novel stochastic computing schemes [97]. Improvement of these 3D crossbar architectures to ensure no cross-talk between neighbouring cells through the suppression of sneak current paths is currently being refined to implement real-life devices by companies such as `Intel` and `Micron`.

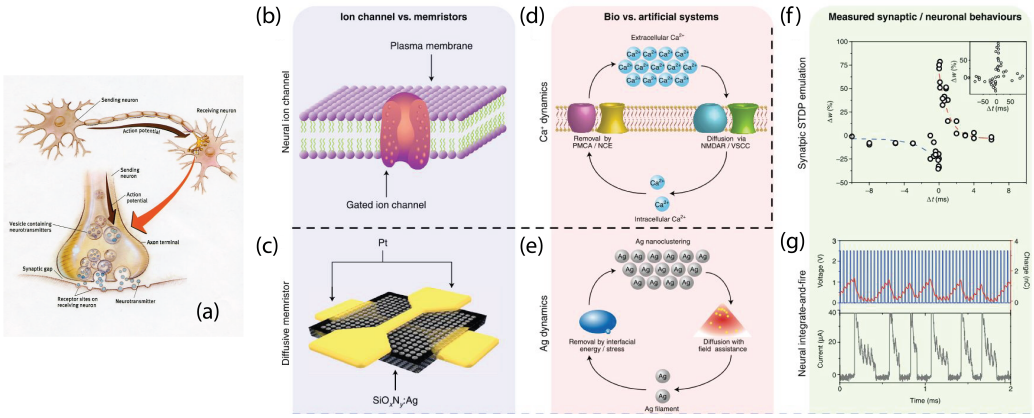

Figure 2.12: **Memristive synapses and neuromorphic behaviour.** **(a)** Artist's rendition of the post-synaptic and pre-synaptic neuronal connection through a synapse [101]. **(b)** Graphic of a neural ion channel, gated by the local concentration of Ca^{2+} cations. **(c)** Schematic of a diffusive resistive switch with Ag-doped dielectrics. **(d, e)** Ag dynamics in a diffusive memristor which emulate the Ca^{2+} dynamics in a neurotransmitter circuit. Ag diffuses into the gap region between Ag nanoclusters under an electric field, forming a Ag filament. Once the voltage bias is removed, the Ag is removed by the interfacial energy or mechanical stress, leading to filament fracture and resistive switching. **(f)** Experimental demonstration of spike-timing-dependent plasticity with the diffusive memristor-based artificial synapse. The plot shows the conductance (weight) change of the synapse with variation in spike-timing, similar to that of the chemical synapse. **(g)** Experimental demonstration of spike-timing-dependent plasticity (STDP) in a resistive switch-based artificial synapse, exhibiting the change to the post-synaptic current caused by an incoming set of training electrical impulses. **(b)-(g)** adapted from [102].

In contrast to current CMOS architecture, nerve cells are characterised by massive connectivity and highly parallelised computational processes whose power consumption is incredibly low. The human inner ear, for instance, is known to operate on $\approx 14\ \mu$W of electrical power [103]. Due to the limited bandwidth and energy costs sunk into accessing memory units microns away from processing units, our current von Neumann schemes are incredibly ineffective for emulating brain functionality, despite being 10^9 times faster [104]. Resistive switches thus promise an analogue method of imitating this behaviour on the hardware level and are being employed in a whole new field aiming to mimic the functionality of the brain - *neuromorphic engineering*. An overview of analogue neuromorphic behaviour is presented in **Fig. 2.12**.

For effective learning, the post-synaptic current has to be modulated such that future inputs no longer modulate the resistance of the synapse. This is called *long term potentiation (LTP)*, or *long term depression (LTD)* in the case of reverse resistance modulation (forgetting rather than remembering), and can be triggered by applying

temporally short voltage spikes past the V_{set} or V_{reset} of a resistive switch [105]. The degree of change to the synaptic strength can also be modulated by changing the width of the training pulse, which has been demonstrated in neuromimetic Ag/Si composites as early as 2010 [106].

2.4.3 Resistive switching in 2D materials

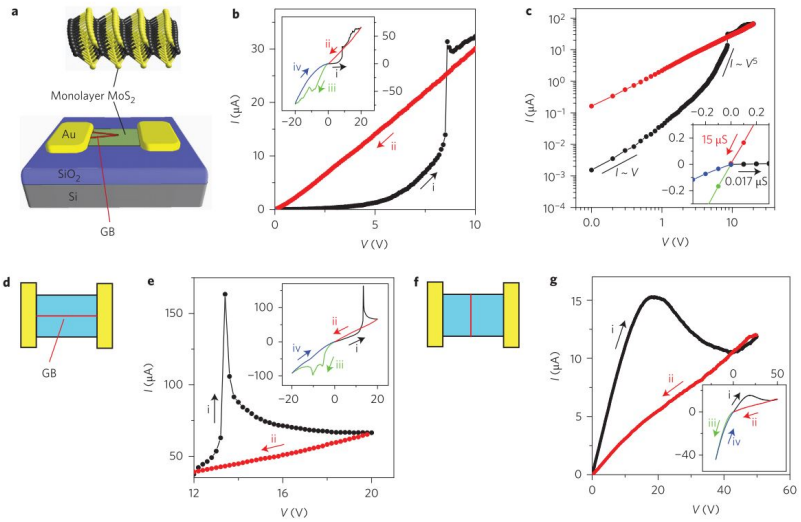

Figure 2.13: ***I–V* characteristics of MoS_2 resistive switches**. **(a)** Schematic of an intersecting-GB MoS_2 memristive device with two GBs connected to one of the electrodes and intersecting at a vertex within the channel. **(b)** Partial *I–V* characteristics of an electroformed intersecting-GB memristor (channel length, $L = 7\ \mu$m) obtained immediately after the electroforming process. The set process occurs at $V_{set} = 8.3$ V with an abrupt twofold increase in current. Inset: Full *I–V* characteristics of one switching cycle. Measurements were performed at a sweep rate of 1 V s^{-1} and $V_g = 40$ V under vacuum (pressure $< 2 \cdot 10^{-5}$ Torr). The voltage was swept in the order 0 V → 20 V → 0V → -20 V →0 V, as shown by the coloured arrows with the four sweeps labelled as *i*, *ii*, *iii* and *iv*. **(c)** Log–log plot of sweeps *i* and *ii* from **(b)**, which shows space-charge limited and ohmic transport in sweeps *i* and *ii*, respectively. Sweep *i* also shows an ohmic *I–V* behaviour at low bias (V < 0.5 V). The inset shows a zoomed-in *I–V* curve from the inset of **(b)** near zero bias, which reveals conductance values ($G \equiv \partial I/\partial V$) in the off (HRS) and on (LRS) states. A schematic **(d)** and partial *I–V* characteristics **(e)** of an electroformed bridge-GB memristor ($L = 7.5\ \mu$m) at $V_g = 40$ V, showing a transient current spike ($V_{set} = 13.2$ V) followed by an NDR regime. The inset shows the full *I–V* characteristics of one switching cycle. The voltage sweeps were conducted in the order *i*, *ii*, *iii*, *iv*, as indicated by the coloured arrows (sweep rate = 2 V s^{-1}). A schematic **(f)** and partial *I–V* characteristic **(g)** of an electroformed bisecting-GB memristor at $V_g = 55$ V, showing a broad current peak followed by an NDR regime. The inset shows full *I–V* characteristics of one switching cycle. Bias sweeps were conducted in the order *i*, *ii*, *iii*, *iv*, as indicated by the coloured arrows (sweep rate = 2 V s^{-1}). All panels and captions adapted from [107].

It is clear to see why research on resistive switching in 2D materials would gain in popularity over the recent five years. The promise of combining memory with logic in individual semiconducting devices with a minimal footprint is enhanced

by the superlative properties of 2D materials. These include inherently low power consumption while preserving high drive currents in the FET geometry, transparency and mechanical robustness, as well as ease of integration with current Si fabrication methodologies. Interest in 2D resistive switches really took off with the 2015 observation of memristive phenomena in monolayer CVD MoS_2 when biasing across grain boundaries naturally occurring in the material from the growth process [107]. As seen in **Fig. 2.13**, when electrodes are deposited across a variety of GB geometries, hysteretic *I-V* behaviour emerges in the output characteristics of monolayer MoS_2 FETs at high drain-source biases. Sangwan *et al.* attributed this observed resistive switching to the electric field-mediated drift of charged sulfur vacancies, V_S, from the GB region. The vacancies are introduced during the CVD process by restricting sulfur gas supply, allowing for the enrichment of boundary regions with field-mobile V_S species, as confirmed by atomic force microscopy (AFM) and photoluminescence (PL) mapping, presented in **Figs. 2.14(a,b)** below:

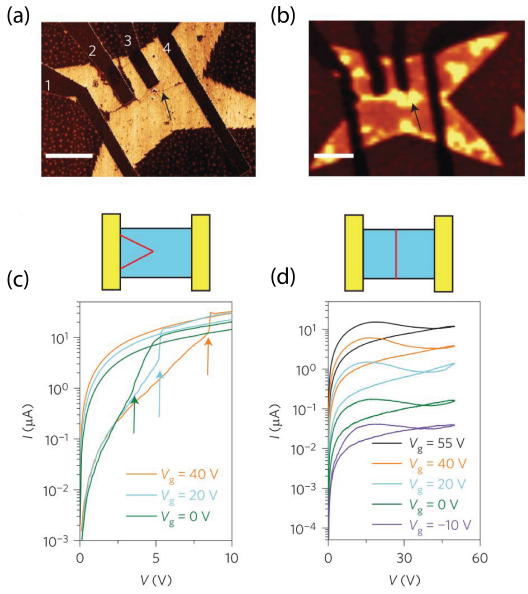

Figure 2.14: **(a)** AFM phase image of an electroformed bridge-GB memristor with a GB that connects both of the electrodes (highlighted by a black arrow). Only electrodes 1 and 4 of the van der Pauw geometry were used for electrical measurement, with electrodes 2 and 3 kept floating. **(b)** Spatial mapping of the area under the PL excitonic peaks *A* and *B* of the MoS_2 device in **(a)** that shows an increased PL intensity in the GB (black arrow). Scale bars **(a,b)**, 4 μm. **(c)** Semi-log plot that shows the *I–V* characteristics of an intersecting-GB memristor at different V_g. The full *V* sweep range is 20 to -20 V. Switching the set voltage (shown by coloured arrows at V_{set} = 3.5, 5 and 8 V) is controlled by V_g. **(d)** Semi-log plot of *I–V* characteristics ($V > 0$ V) of a bisecting-GB memristor at different V_g. The full *V* sweep range is 50 to -20 V. The negative bias sweep range is limited to -20 V to avoid a dielectric breakdown between the gate and the drain electrode. The current in both LRS and HRS is modulated by three orders of magnitude by V_g. All panels and captions adapted from [107].

In addition, because the MoS_2 can be grown on a gate dielectric such as SiO_2, the device retains the functionality of a FET while also now incorporating resistive switching into an atomically-thin device. The degree of hysteresis in the *I-V* loop, or the resistance ratio of the device, can thus be tuned by applying the field effect during the *I-V* sweep **Figs. 2.14(c,d)**. This opens up new device architecture possibilities by now incorporating a third modulating terminal into what are traditionally two-terminal devices.

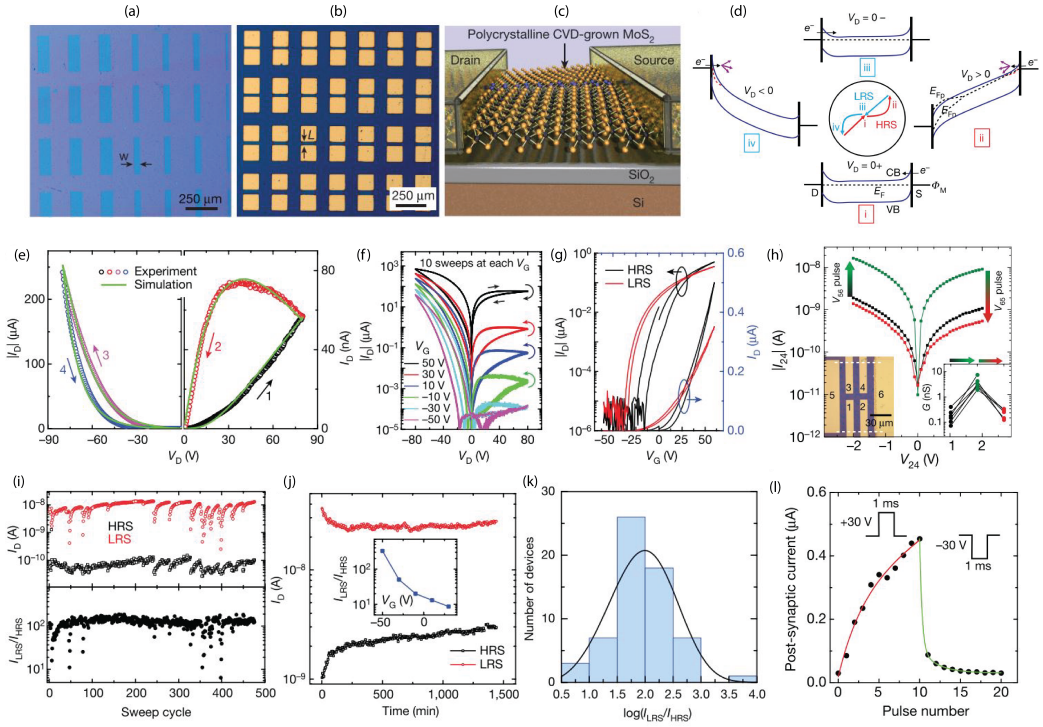

Figure 2.15: **(a)** Optical micrograph of an array of MoS_2 monolayer strips with varying width, W, etched by reactive ion etching before **(b)** metallisation. **(c)** Schematic of a MoS_2 memtransistor showing the GB in purple. **(d)** Schematic showing the energy band diagram of a memtransistor at the four switching stages shown in the representative *I-V* curve in the centre panel. **(e)** I_{ds}-V_{ds} curve of a MoS_2 memtransistor (L = 5 μm, W = 100 μm) at V_g = 10 V. The sweep rate is 10 V s^{-1} throughout. The solid green line represents simulated data from a modulation-doped memtransistor model. **(f)** I_{ds}–V_{ds} curves for ten consecutive sweeps at each gate bias V_g for the same device. **(g)** Transfer characteristics of a memtransistor at V_{ds} = 0.1 V, showing a shift in V_{th} and μ_{fe} from V_{th} = 20 V and $\mu_{fe} \approx 0.6$ cm^2 V^{-1} s^{-1} in HRS to V_{th} = 10 V and $\mu_{fe} \approx 0.3$ cm^2 V^{-1} s^{-1} in LRS. **(h)** I_{24}–V_{24} curve between terminals 2 and 4 of a six-terminal MoS_2 memtransistor, showing heterosynaptic plasticity. **(i)** Endurance of the current (top) and I_{LRS}/I_{HRS} (bottom) at V_{ds} = 0.5 V in HRS and LRS for 475 consecutive sweep cycles. **(j)** Retention of the HRS and LRS currents at V_{ds} = 100 mV and V_g = 0 V in a 24 h period. The inset shows the gate tunability of I_{LRS}/I_{HRS}. **(k)** Histogram showing I_{LRS}/I_{HRS} ratios of 62 distinct memtransistors, with mean and variance (in $\log(I_{LRS}/I_{HRS})$) of 1.96 and 0.54, respectively. **(l)** Post-synaptic current versus pulse number, showing LTP and LTD with 30 V and -30 V pulses. The solid lines are biexponential fits. All panels adapted from [108].

The authors followed up on their 2015 prototype study on individual flakes by fabricating multi-terminal large-area *memtransistors* based on these GB-containing monolayer films in 2018 [108]. They demonstrated fabrication scalability by depositing contacts across pre-patterned films containing an unknown spatial distribution of randomly-oriented GBs (**Fig. 2.15**). This resulted in the creation of 62 well-performing gate-tunable bipolar resistive switches, with a resistance ratio of $\sim$ 100. The devices showed good cycling endurance (475 switching cycles, or *epochs*) and retention of resistance states (1500 minutes). Although these numbers are not reaching the hundreds of thousands necessary for actual consumer devices, they are certainly a step in the right direction for lateral on-dielectric-grown components. In addition, multi-terminal conductance modulation was demonstrated between two given terminals by electrically stressing another pair of orthogonal terminals. Neuromorphic functionality was observed with LTP and LTD habituations within $<$ 10 training pulses at time scales in the ms range. Tuning of the artificial synaptic weights with varying pulse width was also demonstrated. This lateral in-plane neuromorphic functionality of polycrystalline monolayer MoS_2 was also later shown to function at V_{ds} as low as 6 V on the wafer scale [109, 110] and also in mechanically-printed multilayer MoS_2 films [111]. In all cases, the functionality of the devices was attributed to the drift of sulfur vacancies in the MoS_2 lattice. The model described by Sangwan *et al.* relies on V_S piling up at one of the MoS_2/electrode contacts and thus modulation-doping the metal-semiconductor interface; hence changing the dynamics of charge injection into the channel through the effective modulation of the Schottky barrier height.

Other works in this area have focused on utilising vertical stacks of 2D materials to achieve resistive switching (**Fig. 2.16**). TMD monolayers and bilayers [112], as well as hexagonal boron nitride [113, 114], have been employed to act as matrices for the drift of active metal ions between electrodes separated by at most several nanometres. The formed filaments thus require biases only as low as 100 mV to form conducting channels between contacts [115], leading to abrupt switching into LRS through the mechanism of electro-chemical metallisation. These sorts of devices have been shown to operate at radio frequencies [116] and are highly robust to mechanical stressing [112].

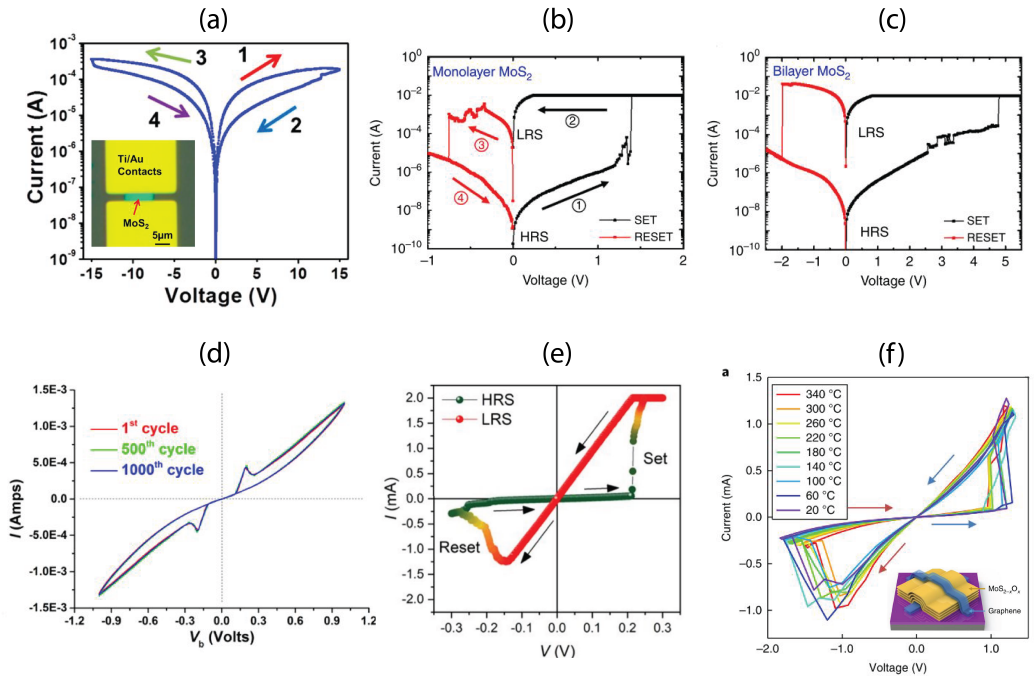

Figure 2.16: **(a)** Hysteretic *I-V* curve of a mechanically-printed 15 nm-thick MoS_2 device (optical micrograph in the inset) [111]. **(b,c)** Resistive switching in vertical 1L and 2L MoS_2 respectively, contacted with Au electrodes [116]. **(d)** Pseudo-ideal memristive characteristics of 1T-MoS_2 sandwiched between Ag electrodes [117]. **(e)** Sub-1 V V_{set} in bilayer MoS_2 between a Cu/Au stack. **(f)** Temperature-stable cycles of defect-rich multilayer MoS_2 contacted with graphene electrodes [118].

Vertical memristive elements incorporating 2D materials have some ostensible advantages over planar devices. Namely, the electric field needed to drive the filament/vacancies in order to switch states is much lower, leading to power consumptions as low as fJ [114]. This also results in shorter time frames required for switching and thus an improved neuromorphic response. However, the device fabrication process is often very involved (requiring either an additional lithography step or sample transfer), and the throughput is limited. The lateral devices, in turn, have the advantage of fabrication scalability but depend on the location-agnostic CVD process to deliver a required distribution of GBs to the FET channel. This may result in performance inhomogeneity between devices and is not site-specific. In this thesis, inspired by the work of Sangwan *et al.* [107, 108], we will show that the helium ion beam can be utilised to deliver site-specific memristive functionality to planar monolayer MoS_2 devices in the post-metallisation stage. We will then compare and contrast the performance benchmarks of our devices against those seen in the literature.

Chapter 3

MoS_2 modification and functionalisation

In this chapter, we will review the literature on the modification of 2D MoS_2 utilising plasma treatment and helium ion beam irradiation. We will focus on plasma generation & processing, and the impact of plasma exposure on the structural and electrical properties of TMDs. In the case of He^+ ion beam irradiation, we will present some background on gas field ion source microscopy and the theory of beam-sample interaction before summarising the effects of ion beam modification on the structural and electrical properties of 2D MoS_2.

3.1 Plasma functionalisation

The precise tunability of electronic properties of 2D nanomaterials is a key goal of current research in this field of materials science. Progress demands that a nanofabrication methodology is developed to control the structure and properties of semiconducting layered crystals so that desired functionalities are obtained for these materials in the future. These may include phase transitions [28, 40] or conductivity modulation for next-generation data storage [117]. The interaction of low-energy radio frequency–generated plasma ions with MoS_2 has already led to the creation of a multitude of devices, including rectifying diodes, photovoltaics, and nonvolatile memories [119, 120]. Plasma power and exposure time have emerged as key variables to delineate between chemical etching and physical sputtering regimes [121, 122, 123]. Importantly, treatment with oxygen-containing plasma leads to the formation of molybdenum trioxide (MoO_3) centres, which have been reported to increase the resistivity of the material and inhibit carrier transport, while retaining relative structural integrity of the now oxide-containing MoS_2 heterostructure [124, 125]. Plasma processing has thus emerged in recent years as a promising candidate to enable large-scale modification of 2D materials in a time-efficient and cost-effective manner. This is in contrast to more involved site-specific methods such as ion beam irradiation, requiring more specialized equipment such as a helium/neon ion microscope and having limited throughput. On the other hand, traditional chemical functionalisation is limited to only certain active species, often requires catalysts and/or high temperatures, as well as application-incompatible wet preparation steps [126, 127, 128]. ultraviolet (UV)-ozone treatment, which can be viewed as a

combination of the physical and chemical treatments, tends to be harsh and severely alters the crystal structure of TMDs [129], degrading their FET performance [130].

It is well-known that atmospheric atoms such as oxygen and nitrogen act as common substitutional dopants in inorganic 2D materials, without causing major lattice deformations. Frequently-reported types of plasma rely on ionising these and other gas species in order to introduce a charged reactant to the surface of an ultra-thin semiconductor. As a result of the strong electronegativity of some of these species (O, F, Cl), such reactions are favourable and can occur on a large scale, at multiple reaction sites on micron-sized flakes. As the charged plasma plume can be accelerated in the resultant electric field inside the treatment chamber, these reactants often impact the reaction site with significant kinetic energies (up to 100 eV). As such, they can sputter atoms away from the sample crystal lattice, creating non-negligible vacancy concentrations and thus affecting the doping level of the specimens. The fine combination of these chemical and physical regimes can be controlled to manipulate the electronic and optical properties of the exposed materials, tune their long-term stability in air and vary their layer thickness. Hence, plasma processing is positioned to become a powerful tool for both subtractive (etching) and additive (functionalisation) chemical technologies [131], which have the unique capability of rapid large-area sample modification; the degree of which can be controlled by varying the delivered plasma dose, i.e. the exposure time.

For a typical TMD, consisting of a metal, M, and chalcogen, X, the chemical reaction occurring at the surface when exposed to, for example, oxygen plasma can be written as:

$$MX_2\ (s) + 3.5O_2\ (g) \longrightarrow MO_3\ (s) + 2XO_2\ (g) \tag{3.1}$$

where the gaseous product is removed by the pump evacuating the reaction chamber, while the resulting metal oxide may also be volatile in ultra-high vacuum (UHV) environments [132, 133, 134, 135]. It is worth noting that a commonly used plasma species, Ar, is in a class of its own as it cannot react chemically to form new compounds. This limits its ability to functionalise the surface of materials such as MoS_2, and places it closer to low-energy inert ion beam irradiation. The use of plasma to achieve this type of physical modification may have several key advantages as the lower impact energy of the charged ions alleviates beam-induced hydrocarbon deposition, back-scattering damage from the substrate and re-deposition of sputtered material on the surface.

3.1.1 Plasma generation & types of species used for processing of TMDs

In a strict sense, a plasma is defined as a distinct state of matter where a heated gas becomes mostly ionised, producing a highly-charged plume of atomic nuclei and free electrons. Conventional plasmas are generated by high-energy charge carriers colliding with gaseous atoms and molecules or with the surface of an electrode [136] and can be broadly divided into three types depending on the power source, i.e. microwave (MW) plasma (commonly 2.45 GHz), radio frequency (RF) plasma (commonly 13.56 MHz) and direct current (DC) plasma. A MW plasma is generated in an electrode-less chamber by sustaining a high-frequency electromagnetic field. A directionally-coupled waveguide moves the microwave field from the source to the chamber, where it transfers its energy to the injected gas by heating; exciting a discharge of electron densities of up to 10^{12} m^{-3} [137]. A RF plasma discharge can be categorised as either capacitively-coupled discharge (CCD) or inductively-coupled discharge (ICD). CCD is based on the principle that a high-frequency electric field between a pair of parallel plate electrodes initiates a dielectric breakdown, sustaining a bulk plasma discharge between the electrodes which are powered by an impedance-matched source. The resultant electric field collides the ionised plume into a biased metal electrode, leading to further ionisation. For a typical CCD, the generated plasma density is 10^{9}-10^{10} m^{-3} - lower than most other plasma sources [138]. The pressure of operation is also quite high (up to 1000 Pa), introducing possible contaminants to the electrode surface due to particle deposition. This makes it a poor candidate for the treatment of functional electronic devices. Unlike CCD, ICD has the advantage of higher charge densities (10^{12} m^{-3}) [139] and a lower ion impact energy due to kinetic losses from electron collisions. The RF power in an ICD is coupled axially around a dielectric vessel by an inductive circuit element. The changing magnetic field generated by a current-carrying coil induces an oscillating inductive electric field that can accelerate plasma electrons, which are subsequently thermalised in capacitive RF sheaths. There are three major types of ICP geometries: planar, cylindrical, and half-toroidal. The planar coil configuration driven at 13.56 MHz or below is commonly used for materials processing, typically generating uniform low-aspect ratio plasmas. The relatively simple design and ease of implementation make ICP systems promising candidates for meeting the needs of 2D material nano-processing. For a diagram of a typical plasma chamber see **Fig. 3.1(a)**. DC glow plasmas work by application of a DC bias (several hundred volts) between the anode and cathode to sustain a constant discharge through current flow, following the Townsend avalanche scheme. Electrons emitted

from the cathode move into the discharge space and ionise the present gas species, leading to a drastic increase in the concentration of charged carriers resulting in further ionisation and species fragmentation which generates a large quantity of highly-reactive particles. Typical operational pressures of 1-10^3 Pa allow for the generation of electron densities in the 10^{15}- 10^{16} m^{-3} range, which can readily react with the surface of 2D materials (**Fig. 3.1(b)**). For an example of how a toroidal geometry may facilitate the functionalisation of MoS_2, see **Fig. 3.1(c)**.

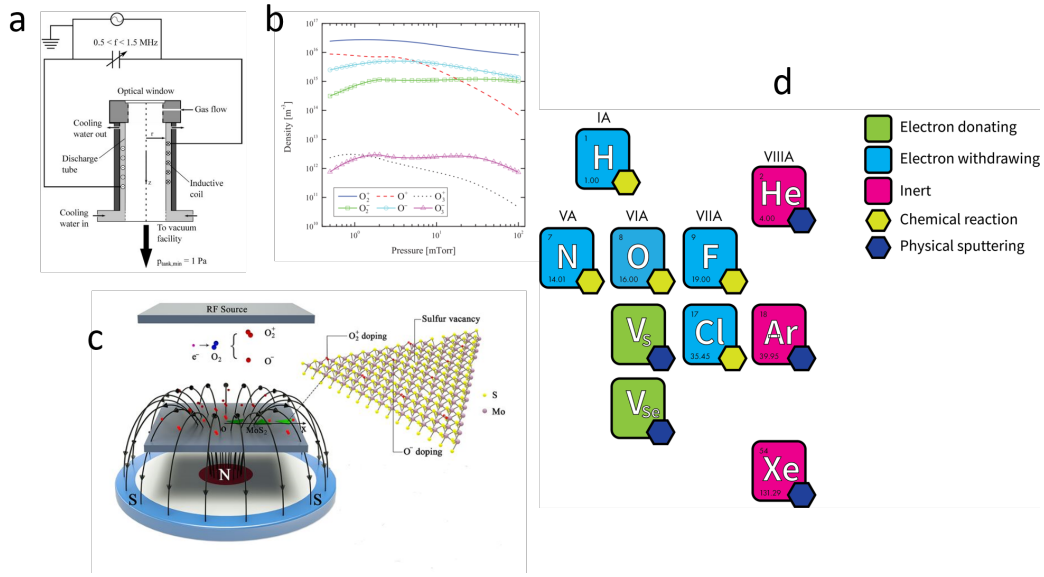

Figure 3.1: **Overview of plasma generation and species used for the modification of layered semiconductors**. **(a)** Sketch of a typical inductive plasma generator, adapted from ref. [140]. **(b)** Mean density of charged species as a function of pressure for a stainless steel cylindrical chamber of radius = 15 cm, length = 30 cm and power = 500 W. Note that the typical pressure range for the processing of 2D materials is in the tens of mTorr, adapted from ref. [141]. **(c)** Schematic of a toroidal magnetic field-controlled oxygen plasma doping process and atomic structure of an oxygen-doped MoS_2 film, adapted from ref. [142]. **(d)** Colour-coded periodic table legend of typical elements used to generate reactive species during plasma treatment of 2D semiconductors. Chemical reaction and physical sputtering regimes are highlighted. V_S; sulfur vacancy, V_{Se}; selenium vacancy.

Detailed theoretical studies of the chemical kinetics between plasma-created chemical species and TMDs have not been performed. For the often-reported oxygen plasma blast, the plume is populated with various molecular species in different energy states. These particles include: ground state molecular oxygen, $O_2(X^3\Sigma_g^-)$, metastable molecular oxygen, $O_2(a^1\Delta_g)$ and $O_2(b^1\Sigma_g)$, ground state atomic oxygen, $O(^3P)$, metastable atomic oxygen, $O(^1D)$ and ionised oxygen, O_2^+, O^+ and O^- [143], Notably, the dominating ionic species are the positively charged O_2^+ and O^+, whose

density outweighs that of negatively-charged oxygen by orders of magnitude [141]. However, in mixed Ar:O_2 plasmas, especially where the oxygen fraction is much smaller and its dissociation rates are suppressed [144], densities of negative and positive ions can be similar, while the molecular species dominate largely over the atomic species [145]. Early work on the physical effects of oxygen incorporation into the commonly-used sputter-deposited MoS_2 thin films [146] revealed some physical characteristics of compounds formed when oxygen adsorbs on the TMD surface. An early UV photoelectron spectroscopy study confirmed that O incorporates at S vacancy sites in MoS_2 through electron depletion from the Mo d_{z^2} orbital [122]. This can lead to elongation along the crystallographic *c* axis in oxygen-containing 2H-MoS_2 [147, 148], and an observed rise in material thickness. However, in the case of plasma processing, where reactive oxygen is not only present in excess but also energetic when incident on the sample surface, etching may also occur. **Fig. 3.1(d)** presents a colour-coded periodic table legend of typical elements used to generate reactive species during plasma treatment of 2D semiconductors. Chemical reaction and physical sputtering regimes are highlighted. Note; as plasma power (P), operational pressure (p) and exposure time (t), are the key variables which inform the material processing, where possible in this overview, we list all three parameters for each discussed study.

3.1.2 Impact of plasma treatment on the structural properties of TMDs

Control of layer number is a key research goal in the processing of layered semiconductors. As these materials show drastically different properties depending on layer number, including indirect-to-direct band gap transitions in the monolayer limit, it becomes imperative to control the material thickness precisely. For example, the opening of monolayer windows in multilayer films can facilitate localised photoemission for optoelectronic and photonic applications. Plasma processing may also be utilised to thin down samples whose growth procedure is not suitable for monolayer synthesis. In order for these processed materials to then be successfully implemented into functional devices, the removal of the top-most layers from van der Waals semiconductors must preserve pristine interfaces, reduce unwanted ambient oxidation and other saturation of defective sites with adventitious dopants.

Etching of bulk molybdenite with RF plasma has been studied extensively as far back as the 1990s, where AFM studies showed an increased surface roughness of bulk MoS_2 crystals as a function of increasing oxygen plasma exposure and plasma power, respectively [121, 149]. At the same time, the growing inclusion of different

oxygen-containing Mo species on the sample surface was observed as a function of changing plasma power, while inert Ar sputtering left behind no oxides [150]. Residue-free layer-by-layer etching of layered semiconductors in the few-layer limit has since been demonstrated with various types of plasma species.

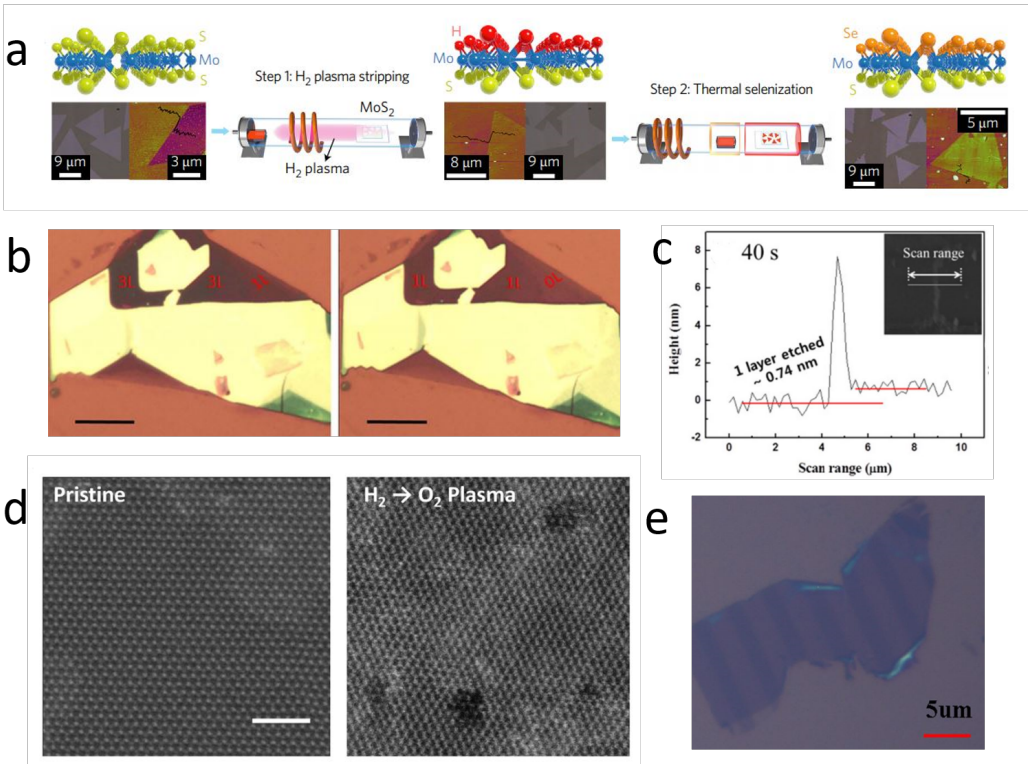

Figure 3.2: **Etching of layered semiconductors with plasma**. **(a)** Selective removal of the top chalcogenic layer from MoS_2 with H_2 plasma, allowing for the formation of a Janus structure upon selenisation, adapted from ref. [151]. **(b)** Example of controlled atomic layer-by-layer etching of exfoliated MoS_2 with SF_6 + N_2 plasma. *(left)* Sample before etching, *(right)* sample after controlled uniform removal of 2 molecular layers. Scale bar is 10 μm, adapted from ref. [152]. **(c)** AFM scan showing layer-controlled removal of MoS_2 material with CF_4 plasma, adapted from ref. [153]. **(d)** ACSTEM of monolayer MoS_2 before and after exposure to sequential H_2 and O_2 plasmas. Scale bar 2 nm, adapted from ref. [135]. **(e)** Example of selective patterning down to monolayer thickness with Ar plasma on polymer-protected MoS_2, adapted from ref. [154].

Two distinct regimes have also been isolated: the finely-tuned removal of just the top-most chalcogenic layer, often followed by functionalisation; and the removal of a full molecular X-M-X layer. In the first case, H_2 plasma stripping of the top sulfuric layer in 1L MoS_2 has allowed for the formation of Janus monolayers of MoSSe when the defects are healed with selenium gas [151]. The healing of the hydrogen plasma-removed (P = 400 W, p = 200 mTorr, t = 2 s) top layer with oxygen plasma

(P = 100 W, p = 100 mTorr, t = 2 s) can lead to the formation of an ultra-flat oxide that can effectively screen the FET channel in the monolayer limit [135]. Sequential oxidation of MoS_2 with soft O_2 plasma (P = 20 W, p = 0.4 Torr, t = 10 s) creates a surface oxide, which can be dissolved away in deionised water, leading to layer stripping [155]. A follow-up step of CVD re-sulfurisation then allows for arbitrary thickness manipulation, opening avenues for the fabrication of more complex and stacked structures.

In some cases, the etching is observed to be self-limiting. Once the layer of oxide forms, it can inhibit further introduction of oxygen reactants into the TMD lattice, capping the sample with a protective layer of ultra-thin oxide whose root mean square (RMS) surface roughness is less than that of the pristine TMD [156, 157]. In the case of WSe_2, the formed oxide layer can also be removed with potassium hydroxide to recover a thinned TMD sample [158]. In turn, precise full molecular layer stripping on ultra-thin TMDs has been demonstrated using various plasma species including: XeF_2 [159], Ar [154], O_2 [160, 161, 162, 163], CF_4 followed by H_2-mediated removal of F residue [153], Cl_2 followed by Ar^+-mediated removal of the functionalised top layer [164, 165] and SF_6 + N_2 at a critical plasma power density of 1.5 mW cm^{-3} [152]. RF Ar^+ plasma has also been shown to thin down few-layer black phosphorus (BP) to monolayer phosphorene, with no significant structural difference detected between plasma-processed and pristine tape-exfoliated monolayer samples [166, 167]. O_2 plasma pre-treatment also allows for layer-precise thinning and oxidation of BP that facilitates passivation against the ambient after deposition of a protective film of Al_2O_3 on the surface oxide [168].

Various etching mechanisms have been proposed to explain the atomistic picture of how layer-by-layer etching may occur in these materials. The individual layer removal picture is often contrasted with the pit-mediated mechanism. In this description, already defective sites are considered more likely to continue etching [169]; often deep into the material as opposed to laterally across the top-most layer. The formation of these voids has been observed experimentally using ACSTEM in MoS_2 [134, 135, 170] and deduced from a combination of AFM and optical measurements [156]. More nuanced studies with carefully-controlled plasma power and times need to be carried out to comprehensively elucidate the atomistic nature of the etching phenomenon. Detailed knowledge of the exact evolution of defects with these parameters can then be leveraged to design highly-localised, tailored heterostructures with precisely-tuned electronic properties. Plasma exposure can additionally facili-

tate the removal of polymeric residue on processed devices [171, 172]. As ultra-thin materials react readily with the plasma, this procedure requires low plasma energies and short exposure times as to not damage the underlying crystal lattice. For a review of plasma-assisted etching of 2D materials see **Fig. 3.2**.

3.1.3 Effects on the electrical properties

3.1.3.1 p-type doping

Intrinsic chalcogen vacancies present in ultra-thin layered TMD FETs can be passivated by oxygen-containing plasma. This tends to shift the V_{th} of the FET towards positive gate biases, and can be used to change device functionality. Kang *et al.* treated multi-layer $HfSe_2$ FETs with oxygen plasma (P = 50 W, p = 500 mTorr, t = 26 mins.). This led to a 4 orders of magnitude improvement in the FET on/off ratio, a multi-fold decrease in the subthreshold swing without a major mobility sacrifice, and a shift in V_{th} from depletion to enhancement mode for the n-MOSFET [173]. Full type conversion was achieved on 6L MoS_2 with toroidal magnetic field-controlled O_2 plasma (P = 10 W, p = 90 mTorr, t = 30 s) [142]. This sort of processing creates a FET with a hole mobility of 115.2 $cm^2\ V^{-1}\ s^{-1}$ at room temperature, completely converting the majority carrier from electrons to holes. This efficient doping scheme was attributed, using density functional theory (DFT) calculations, to the enhanced ratio of O_2^+ species created during plasma production. Local masking with a resist also allows for the fabrication of a rectifier by selective hole doping of the device channel. A similar diode junction made by p-doping one half of a polymer-protected device was demonstrated on 3L MoS_2 with O_2:Ar (1:4) plasma (P = 100 W, p = 250-350 mTorr, t = 20 s) [174], yielding an ideality factor of 1.73. Few-layer MoS_2 rectifiers were also demonstrated by p-doping with SF_6, CF_4 and CHF_3 plasmas (P = 100 W, p = 10 mTorr, t = until sample was 67% of initial thickness).

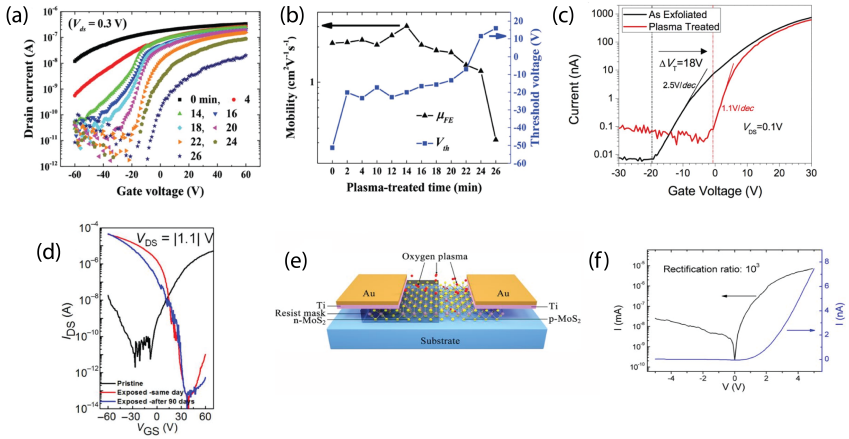

Figure 3.3: **(a)** Gate curves of multilayer $HfSe_2$ as a function of increasing oxygen plasma exposure, adapted from ref. [173]. **(b)** Changes to the carrier mobility (black) and FET threshold voltage (blue) of $HfSe_2$ with increasing O_2 plasma treatment time, adapted from ref. [173]. **(c)** Charge-neutral MoS_2 FET engineered with oxygen plasma exposure, adapted from ref. [175]. **(d)** Carrier type reversal and stability of O_2-plasma treated WSe_2, adapted from ref. [133]. **(e)** Schematic of the rectifier device fabricated by site-specific plasma exposure facilitated by polymer protection, adapted from ref. [142]. **(f)** Rectifying *I-V* curve of such a device, adapted from ref. [142].

This mixture ratio of oxygen to argon at the above plasma parameters tends to shift V_{th} to positive gate biases and reduces device conductance regardless of MoS_2 layer thickness [125]. Downstream pure O_2 plasma (P = 20 W, p = 200 mTorr, t = 2 mins.), in turn, can be used to passivate V_S sites in order to shift V_{th} towards $V_g = 0$ V; attaining a charge-neutral n-type MoS_2 FET [175], less than 5 layers in thickness. A mobility increase of up to 190-fold was noted, while the device-to-device variability was severely reduced. Chen *et al.* found that multilayer MoS_2 FETs whose V_{th} has been up-shifted with O_2 plasma (P = 100 W, p = 10 mTorr, t = 1 min.) are more sensitive to an increase in the relative humidity (RH) of the environment than pristine MoS_2 devices; with transfer characteristics severely degrading above 35% RH [176]. This may show promise for low-dimensional chemical sensing devices and environmental analyte processing in the current-time domain. The same study investigated fluorine doping through CHF_3 plasma exposure, using the same processing parameters. The degree of p-doping achieved with the highly electronegative F species was found to be more prominent as MoS_2 channel thickness was reduced; estimating the generated space-charge layer at $\sim$ 22 nm in very thick flakes. In the case of few-layer WSe_2 devices, remote oxygen plasma treatment (P = 400 W, p = 15 mTorr, t = 60 s) was shown to change majority carriers from electrons to holes; with the reversal persisting for > 90 days [133], highlighting the stability of plasma-treated devices and the suitability of the method for low-dimensional FET

engineering. Pure O_2 plasma (P = 20 W, p = 470 mTorr, t = 60 s) has also been utilised to shift the V_{th} of multilayer n-type ReS_2 FETs to more positive gate biases by as much as 10 V [177]. Other plasma species have also shown the capability of providing acceptors to the MoS_2 channel. N_2^* plasma (P = 300 W, $p < \mu$Torr, t = 3 mins.) doping of CVD-grown MoS_2 has resulted in p-type doping as monitored by X-ray photoelectron spectroscopy (XPS) [178], while Ar plasma (P = 50 W, p = 15 mTorr, t = 2 mins.) was shown to revive degraded FET transfer characteristics after 200 days of storage without passivation [179]. Covalent nitrogen doping in MoS_2 was demonstrated with N_2 plasma (P = 100 W, $p = 7 \cdot 10^{-3}$ mbar, t = 15 mins.), leading to a strong V_{th} shift to positive gate biases but no hole branch conduction in the transfer characteristics [180]; most likely due to Fermi level pinning at the contacts [91]. For a review of p-doping of 2D materials see **Fig. 3.3**.

3.1.3.2 n-type doping

Degenerate n-type doping of TMDs has been achieved through various plasma exposure schemes. While we highlighted the role of oxygen-containing plasma in providing electron-withdrawing species on the surface of TMDs in the previous section, some studies utilising oxygen species report specific exposure time windows after which devices behave in a pseudo-metallic manner, i.e. exhibiting a reduced tunability of channel conductivity by the gate field. The first discovery of this effect by Kim *et al.* in 2016 [161] occurred during layer-by-layer stripping of sulfuric layers from mechanically-exfoliated MoS_2. Flat gate curves after pure oxygen plasma treatment (P = 21 W, p = 200 mTorr, t = 12 s) were observed in both 2L and 1L devices, with suggestions that this degenerate n-doping had its origin in the increased concentration of V_S in the underlying layers. The same type of dose-dependent recovery was also observed in CVD-grown 5L MoS_2 [181]. Similar gating phenomena have been yielded by benzyl viologen doping [128], confirming the role of chalcogen vacancies.

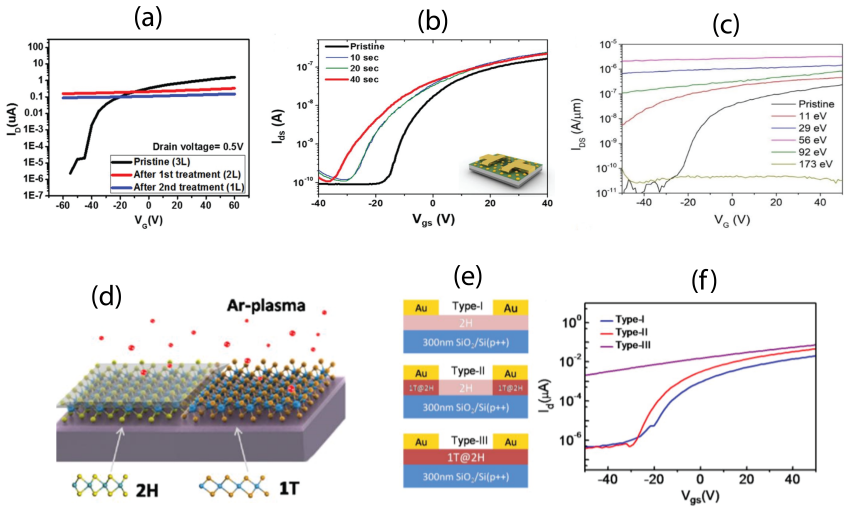

Figure 3.4: **(a)** Metallic-like response to the gate field on monolayer and bilayer oxygen plasma-treated MoS_2, adapted from ref. [161]. **(b)** V_{th} shift to negative gate biases mediated by the delivered dose of Ar plasma, adapted from ref. [182]. **(c)** Low-energy He plasma preferentially creating sulfur vacancies in MoS_2, leading to degenerate n-type doping, adapted from ref. [183]. **(d)** Rendering of a polymer-protected monolayer MoS_2 device being locally converted from the 2H to the 1T polytype by Ar plasma exposure, adapted from ref. [184]. **(e)** Illustration of different device exposure schemes to the Ar plasma and the resulting gate curves **(f)** obtained for each type, showing a metallic-like response after channel conversion between polytypes, adapted from ref. [184].

This same metallic-like sub-stoichiometric Mo oxide was observed in monolayer MoS_2 treated with cycled remote H_2 plasma (P = 400 W, p = 200 mTorr, t = 2 s) followed by passivation with oxygen plasma (P = 100 W, p = 100 mTorr, t = 2 s) [135]. The inter-defect distance at the emergence of this metallic-like conduction, estimated from the dose-dependent Raman spectra evolution, was calculated to be 2.1 nm, and evidenced in ACSTEM. Meanwhile, XPS shifts around this time indicate n-type doping of the surface. A resistor-loaded inverter was fabricated on a 1L flake, containing two FETs in series, by the poly(methyl methacrylate) (PMMA)-protected plasma exposures to the first channel, truly demonstrating the applicability of plasma processing for atomically-thin circuitry. Surface shielding with polydimethylsiloxane structures also allows for periodic patterning with Ar plasma (P = 60 W, p = 15 mTorr, t = 40 s) [182]. n-doping levels of up to 8.1 $\times$ 10^{11} cm^{-2} can be achieved on MoS_2 and WS_2 due to V_S generation, while utilising O_2:Ar plasma over the same amount of time leads to p-doping.

In general, this type of behaviour can also be induced by employing an inert plasma species (Ar, He) or hydrogen. Recently, Huang *et al.* have demonstrated the selective sputtering of S atoms from mechanically-exfoliated 1L MoS_2 by using He plasma at

energies as low as 11 eV (p = 0.1 mTorr, t = 10 min.) [183]. Up to 34% of S atoms can be removed in this manner without damaging the Mo sub-lattice, due to differing displacement threshold energies for Mo and S in the crystal lattice. By utilising plasma of a sufficient kinetic energy to remove S (17.4 eV), but undershooting the energy required for Mo removal (130.2 eV), V_S and V_{2S} defects preferentially form in the material, as identified in ACSTEM. Plasma energies of 11 - 92 eV thus lead to the flattening of the gate curve due to metallic behaviour arising from mid-gap states formed by the vacancies [185]. These states can additionally be passivated with oxygen or H_2O to recover a higher on/off ratio on the FET. Moving the plasma species to kinetic energies higher than 130 eV effectively removes Mo too, destroying the material and quenching its electrical conductivity. n-doping of WSe_2 can also be achieved by H plasma treatments (P = 5 W, p = 140 mTorr, t = 5 s) forming Se vacancies [186]. Su *et al.* have also found that - nitrogen plasma (P = 50 W, p = $2.7 \cdot 10^{-4}$ Pa, t = 5 min) reduces the work function of few-layer MoS_2 from 5.4 eV to 5.06 eV (increasing the electron concentration) [187], suggesting that N_2 may be a useful avenue to pursue in doping studies of layered chalcogenides. Linearising the gate curve can also be achieved when the 2H polytype of MoS_2 undergoes a structural phase transition to the 1T polytype, as observed after Ar plasma treatment (P = 20 W, p = 0.7 Torr, t = 40 s) in the monolayer limit [184] and confirmed by Raman, PL and XPS. For a review of n-doping of 2D materials see **Fig. 3.4**.

3.2 Helium ion beam irradiation

The other major method of modifying the structure and properties of 2D MoS_2 employed in this thesis is irradiation by a high-energy beam of ionised helium atoms. This is a technique that contrasts strongly with plasma treatment, whereby the modification of the target sample is highly localised and well-controlled, but suffers from low throughput and requires specialised equipment. In the following sections, we will describe the functionality of a helium ion microscope and the fundamental physical interaction between an accelerated ion and its target upon collision. We will then give a brief overview of how these charged particle beams have been used in recent years to modify both the structure and physical properties of 2D TMDs, with a focus on tuning the electrical properties.

3.2.1 Background on GFIS microscopy

The helium ion microscope belongs to the class of gas field ion microscopes, which utilise gaseous species of elements such as nitrogen, argon, neon or helium as the

charged particle medium through which high-precision imaging or patterning of a sample is achieved. It was first commercialised in the form of the HIM in 2007 by *Carl Zeiss Microscopy* and utilises what is known as a gas field ion source (GFIS). In contrast to conventional focused ion beam (FIB) systems, such as Ga^+-based microscopes which use liquid metal sources to produce the ionised species, the GFIS relies on a gun composed of a liquid N_2-cooled sharpened metal tip, biased with a positive voltage with respect to an adjacent electrode [188] (**Fig. 3.5(a)**). This tip has a stable configuration with three atoms at the apex (a *trimer*, **Fig. 3.5(b)**) and needs to be "built" again by electric field-based stripping when it deteriorates to a single atom or two-atom (dimer) source due to extensive use. The gun is housed in a UHV chamber connected to a gas delivery system which inlets the imaging gas in the vicinity of the tip at a rate of $\sim 10^{16}$ atoms s^{-1}. An electric field set up between the tip and the extraction electrode needs to reach magnitudes of ≈ 4.4 V $Å^{-1}$ to ionise the introduced helium gas.

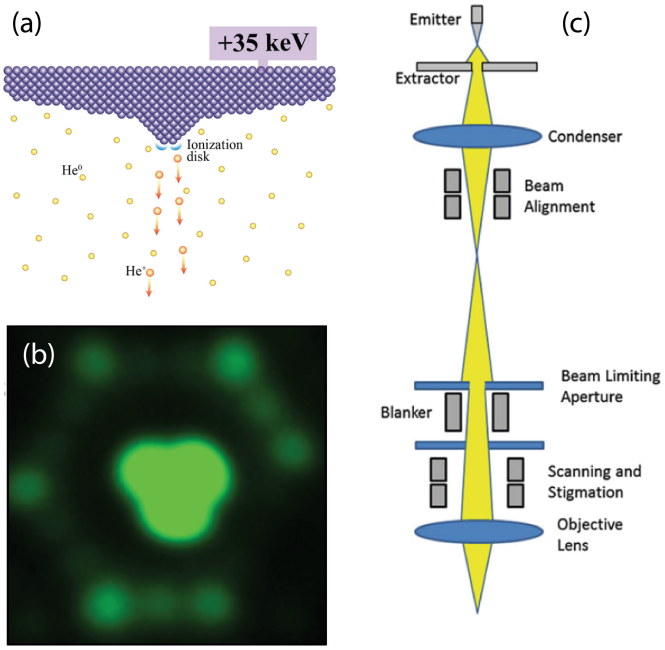

Figure 3.5: **(a)** Illustration of the GFIS emitter [189]. **(b)** False-colour micrograph of the formed trimer, imaged through the field ionisation effect [189]. **(c)** Sketch of the scanning ion microscope optical column [188].

This ionised gas can then be accelerated through a set of electromagnetic lenses which align the ion beam, magnify the image and correct for astigmatism, while also rastering the beam across the sample surface. A beam-limiting aperture can be inserted into the column to control the amount of probe current delivered to the

specimen. An overview of the column structure is given in **Fig. 3.5(c)**. The final size of the probe is ultimately limited by the size of the source image, spherical and chromatic aberrations and diffraction. For the HIM operating at 30 kV with a probe current of 0.5 pA, a probe size of 0.35 nm is achievable [188]. There are several advantages of using the HIM over another instrument like a scanning electron microscopy (SEM) for imaging samples. The HIM offers higher secondary electron yield and greater surface sensitivity due to its higher *stopping power*, higher resolution due to its shorter de Broglie wavelength and longer depth of focus due to lower beam divergence when compared with a standard SEM.

3.2.2 Beam-sample interaction

Energetic ions incident on a solid surface will penetrate into the bulk of the material and will bleed kinetic energy according to the specific *stopping power*, i.e. the rate at which the energy is converted; which is particular to the incoming beam energy and target material density. The average maximum depth to which the ions can travel is known as the *beam range* and it is most often described by the Kanaya-Okayama model:

$$R\rho = \kappa E^p \tag{3.2}$$

where R is the beam range, ρ is the density of the irradiated material, κ is a parameter that varies depending on the incident species (electron, ion type, etc.), E is the beam energy and p is a constant. Importantly, the penetration depth depends only on the material density for a given E, not the mass or atomic number. At the same beam energy, the range of He^+ ions when penetrating the same substrate is an order of magnitude lower than that of electrons [190]. The interaction volume of the helium ion beam with the target sample, at the same beam energy, is more confined to the surface than that of an electron beam (see comparison in **Fig. 3.6(a)**).

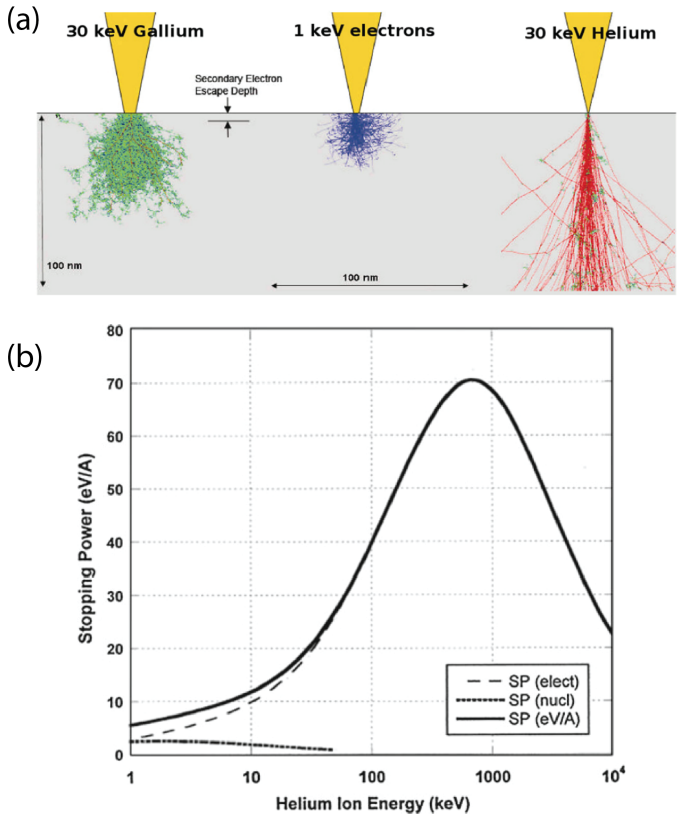

Figure 3.6: **(a)** Comparison of the simulated interaction volume of He^+ incident on Si; relative to electrons and Ga^+ [189]. **(b)** The stopping power of He^+ ions as a function of beam energy. The dotted line outlines the losses due to nuclear stopping potential only, while the dashed line outlines the losses due to electronic stopping potential only [188].

As the ions enter the sample, their halting will initially be dominated by energy transfer to electron clouds (*electronic stopping potential*) of the target material in the first few hundred nanometres. As they penetrate deeper into the substrate and lose a significant amount of energy, their cross-section for interaction with atomic nuclei of the target increases. Thus, the dominant stopping mechanism in the final stages of the beam range is due to the *nuclear stopping potential*. Hence, greatest atomic displacements due to knock-on energy transfer to nuclei also occur in this nuclear stopping region. For a comparison of the two stopping potentials see **Fig. 3.6(b)**. Crucially, the stopping power is ultimately governed by the ion velocity and not its total kinetic energy, when one scales for the large mass of the ion.

In the limit where this knock-on damage begins to lead to atomic displacements and material sputtering, we consider the ion *dose* or *fluence*, Φ, delivered to the material surface. The typical imaging dose delivered by the ion beam is of the order of 10^{11} - 10^{12} ions cm^{-2} during standard operation. With this low dose, the

imaging normally causes negligible sample damage due to limited occurrences of sputtering and atom displacement events. As the dose increases, the effects of ion-induced atom displacements get significant, which induces sample amorphisation and removal of atoms. As we will see for the case of on-substrate 1L MoS_2, this Φ is several orders of magnitude higher.

These collisions can be approximated by the Rutherford scattering model, which employs the idea of a *differential cross section* to track the probability of a displacement event (see sketch in **Fig. 3.7**). The probability scales with material density and is linearly proportional to the differential displacement cross section defined as [191]:

$$\mathrm{d}\sigma_d(E,T) = \pi \frac{M_1}{M_2} Z_1^2 Z_2^2 e^4 \frac{\mathrm{d}T}{T^2 E} \tag{3.3}$$

where T is the transferred energy during a collision, M_1 is the accelerated ion mass, M_2 is the target atom mass, Z_1 and Z_2 are the corresponding atomic numbers, e is the electronic charge and E is the beam energy. If we integrate the above expression between the displacement energy, T_D, i.e. the energy necessary to remove an atom from its unit cell, and the maximum transferable energy during a collision, T_m, we obtain the displacement cross section as:

$$\sigma_d(E) = \pi \frac{M_1}{M_2} Z_1^2 Z_2^2 e^4 \frac{1}{E} \left(\frac{1}{T_D} - \frac{1}{T_m} \right) \tag{3.4}$$

where the maximum transferable energy is:

$$T_m = \frac{4 M_1 M_2}{(M_1 + M_2)^2} E \tag{3.5}$$

σ_d leads to a given probability of material sputtering when scaled for the sample density. For a given delivered dose, the probability may exceed the density of the target material - marking the onset of the milling regime.

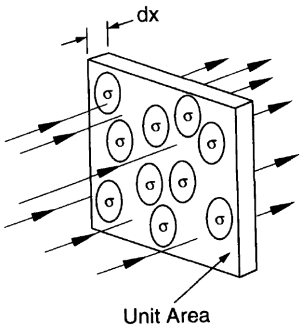

Figure 3.7: Sketch of a target unit area of infinitesimal thickness dx with each target atom presenting an effective scattering area σ obtained by integrating the cross section with respect to energy. [191].

3.2.3 Ion beam modification of 2D MoS_2

Light noble gas ion beam irradiation has been established in recent years as a successful method of defect engineering in 2D materials. The field has been opened to explore the effects of high-precision structural modification of TMD devices on the nanometre scale. The localised formation of defects by ion irradiation has been shown to induce unusual electronic properties in materials like MoS_2 [192], $MoSe_2$ [193] and WSe_2 [194], and is poised to become the primary method of nanoribbon formation [195, 196] and single-defect implantation [197, 198, 199] in the coming years. A detailed account of the progress can be found in the review articles by Li *et al.* [200] and Stanford *et al.* [201], while here we will mostly give a brief overview of relevant phenomena observed in ion-irradiated MoS_2.

Work done in our group in 2014-2015 (**Fig. 3.8**) has shown that dose-controlled irradiation with 30 keV helium ions leads to the preferential sputtering of sulfur atoms from monolayer MoS_2; while retaining micron-scale structural integrity for doses up to 10^{16} ions cm^{-2} [192]. A dose-dependent study of 1L MoS_2 samples irradiated while suspended on the supporting carbon film of a transmission electron microscopy (TEM) grid revealed the increased milling of material with increasing dose of the ion beam.

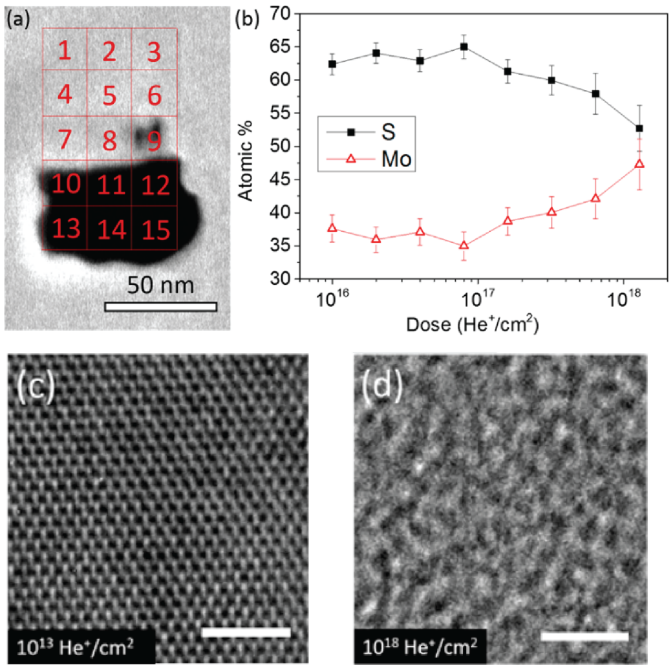

Figure 3.8: **(a)** STEM image of a suspended MoS_2 flake irradiated with 15 different doses, each twice the dose of the previous region. The first region is $1 \cdot 10^{16}$ ions cm^{-2}, milling occurs from region 9 ($2.56 \cdot 10^{18}$ ions cm^{-2}). **(b)** Concentration of Mo and S as a function of He^+ dose, extracted from EDX analysis in the TEM. **(c)** HRTEM image of pristine 1L MoS_2 after receiving a low irradiation dose of 10^{13} ions cm^{-2}. **(d)** HRTEM of MoS_2 after receiving a high dose of 10^{18} ions cm^{-2}. Scale bars in **(c)** and **(d)** are 2 nm. All figures from [192].

In addition, it was shown that the stoichiometry of MoS_2 can be tuned locally by site-specific He^+ ion beam irradiations. Spectroscopic analysis carried out in the TEM on samples which have been irradiated while suspended on a TEM grid revealed the onset of preferential removal of sulfur from the amorphised crystal lattice beginning in the region of 10^{17} ions cm^{-2}. A similar degree of damage was also observed in irradiated WSe_2 [202] for doses close to one order of magnitude less than those observed for MoS_2 - a discrepancy arising from the difference in $\sigma_d(E)$ of S and Se upon He^+ irradiation. A key consideration of this type of experiment is whether the sample is irradiated when suspended on the carbon film of a TEM grid or supported by a thick substrate like SiO_2. It has been noted that the dose necessary to induce the same amount of damage for on-substrate 2D materials is about an order of magnitude lower than that for suspended samples [203], and that the substrate governs defect production in supported samples due to additional contributions from secondary atom collisions and back-scattered primary ions [204].

The effect of this stoichiometric tuning on the electrical transport properties of MoS_2

was investigated on mechanically-exfoliated bilayer samples through full-channel irradiations with a broad (unfocused) helium ion beam.

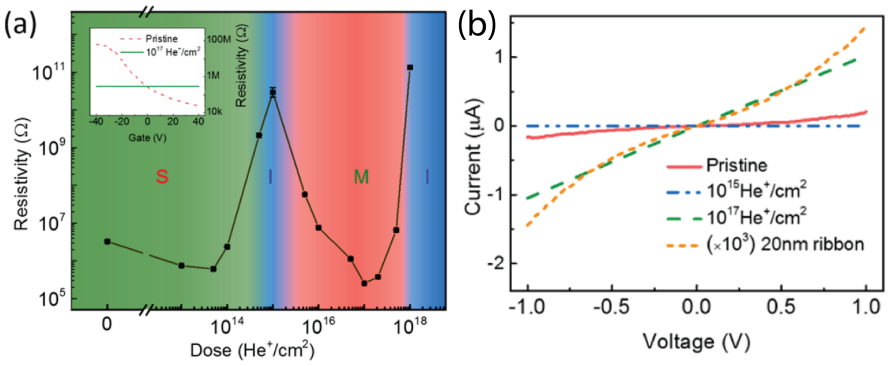

Figure 3.9: **(a)** Log-log plot of the resistivity of bilayer MoS_2 as a function of irradiation dose. The letters S, I and M mark the coloured regions corresponding to semiconducting, insulating and metallic-like behaviour respectively. Inset shows a comparison of the transfer curves of the pristine and metallic-like samples; highlighting the lack of field-effect tunability in the sample irradiated at 10^{17} ions cm^{-2}. **(b)** Low-bias *I-V* response of the MoS_2 sample as a function of dose. The oscillation in channel conductance with increasing dose is readily observed. Both figures from [192].

The sample resistivity evolves in an unusual manner with respect to the increasing bombardment dose; exhibiting four distinct stages:

- *Semiconducting* - in the first stage, the resistivity of the sample is dropping as the delivered dose is increased by as much as 28% up to 10^{14} ions cm^{-2}.
- *Insulating* - the second stage shows a dramatic increase (5 orders of magnitude) in the resistivity over a narrow dose range between 10^{14}-10^{15} ions cm^{-2}.
- *Metallic* - the third stage is characterised by a sudden drop in the resistivity to values below that of the initial pristine sample. In this region ($\sim 10^{17}$ ions cm^{-2}), the conductance of the FET channel is not tunable through the application of the field effect (flat gate curve in the inset of **Fig. 3.9(a)**; current variation across 80 V of gate bias is only 3%) and the *I-V* characteristics are highly linear (**Fig. 3.9(b)**).
- *Insulating* - the last stage sees a massive increase in the resistivity again, by six orders of magnitude after doses of $\sim 10^{18}$ ions cm^{-2}.

With the increasing amorphisation of the crystal lattice and the associated production of point defects by the ion beam, one would expect the electrical properties of MoS_2

to worsen significantly at high doses. The pseudo-metallic phase transition observed at $\sim 10^{17}$ ions cm^{-2} (at room temperature) may stem from the changing Mo:S ratio in the FET channel, or be mediated by more exotic effects associated with the increased concentration of electron-donating sulfur vacancies, which would require temperature-dependent characterisation to elucidate. Notably, a similar transition was reported in He^+-irradiated WSe_2 and characterised down to liquid nitrogen temperatures [194]. The observed charge transport mechanism above 125 K was the NNH mechanism (T^{-1} scaling), which transitions abruptly to the VRH mechanism ($T^{-1/3}$ scaling) below 125 K. Related crossovers have been observed in disordered semiconductors before [45] while VRH has also been associated with the presence of higher V_S densities in 2D MoS_2 [42]. In the case of helium-irradiated WSe_2, the damage induced by the beam to the crystal lattice is proposed to create percolating edge paths along extended defect sites, forming a network throughout the FET channel (**Fig. 3.10**) and allowing for the formation of a conductive metallic-like path, whose NNH transport would be gate-independent.

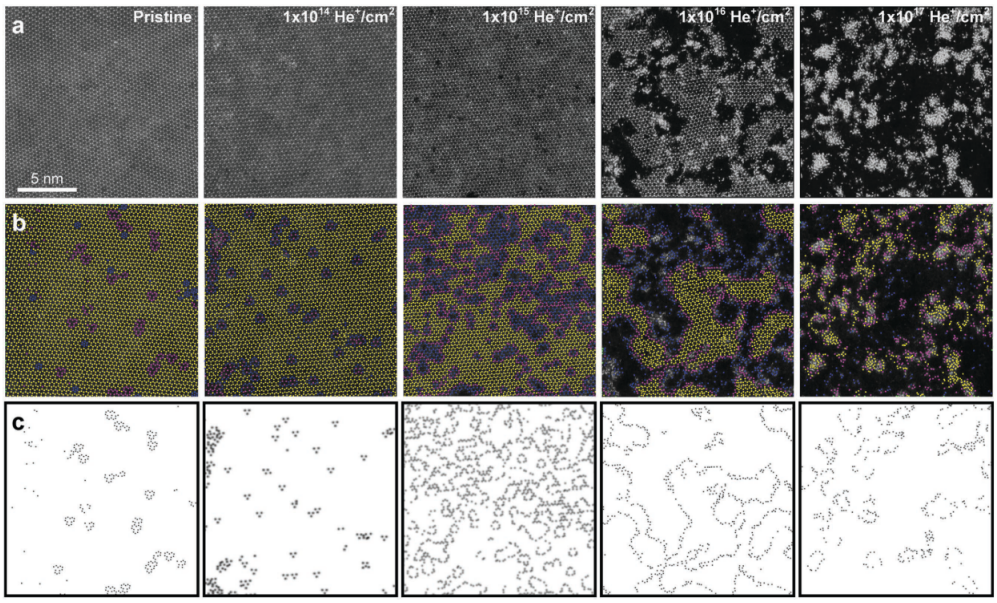

Figure 3.10: **Percolating path formation along defect edges in He^+-irradiated WSe_2 as a function of dose.** **(a)** STEM images of the irradiated samples. **(b)** Filtered images, marking atoms which are missing their nearest neighbours in red. **(c)** Only the boundary atoms from the STEM images. All figures from [194].

More work needs to be done by the community to elucidate the exact origin of the irradiation dose-modulated conductivity oscillation. In either case, we have established that we can finely tune the stoichiometry of MoS_2 by the localised

irradiation with a helium ion microscope. In addition, other FET parameters can be controlled by the purposeful introduction of V_S into the MoS_2 crystal lattice with inert ion irradiation. 500 eV Ar^+ irradiation has been employed to drastically shift the threshold voltage of monolayer MoS_2 [205]. When V_S concentrations reach 1%, V_{th} is found to shift by as much as Δ20 V, while V_S reaching 5% leads to staggering V_{th} shifts of $\sim \Delta$50 V. Interestingly, depending on the exact structure of the formed defects, these beam-formed dopants can either be electron donors or acceptors. It has been found that the formation of a dislocation-divacancy complex in MoS_2 can lead to significant n-type doping, which shifts the V_{th} to higher negative gate biases [206]. These complex states can also improve the carrier mobility by forming stable impurity bands near the conduction band [185]. As the spread of a typical focused He^+ ion probe is several nanometres, the formation of other defects in the irradiated 2D lattice is also expected. Thus, the deep n-type doping behaviour achieved by ion sputtering depends not only on the fluence of the beam, but also the absolute number of defects which are introduced and their overlap/coupling of electronic interactions in the lattice.

Hence, device performance can be tuned by Φ-controlled exposures, while the effective dopant concentration and introduced scattering potentials need to be tailored accordingly to achieve the desired functionality. In the experimental results chapters of this thesis, we will consider the effects of introducing localised and global defect populations into MoS_2 FET channels of various layer number with the He^+ ion beam.

Chapter 4

Device fabrication and characterisation techniques

> "the *Information:Action Ratio* is the place to go"
>
> - Alex Turner,
> *Four Out of Five*, 2018.

This chapter details the material synthesis, device fabrication, modification and characterisation techniques employed throughout this work. We will summarise the MoS_2 chemical synthesis and physical exfoliation, the device fabrication steps using electron beam and optical lithography, as well as sample transfer. We will then review the experimental approaches used herein for plasma functionalisation and helium ion beam treatment of 2D MoS_2. Finally, we will briefly overview the characterisation techniques employed throughout this work. These have been categorised into microscopic, spectroscopic and electrical methods.

4.1 Material synthesis and device fabrication

In this section, we will describe the synthesis of ultra-thin specimens of molybdenum disulfide which serve as the test platform for the devices we fabricated and studied. Methods of device fabrication, both by optical and electron beam lithography, will also be overviewed here. The availability of starting material was crucial to the success of the work described in this dissertation, both in terms of monolayer yield and specific layer number control. As such, we split the sample synthesis section into two subsections that focus on both of these issues: **(1)** the consistent growth of large-area, single-crystal MoS_2 monolayers by chemical vapour deposition, and **(2)** the mechanical exfoliation of MoS_2 from the bulk, allowing for specific layer number control and high-quality naturally-occurring samples.

4.1.1 Chemical vapour deposition of 2D MoS_2

The following methodology has been developed in the lab of Prof. Georg Duesberg in the School of Chemistry, TCD, and the results we go on to describe are the outcome of synthesis work carried out by Conor Cullen in that same lab. Throughout this

thesis, whenever referring to results obtained on CVD-grown monolayers of MoS_2, we assume they were synthesised by Mr. Cullen. Mainly based on the report by O'Brien *et al.* published in 2014 [207], this method has since been honed to consistently produce large-area (tens of microns), good-quality (defect density < 0.5% by concentration), isolated triangles of monolayer MoS_2, which are easy to contact electrically and can exist in populations of tens, if not hundreds, on a single chip.

The methodology described herein is often referred to as the "microreactor" method or the "close proximity precursor" method, where the growth of the final product occurs very close to the starting material - in contrast to standard CVD schemes employed to grow TMDs in the last decade [208, 209, 210]. In addition, this particular process makes use of another scalable large-throughput method of thin film production to prepare the reaction precursor; namely liquid phase exfoliation (LPE). This technique, developed in 2008 [24], utilises ultrasonic energy to cleave the van der Waals bonds in layered materials and separates them into thin sheets in a stabilising solvent. Thin platelets of MoO_3 were prepared by John B. Boland, Coleman Group, School of Physics, TCD using the LPE method [211] and were dispersed in propan-2-ol (IPA) and drop cast using a pipette onto 285 nm SiO_2/Si substrates. The chip was then heated on a hot plate to 150°C to allow the IPA to evaporate off.

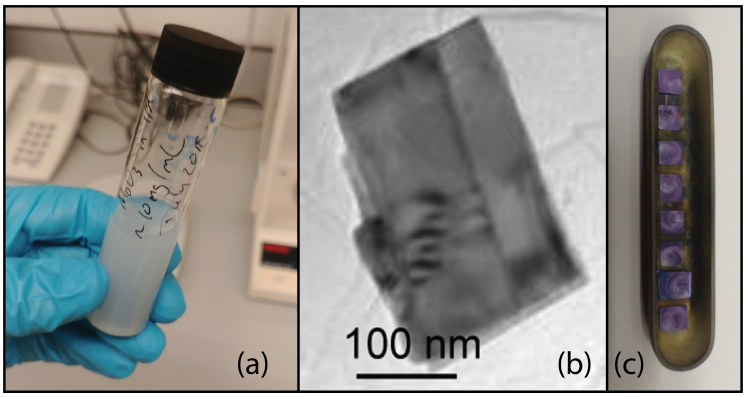

Figure 4.1: **(a)** Photograph of an IPA:MoO_3 dispersion used to deposit the precursor on the substrates. **(b)** TEM micrograph of a typical MoO_3 flake drop-cast post-LPE, using the method described in Hanlon *et al.* [211]. **(c)** Ceramic boat containing multiple chips (~ 1 cm^2) with the dispersed MoO_3 precursor.

The MoO_3 seed films (**Figs. 4.1(a,b)**) were then placed in a small ceramic boat, where several of them can be housed at once (**Fig. 4.1(c)**); allowing the growth of

hundreds of flakes of MoS_2 across many chips in the same run. The blank target SiO_2/Si substrates were then placed face-down directly on top of the precursor chips for the close-proximity growth (**Fig. 4.2(a)**). The chip-containing boat was loaded into the hot zone in the centre of the quartz tube furnace (**Fig. 4.2(b)**) and the furnace was heated to 750°C. Sulfur powder (*MaTecK, 99%*) was used to fill another ceramic boat (**Fig. 4.2(c)**) which was then inserted into an independently-heated zone upstream from the sample boat (**Fig. 4.2(d)**). The powder was heated to ~ 120°C and transported through the quartz tube over the hot zone with carrier Ar gas, whose pressure was monitored and maintained at ~ 0.7 mTorr (**Fig. 4.2(e)**). This transport process, which sulfurises the oxide precursor (**Fig. 4.2(f)**), usually takes about 20 minutes and is followed by an annealing step in the hot zone for a further 20 minutes in the presence of Ar gas. The boat is allowed to cool to room temperature by opening the furnace. A liquid nitrogen sheath is used to condense and collect spurious S vapour from the powder-heating zone, ensuring the tube is not over-saturated with gaseous sulfur.

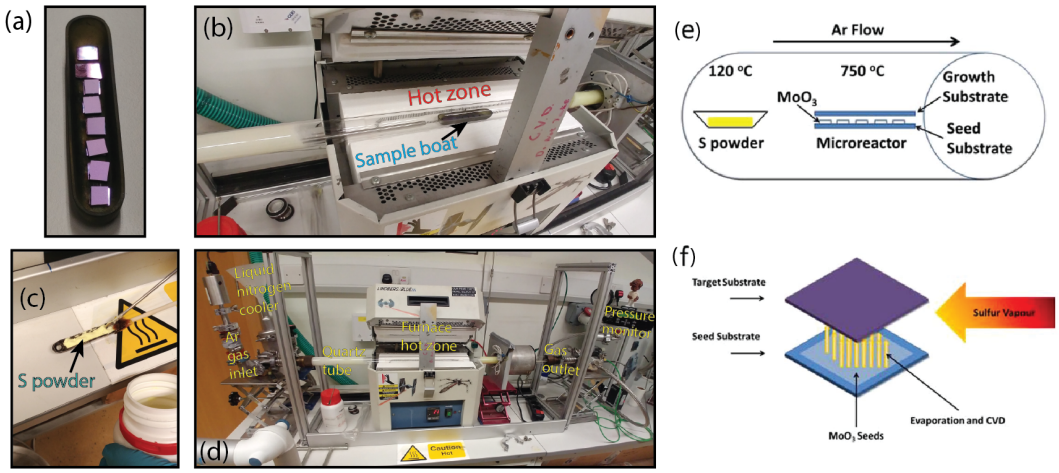

Figure 4.2: **(a)** Ceramic boat containing multiple chips with the dispersed MoO_3 precursors covered by face-down blank target substrates. **(b)** Photograph of the inside of the furnace hot zone, with the boat containing the chips being placed in the middle of the quartz tube. **(c)** Ceramic boat being filled with S powder; to be placed between the gas inlet and the sample boat. **(d)** Overview of the CVD furnace structure. **(e)** Diagram of the growth process flow inside the reactor. **(f)** Illustration of the evaporation of the precursor onto the target substrate in the close-proximity regime.

With appropriate tuning of the S flow rate, the time taken for sulfurisation, annealing and cooling, the resulting products of this chemical process are well-defined, isolated triangles of monolayer MoS_2 that can be anywhere from 1 to 50 μm in size (**Fig. 4.3(a,b)**), and can merge into larger films, stitching together at grain boundary

regions. The films are high-quality monolayer MoS_2, as confirmed by PL spectroscopy & Raman spectroscopy (**Fig. 4.3(c,d)**), as well as XPS [207]. Naturally, depending on the time when the reaction was stopped, thicker areas (especially around the Au lithography markers on the target substrate) are also synthesised. In many cases, incomplete bilayer regions are present on the top of monolayer specimens, as the layer-by-layer growth process was suddenly stopped.

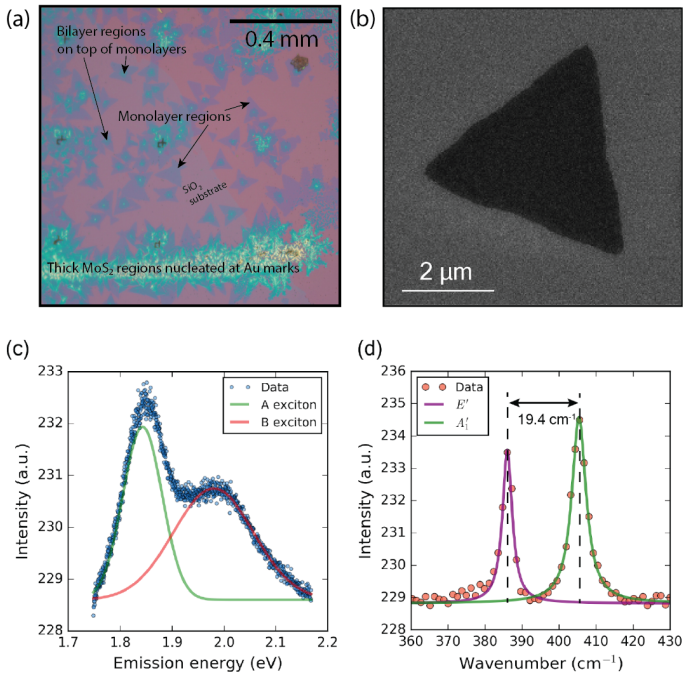

Figure 4.3: **(a)** Optical micrograph of as-grown MoS_2 flakes distributed on the growth substrate. Labels point to the monolayer, bilayer and thicker regions on the SiO_2 chip. **(b)** SEM image of a monolayer triangle on the SiO_2 growth substrate. **(c)** PL spectrum of 1L MoS_2, exhibiting the direct (A) and spin-orbit split (B) emission peaks. **(d)** Raman spectrum of the first-order modes of monolayer MoS_2, exhibiting well-defined in-plane and out-of-plane vibrational peaks of the as-grown samples.

Thus, we have established a reliable and scalable method of obtaining monolayer MoS_2 samples in order to fabricate devices in the single-layer limit. Next, we focus on obtaining MoS_2 flakes of a particular layer thickness, as necessitated by some aspects of this work.

4.1.2 Mechanical exfoliation of 2D MoS_2

This method of obtaining ultra-thin crystals of TMDs has been known to yield films only few molecular layers-thick since the 1960s [212]. Fine-tuned by the group of A. Geim to isolate graphene in 2004, this method of exfoliating van der Waals crystals

led to the Nobel Prize in Physics in 2010 for the Manchester scientists, and started a boom in the field of materials science when other groups began re-discovering "boring" materials like MoS_2 in the monolayer limit by employing this technique. It works on the basis of physical cleavage of the individual van der Waals layers by applying a force which overcomes the inter-layer bonding. For a material like MoS_2, long used as a lubricant in engine oil, this is relatively easy to achieve on the macro scale. A simple mechanical tool, like a pair of tweezers or a small chisel, can be used to separate layers of this material from naturally-found molybdenite ore. As is the case with LPE and chemical intercalation methods, what proves key to the cleaving process is the value of the surface energy of the nominally non-reactive basal plane of the MoS_2 crystal. The cleavage energy of the (0001) plane in MoS_2 is relatively weak, making the crystal more likely to part along this plane than any other planes.

It turns out that a sequential peeling process using an adhesive tape can readily produce monolayers of 2D MoS_2. The approach is incredibly simple, though its throughput is only a few samples per exfoliation round, found in random locations on the chip. In our case, thin (< 1 mm) flakes of bulk MoS_2 (*SPI Supplies*) are placed and gently pressed into the middle of a strip of adhesive tape (*Scotch*) with metal tweezers. The ends are folded in to make handles, and the tape is folded over and opened repeatedly so that the MoS_2 material migrates from the middle of the tape out towards the edges and begins to cover the whole strip (**Fig. 4.4(a)**). The tape will be covered fully in grey debris, but will look translucent when held up against a light. At that point, it is ready to be pressed into a target substrate (**Fig. 4.4(b)**) (in our case a 285 nm silicon dioxide layer on a silicon wafer, which has been pre-cleaned with acetone, IPA and deionised water) with a gentle press of a fingertip.

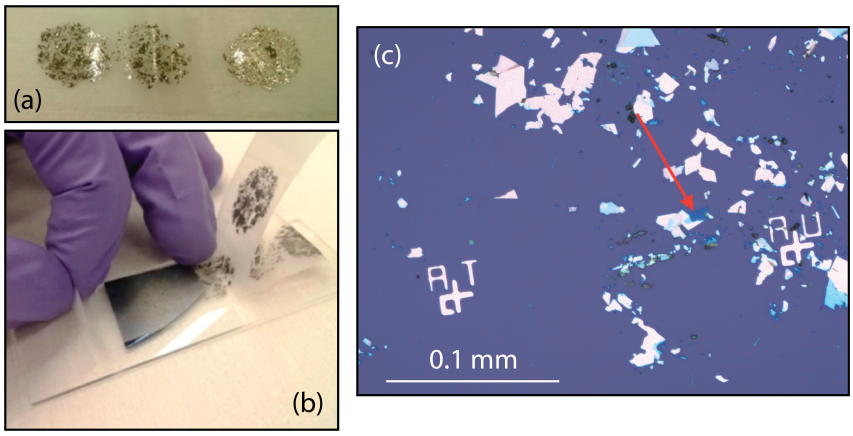

Figure 4.4: **(a)** Peeled bulk material on the adhesive tape [213]. **(b)** Deposition of the exfoliated material onto a substrate [213]. **(c)** Low magnification optical micrograph of the substrate post-deposition of exfoliated flakes, as carried out in our lab. The red arrow points to a candidate bilayer sample.

A soft object, such as a pencil rubber or a rubber pipette filler, is then used to lightly tap the back of the tape into the chip for a few minutes to improve the adhesion of the bottom-most layer of the exfoliated MoS_2 to the substrate. The tape is then peeled back from the chip at a very shallow angle *as slow as possible*. This procedure will cover the chip surface with MoS_2 samples of various thickness (**Fig. 4.4(c)**). More than one monolayer region can be present on a 1 cm^2 chip, but there are no guarantees - and oftentimes it will not be an isolated sample, but rather an area sticking out from the side of a larger, thicker flake. All things considered, tens - if not hundreds - of flakes which are less than ten molecular layers in thickness may be present on the substrate when this methodology is patiently followed.

Due to thin film interference of light with the underlying 285 nm-thick SiO_2, the optical contrast of samples of varying layer number resting on the substrate will be quite different. This allows for fast and accurate identification of layer number based on the red, green and blue (RGB) values when cross-referenced against other characterisation methods sensitive to layer number, like Raman spectroscopy or AFM. With software like `ImageJ` installed on the same computer which operates the optical microscope, layer thickness can be determined very quickly and accurately from the intensity difference of the RGB channels between the bare substrate and the on-substrate flake. This can be done while the operator is searching for samples under the microscope, making sample identification relatively high throughput in the pipeline towards lithography.

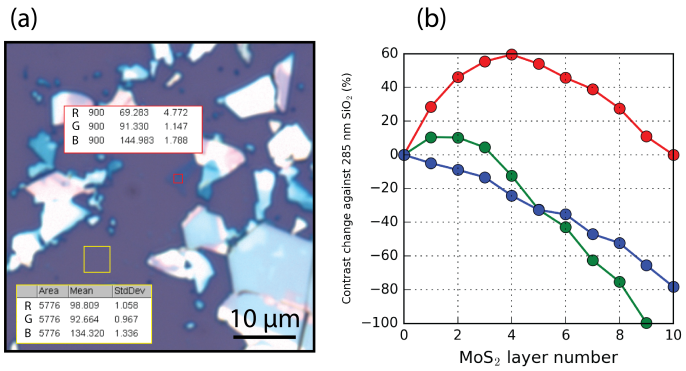

Figure 4.5: **(a)** Optical micrograph of exfoliated MoS_2 flakes showing regions from which contrast was evaluated. The red, green and blue channels were averaged in `ImageJ` from the substrate (yellow) and a candidate monolayer sample (red). **(b)** Plot showing experimental values of contrast change taken in our lab as a function of MoS_2 layer number for samples exfoliated onto 285 nm SiO_2/Si substrates. These values were cross-correlated against AFM measurements in CRANN by Prof. Yangbo Zhou.

The optical contrast is defined as:

$$C = \frac{I_{\text{flake}} - I_{\text{substrate}}}{I_{\text{flake}} + I_{\text{substrate}}} \tag{4.1}$$

where I is the reflected intensity for normal incidence white light, which depends strongly on the refractive indices of the involved media [214], i.e. MoS_2, SiO_2 and the semi-infinite under-layer of Si [215]. The MoS_2 acquires a darker blue colour to the eye if the sample is thinner than 5 layers on the 285 nm SiO_2 substrate. Specimens in the 5-10 layer range, in turn, have a bright turquoise colour, while samples much thicker than 10 layers have a yellow-like appearance (see the variation in colour of the deposited samples in **Fig. 4.5(a)**). Thus, with experience, it becomes easy to determine the approximate layer thickness of the sample just by a quick glance in the optical microscope - allowing for quicker identification of samples in a desired thickness range. For our purposes, we can also just use the percentage contrast change in the RGB channels between the bare substrate and the on-substrate flake [216], which has been correlated to AFM measurements by Prof. Yangbo Zhou in our lab and is presented in **Fig. 4.5(b)**. In the sub-5 layer limit, the red channel intensity is particularly sensitive to layer number, so a quick determination of the red channel contrast is often the simplest way to know how thin the sample is. For a final confirmation when looking for a monolayer, Raman and PL are the most reliable avenues for recognising single-layer samples from the Raman peak separation and the PL direct-gap emission; as we will outline in the following chapter. If one

desires a sample that is specifically 4 layers, for example, then AFM needs to be employed to double-check the layer thickness, as surmised from optical contrast after exfoliation.

4.1.3 Electron beam lithography

Once the flakes are on the substrate and ready for further processing, they need to be contacted electrically with a conducting material so that their electrical properties can be reliably tested and functional devices can be fabricated. The main fabrication method utilised throughout this thesis is electron beam lithography (EBL). The method involves using a scanning beam of electrons to draw bespoke patterns on a surface covered with a polymer called a *resist*. The resist's chemical structure is such that its chemical bonds can be altered by the energy of the localised electron beam. This selectively *exposes* the resist and changes its local solubility in a given solvent (the *developer*), allowing for the selective removal (in the case of a *positive* resist) or retainment (in the case of a *negative* resist) of the exposed areas, meanwhile leaving behind the unexposed positive resist or removing the unexposed negative resist. The opened windows in the resist film can then serve as pits for the selective deposition of a metal onto the sample and/or substrate, while also covering the remaining resist areas. Following this deposition step, the resist can be *lifted-off* by using a remover solvent. This will strip the entire resist off the processed substrate, including the metal film on top of the resist, but will detach the metal film from the areas in the beam-exposed pits, effectively leaving behind a metallised pattern that was exposed by the electron beam for a positive resist, or leaving behind the only areas not covered in a metal for a negative resist. The process flow chart for EBL is visualised in **Fig. 4.6**.

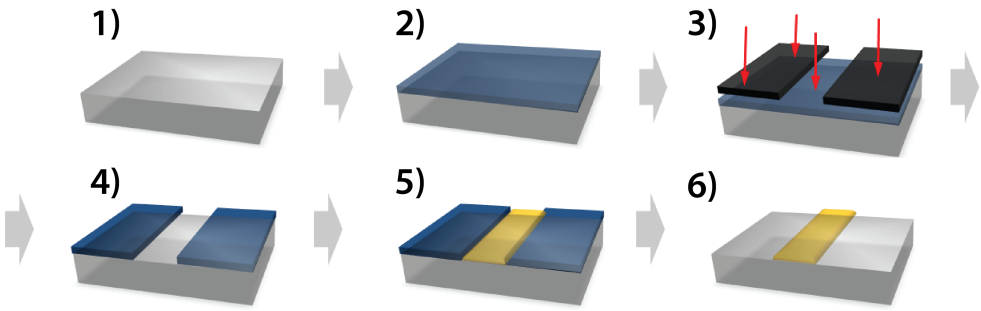

Figure 4.6: Process flow chart of electron beam lithography. **1)** Substrate (grey) ready for resist deposition. **2)** Polymer (navy) is spun onto the substrate. **3)** An area of interest is exposed to the electron beam (red arrows). In the case of photolithography, an optical mask is used (black). **4)** Treatment with a developer removes the exposed areas in the case of a *positive* resist such as PMMA. **5)** Metal film (yellow) is deposited in the window opened by the electron beam exposure. **6)** The remains of the polymer are lifted off in a remover solvent such as acetone. This leaves behind the metal structure deposited in the pre-determined areas. Diagram adapted from [217].

Throughout this thesis only positive resists were used (PMMA & *S1813*), so the following discussion will pertain to resists which dissolve in the developer after exposure to the electron beam. In addition, only 285 nm SiO_2/highly p-doped Si (ρ = 0.005 Ω cm) substrates were used, so from here on we will refer to them as *chips*. The chips are usually 1 cm^2 or less in dimension and are chipped away from a larger pre-ordered wafer (*Graphene Supermarket*) using a diamond scribe against the edge of a glass slide. The individual chips can then be used as substrates for the CVD growth or the mechanical exfoliation. It is vital that the chips contain visible *markers*, e.g. periodic metal structures deposited on the chip surface using optical lithography before sample deposition. These are usually sequential numbers or letters of the alphabet extending in the x and y directions, allowing for the identification of the sample location relative to this pre-existing orientation system on the chip surface. In this work, we often used alphabetical markers, extending from A to Z, with the exception of the letter Q, to allow for 25 periods of 200 μm that cover a distance of 5 mm. In the case where a chip is large enough to contain several alphabets, the first occurrence of a given letter from the bottom left corner of the chip was labelled as being in the 0^{th} period, and the next occurrence of that letter 5000 μm away in the x or y direction is in the 1^{st} period, and so on.

Samples were identified under an optical microscope (*Olympus BX53M*), taking images using the 20× objective lens, which allows for the inclusion of two consecutive markers in the same field of view. These images were then imported into

computer-aided design (CAD) software `DraftSight`, appropriately scaled, rotated and centred around the marker which would serve as the origin of the EBL pattern at that location. The generated `.dxf` file was then imported into `Raith Elphy Quantum` software, where electrode patterns could be drawn and assigned their appropriate exposure parameters. A typical experimental EBL process flow, or *recipe*, involves several steps and is described in detail in **Appendix A**. **Figure 4.7** shows the work flow of device fabrication on an example device location ($S^0 \perp K^0$); including the identification and designation of device channels (labelled here 0.4 & 0.5), in a series of optical micrographs and CAD patterns. Care must be taken to contact the electrodes such that no shorting occurs across the large-area multilayer film often surrounding individual triangles.

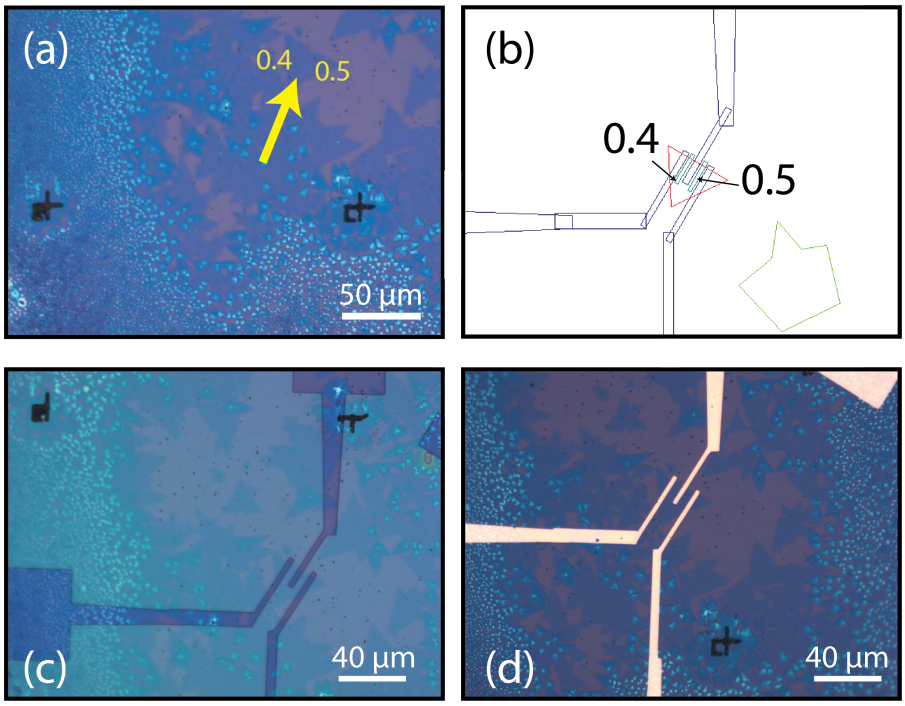

Figure 4.7: **(a)** Optical micrograph of the as-grown CVD film at mark location $S^0 \perp K^0$, with the yellow arrow pointing to a chosen monolayer flake designated for the fabrication of channels with channel-to-irradiation ratios, I_R, of 0.4 and 0.5. **(b)** CAD pattern of the devices, including He^+ irradiation areas designated as a different exposure layer. **(c)** Post-EBL micrograph showing the exposed PMMA film with the outline of the electrodes. **(d)** Post-metallisation image, showing the device with two channels before any He^+ exposures.

The resolution of EBL is ultimately defined by the *proximity effect*, which limits the minimal distance between two on-substrate patterns to the separation at which the dose distributions from the two respective patterns begin to overlap and over-expose

the resist. In this thesis, we are not concerned with pushing these resolution limits (which are in the tens of nm range), as our devices tend to have channels which are > 1 μm in length.

4.1.4 Optical lithography

Optical lithography (or *photolithography*) can also be employed to deposit electrodes on the sample. The process flow is similar to that of EBL, but instead of using an electron beam to expose the resist, UV light is used. This has several advantages over EBL; namely throughput (a single exposure takes ≈ 6 seconds) and processing scale (it is easy to expose multiple chips in a single session once the mask aligner is in place). The trade off against EBL is the pattern resolution which is limited by the wavelength of the used light; although industry-standard extreme UV methods utilising CO_2 lasers through *steppers* have pushed feature sizes into the nm range [218].

In our case, we use *S1813 Microposit* positive resist (propylene glycol monomethyl ether acetate, including diazo photoactive compounds), spun for 1 minute at 5000 revolutions per minute (rpm). This produces a 1.3 μm thick film, allowing for easy lift-off of the polymer due to the height discrepancy between it and the sample. The resist is soft-baked at 115°C for 75 s. An *OAI* mask aligner is used to align a quartz mask containing pre-defined electrodes in the field of view of an optical microscope to the sample of interest. This is followed by exposure for 6.5 s using the 385 nm UV lamp. The patterns are developed in commercial *metal-ion-free 319* developer for 50 s, finished with a deionised water wash. The resolution of the *OAI* system is ≈ 1.5 μm. This allows for the fabrication of multiple channels on a single flake, as well as the fortuitous contacting of flakes which happen to be in the way of the electrodes. As such, many flake channels can be shorted with larger flakes, and those MoS_2 areas need be scratched away with the micromanipulator needle under the optical microscope to make sure that current only flows through the desired flake channel. Examples of photolithography-fabricated devices are presented in **Fig. 4.8**.

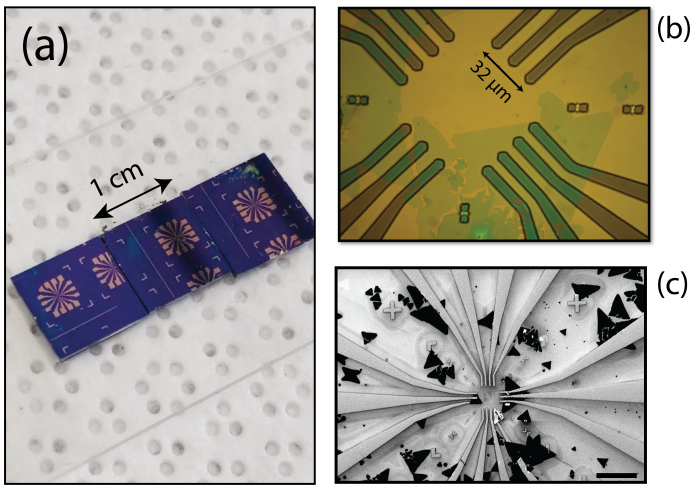

Figure 4.8: **(a)** Three chips on a glass slide, processed using optical lithography. The large electrodes are clearly visible to the naked eye. **(b)** High-magnification (100×) optical micrograph showing an exposed pattern of electrodes on MoS_2 monolayer flakes. **(c)** SEM image of optical lithography-defined electrodes deposited on MoS_2 samples. Scale bar in the bottom left corner is 100 μm.

4.1.5 Sample transfer

Sometimes, we must move MoS_2 samples from their growth substrate to another location - be it another substrate or, more commonly in this thesis, a TEM grid for microscopy experiments. We can do this by the polymer *stamp transfer* method, initially developed for graphene transfer by our former postdoc Prof. Yangbo Zhou [219]. This method can either be global or site-specific, giving it several advantages, such as the ability to move a specific treated flake onto a TEM grid for subsequent microscopic and/or spectroscopic characterisation. A polymer of sufficient thickness (usually ~ 200 nm PMMA A3) is spun onto a chip containing the TMD flakes we are interested in moving. In the case of specific samples, we carry out a round of EBL exposure around this flake location, to open up a malleable frame around the sample to be transferred, whose corners are still attached to the main polymer matrix, holding the area containing our sample in place. Edges of the chip are then scratched all around with a razor blade in order to expose the oxide layer underneath the PMMA. The chip is floated on top of either concentrated hot (90°C) sodium hydroxide (4M NaOH) solution, or room temperature concentrated potassium hydroxide (4M KOH) solution. The edges of the chip are lightly submerged in the solution to speed up the oxide dissolution. In the case of the heated reaction, the dissolution of the oxide might take anywhere from 30 minutes to several hours, while the ambient solution is usually left in the beaker overnight to eat away at the SiO_2 underneath the polymer.

A disadvantage of the heated method is the formation of gas bubbles in the solution, which can lead to crumpling of the polymer and the destruction of the selected stamp region.

Once the oxide is dissolved, the Si chip falls to the bottom of the beaker, leaving the PMMA floating on top. The polymer has TMD flakes attached to its underside, meaning that it can now be fished out of solution, moved onto a new location and dissolved away to retain the flakes on the target substrate or grid. In the case of global transfer, the film can just be moved directly to the location and dissolved, with some useful samples hopefully landing nicely, so that we can work with them. In the case of site-specific transfer, we need to fish out the polymer film with a coiled Cu wire frame and place it on a glass slide underneath an optical microscope objective. The stamp can then be accessed using a sharpened glass needle on the end of a micromanipulator. The needle is tapered using a heated filament capillary puller, in order to be tens of nanometres sharp. It can then be used to physically poke through the stamp pattern and to rip it out of the rest of the PMMA film suspended over the copper wire frame. Once the sample-containing stamp is hanging over the end of the glass needle, the manipulator can be used to slowly lower it onto a new target location and press it into the substrate to detach it. Thus, the stamp is transferred and after an acetone/IPA wash, the sample is ready for further experiments on the new substrate. The details of the procedure, as first developed for graphene on Cu foil in 2011 [219], are shown in **Fig. 4.9**. In the case of our MoS_2, the procedure remains the same but we dissolve the SiO_2 (rather than Cu) with a hydroxide solution (rather than $FeCl_3$ + HCl), as mentioned before.

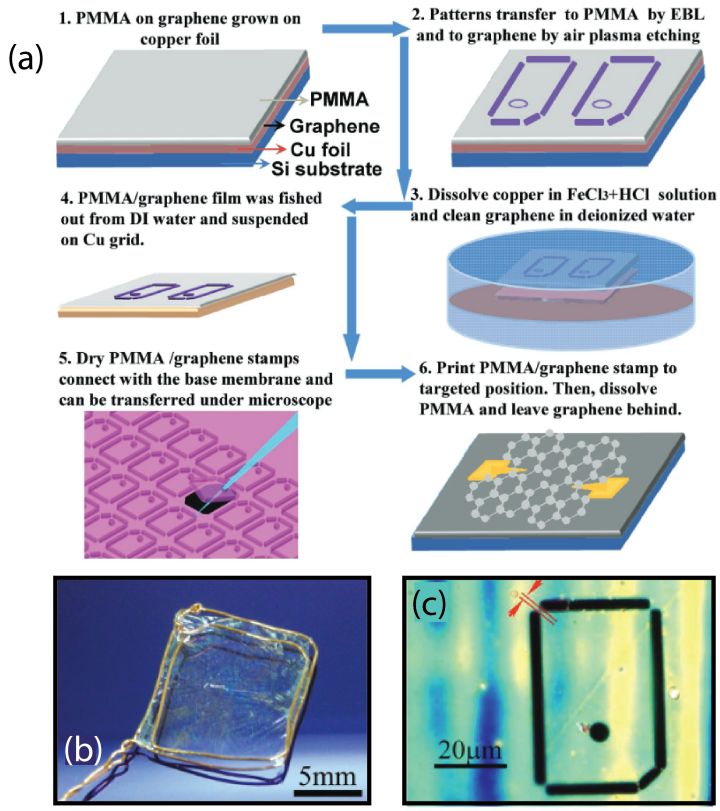

Figure 4.9: **(a)** Transfer-print process flow for inter-substrate 2D nanosheet transfer. Panels (1–4) illustrate how to produce arrays of suspended and patterned PMMA/graphene stamps. Panels (5,6) show the deployment of the prepared graphene sheets to construct a device on another substrate. **(b)** The suspended polymer film after being fished out of solution with a wound copper wire. **(c)** Optical image of the PMMA/graphene stamp connected with the base membrane; the red arrows indicate the width (1.5 μm) of the connection area. All figures adapted from [219].

4.2 Material modification

4.2.1 Plasma treatment

In this work, all plasma exposures were undertaken in a *Fischione Instruments 1020* plasma cleaner, nominally used for the pre-treatment of TEM specimens. The instrument cross section is presented in **Fig. 4.10(a)**. Exposures were always carried out in bursts of 2 s, utilising O_2:Ar (1:3) gas at a pressure of $\sim$ 5 mbar. The chip containing the MoS_2 devices was inserted into the chamber supported by carbon tape on an aluminium stub screwed onto a stainless steel rod holder. The chip location did not change to within $\pm$ 1 mm between exposures to ensure a consistent plasma dose delivery every time, as well as impact energy of the plasma species. As seen on the chart in **Fig. 4.10(b)**, the plasma ion energy changes significantly subject to the chamber gas pressure and the location away from the high-frequency antenna.

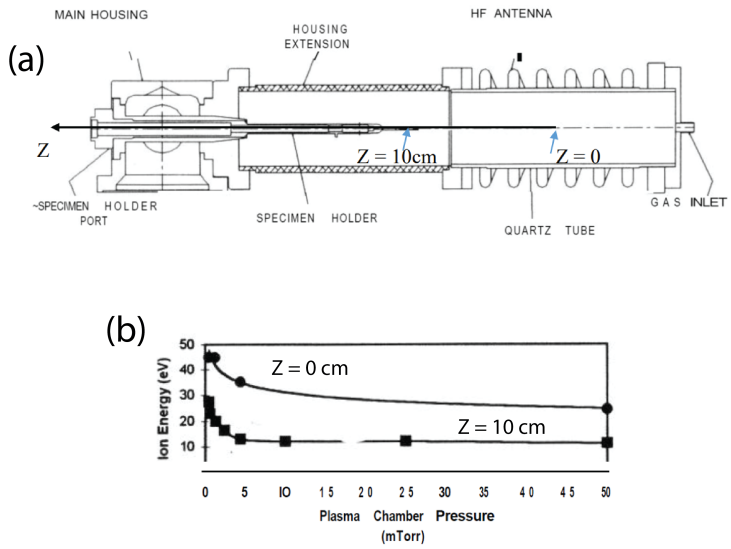

Figure 4.10: **(a)** Cross section of the plasma cleaner. HF; high-frequency. **(b)** Variation of the impact energy of the generated species as a function of position in the plasma chamber. The MoS_2 chip was placed at the $Z = 15$ cm zone (where $Z = 0$ cm is in the centre of the high-frequency antenna), with its position not varying on the sample holder to within ± 1 mm over different exposures. Figures adapted from [220].

Our MoS_2 chips were always placed in the middle of the holder rod, leaving them to be exposed at the $Z = 15$ cm position in the chamber. This lowered the impact of the ionic species significantly, meaning the plasma interacted more gently with the MoS_2, at a kinetic energy of only a few eV.

4.2.2 Helium ion beam irradiation

4.2.2.1 Determining the probe size and the delivered dose

Prior to exposure of the MoS_2 channel, the probe size of the helium ion beam was established from images of nearby gold markers elsewhere on the substrate (within tens of microns away from the target device). As gold has a much higher secondary electron (SE) emission intensity than the underlying oxide substrate, it is assumed that the edge of the gold marker is ideally sharp.

`ImageJ` software was used to fit the intensity drop-off over the edge of the gold mark on a 2048 pixel^2 micrograph taken with a scan dwell time of 5 μs. The equivalent full-width-at-half-maximum (FWHM) of the fit is taken to be the probe size as dictated by the Gaussian spatial distribution of the ions in the impinging beam (see evaluation in **Fig. 4.11**).

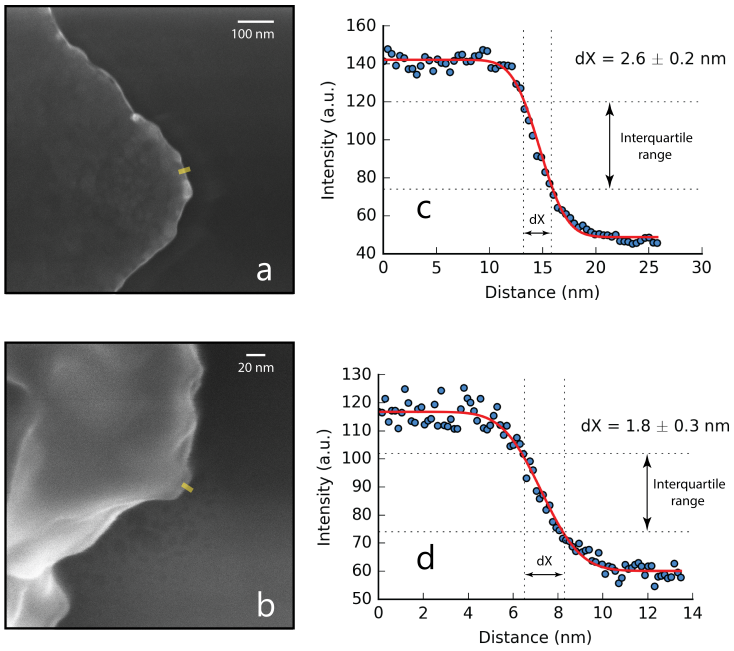

Figure 4.11: **Evaluation of the He^+ probe size before memtransistor fabrication. (a,b)** HIM images of the edges of deposited gold markers near an irradiation site. **(c,d)** Probe size estimation using the 25/75% profile method from line profiles seen on the HIM images in yellow.

As the monolayer samples tend to be relatively large (> 20 μm), some real estate on the chip can be saved by designing multiple channels on the same flake, using inter-digitated electrode patterns. The length of the FET channel (L), i.e. the electrode-to-electrode length, was usually > 2 μm throughout this thesis in order to keep the devices as uniform as possible. This ensures two potential problems are kept in check:

1. the average initial defectivity of the channel should be of the same order. This is important to preserve similar carrier mobilities and channel conductances for the initial device comparison, so that any changes induced by the He^+ beam are easier to distinguish from the device performance post-exposure. A low device-to-device variance then lets us talk about the effect of ion irradiation on transport properties as a function of irradiation area more confidently.

2. in the case of sub-micron L, the effect of beam spread due to the previously-discussed *proximity effect* is non-negligible for large irradiation areas, where the beam may impinge on the electrode/MoS_2 interface. By keeping $L >>$ penetration depth, we can vary the area of irradiation safely, knowing that the contact interface will not be damaged by the beam significantly.

The ion beam exposures were always carried out at a beam energy of 30 keV and He gas pressure of 2×10^{-6} mTorr using the *Zeiss Nanofab* microscope. The as-made MoS_2 FETs were placed in the HIM after initial electrical testing and were irradiated with the stage tilt set to 0°, unless otherwise specified. In cases when the total areas of irradiation were quite large, it was sometimes necessary to maintain a high beam current throughout the exposure in order to allow for high-dose unidirectional scans that would cover the designated area in a reasonable amount of time. The beam current was recorded before the delivery of each irradiation pattern, the example distribution of which is shown in the histogram in **Fig. 4.12**, with the average current equal to 37.5 ± 0.4 pA, and the evaluated probe size being ≈ 7 nm.

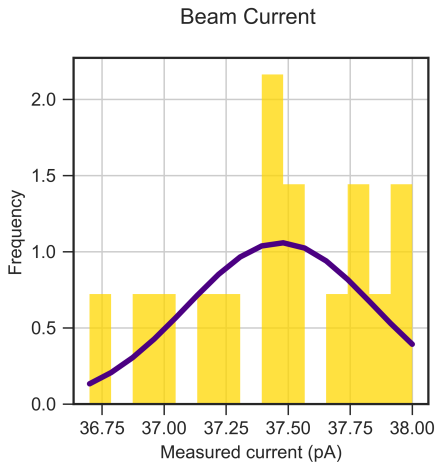

Figure 4.12: **Distribution of measured beam current prior to pattern irradiation.**

We can now define the ion dose (in *ions* cm^{-2}) as:

$$\Phi = \frac{I_b \cdot t}{A} \tag{4.2}$$

We can see that for a given exposure area, A, upping the beam current, I_b, will significantly reduce the time, t, necessary to deliver a given dose, Φ. The dose is being delivered at every dwell site for a given amount of time (*dwell time*) and each dwell site is separated by a pre-defined *step size* (always 1 nm in our case).

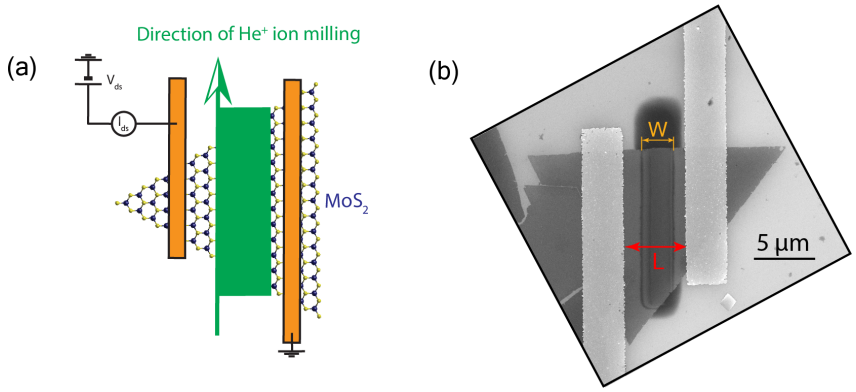

Figure 4.13: **(a)** Sketch of the irradiation geometry. The pattern in green always extends out onto the substrate to ensure full coverage of the MoS_2 channel between the electrodes. V_{ds}; drain-source bias, I_{ds}; drain-source current. **(b)** SEM image of an irradiated device, showing the evaluated W and L parameters needed to calculate the irradiation-to-channel ratio, I_R.

Figure 4.13 shows a sketch of the irradiation geometry and a SEM image of an irradiated device. The marked distances W and L denote the width of the irradiated region and length of the FET channel respectively. We can thus obtain an irradiation-to-channel ratio, $I_R = W/L$.

4.2.2.2 Asymmetric irradiation modelling

For some aspects of this work (**Chapter 10**), the stage of the HIM was tilted during the ion beam irradiation. We can simulate the dose distribution in the Gaussian probe of the He^+ ion beam and how it evolves as we tilt the substrate onto which the dose is delivered. Consider the sketch in **Fig. 4.14(a)**. We define γ as the tilt angle of the stage (and sample) relative to the normal incident beam, α is the semi-angle of the beam convergence and h is the distance from the focal point of the beam. It can be shown analytically that the skeweness of the Gaussian probe as it delivers the ion dose about the central lateral coordinate x is given by:

$$\Phi(x,\gamma,\alpha,h) = \frac{1}{\sqrt{2\pi(h \pm x\sin\gamma)^2\tan^2\alpha}}\exp\left(-\frac{x^2\cos^2\gamma}{2(h \pm x\sin\gamma)^2\tan^2\alpha}\right) \tag{4.3}$$

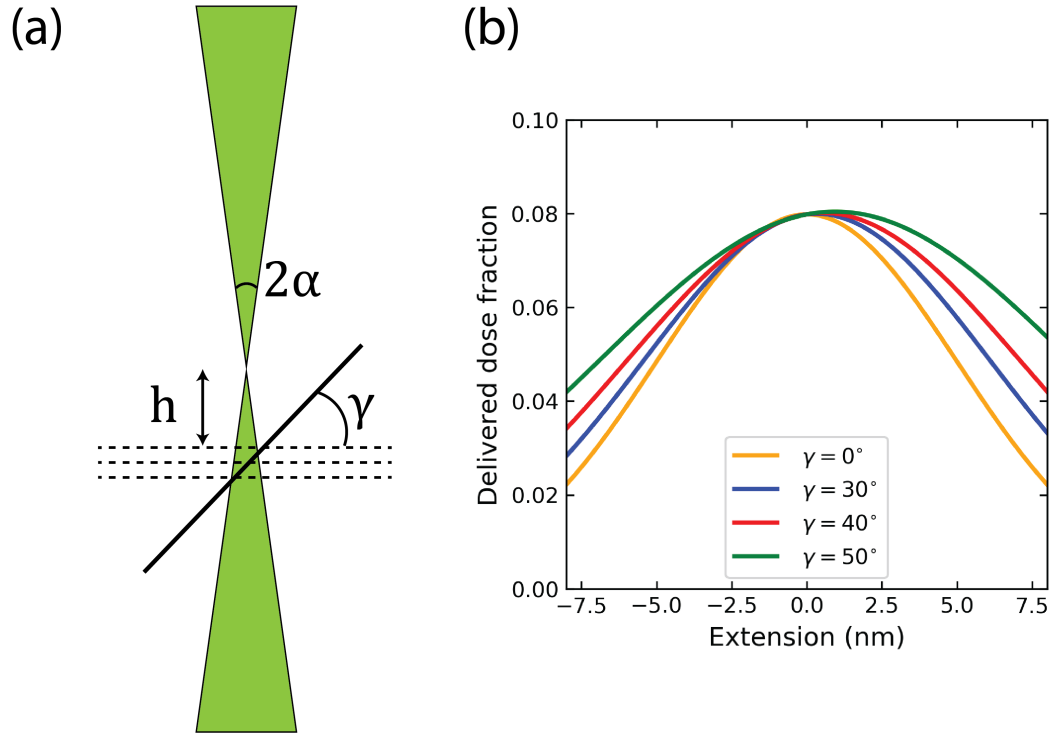

Figure 4.14: **Asymmetric dose delivery. (a)** Sketch of the experimental geometry when the stage is tilted during ion beam irradiation. h is the distance to the focal point, γ is the tilt angle, α is the semi-angle of the beam convergence. **(b)** Plot of the simulated dose delivery (based on **Equation 4.3**) about the lateral coordinate x (labelled as *Extension* on the abscissa) when γ changes, with h and α fixed.

We plot the evolution of this dose distribution in the beam probe as a function of changing sample tilt, γ, in **Fig. 4.14(b)**. The graph is effectively a cross-sectional look of the irradiation site. The lateral spread from the centre of the impact site, x, is labelled as *Extension* on the abscissa. As γ is increased, the delivered dose distribution about the centre of the irradiated pattern is seen to become more and more asymmetric. We note that not only is it skewed spatially, but the magnitude of the delivered dose changes accordingly, across the whole extension of the fissure. The consequences of this effect on the electrical properties of MoS_2 will be explored in the final chapter of the thesis.

4.3 Characterisation methods

4.3.1 Microscopy

4.3.1.1 Atomic force microscopy

AFM is a scanning probe microscopy technique developed in the 1980s which allows us to study the surface topography of samples on the nanoscale. It functions on the

basis of force interaction between a very sharp tip on the end of a cantilever and the sample surface itself. In so-called *tapping mode*, the tip vibrates very close to the specimen surface (**Fig. 4.15(a)**, in our case, at 140 kHz) with an amplitude of tens of nanometres. Depending on the strength of the interaction (F) with the scanned surface, the cantilever is deflected by a given distance (x) - subject to the spring constant (k) of the material from which it is made and its machining. This interaction is captured through Hooke's law: $F = -kx$. The resultant deflection is monitored by a laser reflecting from the cantilever onto a four-quadrant photodetector (**Fig. 4.15(b)**); which converts differences in light intensity to voltage. The resolution of the technique is ultimately governed by the shape of the tip - its radius at the apex will determine the nature of the interaction with surface features. Typically, a good AFM tip with a high aspect ratio will allow for atomic resolution in the z direction, along with force measurements on the nN scale. In the lateral direction, the resolution is limited by the convolution of the tip curvature and the dimension of surface features, which can lead to artificial drag of the tip in the horizontal direction, creating "smears" in the scan where one would expect sharp edges.

Two scanning strategies exist:

- *constant force* - a feedback loop is set up so that a constant force is maintained between the tip and the sample by adjusting the z height of the tip.
- *constant height* - the feedback loop is opened, setting an absolute z value for the tip, allowing for more rapid surface scans (usually only done when surface roughness is known to be very small).

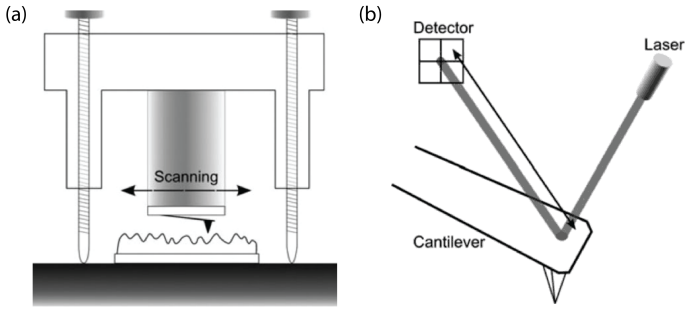

Figure 4.15: **(a)** Sketch of the microscope stage, showing the scanning strategy of the cantilever tip across the sample surface. **(b)** Illustration of the optical detection of the cantilever deflection. Both diagrams adapted from [221].

AFM has many advantages as a nanoscale characterisation technique. It usually does not require intensive sample preparation steps, it can be carried out in air,

is not limited to samples of a certain electrical conductivity and serves to provide accurate information about the sample surface roughness and its topography in the z direction. It does however have a limited height range, so the operator has to be careful not to crash the delicate tip into the surface. Blunting the tip will limit the resolution and will require restarting the experiment with a new tip, while the sample may also be damaged. The field of view is also limited by the scan parameters and oftentimes many scans need to be performed to image the exact region of interest. This also takes time, depending on the chosen resolution, but a standard scan will usually take as long as 20-30 minutes, meaning that the throughput is not as high as in techniques such as SEM.

The height information is obtained in so-called *amplitude mode*, where the amplitude of the tip vibration is tracked during the scan. Another functionality known as *phase mode* opens up some degree of chemical analysis of the surface, as the phase of the tip oscillation is affected by different material compositions that exist on the surface:

$$d = A\sin(2\pi f t + \phi) \tag{4.4}$$

where d is the tip deflection, A the amplitude of oscillation, f the oscillation frequency, t the time and ϕ the phase shift between the drive and the response [222]. ϕ is nominally $\frac{\pi}{2}$ at resonance (or some other constant, depending on the manufacturer). If the tip comes into contact with a material which begins to selectively attract or repel the tip relative to another material on the surface, the resonant frequency of the oscillation will shift, as will the phase. This will show up as contrast in a phase scan, allowing the operator to surmise that a *different* material property governs the tip-sample interaction in that region, e.g. surface adhesion, material stiffness, elasticity, etc.; although one cannot know exactly which it is, making exact chemical interpretations very difficult.

Throughout this thesis, all of the presented AFM results were collected in air on the *Oxford Asylum* system in the Boland lab in CRANN, with the assistance of Darragh Keane. The Si tip resonant frequency was 140 kHz and the AFM was operated in tapping mode.

4.3.1.2 Scanning electron microscopy

SEM is a commonly used technique for characterising samples in all aspects of materials science, from the fundamental studies of material properties and compo-

sition, to electronic device failure and high-resolution imaging. The operational principles of a SEM make use of the nature of the charged particle beam-target interaction to collect information about a given specimen. An electron is emitted from the *electron gun* at the top of the SEM column. This electron source can be either a *thermionic source*, i.e. a filament similar to one you might find in a light bulb (usually tungsten) is heated to high temperatures until it begins to emit electrons (also known as *Schottky emission*); or a *field emission* source, i.e. a material like LaB_6 carved into a very sharp tip, which upon the application of a high bias will begin to emit energetically-promoted electrons from the solid into vacuum through a process known as field emission. The electron source needs to be bright (produce many electrons), physically small to improve resolution by mimicking a point source object, monochromatic (produce electrons of a similar energy) and stable. Any unwanted adsorbates which may deposit on the gun surface will reduce the stability and resolution of the microscope, which means the gun is housed at UHV ($\sim 10^{-9}$ mbar) and rarely exposed to air during the lifetime of the microscope. The SEM chamber itself, where the sample is tested, is kept at a relatively high vacuum of $\sim 10^{-4}$ - 10^{-7} mbar, depending on the system.

Through the application of an accelerating voltage (typically 0.5 - 20 kV), energetic electrons are moved through a set of focusing electromagnetic lenses that shape the electron beam into a probe, which enters the specimen chamber through the *pole piece*. For a look at the SEM instrument geometry see **Fig. 4.16(a)**. Once the sample z height and focus are properly adjusted, the probe can then be scanned across the sample surface by adjusting the current in the scanning coils, which raster the beam back and forth across the field of view. When the primary electron beam arrives at the specimen surface, it collides with the target atoms and knocks out electrons from their atomic orbitals. This causes the emission of low-energy (< 50 eV) SE particles from the surface, which can be collected into a positively-biased scintillator housed in a Faraday cage on the side of the microscope chamber, known as the Everhart-Thornley (ET) detector. The relative intensity of the converted electron-to-photon signal at each scanned pixel then determines the brightness and contrast of the generated grey scale SE micrograph, which can be adjusted manually on the microscope control panel.

An additional SE detector known as the *in-lens* detector, which is located inside the pole piece, can also be employed to obtain different information about the sample surface. The in-lens detector is much more sensitive to low-energy electrons gener-

ated from the sample surface [223] and reveals information that is inaccessible to ET detectors on the side of the SEM chamber, which also globally collect spurious tertiary electron information from delocalised interactions with the chamber walls and microscope components [224]. This becomes crucial when studying really thin material films like MoS_2, and the material composition of their functionalised surface. Thus, the majority of images of MoS_2 taken in the SEM for this work are in-lens detector images owing to the superior contrast. Due to the differing work function contrast of 2D materials with changing layer number [225], as well as work function contrast of oxides on the surface of chalcogenide 2D materials, the in-lens detector can reveal changes to the topography and chemical composition of functionalised MoS_2, if any impurities or contaminants are present on the surface, simply from the recorded SE intensity. The attenuation of SEs emitted from multilayer samples can also ostensibly discriminate the layer number in these van der Waals materials.

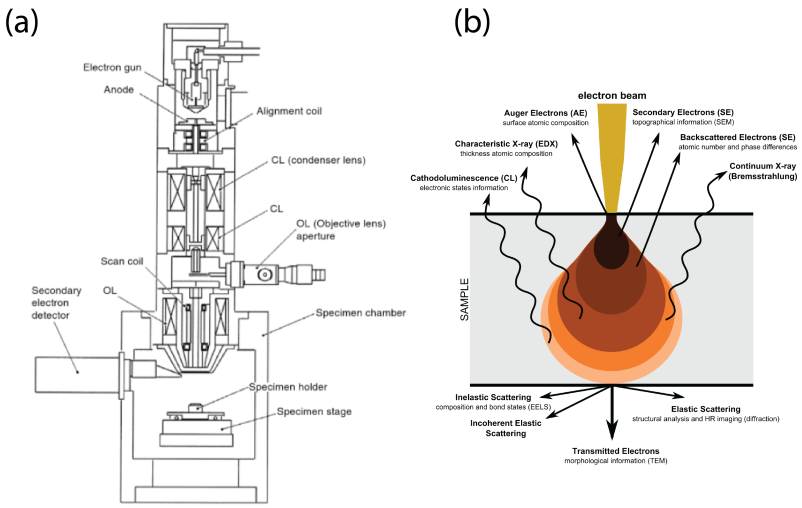

Figure 4.16: **(a)** Diagram of the SEM column, outlining the electron lenses, locations of the sample stage and detector in the chamber [226]. **(b)** Illustration of the physical processes occurring when an electron beam interacts with a sample inside the SEM [227].

Importantly, numerous consequences result from the electron beam-sample interaction. The rich zoo of physical processes that take place during this interaction is visualised in the diagram in **Fig. 4.16(b)**. The tear drop-shaped interaction volume that generates electrons and photons is defined by the previously-mentioned *electron range*, i.e. the depth to which electrons will penetrate the target material - subject to the used beam energy. SEs exit the surface and are collected into a detector to reveal the topological information. The removal of these SEs from the inner energy shells of a target atom will leave behind an electron hole, which gets filled

by an electron from a higher energy shell in that atom. To conserve energy, this difference will then be emitted in the form of an X-ray photon. This photon energy is a characteristic fingerprint of the excited atom and thus its elemental nature can be determined using energy-dispersive X-ray spectroscopy (EDX) - which will be discussed in more detail in the spectroscopy section below. Thus, the SEM can be employed to study both the structural information about the surface of materials, and the chemical composition of their microstructure underneath the surface.

SEM images presented throughout this work were collected using *Zeiss Supra*, *Zeiss EVO* and *Zeiss Ultra* microscopes located in CRANN's Advanced Microscopy Laboratory. The acceleration voltage was varied accordingly, depending on the necessary surface sensitivity/resolution trade-off.

4.3.1.3 Transmission electron microscopy

TEM is the pioneering electron microscopy technique, whose origins trace back to the Weimar Republic in the 1920s. The operating principles are very much similar to that of a SEM, but acceleration voltages in the TEM are extremely high - reaching hundreds of thousands of volts - and the electrons arrive at the surface in a highly-energetic parallel beam. TEM samples are prepared to be extremely thin (typically less than 100 nm), thus allowing many electrons to pass through the sample. The magnified image of the electron-illuminated object is then reconstructed from the signal that has passed through the sample. As the kinetic energy of an electron is increased, its wavelength (due to the de Broglie hypothesis) decreases. This means the resolution limits of photons can be easily surpassed by using electrons, allowing for TEM imaging of individual atoms in a crystalline material. In addition, by manipulating the lenses inside the optical column, the beam can also be focused into a probe and rastered across the sample in a scanning TEM (STEM) mode.

The information contained in a TEM image is a two-dimensional projection of a 3D object, making interpretation of the observed contrast difficult. *Mass-thickness contrast* is one way in which the intensity variation can be interpreted, whereby the recorded intensity is modulated due to non-uniform thickness and/or elemental composition of the sample. *Diffraction contrast* arises in crystalline materials when the electron beam satisfies the Bragg equation and interferes constructively when diffracted through the atomic planes. *Phase contrast*, also denoted as high-resolution TEM (HRTEM), allows for the imaging of atomic columns in a crystal lattice based on the interaction of the incident electron plane wave with the crystal

atoms. Changes to the phase of the electron accrued as it moves through the specimen present themselves as intensity variations in the exit wave and the final image wave formed at the detector. The interpretation of this contrast mechanism is a continuing field of research into the 21st century, with the exact role of microscope aberrations described in the mathematical *contrast transfer function*.

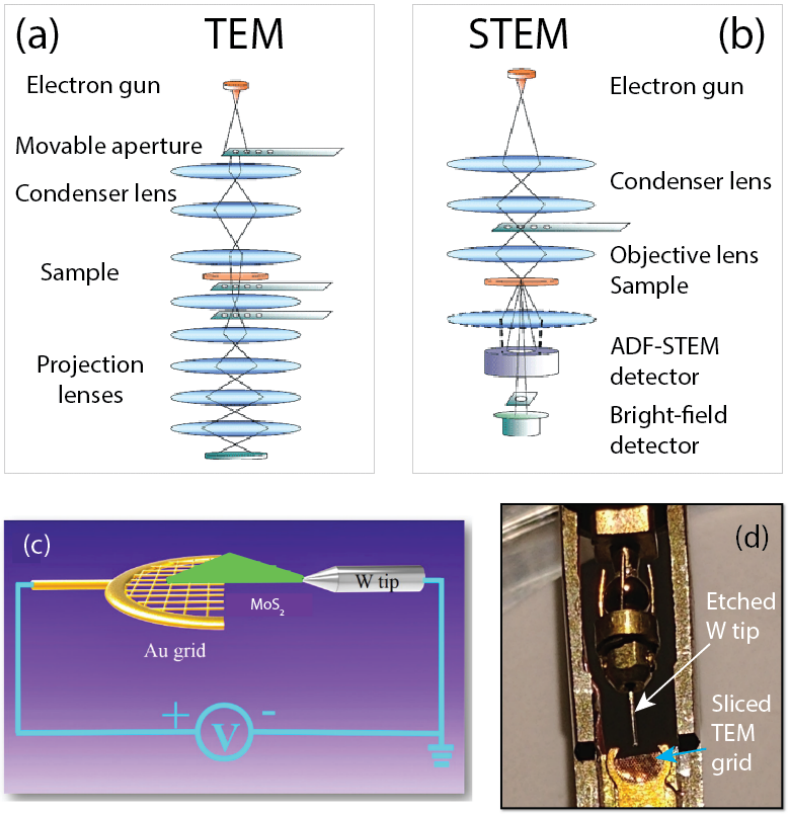

Figure 4.17: **(a,b)** Diagrams of the TEM & STEM columns respectively, showing the path of the electron beam rays during image formation. Adapted from [228]. **(c)** Illustration of the *in-situ* biasing set-up utilising a W tip in the TEM. Image adapted from [229]. **(d)** Photograph of the *in-situ* setup in the Gao lab at Peking University, with the sliced TEM grid containing MoS_2 placed in the holder against the W tip.

In STEM mode, the electron probe focused in the sample plane scans across the surface and the post-interaction information is collected beneath the specimen in an *annular dark field* detector at high or medium angles. The dominant contrast mechanism obtained by these detectors in STEM images is atomic number, or Z contrast. It depends on the scattering probability of incident electrons from atomic nuclei, and thus is highly sensitive to the position of a given element in the periodic table. Interpretation of STEM contrast is more straightforward, with bright areas representing the location of scattering centres (atoms) and the dark

areas representing the lack of material (inter-atomic spacing), thinner regions or lighter atoms. This makes it easy to identify regions of different layer thickness in 2D materials [230], as well as areas containing impurities/functionalised regions. Atomic resolution is readily achievable in ACSTEM systems with a bright electron source and a highly-stable sample stage, while spectroscopies can also be performed [231]. For a comparison of the TEM and STEM optical columns see **Figs. 4.17(a,b)**.

In addition, some TEM systems allow *in-situ* experiments to be performed on the sample while it is being imaged. This has several advantages, as processes happening on the nanoscale can be revealed in real time when the sample is, for example, exposed to a gas or heated. In this work, *in-situ* electrical biasing experiments were performed on monolayer MoS_2 inside the TEM. A tungsten tip was sharpened by etching in an electrochemical solution of NaOH for a few minutes. This tip is then inserted into a special holder against a TEM grid which has been sliced in half to accommodate the tip approaching a specimen overhanging the edge of the grid (see **Figs. 4.17(c,d)**). Once the W tip makes contact with the nanomaterial of interest, the metal grid itself and the tip then serve as electrodes that pass current through the sample which can be imaged at the same time - both in video and static image modes.

(S)TEM results presented in this thesis have mostly been collected on the *FEI Titan 80-300* system in the Advanced Microscopy Lab with the assistance of Drs Danny Fox, Eoin McCarthy & Pierce Maguire at various stages, utilising a 300 keV beam. The *in-situ* biasing experiments in the TEM were performed in the Electron Microscopy Lab at Peking University, with the assistance of Mingqiang Li (Prof. Peng Gao's Group) on the *Philips EM-400* microscope at 120 keV. ACSTEM results and associated spectroscopic data were collected on the *Nion UltraSTEM 200 microscope* in the Advanced Microscopy Lab by Clive Downing.

4.3.2 Spectroscopy

4.3.2.1 Raman spectroscopy

Raman spectroscopy is a non-destructive optical characterisation method used to identify compounds in a solid. It relies on some fundamental aspects of condensed matter physics, such as the crystal symmetry and photon-phonon interactions, and has proven particularly useful during the 2D materials boom of the last 15 years, as on-substrate flakes can be identified easily from their Raman modes. At the same time, changes to the Raman modes (intensity, peak position, splitting & broadening)

are characteristic of the level of defects/dopants present in the sample after particular treatments. This technique is highly automatised, extremely high-throughput and provides a vast amount of rich information about the crystal structure of a studied specimen when interpreted accurately.

A given sample has certain vibration modes, i.e. spatial displacements of atoms, which are symmetry-locked to the crystal space group which a given material represents. These Raman-active displacements have a characteristic energy associated with them, which is a function of the bonding nature in that particular compound. When monochromatic laser light is incident on a crystalline sample, it is absorbed and re-emitted shortly thereafter (the target atom does not enter an excited electronic state like in the case of *fluorescence* or *phosphorescence*). Most of these photons interact elastically with the crystal lattice and do not change their energy upon re-emission - in a process known as *Rayleigh scattering*. However, some photons will scatter inelastically from the target sample; with a notable energy shift from the incident photon. These energy shifts are characteristic of the phonon modes inside the sample, and thus can be used to analyse its crystal structure. The energy shift can be represented, in wavenumbers (cm^{-1}), as:

$$\Delta\nu = \frac{1}{\lambda_0} - \frac{1}{\lambda_1} \tag{4.5}$$

where λ_0 is the incident wavelength and λ_1 is the Raman wavelength. The incoming photon induces a momentary dipole moment in the electronic cloud of the sample, changing the polarisability of the chemical bonds (especially those in non-polar compounds). As the dipole is relaxed, light of a different frequency is emitted and can be collected in a detector as a function of energy using a monochromator. Changes to this frequency can be bi-directional, categorised by either a *Stokes* or *anti-Stokes* process, where the photon energy is decreased or increased respectively. A *Jabłoński diagram* in **Fig. 4.18** illustrates the possible scenarios in the vibrational energy level landscape during the Raman scattering process:

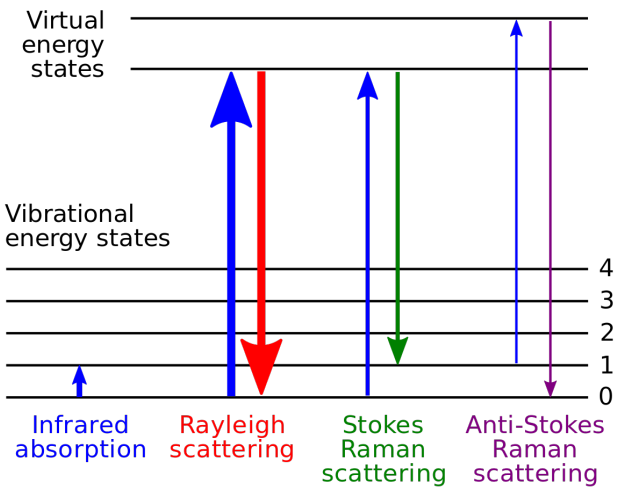

Figure 4.18: Jabłoński diagram showing the radiative transitions between energy states involved in the Raman scattering process [232].

As MoS_2 is the main solid-state system studied in this thesis, it is worthwhile to give a brief background on the Raman characteristics of this molecule and its emergent 2D nanosheets in the crystal limit. The two first-order Raman-active modes in bulk MoS_2 are the E^1_{2g} and A_{1g} modes at $\sim 383\ cm^{-1}$ and $\sim 408\ cm^{-1}$. Respectively, these correspond to the in-plane vibrations of the S atoms relative to the Mo molecular centre moving in the opposite direction; and the out-of-plane vibrations of the S atoms relative to a stationary Mo centre (see cartoon in **Fig. 4.19(a)**). As the van der Waals sheets are thinned to a single layer, the point group of MoS_2 changes from D^6_h to D^3_h; resulting in a shift of the first-order modes closer in energy to one another ($\sim 385\ cm^{-1}$ & $\sim 405\ cm^{-1}$) and a change of notation to E' and A'_1. As such, Raman spectroscopy serves as an excellent tool for the identification of layer number in thin MoS_2 samples, as the spectra are clearly differentiated as a function of layer number (see trends in **Figs. 4.19(b,c)**).

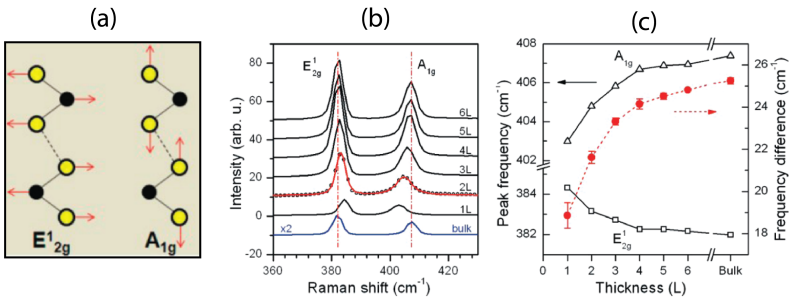

Figure 4.19: **(a)** Cartoon of the atomic displacements in the Raman-active E^1_{2g} and A_{1g} modes. Black is the Mo centre, yellow are the S atoms. **(b)** Raman spectra of MoS_2 samples of different layer number. **(c)** Frequencies of the first-order Raman modes as a function of layer number. All panels from [233].

The raw spectral peaks need to be fitted with appropriate Gaussian or Lorentzian functions, depending on the tested material, in order to extract accurate parameters such as the peak centre, FWHM and intensity. Alterations of the crystal lattice, such as the introduction of dopants, defects or surface impurities will largely affect the intensity of the signal, as well as its energy and width of the peak. The large broadening of peaks in defective MoS_2, for example, is characteristic of the emergence of smaller shoulder peaks which convolute the observed spectra; while the blue-shift of the A'_1 peak is associated with electron acceptor adsorption on the surface [198].

Some Raman systems allow for the collection of spectra at individual pixels of a given optical micrograph. Hence, a Raman *map* of a given sample area can be collected, whose resolution is ultimately limited by the wavelength of the incident laser. For the purposes of this work, Raman spectra and maps were mostly collected on the *WITec Alpha 300R* micropscope in the lab of Prof. Georg S. Duesberg/Dr. Niall McEvoy in the School of Chemistry, with the assistance of Conor Cullen. The excitation wavelength used was 532 nm with a diffraction grating of 1800 lines/mm. The numerical aperture of the microscope was 0.95, the laser spot size was $\approx$ 300 nm when using the 100$\times$ microscope objective lens. The power of the laser was usually kept below 60 μW to ensure there was no unnecessary heating of the samples. The acquisition rate was adjusted accordingly depending on the sample, studied area and time. A typical 60 px^2 map on a 4 μm^2 area may contain 900 spectra and take about half an hour to collect. The spectra/maps were then analysed using `WITec Project 4.0` software by Dr. Pierce Maguire. In some cases, spectra were collected using the *HORIBA Jobin Yvon* system in the Photonics Lab in CRANN with the assistance of Dr. Jing-Jing Wang, using a 488 nm laser

with a 1200 lines/mm grating, 100× microscope objective lens and 10 acquisitions per second. When the presented spectra were collected using this system throughout this thesis, they will be indicated as such. Otherwise, it should be assumed that the results come from the *WITec* system.

4.3.2.2 Photoluminescence spectroscopy

PL spectroscopy is a particularly useful characterisation technique when dealing with semiconductors like MoS_2. When an electron is moved into an excited state in the conduction band of a semiconductor, it leaves behind a hole in the valence band. When the electron-hole pair (otherwise known as an *exciton*) recombines, energy is released in the form of a photon in a process known as *luminescence*. When the initial exciton creation is due to the absorption of an incoming photon whose energy is sufficient to overcome the material band gap, the process is termed *photoluminescence*. In semiconductors, whose band gap is *direct*, i.e. the minimum of the conduction band and the maximum of the valence band occur at the same point in reciprocal space; the exciton recombination is largely *radiative* and the yield of luminescence is high. If the band extrema are offset in k-space, the recombination is additionally mediated by phonons and is termed *non-radiative* - lowering the yield of photons emitted through luminescence.

As it turns out, monolayer MoS_2 is a direct-gap semiconductor and it becomes an indirect-gap semiconductor when it has 2 molecular layers or more. The direct-gap emission is due to the so-called *A exciton*, usually centred at ~ 1.85 eV. In addition, another emission component is present at ~ 2 eV. This energetically-offset and less-intense *B exciton* emission arises due to spin-orbit coupling in the material's band structure [15]. Due the interaction of the electron spin magnetic moment with the magnetic field produced by the orbit of that moving electron, the valence band of MoS_2, which would otherwise be degenerate, attains an additional splitting in energy of ~ 150 meV at the $\mathcal{K}$ ($\mathcal{K}'$) points in k-space [234]. This allows photons of sufficient energy to excite electrons into an excitonic state of slightly higher energy and results in the emission of PL photons of this higher energy. The origins of this physical phenomenon are not entirely understood for MoS_2, but are suspected to arise from the large contribution of Mo d-orbitals to states near the band gap [235], i.e. the importance of anti-bonding orbitals present on the surface of monolayer MoS_2.

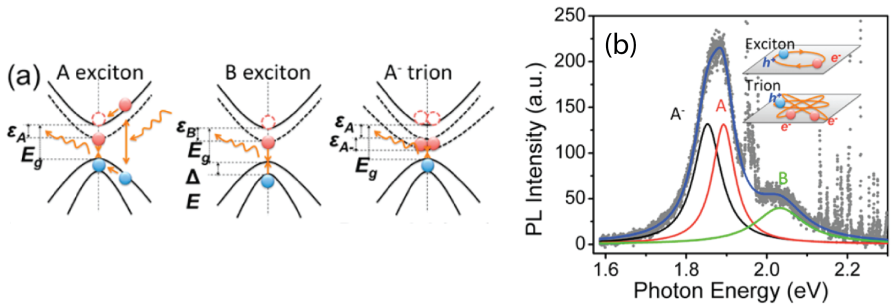

Figure 4.20: **(a)** Illustration of the formation processes of the direct-gap excitons in monolayer MoS_2 during photoluminescence **(b)** Typical spectral components of the PL spectrum of 1L MoS_2. Graphics adapted from [236]. h^+; hole, e^-; electron.

In certain conditions, such as after superacid treatment [237], charged excitons (*trions*) can also emerge in the MoS_2 PL spectrum, while exotic quasi-particles known as *biexcitons* have also been observed at ultra-fast time scales [238]. The intensity of the PL emission, as well as the exact emission energy and its FWHM will signify the quality of the crystal lattice, changes to the band gap energy, termination of the flake edges, and other phenomena upon the functionalization of the MoS_2 basal plane. In addition, the choice of substrate, lattice strain, temperature and environmental conditions will largely affect the PL characteristics of MoS_2 [239, 240]. For an overview of the exciton types in MoS_2 see **Fig. 4.20**.

A large advantage of PL is that the spectra can be collected using the same instrument as in the case of Raman - the photon energies are just much higher and need to be collected using a different diffraction grating (600 grooves/nm in the case of our *WITec* system). The technique is non-destructive, high-throughput and mapping can also be performed. Anecdotally, the PL signal tends to also be more sensitive to any small changes in crystal quality and the presence of defects/impurities than Raman spectroscopy.

4.3.2.3 Energy-dispersive X-ray spectroscopy

As mentioned previously, chemical information can be garnered from photon signals ejected from a sample surface following an interaction with a highly-energetic charged particle like an electron. X-rays are continually isotropically emitted from the surface under electron beam irradiation from various depths within the sample, as the primary beam is halted by scattering on its way into the substrate. This leads to the production of a background spectrum of X-rays known as *Bremsstrahlung*; or "halting radiation". We differentiate between this continuous radiation and the

characteristic X-ray emission coming from the energy-conserving drop of electrons into core-shell levels caused by the electron-sample interaction (**Fig. 4.21(a)**). The Bremsstrahlung spectrum (**Fig. 4.21(b)**) of photon intensity (I) roughly follows Kramers' law:

$$I(\lambda)\,\mathrm{d}\lambda = K\left(\frac{\lambda}{\lambda_{\min}} - 1\right)\frac{1}{\lambda^2}\,\mathrm{d}\lambda \tag{4.6}$$

where λ is the wavelength of the emitted photon, K is a constant and $\lambda_{\min}$ is the cut-off wavelength determined by the energy of the incoming beam.

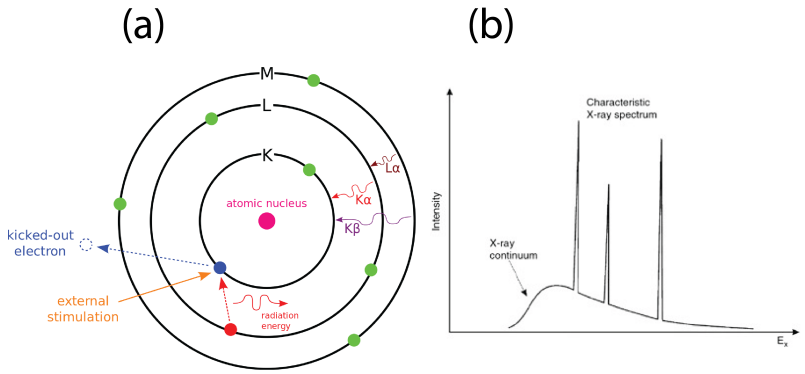

Figure 4.21: **(a)** Diagram of the EDX process upon the impact of an electron on a target atom [241]. M, L, K represent the core energy levels. **(b)** Illustration of the typical Bremsstrahlung background in an EDX spectrum [242]. E_x is X-ray energy.

EDX signal is collected in the SEM chamber using a *silicon drift detector*, whereby the incoming X-rays ionise the detector material, creating electron-hole pairs which are separated by biased electrodes. The produced charge is then detected and converted to photon intensity. As a single spectrum can be collected at a given pixel of a SEM image, a collection of spectra acquired at each pixel forms an EDX *map*. These maps can be filtered for specific peak energies to reveal information about the relative concentration of a given element throughout the imaged sample surface. Importantly, this spectroscopic characterisation can be carried out both in the SEM and TEM. Quantitative EDX is notoriously difficult to perform due to resolution limitations, smearing of information generated from a given interaction volume, coincidental energies for some elemental peaks, intensity doubling due to the arrival of X-rays of the same energy at the same time in the detector, and other factors. Thus, the relative elemental concentrations as evaluated by integrating peak intensities from the spectra will never be accurate, and should be taken with a grain of salt.

EDX spectra presented in this work have already had the Bremsstrahlung background subtracted by the analysis software *Bruker esprit 1.9*. The data were collected using the `Bruker Nano XFlash 5030` detector mounted on the side of the *Zeiss Supra* SEM, utilising an appropriate beam energy to cover the desired emission peak range, and choosing an appropriate scan step size and detector dead time for the given mapping conditions. The sample stage was tilted by 15° towards the detector, using the largest available aperture (120 μm) to increase the counts by providing the largest possible beam current and a favourable collection angle for the detector.

4.3.2.4 Electron energy loss spectroscopy

Electron energy loss spectroscopy (EELS) is a somewhat complementary technique to EDX. In this case, we make use of the primary electrons that have passed through the sample, rather than those emitted from the sample. Thus, this technique is performed in the TEM. The electron beam enters the sample at some kinetic energy defined by the accelerating voltage. Most of them will move through the thin TEM sample without any interaction, but some will lose their energy through various inelastic collisions that may occur as the beam passes through the specimen. Those energy losses tend to be characteristic of elements present in the sample, due to specific amounts of energy needed by the primary beam to induce inner shell ionisations in different elements. In addition, other energy loss mechanisms in the sample, such as plasmon and phonon excitations, will lead to the detection of electrons with a loss in energy in the EELS spectrum. This spectrum is collected with the help of a magnetic prism, whose field will divert electrons of varied kinetic energies by a different amount around a curve (see diagram in **Fig. 4.22(a)**); allowing the detector to resolve the intensity of electrons as a function of energy loss.

A typical EELS spectrum is presented in **Fig. 4.22(b)**. Electrons with no meaningful energy loss contribute to the so-called *zero-loss peak*, centred around 0 on the energy loss axis - usually expressed in units of eV. Near the zero-loss peak (up to 50 eV), some materials will exhibit broad *plasmon peaks* which can arise due to the collective excitations of valence electrons. This region of the spectrum spanning up to 50 eV is called the *low-loss region*. At higher energies (hundreds of eV), we begin to observe *characteristic edges* which can serve to fingerprint elements and their concentrations in the sample, as they correspond to the energies needed to remove electrons from a given shell of an atom. Depending on the monochromaticity of the incoming beam,

these peaks can be resolved to within tens of meV, which permits the study of the behaviour of phonons or other low-energy excitations in the crystal lattice.

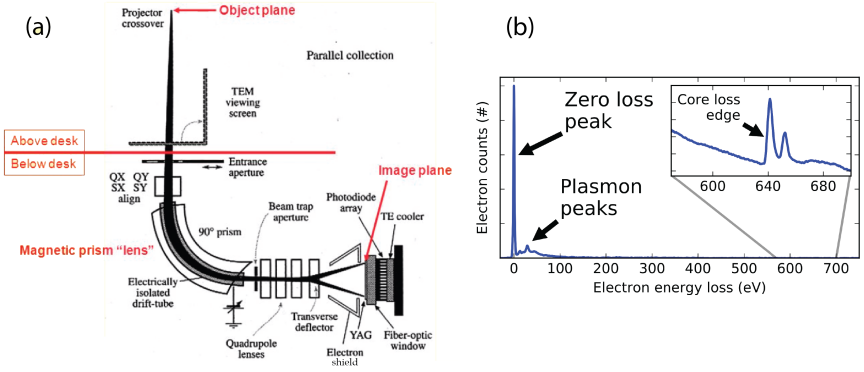

Figure 4.22: **(a)** Diagram of the EELS prism/detector set up underneath a TEM. Adapted from [243]. **(b)** Sketch of an example EELS spectrum, demonstrating the zero-loss peak, the plasmon peak and a magnified look at an inner shell characteristic loss edge. [244].

Just as in the case of EDX, maps of EELS signal can be produced by scanning the beam through each image pixel and collecting an EELS spectrum at each point. However, since these often occur on the nanoscale, sample drift over time must be considered and the mapping times should be adjusted accordingly. The maps can also be filtered for energy to visualise the local distribution of a given element in the sample. In this work, EELS spectra and maps were acquired by Dr. Danny Fox and/or Dr. Eoin McCarthy on the *FEI Titan 80-300* TEM at a beam energy of 300 keV using the *Gatan* detector, and Clive Downing on the *Nion UltraSTEM 200 microscope* in ACSTEM mode.

4.3.2.5 X-ray photoelectron spectroscopy

XPS is one of the premier techniques for the analysis of the chemical state of material surfaces. It works on the basis of the photoelectric effect, whereby photons cause the emission of electrons from the surface of a material. If the energy of an incident photon is above a certain threshold determined by its frequency, i.e. $E = h\nu$, and that energy is absorbed by an electron in the material such that it can overcome the work function of the material; the electron will be ejected into vacuum. In XPS, the surface of a material is illuminated with photons in the X-ray frequency range (usually monochromatic Al K_α photons with $E = 14876.7$ eV) in a UHV environment ($< 10^{-9}$ mbar) to improve the collection efficiency of emitted photoelectrons. The ejected electrons are guided through a hemispherical analyser

Fig. 4.23(a), whose magnetic field will discriminate between electrons of different kinetic energies as they move around a bend.

The technique probes the *binding energies* of electrons in different atomic shells in the target atom. During ionisation by an X-ray photon with energy $h\nu$ (where ν is the frequency) if an electron is emitted from the surface with a kinetic energy E_k, leaving the atom with initial state energy E_i as an ion with a final energy state E_f, then the following relations hold:

$$\begin{aligned} h\nu + E_i &= E_k + E_f \\ h\nu - E_k &= E_f - E_i = E_b \end{aligned} \tag{4.7}$$

where E_b is the binding energy. Naturally, this means that only elastically scattered electrons can be used for this analysis, i.e. electrons emerging from deep inside the sample will lose their kinetic energy upon interacting with other sample atoms before they escape to the surface and their recorded energies, and by extension binding energies, will be lower than the true values. Thus, XPS is particularly surface-sensitive, only accurately probing the electron energies from the top few nanometres of a material surface.

Importantly, the chemical environment of an atom inside the sample changes the binding energy of electrons to that atom, i.e. an atom in a different oxidation state will emit electrons with a different kinetic energy from its shell. This is a so-called *chemical shift*, which depends on a few factors and can be described as:

$$\Delta E_b \cong \underbrace{\Delta V_a}_{\text{intra-atomic effects}} + \underbrace{\Delta V_{ea}}_{\text{inter-atomic effects}} - \underbrace{\Delta R_{ea}}_{\text{final state effects}} \tag{4.8}$$

The first two terms in the above expression can be categorised in the class of *initial state effects*, arising from several physical phenomena:

- changes to core electron energies due to *charge transfer* in the valence band and changes to valence radius upon ionisation. This is sensitive to factors such as the electronegativity of a given element and its electron density.
- *spin-orbit coupling* - previously mentioned in the PL discussion - this leads to the presence of two peaks in an XPS spectrum arising from a single chemical state; one for each spin state coupling to the orbital angular momentum of

the electron. It only occurs in atomic orbitals which are non-symmetric, e.g. *d*-orbitals.

- the *response of the surrounding atoms* to the photoelectron emission, i.e. local electrostatics may offset emission energies.

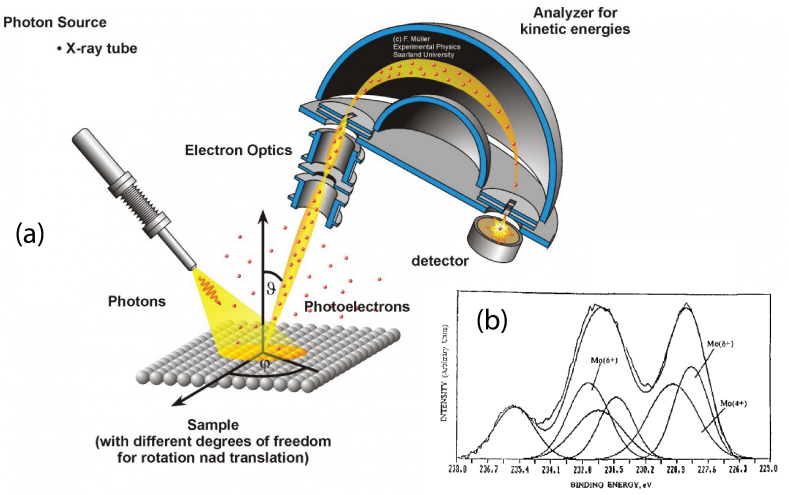

Figure 4.23: **(a)** Diagram of the XPS experimental set-up, adapted from [245]. **(b)** Typical core level spectra of the Mo 3d energy region for a set of molybdenum oxides [246].

Several *final state* effects also exist, such as *Auger* processes, *shake-up* and *shake-off* peaks, plasmon losses and *core-hole* screening. All of these contribute to the shape of the raw XPS spectrum along with a background that is continuously accrued as inelastically scattered electrons are being emitted from the surface with an energy distribution that is skewed towards lower binding energies, i.e. a large amount of kinetic energy has been lost. In fitting routines, one usually takes account of this and uses the *Shirley* or *Tougaard* background to level the spectrum and allow for accurate fitting and integration of peaks.

Fitting procedures for XPS are relatively involved, as intensities depend on a series of factors such as the instrumental precision, cross-section for a given photoemission process and the *inelastic mean free path (IMFP)* - or the distance that a photoelectron can travel inside a given material before it starts losing kinetic energy. The fits in this work were performed with Voigt functions (Lorentzian with a Gaussian component due to instrumental broadening). The 284.8 eV C 1s line coming from adventitious carbon on the surface was used as a reference to correct spectral shifts between

scans. In the case of peak doublets, the integrated area ratio of the spin-orbit-split components was fixed relative to their quantum numbers from the literature, e.g. the area of the Mo $3d_{3/2}$ peak is taken to be 2/3 of that of the Mo $3d_{5/2}$ peak. See example Mo spin-orbit split doublets in **Fig. 4.23(b)**.

XPS results presented in this thesis come from the *Omicron EA 125* system in CRANN and were collected and analysed with the assistance of Prof. Cormac McGuinness. The hemispherical analyser was set to a pass energy of 19 eV for core-level scans, giving a combined instrumental and source resolution of 0.5 eV when using the Al K_α X-ray source. The vacuum level was in the $\sim 10^{-10}$ mbar range. The software used to analyse the data was `CasaXPS`, utilising Shirley background subtraction in the fitting routine.

4.3.3 Electrical measurements

4.3.3.1 Two-terminal devices

Device fabrication steps have been largely described in the methodology sections dealing with EBL and optical lithography. As we are ultimately concerned with device applications, effectively all samples tested throughout this thesis are two-terminal devices. Four-terminal or *van der Pauw* configurations are often employed in materials science to obtain more accurate values for parameters such as R_c and carrier mobility on samples which are continuous films with a well-defined perimeter [247]. In addition, the *transfer length method* can be utilised to ascertain accurate values of contact resistance on MoS_2 by depositing four electrodes in a line, each spaced out from the next by twice the previous distance [248]. Thus, we have ultimately sacrificed some accuracy in obtaining the absolute values of certain parameters throughout this study; in lieu of greater throughput and functional device testing. For example, some of the μ_{fe} values we get may overestimate the carrier mobility significantly [33, 68], but in the low-bias regime on a well-behaving ohmic device, this discrepancy ought not to be too egregious.

As discussed in the theory section, Fermi level pinning locks the Schottky barrier height between the chosen metal and MoS_2, leading to unfavourable rectifying diode behaviour if implemented into devices. We have found that using Cr or Ti as an adhesion layer for Au seems to produce well-behaved ohmic contacts to our MoS_2. Thus, unless stated otherwise for when Cr was used; most of the results come from Ti/Au contacts. It is well-known that true edge contacts to layered TMDs show numerous benefits over top contacts due to in-plane carrier injection into the

channel [249], but due to the difficulty of fabrication we persist with top contacts throughout this thesis. Also, unless stated, all of our measurements were performed at high vacuum inside the chamber of a customised scanning electron microscope (*Zeiss EVO*), as presented below in **Fig. 4.24(a)**:

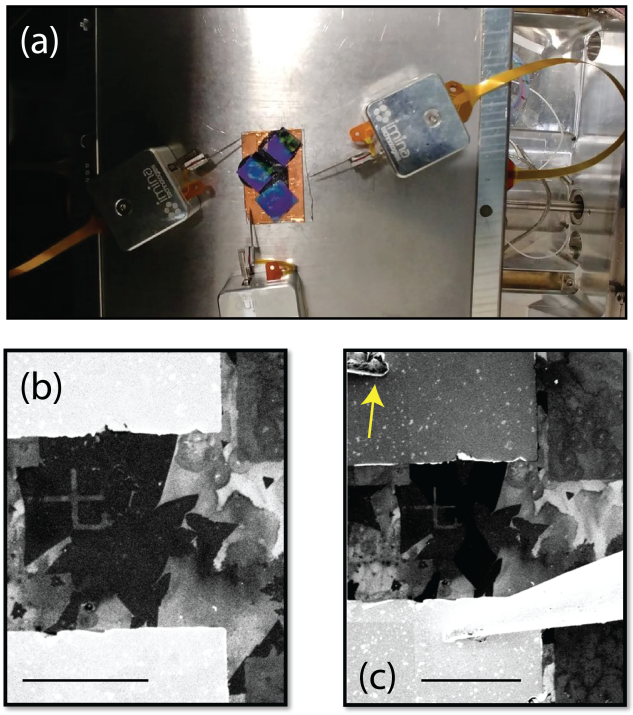

Figure 4.24: **Electrical characterisation in the SEM. (a)** View of the stage and *Imina miBot* micromanipulators installed in the *Zeiss EVO* SEM chamber. Comparison of the SE contrast on a contacted MoS_2 sample when **(b)** the probes are not touching the Au electrodes and when **(c)** the probes are in contact with the metal pads. The yellow arrow notes the point of contact of the top probe, with a large change in SE contrast observed. Scale bar in **(b,c)** is 100 μm.

Running the electrical measurements inside the SEM has an additional practical advantage besides the low pressure. Due to the contrast difference between grounded and charged elements of a SEM image, when the micromanipulator probe comes in contact with the conducting electrode, the SE contrast of the metal pad changes drastically (**Figs. 4.24(b,c)**). This makes it really obvious to the operator when the W needle is fully touching the pads, thus preventing unnecessary pushing of the probe into the electrode which may result in scratching the 40 nm-thin film off.

4.3.3.2 Low-temperature *in-situ* testing in the SEM

The *Zeiss EVO* also has the capacity for installing a cryogenic stage environment from *Kammrath-Weiss* to conduct imaging and electrical measurements *in-situ* at

temperatures down to 77 K. A custom-made flange allows for the inflow and outflow of liquid nitrogen sourced from a 250 L liquid N_2 dewar. A small region of the cryo-stage is constantly cooled by the cold nitrogen flowing around the installed module, drawing heat away from underneath the sample, which is resting on a thermally-conductive but electrically insulating ceramic plate. This allows for gating with a third probe on conductive carbon tape placed between the chip and the ceramic plate.

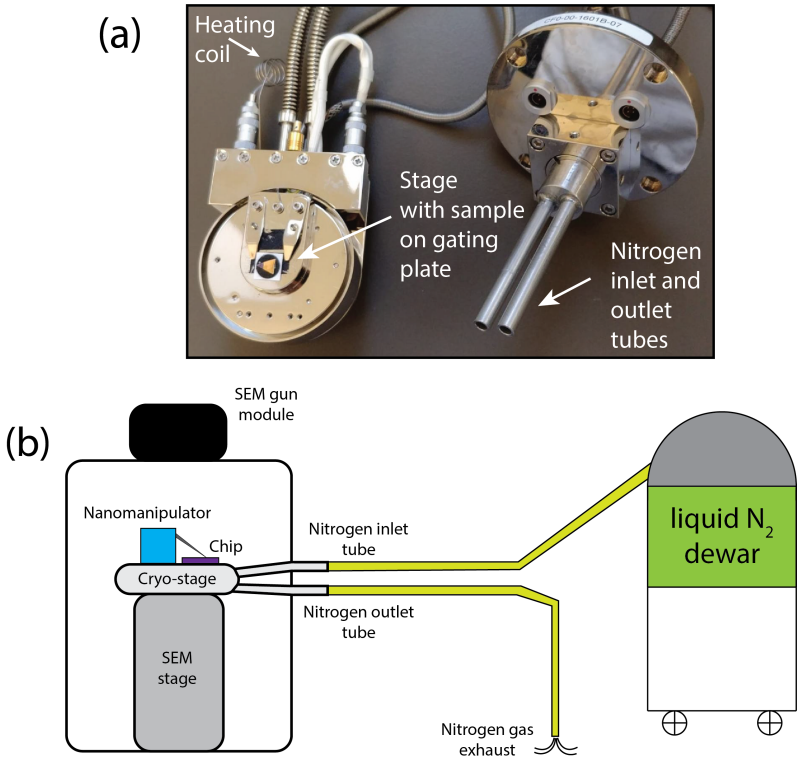

Figure 4.25: **SEM cryo-stage. (a)** Photograph of the *Kammrath & Weiss* stage with the sample on it, before mounting in the *Zeiss EVO* chamber. The resistive heating element, the inlet and outlet exhausts are labelled. **(b)** Diagram of the experimental set-up.

The liquid nitrogen is converted to gas as it makes its way through ≈ 10 m of special plastic tubing and through the module in the SEM chamber. The exhaust tube is placed inside a fume hood to ensure the exhaust nitrogen gas does not fill the lab. The temperature of the stage is controlled by an 8 ampere proportional–integral–derivative controller, which offsets the cold temperature by resistively heating up a wire threaded through the stage. The system is quick to equilibrate, with ± 1 K temperature variations stabilising within 5 minutes, although only a small portion of the stage actually reaches optimal temperatures - thus only one chip can be tested at a time. In addition, the cooling of the SEM contracts

the metal components, and will move the probes if they are lightly touching the pads on the chip; hence the sample needs to be re-contacted every time between temperature steps. As it is more efficient to cool down to the minimum temperature first and raise the temperatures from there, these experiments were done such that room temperature was the final measurement. The stage also has the ability to heat the sample up to 300°C, but this functionality was not utilised for any investigations. The stage layout and a diagram of the SEM during experimentation are presented in **Fig. 4.25**.

4.3.3.3 Cryogenic charge transport testing

Cryogenic charge transport studies were carried out in the lab of Prof. Zhi-Min Liao at Peking University, China with the assistance of Prof. Yangbo Zhou (Nanchang University) and Hua-Ding Song. A top-loading *Oxford Instruments* bath cryostat was used to conduct the experiments. The instrument is effectively a dewar comprising an outer sheath filled with liquid nitrogen and an inner sheath filled with liquid helium. The sample stick is inserted into the evacuated chamber sitting in the middle of the dewar, which is being cooled by contact with the surrounding liquid helium bath. The He bath is separated from the room by another layer of the dewar filled with liquid nitrogen, ensuring that not much He is evaporated out throughout the experiments (it needs to be refilled every 3-4 days). The sample effectively sits about 1 m underground in the bore of a superconducting magnet, allowing for electrical measurements with applied magnetic fields of up to ± 4 T. The chip is wire-bonded with Al wires under an optical microscope to pins of choice on the testing array; one of which is contacted to Ag paint sitting underneath the chip, which is always used as the gate terminal. The array is then inserted into a rotatable module at the end of the stick, contacted through the stick wiring to the electronics stack interfacing with the source measure unit (SMU). Note that all 16 terminals are always switched on during the measurements, i.e. unused terminals are floated to ensure no static charge is grounded inadvertently, which may damage the devices under testing. Thus, every time the electronics box is touched, the operator wears an anti-static wrist band. A device called a *1-K pot* is installed into the cryostat to allow for cooling to temperatures below the 4 K of the liquid He. The vessel contains a small amount of liquid He sourced from the outer sheath. As the chamber is being evacuated by the pumps, the vapour pressure on the surface of the liquid He drops, allowing some He molecules to evaporate off. They carry away kinetic energy, thus cooling the remaining liquid through *evaporative cooling*. Hence, the cryostat we

used for low T electrical measurements could reach temperatures as low as 1.2 K. The experimental set-up is summarised in **Fig. 4.26** below.

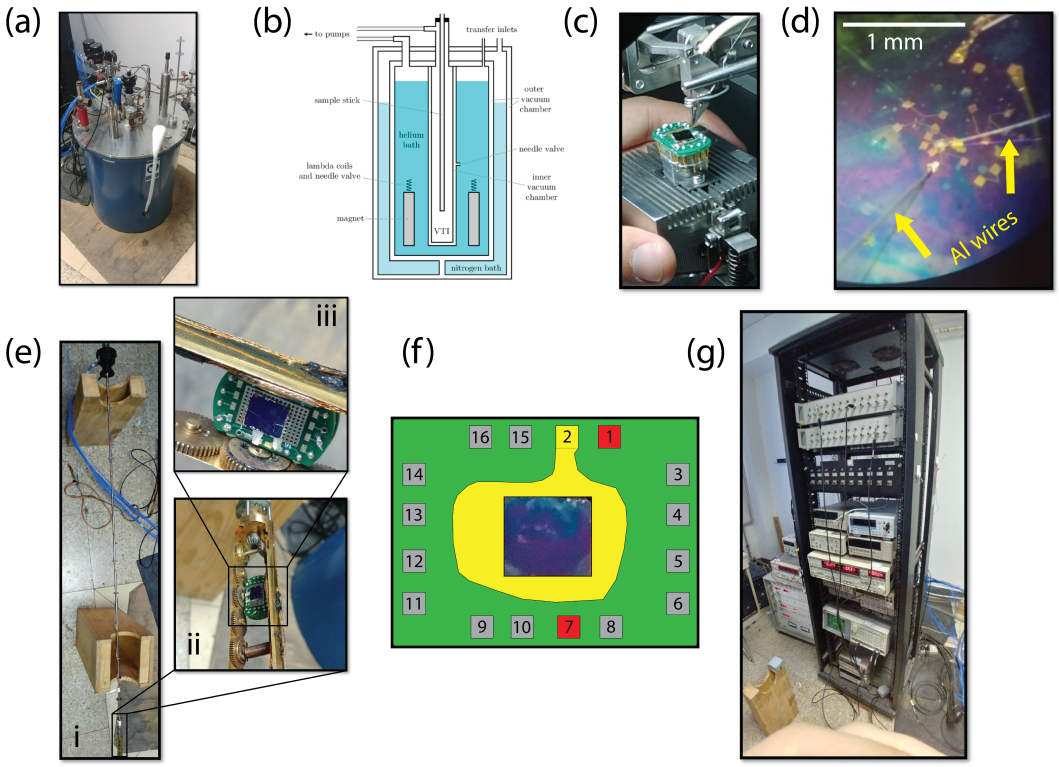

Figure 4.26: **(a)** *Oxford Instruments* cryostat in the Liao lab. **(b)** Diagram of the typical layout of a bath cryostat of this type [250]. **(c)** The chip being wire-bonded to the testing array. **(d)** Optical micrograph of the aluminium wires being bonded to Au contacts on the MoS_2 chip. **(e)** *(i)* Sample stick before insertion into the cryostat, *(ii)* the rotatable module at the end of the sample stick for orienting the sample relative to an applied magnetic field inside the vacuum chamber, *(iii)* closer look at the 16-pin testing array to which the chip is wire-bonded. **(f)** Sketch of the layout of the array with the chip on it. The yellow area represents silver paint used to back-gate the chip from terminal 2. Terminals 1 and 7 are broken; all others can be used to connect to pads on the chip. **(g)** Electronics stack used to apply voltage to the 16 terminals. Coaxial cables with BNC connectors out the front panel are used to connect the terminals to an *Agilent B2912A* dual-channel SMU, interfaced with `Keithley Quick IV` software.

Chapter 5

Oxide-mediated recovery of field-effect mobility in plasma-treated MoS_2

In this chapter, we will demonstrate the tuning of the electrical resistivity of MoS_2 flakes of varying layer thickness (1L-10L) by treatment with O_2:Ar (1:3) plasma. The field-effect mobility, μ_{fe}, of the MoS_2 channel is seen to deteriorate initially but recovers to above-original levels after 6 s of exposure to the plasma. The associated electrical conductivity of the device is noted to increase by an order of magnitude at this stage. Upon further treatment, the conductivity and mobility drop again and no subsequent recovery is seen. In the limited literature regarding this phenomenon, the reason for the apparent recovery remains under debate [251, 181, 252]. Although other means of doping MoS_2 have recently facilitated mobility improvement [70, 253], a molybdenum oxide–mediated n-type doping scheme has not yet been demonstrated. Here, we propose a mechanism of impurity-mediated electrical tuning facilitated by a surface-bound 2D phase of MoO_x, with advanced spectroscopic and microscopic studies to support the electrical characterisation. We infer the presence of this sub-stoichiometric 2D molybdenum trioxide phase, which serves to screen charges associated with plasma-created sulfur vacancies; enhancing the carrier mobility in the underlying MoS_2 layers after 6 s of plasma treatment, which increases the channel conductivity. Recent theoretical work has predicted the 2D phase of MoO_3 to be a material with a distinctly high acoustic phonon-limited carrier mobility ($> 3000\ cm^2\ V^{-1}\ s^{-1}$) [254], whereas experimental 2D FETs made of sub-stoichiometric exfoliated MoO_3 have reported mobilities far exceeding those of MoS_2 ($> 1100\ cm^2\ V^{-1}\ s^{-1}$) [255, 256]. Through complementary mathematical modelling, which confirms conductivity enhancement, we infer the role of a transient 2D sub-stoichiometric phase of molybdenum trioxide (2D-MoO_x) in modulating the electronic behaviour of the material. Deduction of the beneficial role of MoO_x may serve to open the field to new approaches with regard to the tunability of 2D semiconductors by their low-dimensional oxides in nano-modified heterostructures.

5.1 Recovery of μ_{fe} in plasma-treated MoS_2

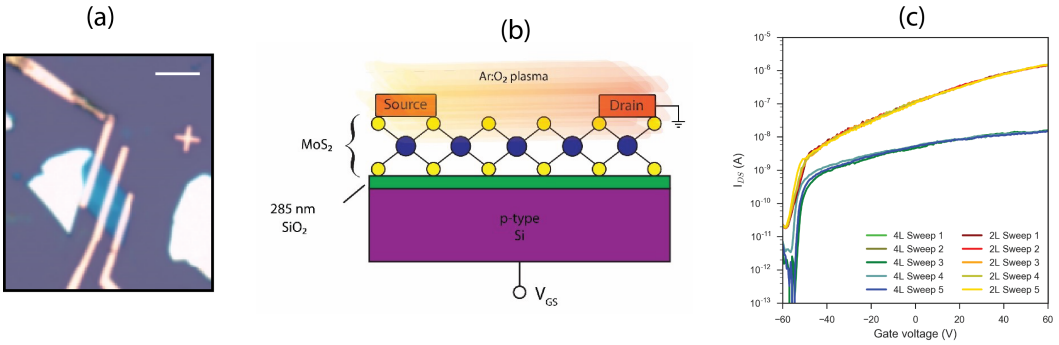

Figure 5.1: **Outline of device geometry and stability**. **(a)** Optical micrograph of an example multilayer exfoliated device. Scale bar is 10 μm. **(b)** Sketch of the experimental geometry. **(c)** Five consecutive gate sweeps on a 4L and 2L device showing the stability of V_{th} for pristine samples before plasma treatment. No hysteresis was observed in the transfer curves at the used sweep rate of 2 V s^{-1}. I_{ds}; drain-source current, V_{GS}; gate-source bias, V_{ds} = 1 V during gate sweeps.

Figure 5.1 outlines the experimental geometry of example devices and demonstrates the stability of the threshold voltage of pristine MoS_2 samples of different layer thickness to consecutive gate sweeps, i.e. any observed hysteresis in the transfer characteristics subsequently shown in this chapter originate from the surface doping with plasma, and not from the manner in which the curves are experimentally sampled.

For the initial plasma exposures, the level of I_{ds} for a four-layer (4L) device varies slightly up until 6 s, when a significant rise in output current is noted, indicating an increase in the conductivity of the channel (**Fig. 5.2(a)**). Subsequent exposures cause a continuing drop in the current level until the noise floor of the instrument (10^{-11} A) is reached after 12 s of plasma treatment. The gate characteristics (**Fig. 5.2(b)**) of the n-type MoS_2 change significantly after 6 s. The level of output current at negative gate bias values increases by several orders of magnitude at 6 s, implying a drastic shift in V_{th} to negative gate biases. Correlated with this is the change in the sensitivity of the output current to the applied gate-source bias, with a much more gradual increase in output current throughout the sweep.

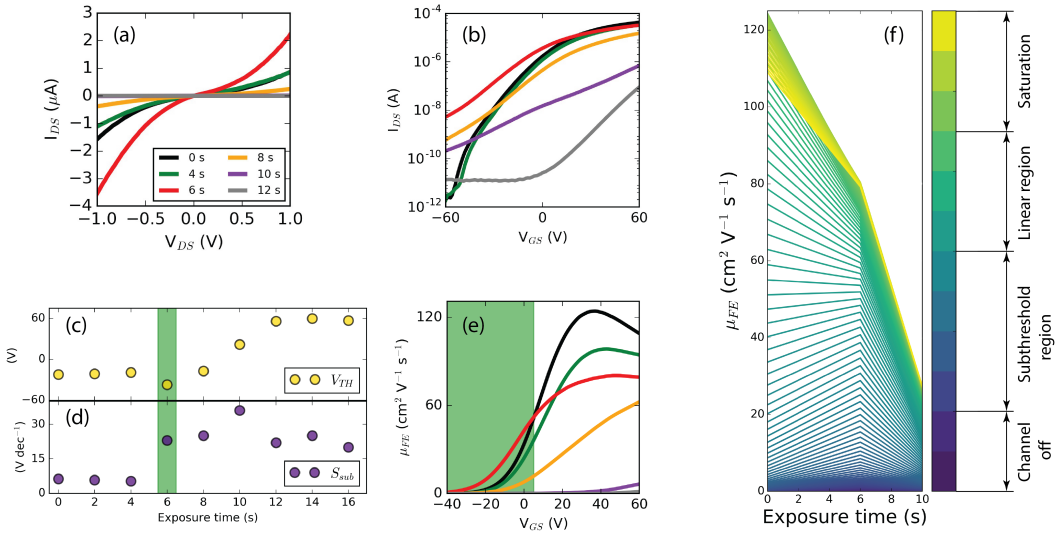

Figure 5.2: **Electrical characterisation of the 4L device**. Note that **(a)**, **(b)**, and **(e)** share the same colour legend and that all measurements were performed at room temperature. **(a)** *I-V* curve evolution over exposure time. All curves are measured at zero gate bias. We note the increased current density observed after 6 s (red). **(b)** Gate sweeps of the same device over exposure time. The curves after 6, 8, and 10 s show a largely linear response in the semi-log plot at low gate biases and do not reach threshold over standard sweep range. Subsequent treatment until 12 s drastically shifts V_{th} to positive gate biases and lowers the current by several orders of magnitude. **(c)** V_{th} for the same device shows a sudden drop at 6 s followed by a steady increase to extremely positive gate biases over treatment time. **(d)** Subthreshold swing variation with exposure time shows a diminished response to the gate field starting at 6 s. The area marked in green in **(c)** and **(d)** indicates the electrical recovery region. **(e)** Extraction of μ_{fe} for the same 4L device across the whole gate bias range (graph begins from -40 V for clarity). The peak mobility reached in the curves is seen to degrade over time. The green region marks the area of the gate sweep where the 6 s exposure attains the highest relative mobility values (red curve). **(f)** Mobility change over plasma treatment time extracted at gate biases between - 60 and 60 V. The colour legend explicitly maps the curves onto different regions of the gate sweep. The increase at 6 s is visualised in the form of rising recovery peaks in the body of the plot, which correspond to 6 s mobilities evaluated in the green area marked in **(e)**. Gate curves taken at V_{ds} = 1 V.

Figures 5.2(c,d) track the evolution of V_{th} and S_{sub} over plasma exposure time. V_{th} is seen to shift from ≈ - 21 V for the untreated device to ≈ - 37 V at 6 s of exposure, and subsequently to large positive gate biases after 10 s. The shift toward negative V_{th} at 6 s implies increased depletion mode functionality for n-type devices, whereas the upshift of V_{th} after further exposure denotes an increase of p-type doping. S_{sub}, in turn, initially shows little change until it increases five-fold at 6 s and up to eight-fold at 10 s relative to the values before treatment. Upon further exposure, it drops again to ≈ 25 V per decade as V_{th} is shifted to large positive gate biases. At 6 s, the sample

shows a marked increase in S_{sub}, indicating that it is less sensitive to variations in the gate field around the region where the FET conductive channel is formed. This is expected to occur if the now-doped few top-most layers of the device have an increased charge trap density [253], originating from the plasma treatment.

μ_{fe} of the device is plotted as a function of gate bias in **Fig. 5.2(e)**. The peak value of the mobility is seen to drop with exposure time, and the gate bias necessary to reach saturation shifts toward larger voltages. For gate voltages in the region from - 40 to 5 V (highlighted green area in the plot), the mobility at 6 s can now be tuned to much higher values than for the untreated device, with the corresponding conductance of the device increasing by more than one order of magnitude in this region. Subsequent treatments at 8 and 10 s decrease μ_{fe} markedly, and no recovery is seen beyond this point. In addition, the change in μ_{fe} over exposure time at each applied gate bias between - 60 and 60 V is charted in **Fig. 5.2(f)** in 1 V steps. The extracted curves are colour-mapped to the palette seen on the right, scaling from extremely low (- 60 V) to extremely high (60 V) gate biases. Inside the decay envelope of the peak mobility evident from the edge contour of this graph, we observe a series of recovery peaks around the region corresponding to a treatment time of 6 s. This recovery is pronounced in the linear regime near V_{th} (that is, where μ_{fe} rises above initial values extracted for the untreated device). This corresponds directly to the green region in **Fig. 5.2(e)**, where the red curve (6 s) attains higher values than the other curves, i.e. across gate biases between - 60 V and 5 V. The subsequent drop in μ_{fe} and the device conductance is a direct consequence of material etching and the introduction of scattering centres that happens after 10 s.

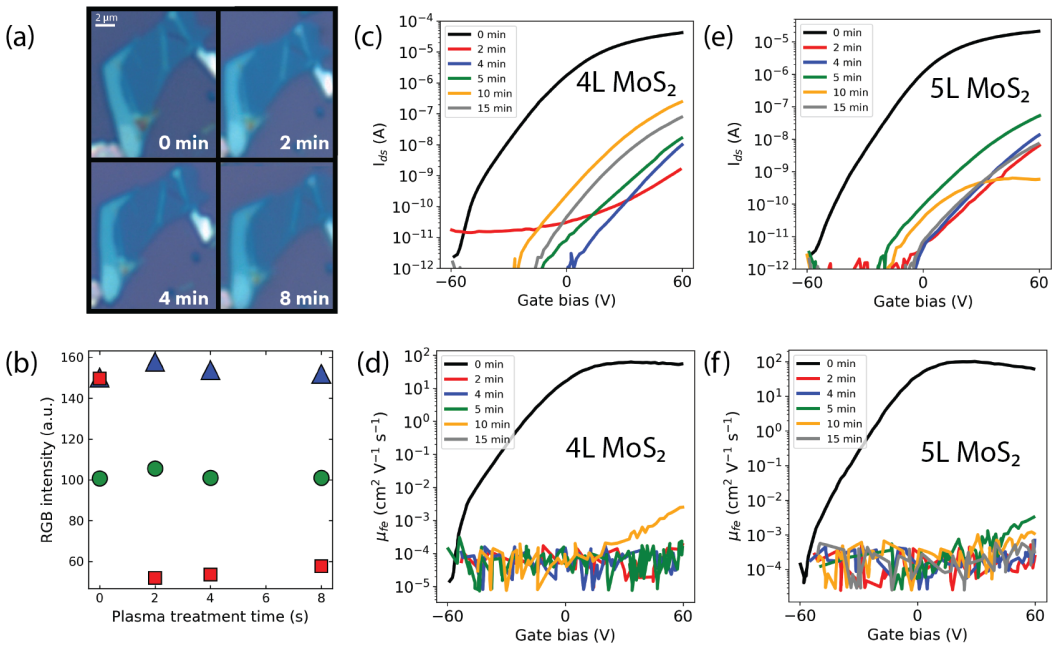

Figure 5.3: **Effects of pure argon plasma**. **(a)** Optical micrographs of a few-layer flake exposed to pure Ar plasma for several minutes. As seen in the chart in **(b)**, the contrast values, other than the red channel, do not change significantly even after several minutes of exposure. **(c)** Evolution of the transfer characteristics of a 4L MoS_2 sample treated with pure Ar plasma. The corresponding μ_{fe} evolution is shown in **(d)**. Analogous gate and mobility plots for a 5L sample are shown in **(e)** and **(f)** respectively. All data taken at V_{ds} = 1 V.

To highlight the role of oxides on the electrical recovery of the samples, a comparative study was carried out using the same plasma cleaner and experimental parameters, but exchanging the oxygen:argon gas mixture for pure argon gas, so that the plasma contained no oxygen radicals available to chemically react with the MoS_2. Initial etching experiments were performed to gauge the time window necessary for measurements (**Fig. 5.3(a)**). The device was seen to be much less susceptible to changes in the RGB contrast on the SiO_2 substrate (**Figs. 5.3(b)**); confirming the big influence of MoO_3 on the sample's refractive index, as we will discuss shortly. When 4L and 5L devices were exposed to pure Ar plasma, no recovery of electrical performance was observed, as seen in **Figs. 5.3(c-f)**. Qualitatively different behaviour is observed than in the case of oxygen-containing plasma, with a heavy shift of V_{th} to negative gate biases never noted. In fact, V_{th} is shifted largely to positive biases in the 4L sample, accompanied by a large drop in the conductance and I_{ds} for the device. Although a flattening of the gate curve is observed at 2 minutes of exposure, the tunability of the mobility is not present in the device, with similarly

poor levels of conductivity observed - but unchanging - even after several minutes of exposure. The 5L device shows nearly identical behaviour, with the defect-induced mobility drop noted with increasing Ar plasma time. When compared with the oxide-modulated devices, the effect of oxygen presence on the recovery of electrical properties in MoS_2 is clear.

The notable increase in current density seen in **Fig. 5.2(a)**; the close-to-linear response to the variation in gate bias at 6, 8, and 10 s (red, orange, and purple curves in **Fig. 5.2(b)**, respectively); and the increase in S_{sub} all hint at the presence of a highly conductive phase in the material comprising the FET channel at 6 s of exposure, which is responsible for the recovery. In the following sections, we go on to infer that this phase is a 2D form of MoO_x produced by a chemical reaction with the plasma. As the chemical modification is confined to the sample surface, we proceed to investigate the structural and chemical change to the topmost layer of the MoS_2 in the following sections.

5.2 MoS_2 surface modification by oxygen insertion

We can use AFM to track the thickness variation and surface roughness of the plasma-treated flake. Phase maps of the same region on a 4L flake are shown in **Figs. 5.4(a-c)**, with notable change in contrast indicating material difference over time. **Figure 5.4(d)** charts the change in the flake edge heights evaluated from line profiles across the edges of the 4L and 5L regions. The initial edge height on the 4L portion increases by $\approx 30\%$ from 0 to 6 s, while that on the 5L area increases by $\approx 21\%$. This is followed by a subsequent drop in height for longer exposure times. This initial oxygen insertion agrees well with the expected height change if the top layer of MoS_2 were to be replaced by a layer of α-MoO_3 or MoO_x with edge-sharing octahedra (29% for 4L and 23% for 5L). The surface roughness in **Fig. 5.4(e)** shows a small peak at 6 s owing to the formation of oxide patches, but the average value does not vary more than the thickness of one layer of MoS_2 or MoO_3 in the first 8 s of exposure.

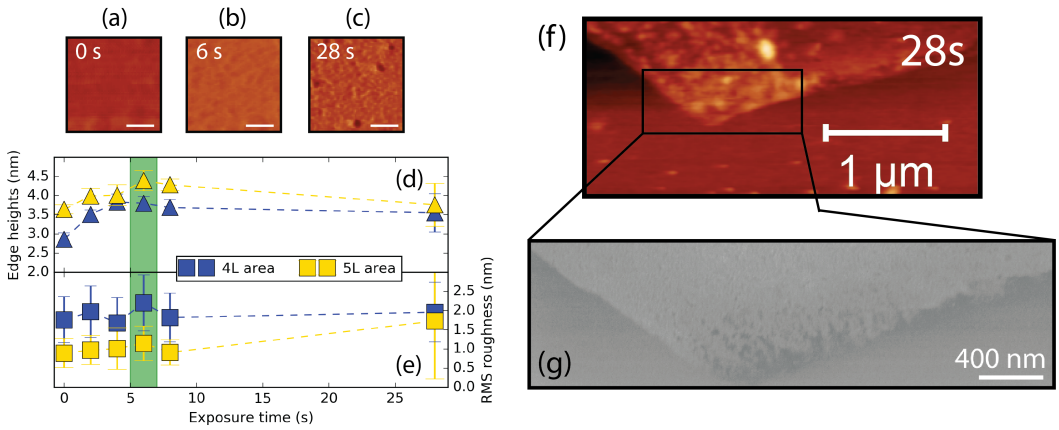

Figure 5.4: **Surface morphology of plasma-treated MoS_2.** **(a)**-**(c)** Phase maps of the same region of a 4L flake, showing notable material contrast on the surface as oxides are formed over time. Scale bars, 200 nm. **(d)** Chart of edge heights extracted along line profiles after each exposure time. The region in green is the edge height peak, which correlates with the electrical recovery time at 6 s. **(e)** RMS surface roughness profiles extracted over time from height maps of the 4L and 5L regions of the flake. **(f)** AFM map of the bottom edge of this flake after 28 s of plasma etching. Visible voids are seen along the bottom of the sample. **(g)** SEM image of the corner of the same flake, exhibiting dark contrast pits on the edge, corresponding to oxidised MoS_2 regions.

The peak in edge height at 6 s is a critical point at which the etching mechanism shifts from one largely dominated by chemical oxygen insertion into the lattice to one where argon-dominated sputtering of material and removal of species from the surface takes over. With increasing doses of the plasma, the integration of oxygen into the mechanically exfoliated 2H-MoS_2 structure will introduce considerable change, including the rearrangement of electronic density and effective lattice deformation, which increases the interlayer distance. Oxygen intercalation between the top layer and the rest of the stack may also occur [257]. All of these factors lead to a rise in the thickness of the thin $MoS_{2-x}O_x$ film [122, 257, 147, 148, 146] and can lead to rupturing [258] while forming oxide- containing patches on the surface at the same time. These fine oxide patches, spectroscopically-observed by Ko *et al.* [156], can be seen in the AFM and SEM micrographs in **Figs. 5.4(f,g)**. The SE contrast is due to the higher work function of MoO_3 (6.6 eV) [259] compared with that of MoS_2 ($\approx$ 4.04 to 4.47 eV) [260].

The structural modification undergone by the MoS_2 in the plasma chamber can also be linked to the change in its optical contrast over time (**Figs. 5.5(a,b)**). The change in optical contrast depends on the dielectric constant of the material and its thickness. If MoO_3 (a wide-gap semiconductor) is present on the surface, its

contribution to the refractive index would largely govern the properties of the sample, as its optical absorption has been demonstrated to be negligible in the visible region [156]. A recent study has shown that sub-stoichiometric MoO_{3-x} can be volatile and even removed by Ar flow at low temperatures [261]. In the O_2:Ar plasma physical sputtering–dominated regime, the surface roughness is seen to increase by more than 1 nm at 28 s of exposure due to Ar^+-related etching and re-deposition of material on the surface [123, 262]. However, the unchanging surface roughness up until 8 s indicates initial direct conversion of MoS_2 into a planar oxide. Most importantly, the edge height trend correlates with the electrical recovery discussed in the previous section, with a peak at 6 s. Examples of the line profiles extracted from each portion of the flake seen in **Figs. 5.5(c-e)** are presented in **Fig. 5.5(f,g)**.

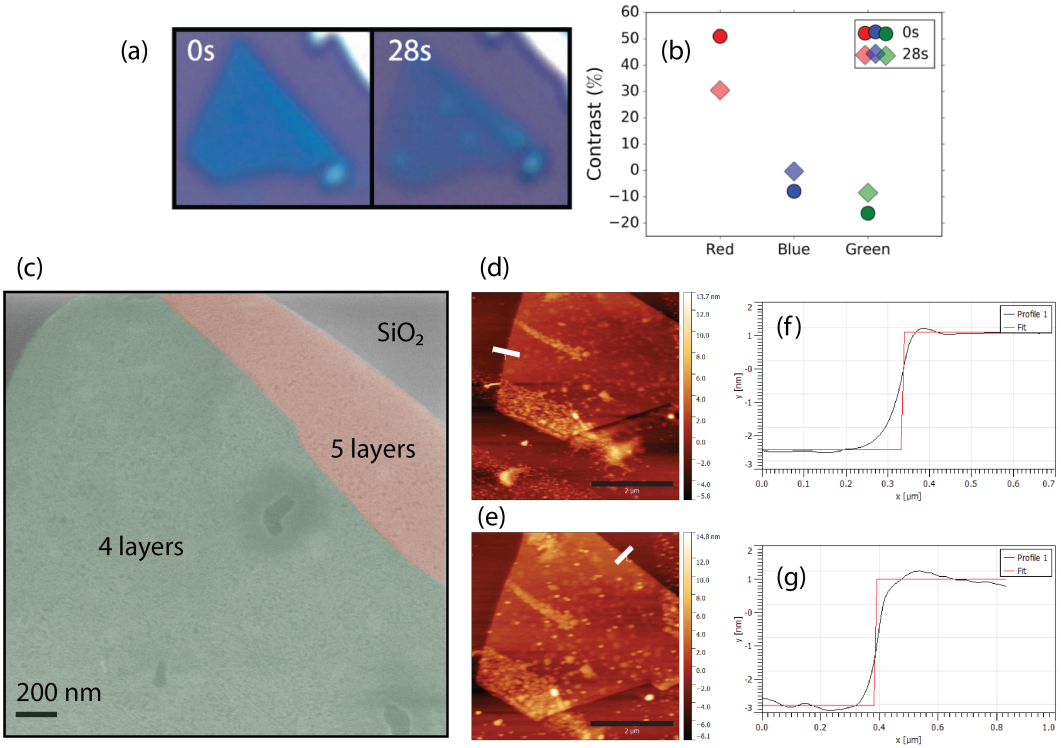

Figure 5.5: **Topography and optical contrast variation of the same 4L MoS_2 flake.** **(a)** A visible drop in optical contrast of the 4L MoS_2 flake after 28 s is seen in the optical micrograph. **(b)** Contrast change of the RGB channels relative to the substrate after 28 s, compared to the untreated flake. **(c)** False-colour SEM image (taken at 15 keV) of the flake after 28 s. The coloured areas mark the larger 4L area of the flake (green) and the step to the 5L region (red). Small dark pits extending to tens of nanometres in lateral dimension are visible on the surface. **(d)**, **(e)** AFM maps of the flake, with the white lines marking the regions from which line profiles were extracted on the 4L and 5L areas, respectively. **(f)**, **(g)** Line profiles recorded from the maps (black) and the respective edge height (y) fits from `Gwyddion` software (red) across lateral distance x in μm.

5.3 Spectroscopic analyses of the surface-bound oxide

We investigate the change to the chemical content of our MoS_2 devices by using Raman, PL, EDX and XPS spectroscopies. The offset Raman spectra of the 4L flake (**Fig. 5.6(a)**) show notable shifts in the characteristic peaks corresponding to the A_{1g} mode at ≈ 407 cm^{-1} and the E^1_{2g} mode at ≈ 384.5 cm^{-1} once the sample is exposed to the plasma. After only 2 s of treatment (and accompanied by a decrease in amplitude) the E^1_{2g} peak blue-shifts to ≈ 385 cm^{-1}, whereas the intensity of the A_{1g} peak increases by $\approx 32\%$ and its position up-shifts slightly; reducing the fitted peak separation (see inset of **Fig. 5.6(a)**). As the Raman spectra evolve over time, the peak separation at the recovery time of 6 s narrows, whereas the FWHM of the A_{1g} out-of-plane mode is reduced. Its intensity now rises above that of the in-plane mode and remains as such for longer plasma treatment times, where both intensities are greatly quenched and peaks begin to broaden and separate. The insertion of oxygen into the MoS_2 crystal lattice by the plasma can account for the change in the dielectric screening environment and the restoring forces between adjacent MoS_2 molecular layers, thereby affecting the frequencies of both characteristic modes. An increase in $\Delta\omega$ occurs when MoO_3 replaces MoS_2 on the surface of MoS_2 [156, 174]. Conversely, the peak separation remains constant in the monolayer or is reduced when no oxides are detected after plasma treatment [40, 257, 160]. In addition, the asymmetric broadening of both peaks over longer exposure times seen in **Fig. 5.6(a)** has been associated with the presence of additional defect-induced phonons originating from oxide centres in plasma-treated MoS_2 [156]. The unusual variation in the intensity ratios for this plasma-treated 4L sample may come from a change to the stacking order of the MoS_2 layers and/or surface reconstructions. If the top layer uncouples from the rest of the MoS_2 lattice, it may affect the on-resonance condition for the Raman scattering in this van der Waals layered system and alter the relative mode intensity ratios [263, 233].

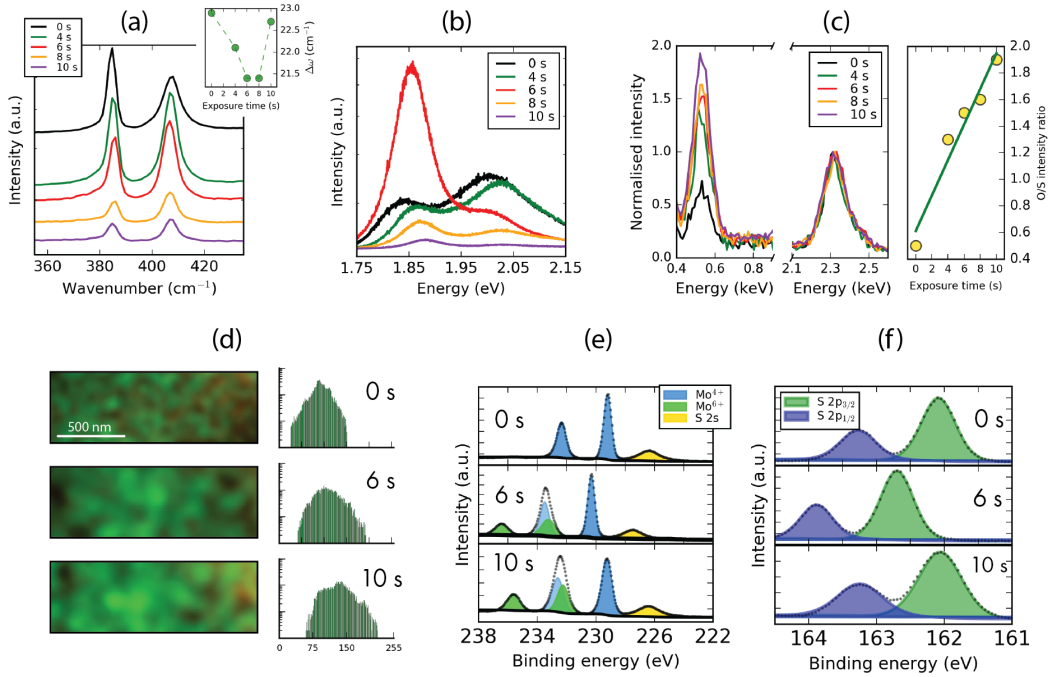

Figure 5.6: **Spectroscopic signatures of oxidised MoS_2.** **(a)** Raman spectrum of 4L MoS_2 over plasma treatment time shown in the semi-log plot. The inset tracks the time evolution of the separation between the E^1_{2g} and A_{1g} peaks. **(b)** PL spectrum of 4L MoS_2 as it changes over plasma exposure time, showing significant *A* exciton enhancement at 6 s of treatment. *au*, arbitrary units. **(c)** *Left:* Time evolution of the EDX spectrum normalised to the sulfur-K_α line taken from a suspended 4L flake. *Right:* Ratio of the O/S elemental signal intensity tracked over exposure time. The green line is a linear fit to the data. **(d)** Areal EDX mapping of sulfur (red) and oxygen (green) content in the same 4L sample at 0, 6, and 10 s of plasma treatment. The associated histograms (in arbitrary units on the y axes) visualise the intensity distribution of the green oxygen pixels in the maps. Scale bar, 500 nm. **(e)** XPS spectra of the Mo 3d region showing increased MoO_3 content over time. **(f)** S 2p region of the XPS spectrum.

The PL spectra of the 4L sample are presented in **Fig. 5.6(b)**. For the initial exposure times, the luminescence intensity associated with the *B* exciton at ~ 2 eV dominates over the *A* exciton intensity at 1.85 eV, which is characteristic of the indirect-gap nature of non-monolayer MoS_2. The energy of both peaks is slightly blue-shifted after initial plasma exposures and their intensity also drops. With further exposure to the recovery time of 6 s, the direct-gap emission is greatly enhanced by ~ 120%. Direct emission persists until it is fully quenched at longer exposure times. This anomalous effect noted at 6 s matches well with the picture of the top layer becoming decoupled from the rest of the MoS_2 stack - an effect previously observed and attributed to oxygen intercalation [257]. Meanwhile, the bi-directional shifts of both peaks over time serve to illustrate the band structure distortion induced

by the plasma treatment. The PL quenching at longer exposure times is due to the defect-induced mid-gap states that inhibit direct excitonic recombination [174, 264].

We plot the relationship of the oxygen K_α and sulfur K_α EDX peak intensities to the plasma exposure time derived from the normalised spectra, which we obtained from the same region of a 4L sample after subsequent treatments (**Fig. 5.6(c)**). Oxygen content has increased more than threefold in the first 10 s of exposure to the plasma and changes almost linearly with time. Areas high in O signal also show a reduced S signal, suggesting that the oxygen has replaced the sulfur in the MoS_2 lattice through an oxide-forming chemical reaction. Areal EDX mapping of the suspended 4L MoS_2 flake (**Fig. 5.6(d)**) suggests the insertion of oxygen into the MoS_2 structure in a patch-like pattern, as previously proposed [124, 265]. We will go on to discuss the size distribution of these patches in the upcoming ACSTEM results section. The associated colour histograms visualise the increased oxygen distribution in the sample with plasma time by the increasing green pixel count originating from the O elemental signal.

Fig. 5.6(e) shows XPS spectra of the Mo 3d region, indicating the increased presence of oxide species over exposure time. For the pristine sample, the peaks around 229 eV and 232 eV correspond to, respectively, the Mo^{4+} $3d_{5/2}$ and Mo^{4+} $3d_{3/2}$ spin-orbit split components. The 6 s spectrum shows a characteristic Mo^{6+} 3d doublet attributed to MoO_3 [266]. After 10 s of exposure, the intensity of the trioxide-associated doublet increases further, with a significant ratio of the surface now containing MoO_3 (estimated at 30 to 40% from integrated areas of each fitted component). In addition, a thickogram calculation [267] reveals that the intensity attenuation of the 10 s spectrum is consistent, within known parameters, with the presence of a bilayer of 2D MoO_3 (that is, a bulk unit cell of α-MoO_3) on the surface at this exposure time and 61% of the bilayer of 2D MoO_3 at 6 s. For the thickogram calculation, refer to **Appendix B**.

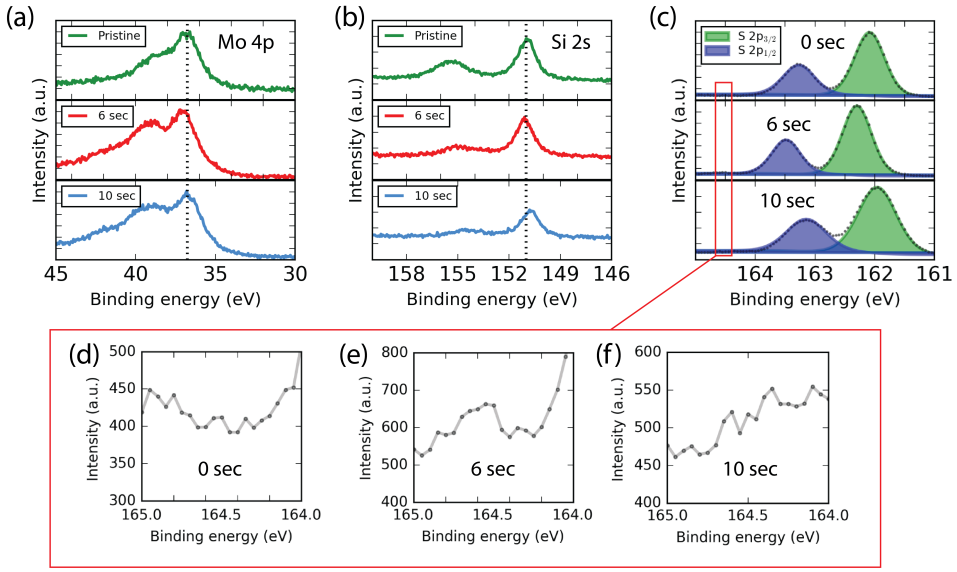

Figure 5.7: **Shifts of XPS spectra and evidence for S-O bonding**. **(a)** XPS spectra showing the Mo 4p region, demonstrating a change to the chemical order of molybdenum with increasing plasma treatment. **(b)** A reference spectrum of the SiO_2 substrate, showing a shift with time and a slight chemical change to the surface of the chip. Dashed vertical lines mark the centres of the pristine sample peaks in **(a)** and **(b)**. **(c)** Extended S 2p region of the XPS spectrum, showing the area in red where one may expect peaks due to S-O chemical bonds. **(d-f)** Graphs of the same binding energy region, marked in red in **(c)**, after 0, 6 and 10 s of plasma exposure. A small S-O peak at $\approx$ 164.6 eV is seen in the 6 second spectrum, indicative of a small presence of oxysulfide species on the surface. Data collected and analysed with the assistance of Prof. Cormac McGuinness.

Fig. 5.6(f) demonstrates the S 2p region. Peak broadening is evident with increased plasma exposure time, indicating a change in the chemical order of the surface. Sub-stoichiometric MoS_{2-x} has also been reported to cause the characteristic broadening of the S 2p doublet [268], consistent with the picture of sulfur atoms being removed from the surface of the MoS_2 flakes. Most interestingly, both the Mo 3d and S 2p signals are up-shifted after 6 s and down-shifted after 10 s in these spectra; which have been corrected to the C 1s core line (see also shifts to the reference Si 2s peaks of the substrate in **Table 5.1**). It is widely accepted that MoO_3 can induce hole doping and concomitant down-shifting of the MoS_2 peaks due to Fermi level realignment [174, 265, 269, 270]. This is in agreement with our transfer curves, with a significant V_{th} shift to positive gate biases observed at higher plasma exposure times in **Fig. 5.2(c)**. The up-shift at 6 s may thus correlate with the n-type doping observed in the transfer curves in **Fig. 5.2(b)**. In addition, the FWHM of the MoO_3-associated doublets decreases between the 6 s and 10 s spectra, suggesting the surface formation of a more stoichiometrically-complete trioxide between 6 and

10 s of plasma treatment (see also the change to the Mo 4p spectra in **Fig. 5.7(a)** and the evidence of a small peak originating from the S–O bond at 6 s in **Figs. 5.7(d-f)**).

Exposure time (s)	Mo^{4+} 3d	Si 2s
0	229.2 eV	150.9 eV
6	229.8 eV	151 eV
10	229. 4 eV	150.8 eV

Table 5.1: Peak shifts with exposure time for the Mo^{4+} $3d_{5/2}$ and Si 2s peaks relative to the C 1s core line, indicating that shifts are due to doping and not substrate charging.

We can study the dynamics of the observed luminescence quenching using time-resolved fluorescence lifetime imaging on the direct-gap monolayer MoS_2. **Figure 5.8(a)** shows the 1L region of exfoliated MoS_2 used to obtain a fluorescence lifetime map in **Fig. 5.8(b)**. The image was recorded using a 700 nm filter (FWHM ~ 30 nm) which shows the long lifetime component of the time-resolved PL emission. The average emission lifetime for an untreated sample was found to be ~ 80 ns. After only 2 seconds of plasma treatment, the lifetime was reduced to below the temporal resolution of the system. Associated monolayer PL spectra collected from the maps are shown in **Fig. 5.8(c)**. The quenching rate increases greatly with the produced defect density, inhibiting the radiative recombination completely after 10 s of exposure; while the time-resolved measurements cannot be performed even after only 2 seconds of exposure.

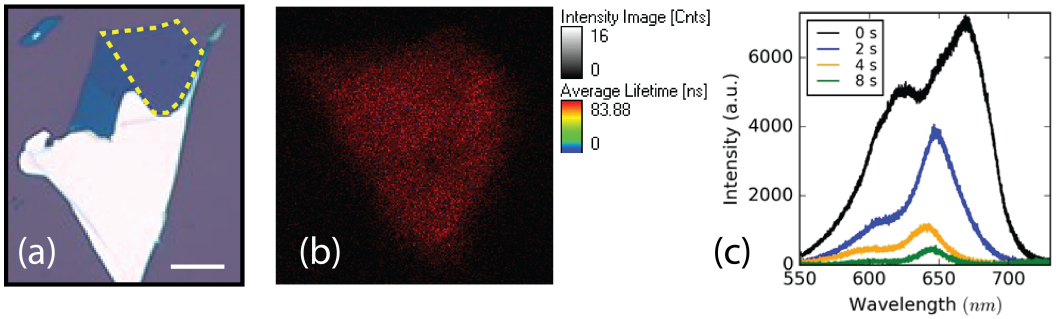

Figure 5.8: **PL signatures of oxidised 1L MoS_2.** **(a)** Optical micrograph of the MoS_2 flake, with the monolayer region marked in yellow. Scale bar is 5 μm. **(b)** Fluorescence lifetime image of the untreated MoS_2 monolayer recorded using a 700 nm filter (FWHM ~ 30 nm) which shows the long lifetime component of the time-resolved PL. **(c)** PL spectra of monolayer MoS_2 following 0 s, 2 s, 4 s and 8 s of exposure to the plasma. Data collected by Dr. John Gough in Prof. Louise Bradley's lab.

All of the above results demonstrate that the plasma-treated MoS_2 undergoes a continuing oxygen insertion and crystal structure distortion. However, the full unit cell of plasma-generated MoO_3 is an electrical insulator [124]. The electrical recovery at the 6 s mark indicates that an intermediary phase of sub-stoichiometric MoO_3 may exist between the pristine MoS_2 semiconductor and the MoO_3-rich insulator, causing the transient recovery of electrical properties within the exponential decay envelope known from the literature. This observed trend may suggest the formation of a highly conductive form of MoO_x reported in the literature [255, 256].

5.4 Nanoscale effects of plasma etching at recovery time

Many etching mechanisms, some contradictory, have been proposed for the surface reaction of oxygen-containing plasma with MoS_2 [156, 271, 272, 161]. To investigate the elusive 2D oxide phase, we go on to study the effects of the plasma etching on the nanoscale by ACSTEM. **Figure 5.9** shows a region of a bilayer MoS_2 flake after 6 s of plasma treatment compared to an untreated flake.

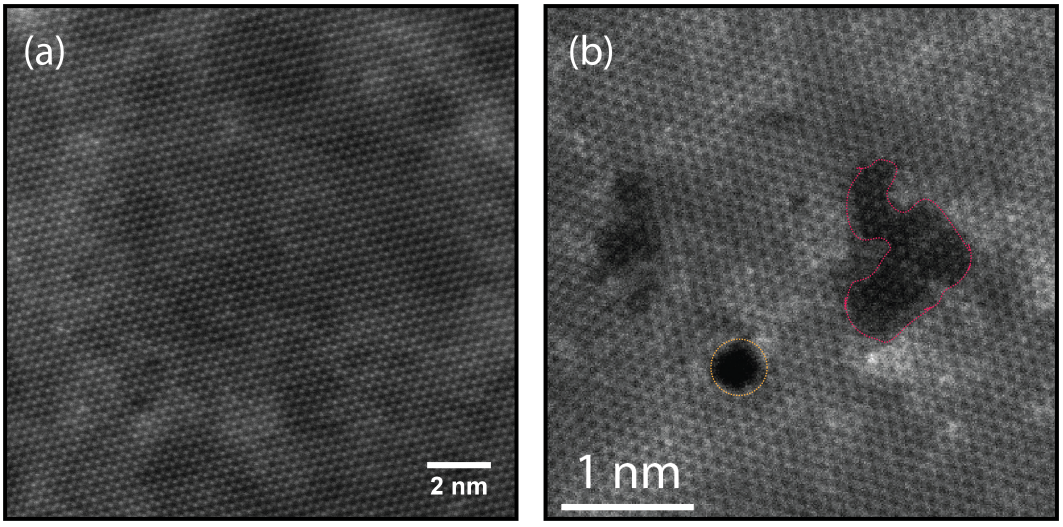

Figure 5.9: **Nanoscale effects of plasma treatment on MoS_2.** ACSTEM micrographs of a mechanically-exfoliated bilayer MoS_2 flake **(a)** before and **(b)** after 6 seconds of plasma exposure. The region marked in magenta shows an etched pit with part of the top layer missing. The area marked in orange shows a perforation where no material remains. Images acquired by Clive Downing; sample transferred by Prof. Yangbo Zhou.

Notable damage to the MoS_2 lattice occurs at this exposure time. Portions of MoS_2 material are completely removed in nanometre-sized regions. This etching phenomenon is seen to nucleate from individual defective sites, spanning only a few nanometres across. Some of these voids are missing a part of the top molecular layer

of MoS_2 after 6 s, leaving behind a bare monolayer region underneath (as confirmed by QSTEM software simulations in **Fig. 5.10**).

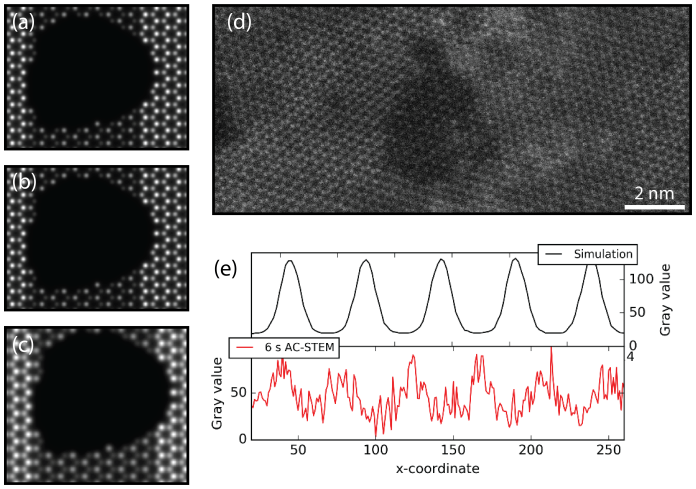

Figure 5.10: **QSTEM simulations of stripped bilayer MoS_2.** **(a)-(c)** Simulated ACSTEM images of 2L MoS_2 with a peeled monolayer area and a perforated void, corresponding to simulated electron probe sizes of 0.6 nm, 0.8 nm and 1 nm respectively. Simulations were performed by Dr. Aleksey Shmeliov. **(d)** ACSTEM image of a stripped pit area, acquired by Clive Downing. **(e)** Intensity comparison between the QSTEM simulation line scan along Mo atoms in the [100] direction in the monolayer pit, with the actual experimental line scan from the micrograph seen in **(d)**.

These pits deepen with increasing plasma exposure time (see also HRTEM images in **Fig. 5.11**) and eventually become perforations on thinner flakes. Mass-thickness contrast in the ACSTEM reveals the removal of MoS_2 material from the pits. Example large-scale ACSTEM micrographs are presented in **Fig. 5.12**. A collection of these images were used to obtain statistics on the dimensions of voids formed by the plasma in the MoS_2 flake after 6 and 8 seconds of exposure.

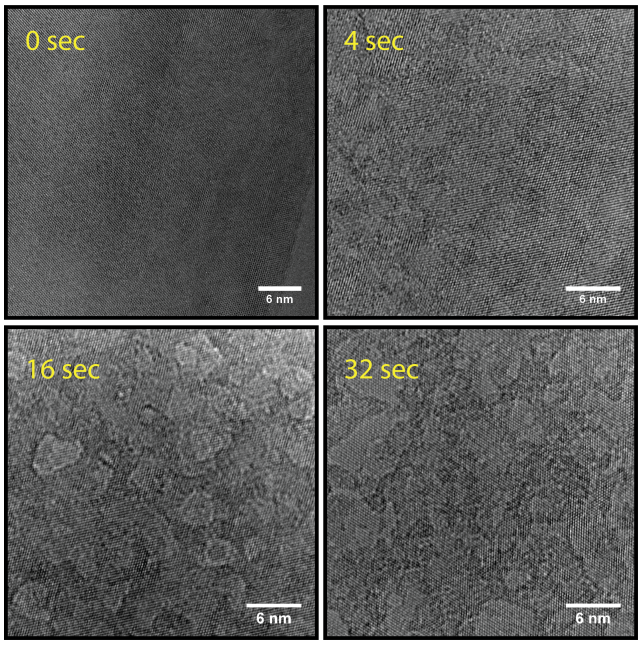

Figure 5.11: **HRTEM images of plasma-treated MoS_2; beam energy = 300 keV**. Few-layer MoS_2 flake after **(a)** 0 seconds, **(b)** 4 seconds, **(c)** 16 seconds and **(d)** 32 seconds of exposure to O_2:Ar plasma. Images acquired with the assistance of Dr. Daniel Fox.

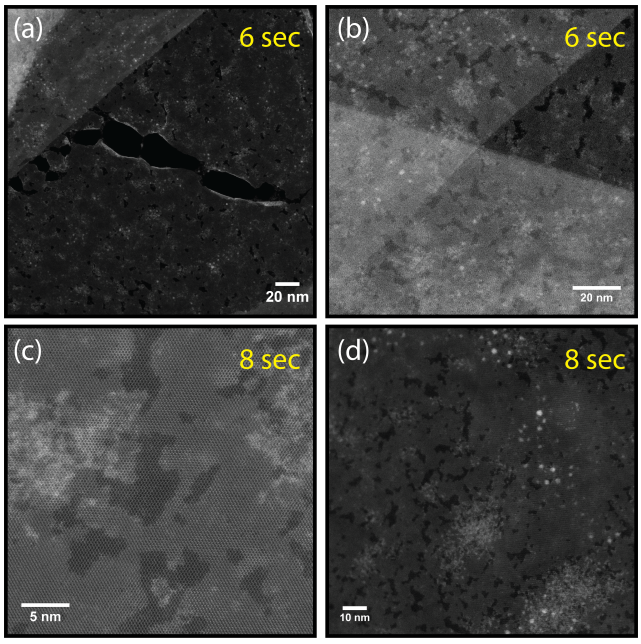

Figure 5.12: **ACSTEM images of plasma-treated MoS_2; beam energy = 60 keV**. Bilayer MoS_2 flake after **(a, b)** 6 seconds, and **(c,d)** 8 seconds of exposure to O_2:Ar plasma. Large-scale images show rips in the suspended MoS_2 flake, as well as a large density of pore-like defects across its whole surface. Fold regions of multiple layers of MoS_2 are also visible with damaged regions clearly seen in the bottom layer of the flake. The sample was transferred onto the grid upside down, with the etched surface in the bottom of this image. White residue on all flakes are left-over hydrocarbons from stamp transfer processing. Images acquired by Clive Downing.

Figures 5.13(a,c) demonstrate the distributions of the extracted widths and lengths of imaged voids on the bilayer flake after 6 and 8 seconds respectively. Top and right hand-side histograms show the width (length) distributions. Length is here defined as the largest lateral void dimension, whereas width is the dimension perpendicular to it (and void area is their product). A positive correlation between the lateral dimensions of the etched voids is extracted from data fitting, showing the close-to-isotropic growth of the voids. The average area of a pore at 6 s is 12.5 ± 0.1 nm^2, while at 8 s this increases slightly to 12.9 ± 0.1 nm^2. The respective histograms of the distributions of different area voids (**Figs. 5.13(b,d)**) reveal the continuing inclusion of new, small voids with increasing treatment time from 6 s to 8 s.

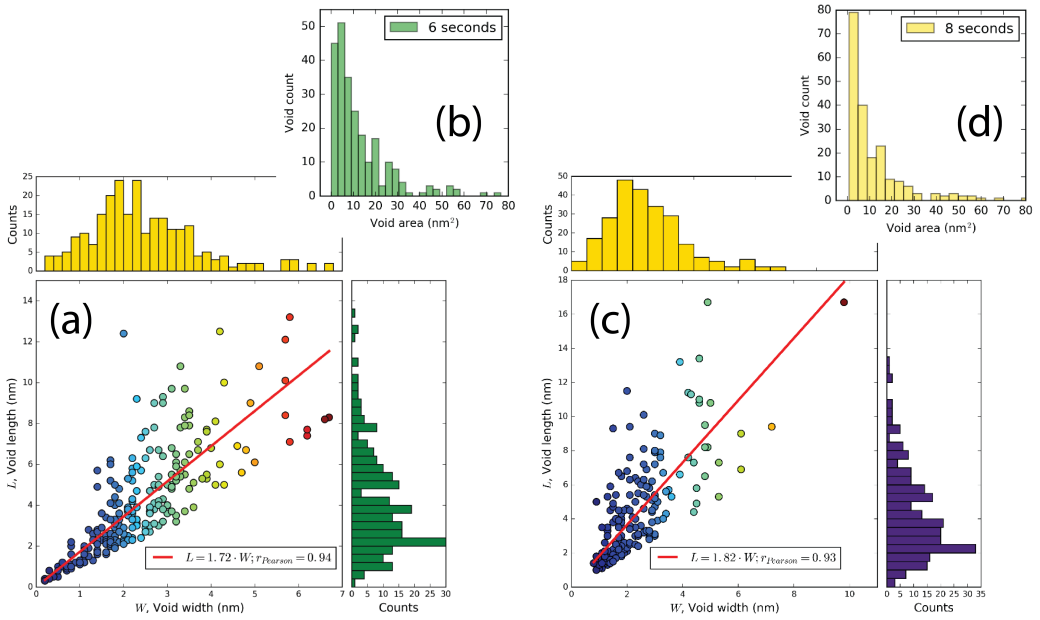

Figure 5.13: **Void dimension statistics from ACSTEM images of plasma-treated bilayer MoS_2.** **(a)** Scatter plot and histograms visualising the distribution of the lateral dimensions of etched voids on the bilayer MoS_2 flake after 6 s of plasma exposure. **(b)** Histogram of the distribution of voids of different areas on the 6 s sample. **(c)** Width and length distributions after 8 s of treatment. **(d)** Histogram of the distribution of voids of different areas on the 8 s sample.

We can utilise the superlative resolution of the 60 pm electron beam probe in the *NION UltraSTEM 200*, and its relatively low beam energy of 60 keV (does not sputter MoS_2 readily), to perform nanoscale EDX and EELS mapping. Markedly, we obtain spectra suggesting very little oxygen presence around the recovery time (**Figs. 5.14(a,b)**).

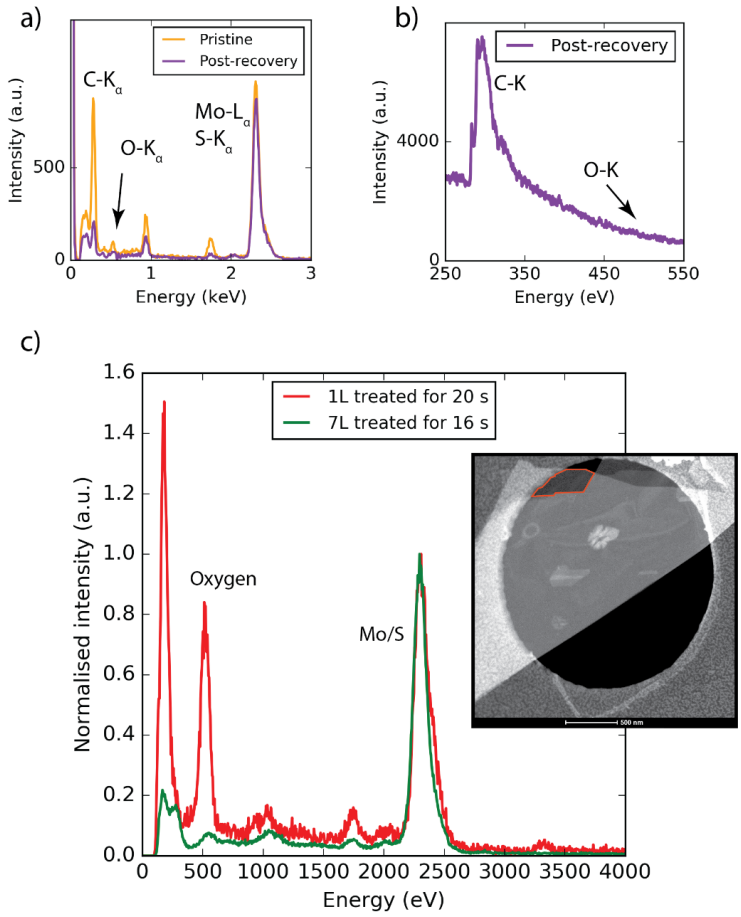

Figure 5.14: **Nanoscale spectroscopies**. **(a)** Atomically-resolved EDX spectrum taken on a bilayer flake in the ACSTEM before plasma treatment (orange) and after 10 sec of treatment (purple). In both cases, the oxygen signal from the mapped area is very weak. **(b)** EELS spectrum taken on the same flake after 10 sec, demonstrating no oxygen presence in the sample following overnight storage in vacuum. **(c)** Normalised EDX spectra taken from a thin monolayer area (marked in red on the inset STEM image with a scale bar of 500 nm) and a thicker (7L) sample after long exposure times. The thinner sample shows a significant oxygen concentration in the post-recovery stage, i.e. when stoichiometrically-complete MoO_3 has been formed on the surface. In the case of the thicker sample, the concentration is lower as the chemical reaction is confined to the surface.

It has been demonstrated that oxygen plasma interaction with molybdenum metal leads to the creation of volatile Mo oxides [132], whereas a recent study has confirmed oxide volatility in oxidised MoS_2 [261]. In addition, a similar study of oxygen plasma-treated 2D WSe_2 samples has failed to detect oxygen in the sample after treatment [133]. We find that the plasma-formed oxide phase studied presently is volatile under UHV. When the sample is left overnight in the SEM testing chamber ($\sim 10^{-6}$ mbar), the n-type depletion mode functionality is reversed by a drastic shift of V_{th} toward positive gate biases (**Fig. 5.15(a)**). Similarly, when inserted into the

vacuum chamber of the ACSTEM overnight ($\sim 10^{-9}$ mbar), the freestanding flakes lose their weakly bound surface oxides. The inability to detect oxygen in these atomically resolved voids leads us to infer that the oxide, which was present initially and is responsible for the electrical recovery, was sublimated under UHV conditions, leaving behind the underlying MoS_2 structure. We remark here on the fundamental considerations of this claim. Intuitively, it may seem that stoichiometric oxides of Mo have a considerable relative molecular mass (143.9 for MoO_3, 127.9 for MoO_2) which may render them difficult to pump off, even by UHV systems. However, an intermediary reduction to methanol (relative mass of 32; heat of sublimation $\approx$ 9 kcal/mol) or another alcohol by partial or complete hydrogenation is a possible way to obtain much lighter molecules, whose evaporation rate off the surface would considerably increase due to the decreased heat of sublimation when the metallic centre is not part of the molecule (values for oxides of molybdenum are much higher and range from 80 to 105 kcal/mol, even at 800°C [273]).

Thus, we can safely assume that the chemical reaction is mainly confined to the surface and any oxygen signal which we can manage to detect by performing an EDX scan in the SEM or TEM shortly after plasma exposure must come from the surface of the sample. Let us consider the spectra shown in **Fig. 5.14(c)**. The normalised intensity of the O/S signal for the 1L flake at 20 seconds is $\approx 83\%$, while for the 7L flake at 16 seconds it is $\approx 8\%$, to the nearest percentage. If we assume 0% oxygen content at 0 seconds of treatment and allow the suspended flake to be oxidised from both sides on the TEM grid, we can take the oxidation time rate to be roughly 8.3% per 2 s per one MoS_2 layer. This equals 4.2% 2 s^{-1} per flake surface, as sketched below:

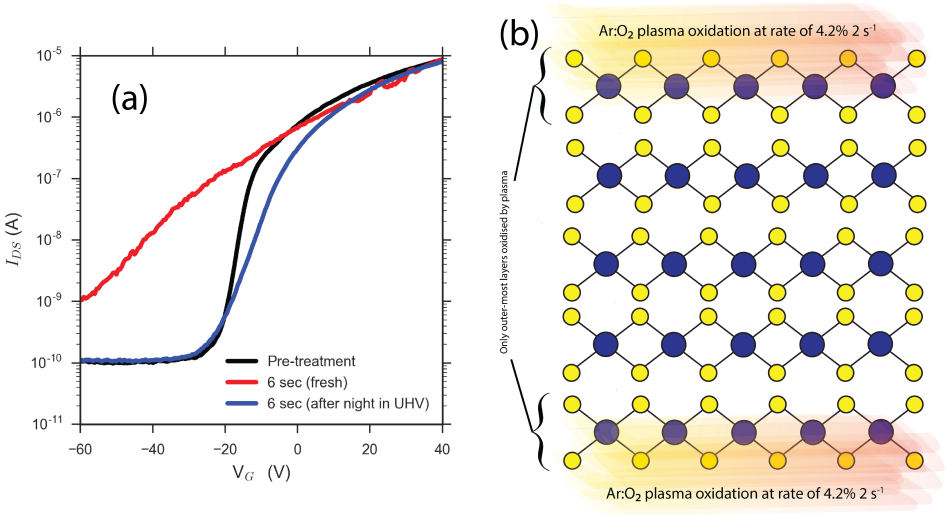

Figure 5.15: **(a)** The effect of keeping a plasma-tuned sample in a SEM vacuum chamber overnight. Data taken at V_{ds} = 1 V. The electrical recovery effect associated with the presence of the 2D oxide which is seen immediately after exposure (red) is reversed once the MoO_x is pumped off at UHV levels (blue). **(b)** Cartoon of a multilayer MoS_2 sample being oxidised by O_2:Ar plasma from both sides when the sample is suspended on a TEM grid. This assumption is made to estimate the distribution of oxygen in the sample from EDX mapping in the TEM.

In 16 seconds, the oxidised amount will be 2 x (4.2% x 8) ~ 67% of 2 outer-most layers. The total ratio for a 7L flake will then be: [(0.67 × 2) + (0.0 × 5)]/2+5 = 1.34/7 ~ 19%. This compares well with the ≈ 8% number obtained from the EDX spectra. This calculation does not account for intrinsic quantification errors associated with EDX mapping and assumes that oxygen content does not increase in the sandwiched middle 5 layers, which in all reality will happen. The experimental 11% error in this case is thus reasonable and supports our picture of what happens to the sample.

5.5 Dependence of the mobility recovery on MoS_2 layer number

To obtain a more informed picture of how the oxide on the top layer of MoS_2 affects the transport behaviour of the FET, we fabricated and tested devices of different thicknesses between 1 and 10 layers, in the same fashion as the device in **Fig. 5.2**. The associated *I-V* curves, gate curves, derived mobilities as well as subthreshold swings at each plasma exposure are all collated sequentially below in **Fig. 5.16**, **Fig. 5.17**, **Fig. 5.18** and **Fig. 5.19**:

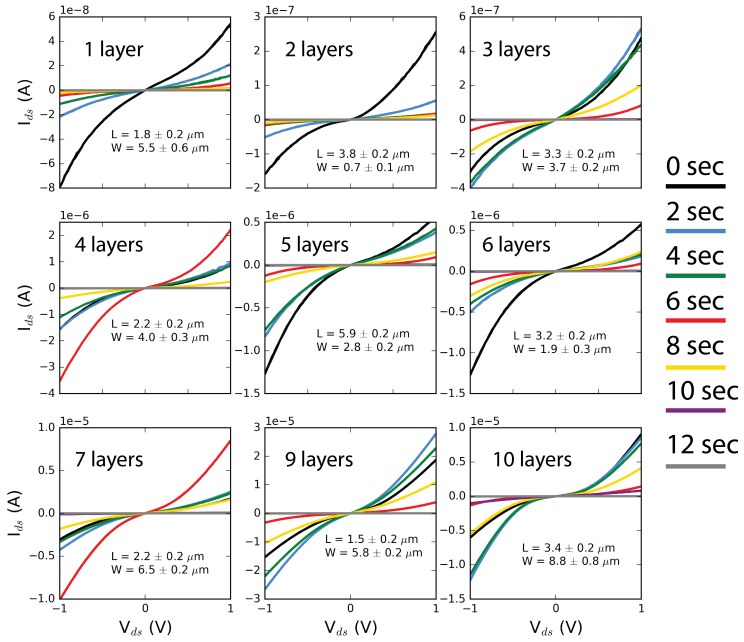

Figure 5.16: ***I-V* sweeps corresponding to devices of particular layer number, all taken at V_g= 0 V.** The FET channel lengths (L) and widths (W) are provided on each plot.

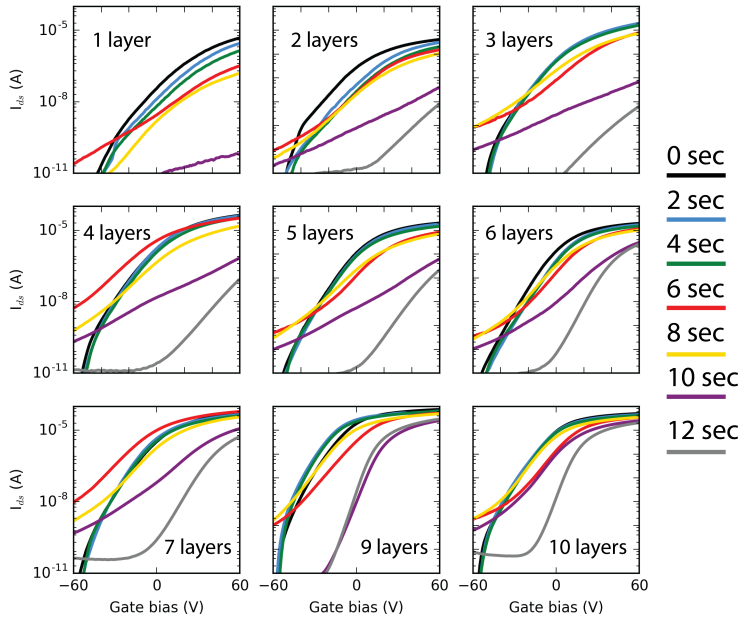

Figure 5.17: **Gate sweeps corresponding to devices of particular layer number, all taken at V_{ds}= 1 V.** In all cases, the flattening of the gate curve can be observed at 6 seconds.

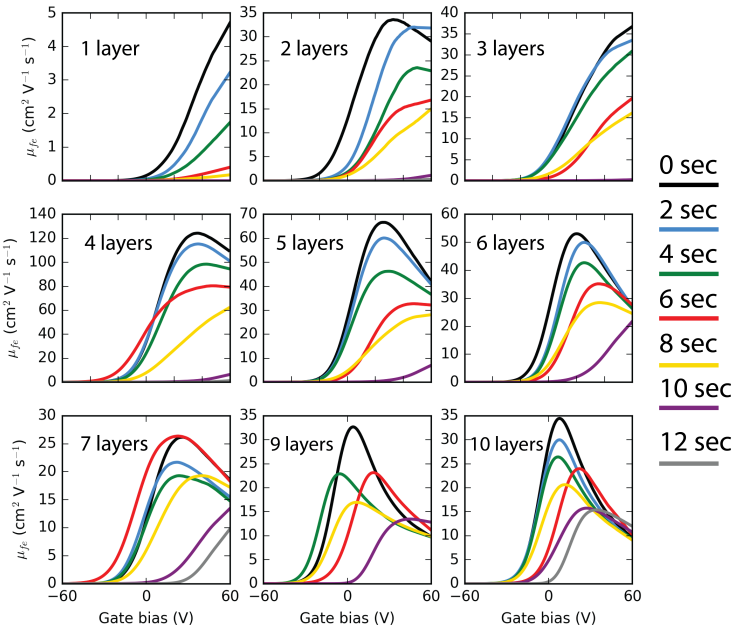

Figure 5.18: **Extracted μ_{fe} corresponding to devices of particular layer number, evaluated at V_{ds}= 1 V.**

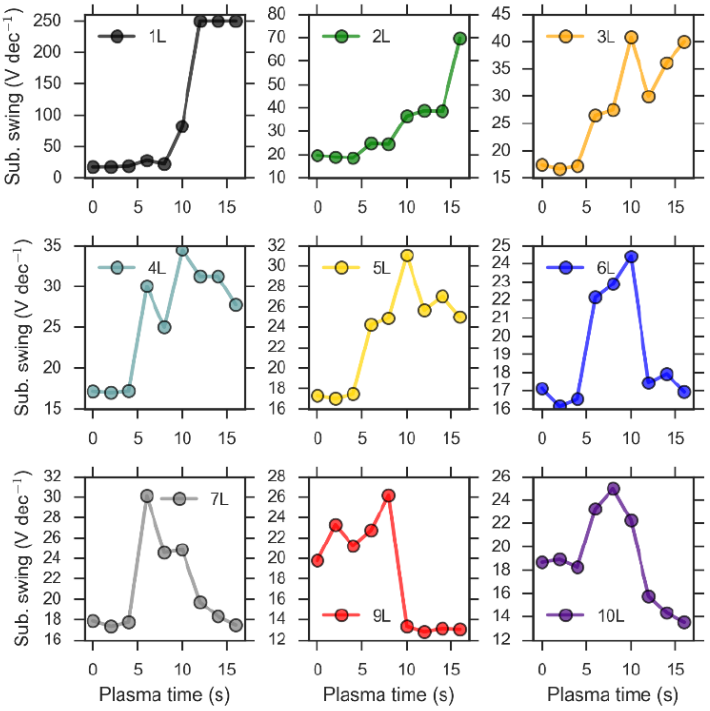

Figure 5.19: **Full data set of subthreshold swings derived for samples of all thicknesses over plasma exposure time.** Note the differing behaviour for 1-3L samples (y axis scale is logarithmic).

The highly consistent feature of transfer curves at times when the 2D MoO_x is

present on the top layer is the drastic shift of V_{th} to negative gate biases. **Figure 5.20(a)** tracks ΔV_{th} for the tested MoS_2 layer numbers. Here, ΔV_{th} is defined as the difference between the threshold voltage before treatment and at the point of mobility recovery. For samples of all thicknesses, V_{th} shifts considerably to negative biases by a similar amount, with the mean shift value of ΔV_{th} = -19 V marked on the plot by the horizontal yellow line. This behavioural consistency and lack of dependence on layer number indicate the key role of the plasma-modified top surface layer. V_S are known to induce n-type doping and a negative V_{th} shift in MoS_2 [69]. If we assume the formation of roughly spherical, $\sim$ 10 nm-sized patches of metallic oxides, we can treat charge transfer from MoS_2 to the surface-bound MoO_x using the Zhdanov model [274]. To maintain the condition of no electric field inside the metallic particle while equalising Fermi levels of the heterojunction, the physical scenario is that of a uniform charge distribution over the whole surface of the metallic oxide. The number of transferred electrons in this simplified spherical geometry is then given by:

$$N_e \approx \frac{r_m \Delta E}{e^2} \tag{5.1}$$

where r_m is the mean size of oxide patches at 6 s seen in ACSTEM, e is the electronic charge and ΔE is the Fermi energy shift between the oxide and the MoS_2.

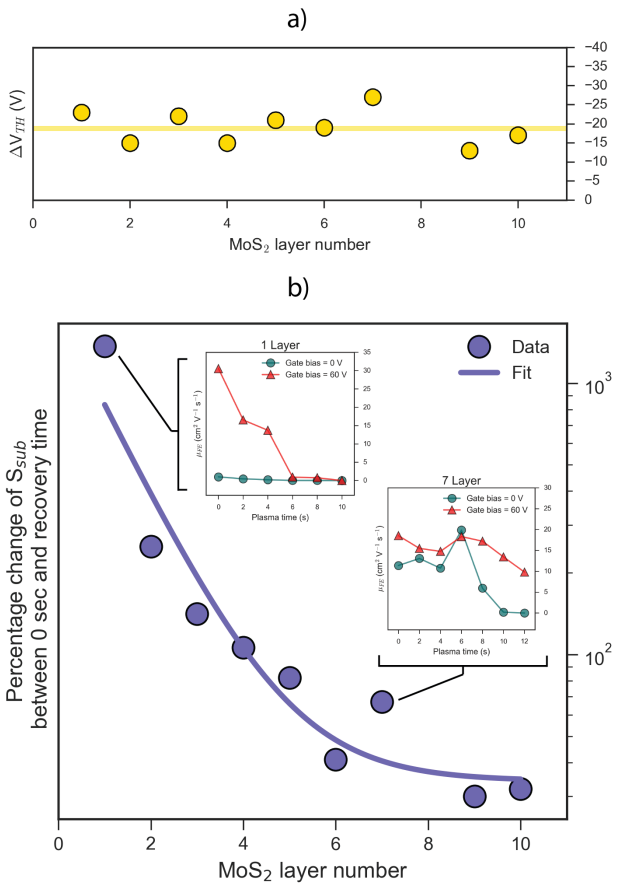

Figure 5.20: **Effect of layer number on the mobility recovery**. **(a)** Change in gate threshold voltage between the recovery time and pristine MoS_2, tracked as a function of layer number. Devices of all thicknesses show a major V_{th} shift to negative gate bias at the time of mobility recovery. The mean shift value of - 19 V is marked by the horizontal yellow line. **(b)** Percentage increase of the subthreshold swing between untreated and recovered stages for samples of all tested thicknesses. S_{sub} increases for all samples at the recovery stage and the effect scales with MoS_2 layer number. Insets track the μ_{fe} evolution over the exposure time, for the 1L and 7L samples in the linear (green) and saturation (red) regimes. The mobility recovery happens for samples thicker than three layers at various stages of the FET channel inversion.

We calculate values of N_e, which are at least one order of magnitude smaller than the concentration of V_S; taking the electron concentration to be:

$$n_{2D} = \frac{C_{ox}\Delta V_{th}}{e} \sim 10^{12}\ \text{cm}^{-2} \tag{5.2}$$

Hence, V_{th} will be largely shifted to negative gate biases as plasma-created V_S strongly n-dope the FET channel at the point of recovery. However, at longer plasma times, the oxide patches turn into insulating MoO_3, which act as effective acceptors [270]. At the same time, the concentration of V_S decreases because they

become preferential sites for oxygen incorporation. The vanishing of V_S and the formation of hole-doping MoO_3 eventually cause an imbalance to this interplay, resulting in a positive shift in V_{th} at longer plasma times (>10 s).

The influence of channel thickness on the screening effect of the metallic patches embedded in the top layer around the recovery time can be well-understood by tracking the subthreshold swing variation for all the samples over exposure time. In **Fig. 5.20(b)**, we plot the percentage change of S_{sub} for MoS_2 devices of all tested layer thicknesses (that is, a measure of how much S_{sub} increases at recovery time relative to no plasma treatment). The extracted data are well-fitted ($R^2 = 0.99$) with an asymptotic exponential function of the general form: $y = a - bc^L$, where a, b, c are constants and L is the MoS_2 layer number. This demonstrates the critical role that MoS_2 thickness plays in allowing the top metallic layer to alter the field effect in the underlying transistor channel. The conductivity of the metallic top layer is not tunable by the back gate [40]. Hence, the on/off ratio at recovery time is severely reduced for samples of all thicknesses, but this effect is felt more severely by thinner samples (hence, the observed much higher S_{sub} values). As the thickness of the MoS_2 stack increases, more undamaged semiconducting material is present deeper in the channel, and the screening from the top layer is felt less strongly.

The defect formation from the plasma effectively destroys the 1L and 2L devices (as evidenced by damage to the bilayer in ACSTEM) before the beneficial effect of the metallic top layer can be experienced by those thin FET channels. The mobility recovery then occurs for thicker samples (> 2L) in the linear regime of the transfer curve. This has its origin in:

1. the metallic 2D MoO_x electrostatically shielding the defect-born charged impurity scattering centres in the underlying layers, resulting in enhanced mobility in the below layers of the now-thinned channel.

2. the distribution of current across the layers. In the linear regime (V_g - $V_{th} \approx 0$ V), the centroid of the current distribution is away from the top layers [275], with the current mainly conducted in the underlying layers. The metallic 2D MoO_x effectively screens the surface charges (V_S and other scattering centres) and results in an enhanced mobility in the underlying layers. In the saturation regime, the hot spot moves to the top layers at high gate voltages [275]. As the top layer is rich in scattering centres, this has a direct consequence in that

the peak mobility in the saturation regime decreases strongly with increasing plasma time.

This interplay is illustrated by the insets of μ_{fe} evolution over plasma time for the 1L and 7L samples (representative of thin and thick layer cases) in **Fig. 5.20(b)**. μ_{fe} in the linear regime (green) does not recover in the 1L case but has a strong recovery peak at 6 s in the 7L case. μ_{fe} recovers when MoS_2 is thicker than 2L for all samples in the linear regime. The peak mobilities measured at saturation (red) decrease strongly for the 1L case and recover slightly for the 7L case. This again shows that thickness is a key parameter, because the 1L sample is rich in scattering centres, whereas the 7L sample still has pristine MoS_2 layers underneath the screening metallic top layer.

5.6 Resistive network modelling of conductivity over time

Modelling of classical conductive networks has proven to be an excellent avenue to describe the global conductive properties of nanoscale devices based on the local properties of a network [276, 277, 278]. An appropriate conductive network model was thus applied to approximate the effect of ideal plasma-generated chemical conversion on the sheet conductance of single-layer MoS_2. The computational model begins with a resistive network of identical conductors of conductance magnitude $g_{S_2} = 1$. During each iteration of the simulation, one randomly picked conductor transitions from its current phase to the next phase with a certain probability, unless that conductor is already in the final MoO_3 phase. If it does not transition, then one of the adjacent sites is chosen and the transition check process is repeated. The probabilities represent the differing transition rates that occur between phases. Although the transition rates are experimentally unknown, an assumption is made that they progress sequentially, such that:

$$(MoS_2 \rightarrow 2D\ MoO_x) \cdot p_1 \tag{5.3}$$

$$(2D\ MoO_x \rightarrow MoO_3) \cdot p_2 \tag{5.4}$$

where p_1 and p_2 indicate relative conversion probabilities for each process, and $p_2 > p_1$. This relationship stems from the fact that the MoS_2 basal plane is

[1] **Note:** this computational work was carried out as a collaboration by the theoretical physics group of Prof. Mauro Ferreira, School of Physics, TCD; in particular his students Colin O'Callaghan and Eamonn Weitz.

chemically unreactive, but any defective nucleation sites will be more likely to facilitate chemical reactions once they are formed [169].

The sheet conductance was then calculated using Kirchhoff's and Ohm's laws (see in-depth description in **Appendix C**). The iterations were continued until all conductors were in the insulating MoO_3 phase. Iterations in the simulation are a proxy to the plasma exposure time, with a certain number of phase transitions (or iterations) per unit time. We note that the phase conversion was instant and did not reflect the crossover between conductance regimes on a localised scale but rather on the scale of the whole network.

Figure 5.21(a) shows a plot of the relative conductance of a simulated MoS_2 network, whose nodes undergo conversion to highly conductive 2D MoO_x and insulating MoO_3 phases over time (in arbitrary units of time). The increase in sheet conductance yielded at the start of the simulation qualitatively mirrors the recovery peaks in **Figure 5.2(f)**. This rise can only be observed if:

1. the conductance of the 2D oxide phase is much higher than that of MoS_2. For other cases of conductance mixing see **Appendix C**.

2. the relative transition rates between phases follow a relationship such that sites that are already defective are more likely to convert.

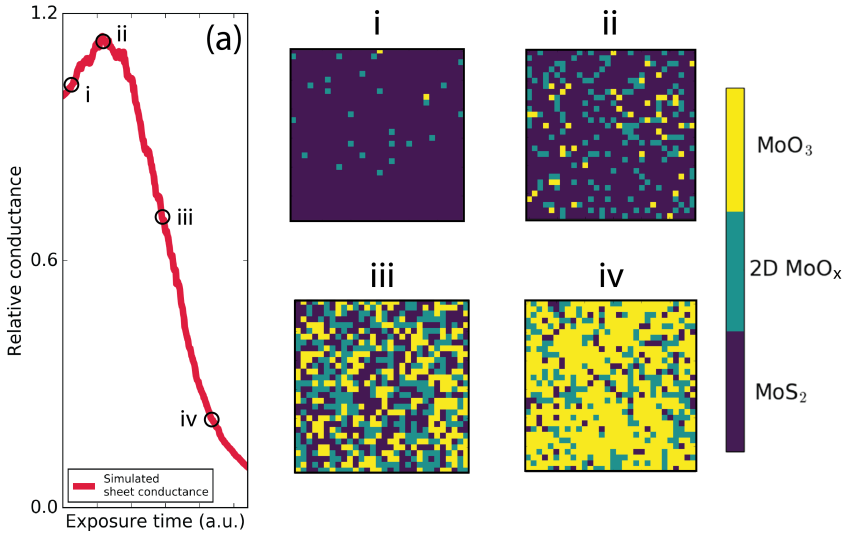

Figure 5.21: **Resistive network simulation of oxidised MoS_2. (a)** Simulated sheet conductance of MoS_2 during the progressive conversion from MoS_2 to 2D MoO_x to MoO_3. Exposure time, which is expressed in arbitrary units, charts the progress of the plasma-induced chemical oxidation as the simulation is iterated. One site undergoes transformation to the next phase during each iteration. Sites are not destroyed in this simulation, and the plasma treatment process finishes when all sites reach the insulating MoO_3 phase. The distributions of phases in the conductive network at four different iteration stages are shown throughout **(i)** to **(iv)**, where the subsequent phases are colour-mapped to the legend shown on the right. The lattice visualized in **(ii)** corresponds to the state of the network at the recovery time. The concentration of 2D MoO_x at that stage is $\approx 15\%$.

We remark that the nodal phase conversion is abrupt for any given iteration, but the emergent recovery phenomenon experiences a gentle crossover between regimes of different conductance. The relative concentration of conductors which exist in each phase is sampled throughout the simulation and visualised through the colour-mapped lattices in **Figs. 5.21(i-iv)**. The chart of phase concentrations across iteration steps is presented in **Appendix C**. The sheet conductance rises initially as the concentration of 2D-MoO_x increases. The conductance (and associated μ_{fe}) reaches a peak, just as observed in experimental results in **Fig. 5.2(e)**, and proceeds to drop off as conductors begin to transition to the insulating MoO_3, eventually reaching the insulating stage (for comparison with site destruction see **Appendix C**). The differing transition rates affect not only the size of the conductance peak but also the phase concentrations for which it occurs. The network map sampled at the conductance peak in **(ii)** shows that the spike in sheet conductance occurs with a relative network coverage of 2D MoO_x at approximately 15%. This differs from the experimentally-determined areal void coverage of $\approx 4\%$ at 6 s, but remains well under the site percolation threshold for a square lattice [279]. The difference

may originate in the underestimation of the area of oxide-born defective sites from ACSTEM images of bilayer flakes. Some voids can become filled with adventitious hydrocarbons over time and/or be obscured by a top molecular layer depending on sample orientation when transferring to a TEM grid. This resistive network model demonstrates qualitatively that a highly conductive intermediate oxide phase may serve to facilitate a recovery in the conductance and associated μ_{fe} of a MoS_2 sheet over increasing plasma exposure time.

5.7 Conclusions and outlook

In this chapter, we have demonstrated a simple and reliable method of tuning the electronic properties of few-layer MoS_2 FETs by using O_2:Ar (1:3) plasma. The apparent recovery of electrical conductivity is attributed to the temporary presence of a 2D phase of MoO_x, which is formed at some point during 4 and 6 s of plasma exposure. Its effect on the performance of the FET serves to provide a transient recovery of electrical conductivity and carrier mobility, despite the ongoing deformation of the MoS_2 lattice. We have also inferred the existence of this transient 2D oxide phase from evidence collected from advanced spectroscopic and microscopic studies and found that it is unstable under UHV conditions. We have unveiled the effect of the top-layer conversion by systematically studying the phenomenon on MoS_2 samples of different layer thickness. In addition, we have demonstrated with a robust simulation that the presence of a conductive phase on the surface of MoS_2 may induce a plasma dose-dependent recovery in the conductance of the material network. Our results are of importance to groups studying novel 2D TMDs and the fundamental properties of their low-dimensional oxides. In addition, the discovery of this phenomenon has broad implications for future van der Waals heterostructure devices and planar circuit architectures. Site-specific plasma modification of MoS_2 can be achieved by polymer protection, creating oxide-rich regions that could operate at negative gate biases and serve as charge storage nodes and/or input valves into further circuit components. We remark that a study published a few months after the work discussed in this chapter showed a similar doping type manipulation in MoS_2 using sub-stoichiometric MoO_3 grown on the surface by atomic layer deposition [280].

In the following two chapters, we will explore the effects of MoS_2 surface oxidation on the low-temperature charge transport of the material, as well as its optoelectronic performance under laser illumination at different powers.

Chapter 6

Low-temperature electrical conduction in plasma-treated bilayer MoS_2

In the previous chapter, we have seen how the nature of introduced surface impurities substantially affects the carrier mobility in layered 2D MoS_2. We have established that plasma treatment is an effective and versatile method of modifying the electronic properties of the material on a large scale for on-substrate and already-metallised flakes. However, to fully harness the potential applications of plasma treatment for 2D nano-devices, a comprehensive understanding of charge transport in these defective systems must be achieved, as atomic vacancies form readily during plasma treatment. In this chapter, we explore the low-temperature electrical behaviour of mechanically-exfoliated bilayer MoS_2 FETs which have undergone treatment with our O_2:Ar (1:3) plasma over controlled short-time intervals (2 s). We study the effect of the plasma treatment on the effective Schottky barrier height (Φ_b) between the MoS_2 and the electrode metal, and its effect on the injection current at different temperatures and gate biases. We find that the ES hopping mechanism governs the conduction behaviour in the pristine device. At low temperatures, below a critical temperature, $T^* \approx 181$ K, the defective plasma-treated MoS_2 system undergoes a crossover to a mixed thermally-activated regime.

6.1 Effects of plasma treatment on the temperature-graded FET characteristics

Bilayer MoS_2 devices were fabricated by mechanical exfoliation in a back-gated geometry on 285 nm-SiO_2/Si chips pre-cleaned with acetone and IPA. The thickness of the samples was confirmed by optical contrast microscopy. The device contacts were 5 nm-Ti/40 nm-Au on areas pre-defined by EBL, utilising PMMA as resist. Fabricated on-chip MoS_2 devices were exposed to the plasma in the same way as in the previous chapter. After each plasma exposure, the device was characterised electrically in a two-probe configuration in an *in-situ* SEM cryogenic stage environment, described in detail in **Chapter 4**, at a pressure of 10^{-4} mbar. *Imina miBot* manipulators once again served as source and drain terminals powered by an *Agilent B2912A* dual channel SMU, with a third manipulator used to back-gate the chip through the underlying carbon tape.

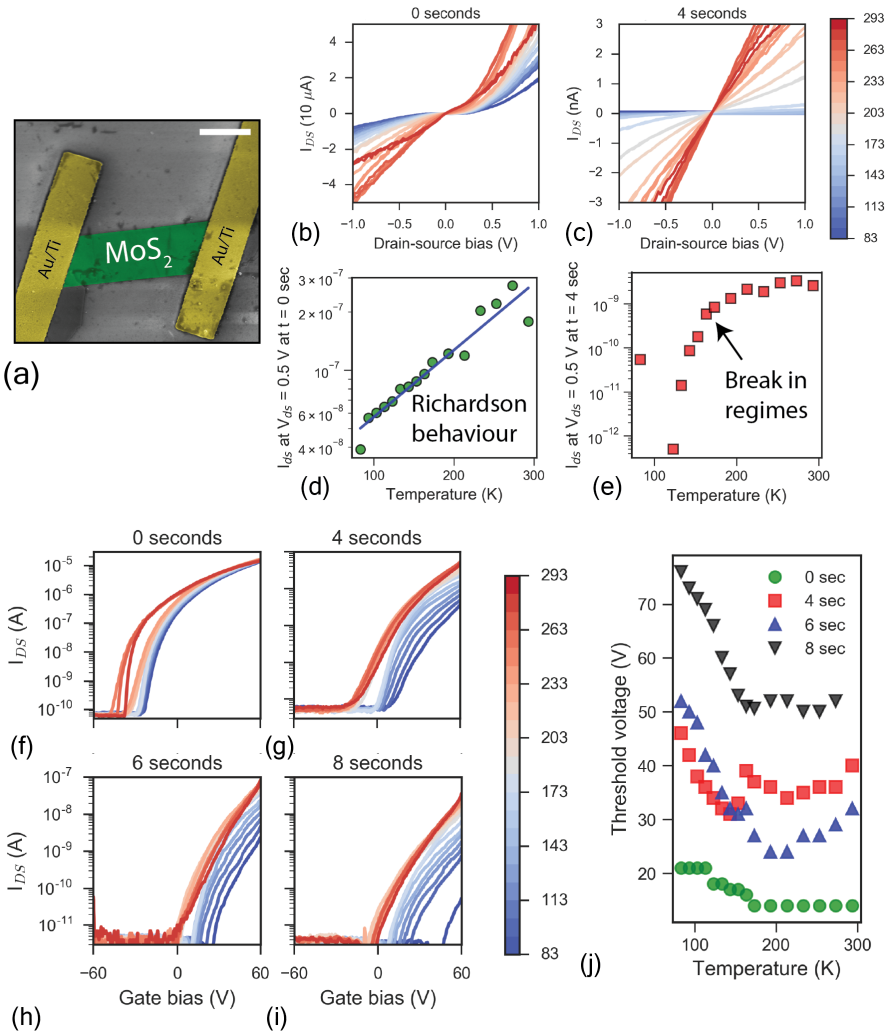

Figure 6.1: **(a)** False-coloured SEM micrograph of a contacted bilayer MoS_2 device. Scale bar is 1 μm. **(b)** *I-V* plots of the device before plasma treatment at different temperatures. **(c)** *I-V* plots of the device after 4 s of plasma exposure. Curves are coloured according to the temperature scale bar on the right (in Kelvin). Data taken at V_g = 0 V. **(d)** I_{ds} at V_{ds} = 0.5 V for the untreated sample plotted across the range of temperatures on a semi-log scale. A good linear fit (R^2 = 0.91) to the data is obtained, indicating the validity of the Richardson model. **(e)** Ids at V_{ds} = 0.5 V for the 4 s sample plotted across the range of temperatures on a semi-log scale. A visible break in the conductance regimes is observed around T = 181 K. **(f)–(i)** Gate curves taken at temperatures mapped to the colour scheme on the scale bar (in Kelvin) at plasma treatment times of 0, 4, 6, and 8 s, respectively. Data taken at V_{ds} = 1 V. **(j)** Threshold voltage shift with temperature at each of the exposure times.

The morphology of the device is shown in the false-coloured SEM micrograph in **Fig. 6.1(a)**. The *I-V* curves measured at zero gate bias shown in **Fig. 6.1(b)** and **Fig. 6.1(c)** demonstrate the effect of plasma treatment on the transport properties of the bilayer MoS_2 as a function of decreasing temperature. Before treatment, the device outputs tens of microamps of I_{ds} at V_{ds} = ± 1 V, even at temperatures

as low as 80 K. The semiconducting nature of the material is evident from the transport gap observed around the zero-bias point at low temperatures, and in the non-linearity of the sweeps. After 4 s of plasma treatment, the output current has dropped several orders of magnitude ($\sim$ nA) and subsequent treatments to 6 and 8 s drop the current levels to the noise floor of the instrument. Importantly, for the 4 s-treated sample, the output characteristics exhibit a clear linear relationship between the applied bias, V_{ds} and the output current, I_{ds}. **Figures 6.1(d-e)** plot the I_{ds} at V_{ds} = 0.5 V as a function of temperature on a semi-log scale for the 0 s and 4 s cases, respectively. This is done to check the validity of the assumption that current injection into the device is contact-limited and scales exponentially with temperature for a constant V_{ds} (Richardson model). A good linear fit (R^2 = 0.91) is obtained for the untreated device, especially at low temperature, suggesting that the Richardson model can be applied to the device before any plasma treatment. For the 4 s treated case, however, we do not observe a continuous linear relationship between current and temperature on the semi-log scale across the whole range of temperatures, suggesting that transport in the device deviates from the Richardson model at around $T^* \approx 181$ K. Thus, subsequent analysis on treated samples needs to be carried out considering that conduction may be bulk-limited due to the increased presence of traps in the MoS_2 channel.

The transfer characteristics of the same device were also tested at different temperatures and are presented in **Figs. 6.1(f-i)**. The untreated MoS_2 gate sweeps follow standard observations, with inversion onset in the negative gate bias region, and the same qualitative temperature dependence for the sweeps noted in both monolayers [37] and bilayers [281] of MoS_2. After plasma exposures, the current magnitude drops significantly as exposure time increases, while the threshold voltage, V_{th}, is seen drastically shifting to larger positive gate biases with decreasing temperature. This dependence is charted in **Fig. 6.1(j)** for all exposure times, indicating an almost linear increase in V_{th} after each exposure time below $\sim$ 155 K. This scaling is in line with the approximate dependence often utilised for MOSFETs [282], and may originate in the temperature-dependent charge carrier density variation in the 2D MoS_2 channel. Around 200 K, a clear gap, ΔV_{th}, develops in the gate sweeps, separating the blue (low temperatures) curves from the red (high temperatures) ones along the gate bias axis. At the same time, the treated devices are seen to deviate from standard MoS_2 FET transfer characteristics. The different regions of the transfer curve cannot be now easily distinguished. With increasing plasma treatment time, the shape of the curves indicates that the channel cannot be strongly inverted in the

tested gate bias range. This is especially evident at low temperatures. As this shift is also seen in the pristine sample, we do not attribute the origin of ΔV_{th} to the plasma exposure process. It is, however, exacerbated with continuing plasma treatment and correlates with the increasing concentration of surface defects. The exact nature of this ΔV_{th} observation in layered 2D semiconductors necessitates further investigation in the future; though it is known that the physical origin of V_{th} is closely linked to the concentration of defects on the surface of 2D FETs [71].

6.2 Impact of plasma-created defects on the temperature-dependent electrical conductance of MoS_2

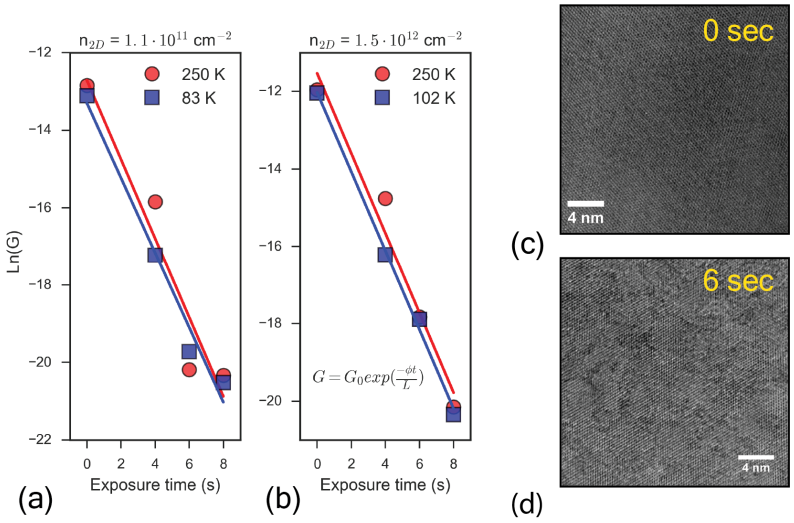

Figure 6.2: **(a)** Conductance, G, plotted on a semi-log plot as a function of plasma treatment time at a carrier density of the order of 10^{11} cm^{-2}. The solid lines are linear fits at high (red) and low (blue) temperatures. **(b)** Similar plot from data extracted at a carrier density of the order of 10^{12} cm^{-2}. Both sets of data fit the exponential plasma time decay model (equation included on the plot), regardless of carrier density. **(c)** HRTEM image of a MoS_2 flake before plasma treatment. **(d)** HRTEM image of a MoS_2 flake following plasma treatment of 6 s. Noticeable amorphisation occurs on the surface of the material due to the formation of molybdenum oxides.

We track the conductance drop in the sample with increasing plasma exposure time at different carrier densities in the high and low temperature regimes in **Figs. 6.2(a-b)**. *Note*: since this is a bilayer sample, we do not expect to see the $\sigma(t)$ recovery effect, as discussed in the layer dependence section in the previous chapter. From the semi-logarithmic conductance vs time plots, we find good linear fits confirming an exponential drop in the conductance with increasing plasma exposure time. The layer number-normalised exponential drop in electron mobility over time, $\mu(t)$, in oxygen plasma-treated MoS_2 has previously been reported to scale as [125]:

$$\frac{\mu(t)}{L} \propto \exp\left(\frac{\phi t}{L}\right) \tag{6.1}$$

where L is the MoS_2 layer number, $\phi = \mu'/\mu$ and μ' is the exposure-time derivative of the mobility. Following this convention, we can extract the plasma-time rate of change of the conductance, G, in our bilayer sample, with $\phi_G = 2.02\ s^{-1}$. The contribution of MoO_3 species formed by the oxygen-containing plasma may lead to the formation of an effective semiconducting medium in the FET channel. This, in turn, may give rise to the exponential dependence of current tunnelling through the newly-formed heterostructure-like interface [125, 174]. Let us note that at this rate of plasma exposure, the bilayer MoS_2 device becomes substantially damaged after 6 s of treatment, as μ_{fe} values at $V_g = 0$ V drop below 1 $cm^2\ V^{-1}\ s^{-1}$ and I_{ds} at $V_g = 0$ V is below the nA range. **Figs. 6.2(c-d)** are HRTEM images of the same few-layer MoS_2 sample before and after 6 s of plasma treatment, respectively. Plasma-induced damage to the surface of MoS_2 is evident from the contrast change after 6 s of treatment. The amorphous oxide which forms on the surface through the sulfur-replacing chemical reaction creates severe defects in the material, as established in the previous chapter. These can then act as sources of short-range scattering which reduce the device conductance [124, 125].

6.3 Plasma-mediated modulation of device emission current and the Schottky barrier height

We go on to analyse the temperature-dependent emission current in the bilayer MoS_2 system as it undergoes modification by the O_2:Ar plasma. As discussed in the background chapter, charge injection from the metal electrode into the 2D semiconductor (at moderate doping levels) is mostly governed by thermionic emission over the Schottky barrier at sufficient temperatures. Furthermore, Fermi level pinning occurs near the bottom of the conduction band of the MoS_2, independent of the metal work function [91]. When considering current injection for this 2D system, the well-known Richardson equation is modified as follows:

$$I_{ds} = A^*_{2D} T^{3/2} \exp\left(\frac{q\Phi_b}{k_B T}\right)\left[1 - \exp\left(\frac{qV_{ds}}{k_B T}\right)\right] \tag{6.2}$$

where A^*_{2D} is the Richardson constant for a 2D system, T is the temperature, q is the Coulombic charge, k_B is the Boltzmann constant, Φ_b is the effective barrier height and V_{ds} is the drain–source bias. We note that effective Φ_b can thus be extracted

from the slope of the $\ln[I_{ds}/T^{3/2}]$ versus $1000/T$ curve. A series of such plots is presented in **Figs. 6.3(a–d)** as the device progresses through increasing plasma treatment. The data are colour-mapped to the scale bar above to denote the gate bias at which the current was extracted.

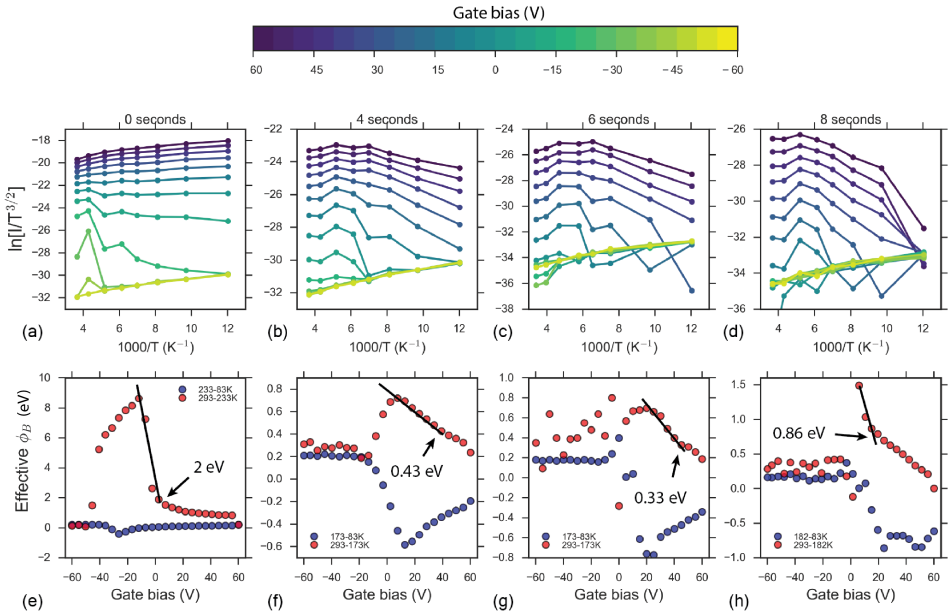

Figure 6.3: **(a)**–**(d)** Richardson plots for the MoS_2 device as it progresses through plasma treatment. The curves are colour-mapped to the extraction gate bias scale on the colour bar above. V_{ds} was set at 1 V. **(e)**–**(h)** Plots of the effective Φ_b extracted from the corresponding above Richardson plots across the whole gate bias range. The values were obtained in the low- and high-temperature ranges shown on each plot. The end of the linear dependencies on each respective plot marks the Schottky barrier height extracted at the flat-band condition, $V_g = V_{fb}$.

The 0 s data fit well to the linear model below 233 K, while at higher temperatures and gate biases between ~ - 50 V and ~ 0 V, a different slope is extracted in the regime corresponding to thermionic emission only. When the device is exposed to the plasma for 4 s and the amorphous oxidised regions start to form on the surface, a significant break in the temperature dependencies occurs beyond ~ 150 K at higher gate biases. In this region, both the tunnelling and thermionic components begin to contribute to transport between the metal and the effective semiconducting medium of oxidised MoS_2. Accompanied by decreased emission current even at higher gate biases, this break in the trend persists in the same temperature range after 6 and 8 s. As discussed in the previous section, the applicability of the Richardson model hence breaks down below $T^* \approx 181$ K, where the data in **Figs. 6.3(b–d)** begin to attain a negative slope at low temperatures (at the same gate bias), whereas it remained positive for the whole temperature range in the untreated sample in **Fig. 6.3(a)**.

This is also the variable range hopping region usually observed in pristine MoS_2 [283], where conductance is limited by the activation energy between localised trap states at low temperatures. We note that even in pristine samples, the enhanced Coulomb scattering originating from metal-induced interface traps throttles electron mobilities in MoS_2 beneath the metal contact relative to the channel regions [284], reducing the transport to a mixed contact-bulk model via gap states that exhibits different temperature scaling from study to study, depending on sample quality and fabrication method [39, 194]. Thus, effective barrier height values extracted above the flatband voltage but below $T^* \approx 181$ K ought to be accurate at low drain source biases even in our highly defective system (we note that for the treated samples, the barrier heights are extracted below 182 K and at V_{ds} = 1 V), while conduction mechanism scaling in the bulk above V_{fb} should also remain accurate in what is ultimately a limited two-probe system.

Figures 6.3(e–h) present effective barrier heights at each gate bias, derived in the high (red) and low (blue) temperature regimes as the reaction with plasma progress. Following the convention of Kim *et al.* [91], we can extract the true barrier heights at the flat-band voltage (V_{fb}) for each plasma time. At high temperatures, one can accurately extract the true Φ_b by considering the end of the linear region of the Φ_b dependence on gate bias. For biases below the flat-band voltage, the contribution of tunnelling to the injection current should be negligible, ensuring only thermionic emission over the true barrier height. At low temperatures, the tunnelling component will be more significant, and so the true barrier height values cannot be readily extracted for a semiconductor with a significant band gap such as MoS_2 [91, 285].

With increasing plasma exposure time, a significant shift of V_{fb} occurs, naturally correlating with the positive V_{th} shift recorded in the gate sweeps in **Figs. 6.1(f-i)**. At the same time, Schottky barrier height lowering is experienced by the MoS_2/Ti–Au interface with increasing plasma treatment. Altering of the barrier for MoS_2/metal interfaces has previously been performed with pure O_2 plasma, allowing for additional hole injection by effective de-pinning of the Fermi level [170]. We do not observe ambipolar FET behaviour in our devices across the tested sweep range of ± 60 V, indicating that the plasma-induced formation of sulfur vacancies is the dominant doping mechanism, and a much larger negative back-gate voltage would be required to enter the hole branch on the transfer curves.

6.4 Evolution of the temperature-dependent conduction mechanisms with increasing plasma exposure time

We investigate the temperature-dependent conductance mechanism for electrons in defective plasma-treated MoS_2 in **Fig. 6.4**. By using the Zabrodskii approach mentioned in **Chapter 2**, we can gauge the scaling of the material conductance with temperature from plots of $\ln(W)$ vs $\ln(T)$. These plots are presented for the various plasma treatment times in **Fig. 6.4**. We note that negative slope values in these plots indicate semiconducting behaviour for the sample after all treatment times. A good linear fit is found for the untreated sample with a slope indicating a conductance exponent of $a = 0.48$, i.e. conductance scales as $T^{-0.48}$. Mott-like VRH [37, 41], which scales as $T^{-1/3}$, has been considered the main conductance mechanism at low temperatures in semiconducting MoS_2. However, mixed transport regimes [40, 194, 286] have been reported recently in polymorphic, defective, and encapsulated layered TMDs, respectively; at various temperatures.

The dependence we find for our mechanically-exfoliated bilayer is in line with ES hopping ($T^{-1/2}$) which has recently been observed in polymorphic low-dimensional MoS_2 [39]. This may be indicative of a highly V_S-rich sample, where electron–electron interactions reduce the density of states near the Fermi level according to the ES model [287].

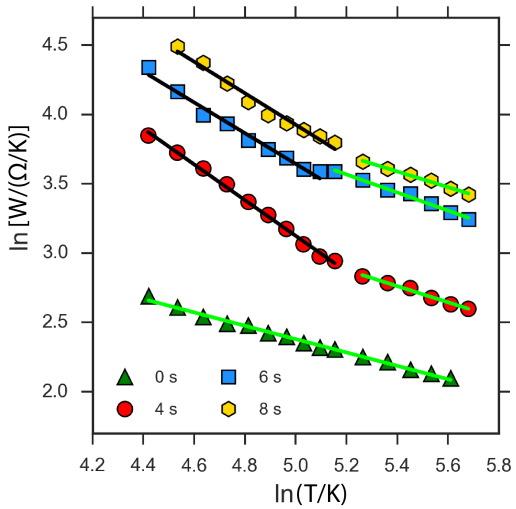

Figure 6.4: Plot of $\ln(W)$ as a function of $\ln(T)$, used to extract the conduction mechanism exponent a. The coloured points are the experimental data for each exposure time, the green lines are linear fits to the data close to the ES regime, black lines are fits close to the T^{-1} regime. The extracted slopes are also tabulated in **Table 6.1**.

As the sample is exposed to the plasma, a change in the conduction regime is

observed, where the critical exponent a is now > 0.5 at high temperatures (see **Table 6.1**). This indicates a mixing of the ES and NNH regimes. Below a critical temperature, $T^* \approx 181$ K, the conduction mechanisms are fitted well with $T^{-1.3}$, $T^{-1.1}$, and $T^{-1.1}$ dependencies for 4, 6, and 8 s, respectively. This scaling at low temperatures follows a quasi-Arrhenius relation, with an increased activation energy likely due to the presence of plasma-generated defective regions. An electronic phase transition [32] due to correlation interactions is expected to occur at high carrier densities ($n_{2D} \sim 10^{13}$ cm^{-2}), as we have discussed in the background chapter. We were not able to reach this order of n_{2D} in this experiment, as a top gate could not be fabricated without losing access to the sample surface. We note here that although the conductivities were extracted at the same n_{2D} past the flat-band voltage, the break in the conductance regimes and the change in the Schottky barrier height could not be decoupled for this analysis in the two-probe measurement scheme. The values of the exponent a for each temperature regime and plasma time are summarised in **Table 6.1**. This type of conduction mechanism shift has previously been studied in hydrogenated amorphous Si films, where an inverse dependence to our one was found for the conduction regime reversal [45].

Plasma exposure time (s)	a **from fit above** T^*	a **from fit below** T^*
0	0.48	n/a
4	0.58	1.3
6	0.65	1.1
8	0.57	1.1

Table 6.1: **Summary of extracted a exponents in each temperature regime for every plasma treatment time.** n/a; not applicable.

We note that our case cannot be treated as a simple amorphisation of the whole material, as the reaction with the plasma proceeds from the surface only. The underlying MoS_2 layer in the bilayer system may not inherit as many defect centres, preserving a degree of crystallinity for the device and contributing to the unusual mixed transport regime. From *Mathiessen's rule*, it is well-known that the residual resistivity in semiconducting MoS_2 at low temperatures is due to the impurity scattering term, μ_{imp}^{-1}, which comprises both the long-range and short-range Coulombic scattering components [36]. In encapsulated and pristine MoS_2 FETs, this has been shown to dominate carrier transport below 100 K [281, 32, 36]. In the presently-discussed case of plasma-modified 2D MoS_2, the impurity concentration may be sufficient to allow for the dominant contribution of disorder-born scattering at temperatures as

high as 181 K. This may arise from the increased presence of amorphous molybdenum oxides on the surface of the flake, as well as V_S traps originating from plasma-etched regions, which we observed in the previous chapter [134]. These mid-gap trap states reduce I_{ds} at zero gate bias, and shift V_{th} to increasingly positive biases as plasma exposure progresses in time. A larger gate voltage is required to tune the Fermi level past the trap states and into the conduction band. This effective band gap increase has also been previously observed with PL measurements in rapidly plasma-oxidised MoS_2 [156, 257].

6.5 Conclusions and outlook

The effects of increasing oxygen:argon plasma treatment on bilayer MoS_2 were studied as a function of temperature. The ES hopping regime of the untreated sample was seen to transition to a mixed ES/thermally-activated regime at high temperatures upon plasma treatment. Another crossover was observed in the defective system, below 181 K, to a strongly short-range Arrhenius regime. We attribute the crossover at such a high temperature to a critical defect density achieved by the continuing plasma treatment. Investigation of the temperature-dependent emission current determined a significant lowering of the effective Schottky barrier height for the bilayer MoS_2 FET with plasma treatment, while preserving the unipolar nature of the transistor. Increased understanding of transport properties in defective 2D materials is crucial to the success of future electronic devices fabricated using plasma treatment. Further studies down to liquid He temperatures therefore ought to inform future research on this topic in the fields of solid-state physics and 2D nano-devices.

Chapter 7

Photoresponsivity enhancement in monolayer MoS_2 by rapid O_2:Ar plasma treatment

In this chapter, we discuss the observation of the up to ten-fold enhancement of the photoresponsivity of monolayer MoS_2 by treatment with our O_2:Ar (1:3) plasma. We characterise the surface of plasma-exposed CVD MoS_2 by Raman and PL mapping, and discuss the role of MoO_x in improving the photocurrent generation in our devices. At the highest tested laser power of 0.1 mW, we find ten-fold enhancements to both I_{ds} and μ_{fe} at the used illumination wavelength of 488 nm. We suggest that the improvement of electrical performance is due to the surface presence of MoO_x resulting from the chemical conversion of MoS_2 by the oxygen-containing plasma. Our results highlight the beneficial role of plasma treatment as a fast and convenient way of improving the properties of synthetic 2D MoS_2 devices for future consideration in optoelectronics research.

As discussed in detail previously, MoS_2 is a semiconductor with a direct band gap of $\sim$ 1.8 eV in the single-layer limit, which allows monolayer MoS_2 FETs to achieve high on/off ratios (10^7-10^9), making them attractive candidates for switching components in future electronics. Recently, optoelectronic devices fabricated from MoS_2 have also received notable attention [288, 289]. MoS_2 phototransistors are easy to fabricate, respond to a wide range of wavelengths [288, 290] and exhibit fast DC photoresponses [291, 292]. In addition, their photoresponsivity can be tuned by various methods, such as back-gating [16, 293], strain engineering [294], layer decoupling [295] and evaporation of sub-stoichiometric molybdenum oxide over-layers [296]. Surface sensitisation of monolayer MoS_2 FETs has also yielded significant enhancements of the measured photocurrent in the case of quantum dots [297, 298, 299], organic molecules [300, 301, 302], and metal nanostructures [303, 304]. However, these methods often involve additional preparation steps in order to fabricate the sensitising species for depositing on the MoS_2 device. Moreover, the surface-deposited dopants may not be robust to mechanical stressing or further material modification without losing their favourable properties.

Plasma functionalisation, in turn, presents a fast and facile way to alter the crystal structure of on-chip layered materials such as MoS_2. It facilitates large-scale, multi-

sample, and rapid tuning of the optoelectronic performance of FETs based on layered semiconductors. In particular, we have already seen in the previous chapters that oxygen-containing plasmas tend to form sub-stoichiometric molybdenum oxides on the surface of MoS_2 [124, 170, 156]. These oxide centres can then act as dopants that alter the charge concentration in the modified MoS_2 transistor channel [174, 134, 305], and ultimately govern the electron conduction behaviour of the newly formed oxide/MoS_2 heterostructure [125]. In this chapter, we demonstrate the enhancement of the photoresponsivity of CVD-grown monolayer MoS_2 by the same O_2:Ar (1:3) plasma treatment. The photoresponsivity is improved ten-fold in back-gated devices only after 2 s of exposure to the plasma (hence *rapid* treatment). At the same time, μ_{fe} of the device under illumination improves by over one order of magnitude. We carry out spectroscopic mapping to characterise the sample after plasma exposure and attribute the observed photoresponse to the suppressed charge recombination mediated by the surface-bound molybdenum oxides.

7.1 The effect of illumination on the output characteristics of plasma-modified devices

MoS_2 samples were synthesised on 285 nm SiO_2/Si substrates by Conor Cullen using the CVD method previously reported [207] and described in **Chapter 3**. The flake thickness was confirmed by optical microscopy and Raman spectroscopy. Standard EBL was carried out to fabricate the FET devices using PMMA resist and development in methyl isobutyl ketone:isopropyl alcohol (MIBK:IPA) (1:3). This was followed by metallisation with 10 nm-Ti/40 nm-Au contacts and lift-off in acetone overnight. Plasma treatment was once again carried out in the same *Fischione Instruments 1020* cleaner for 2 s, utilising O_2:Ar (1:3) gas at a pressure of $\sim$ 5 mbar. The electrical testing was performed at room temperature in a two-probe configuration (*Imina miBot*) using the (*Agilent B2912A*) SMU in the ambient. The devices were back-gated through the heavily p-doped Si substrate underneath the 285 nm SiO_2 over-layer. A 488 nm laser was used for irradiation (Photonics Lab in CRANN, with the assistance of Dr. Jing-Jing Wang and Gen Li). Its power density was tuned at five different levels and controlled to ensure no fluctuation throughout the experiment. The laser was directed through a condenser lens (20×, numerical aperture (NA) $\approx$ 0.4), and the spot size was $\approx$ 1.5 μm. Raman and PL spectra were acquired using the *WITec Alpha 300R* system in the Duesberg lab (λ = 532 nm). A low laser power (< 100 μW) was used during mapping to minimise any laser-induced damage or unwanted heating of the sample.

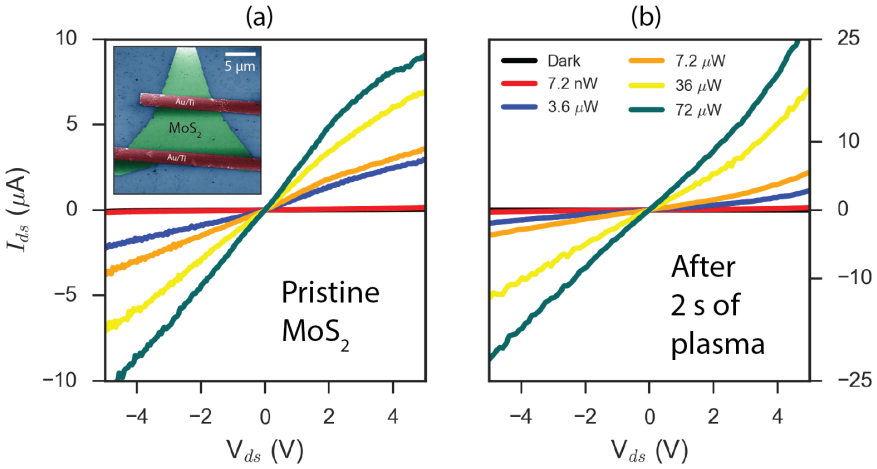

Figure 7.1: **(a)** Output curves of the untreated device, demonstrating a good ohmic contact between the material and the metal electrode. The output current, I_{ds}, increases with increasing laser power under illumination. Inset: a false-colour helium ion micrograph of a typical contacted monolayer CVD MoS_2 phototransistor device. The blue area is the SiO_2 substrate. **(b)** Post-plasma treatment *I-V* curves show a similar trend with increasing laser power. The generated photocurrent at high laser powers has increased by up to 3 times at the same applied voltage after 2 s of plasma exposure. We note that no gate bias was applied. The colour legend applies to both **(a)** and **(b)**. Data acquired with the assistance of Gen Li and Dr. Jing-Jing Wang.

The inset of **Fig. 7.1(a)** is a false-colour helium ion micrograph of a typical contacted device. The contacts in this study were always deposited in a parallel geometry, as visible in the image. The transistor channel length was over 5 μm to confine the laser irradiation solely to the MoS_2 channel region. We collected the output and transfer characteristics of the device under 5 different illumination powers. As the laser spot avoided the Au electrodes during illumination, we assume that all of the measured photo-generated current originated from the MoS_2 semiconducting channel. **Figure 7.1(a)** shows the output characteristics of the device under laser illumination before any plasma treatment. Prior to any exposure to the plasma, the low-bias *I-V* response of the MoS_2 FET shows a well-behaved linear increase with applied bias for both voltage polarities, indicating good ohmic contacts to the semiconductor. Upon successive irradiations with rising laser power, the photocurrent increases, which is typical for semiconducting monolayer MoS_2 devices [288, 291, 16, 306, 307, 308]. The output current reaches nearly 10 μA at V_{ds} = ± 5 V at the highest tested laser power of 72 μW. **Figure 7.1(b)** tracks the *I-V* curves after 2 s of exposure to the plasma. We see that the current increases to nearly 25 μA at the highest illumination power, compared with the untreated sample at the same applied V_{ds}. This indicates that dopants introduced by the plasma treatment to the MoS_2

surface mediate an enhanced charge carrier photo-generation response in the device. However, we found that longer plasma treatments (> 2 s) lead to a significant decay of electrical performance in these monolayer CVD devices and do not enhance the photoresponsivity at all [309]. Thus, we will concern ourselves only with the meaningful 2 s exposures in this chapter.

7.2 Effects on the transfer characteristics and μ_{fe}

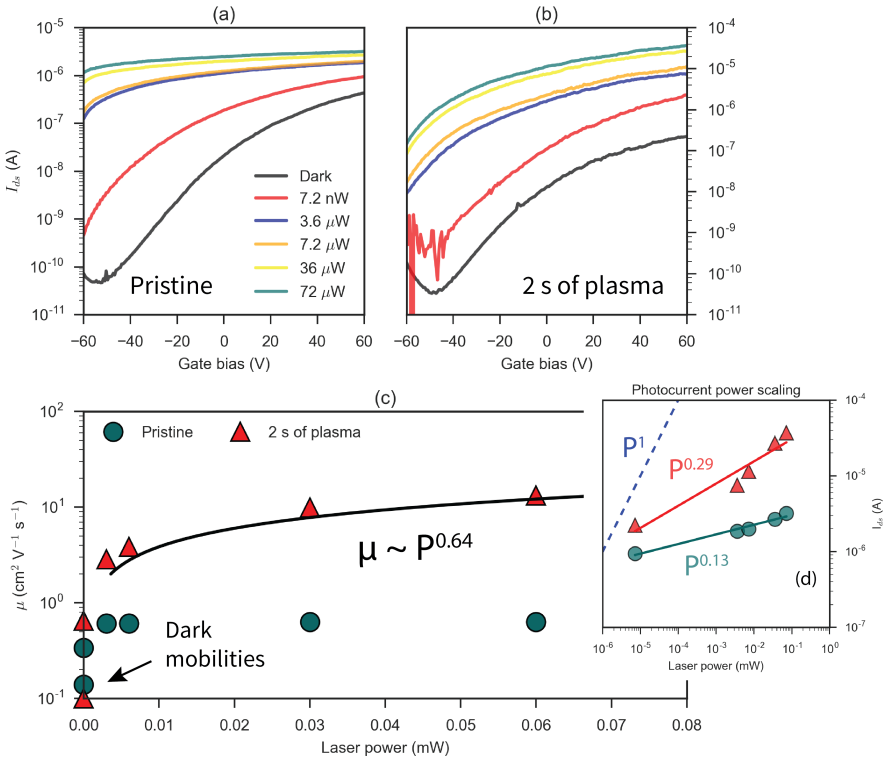

Figure 7.2: **(a)** Transfer characteristics of the untreated device, demonstrating the standard n-type FET behaviour and increase in carrier density in the channel at higher laser powers. **(b)** In the post-treatment gate curves, the level of current has increased by one order of magnitude at all illumination laser powers. The colour legend applies to both **(a)** and **(b)**. Both data sets taken at V_{ds} = 1 V. **(c)** Mobility comparison before and after plasma treatment as a function of laser power. The solid black line is a fit to the mobility scaling of the treated sample above 10^{-3} mW. **(d)** Generated photocurrent scaling with applied laser power (V_{ds} = 1 V). The blue line shows idealised linear scaling, red and green are the raw data points with fits. Data acquired with the assistance of Gen Li and Dr. Jing-Jing Wang.

Figure 7.2(a) shows the transfer curves for the same sample before any plasma treatment. Our as-grown devices perform as standard n-type FETs with a μ_{fe} of 0.13 cm^2 V^{-1} s^{-1} under no illumination, extracted in the linear region of the transfer curve and at V_{ds} = 1 V. Upon successive laser irradiations, we observe a photo-gating

effect, whereby the V_{th} of the transistor shifts to negative gate biases by more than Δ10 V due to increased electron doping. This has previously been observed in ultra-thin TMD FETs and is attributed to the interaction of photo-generated carriers with charge traps in the transistor channel [308, 310]. At the highest incident power, the FET channel is effectively still open at V_g = - 60 V, where the output current stays firmly above 10^{-7} A and leads to a large reduction in the on/off ratio of our device.

Figure 7.2(b) presents the gate curves after plasma treatment. The observed level of I_{ds} in the dark transfer curve drops two-fold when evaluated at V_g = 60 V. Meanwhile, V_{th} is seen to shift to more positive gate biases by $\sim$ Δ5 V. This shift indicates oxygen-related p-type doping in the material, consistent with previous works on oxygen-passivated MoS_2 [134, 175, 70]. In addition, the MoS_2 now possesses a weak ambipolar response, indicating hole-branch conduction caused by the likely presence of plasma-created oxides [270, 269]. After 2 s of plasma treatment, the output current in the saturation region of the gate curve improves by one order of magnitude under all illumination powers (note the scale on the *y*-axis). **Figure 7.2(c)**, in turn, tracks the MoS_2 channel μ_{fe} before and after the chemical reaction with the plasma. With no laser illumination, the mobility is seen to decrease slightly after 2 s, which we have explored in the previous chapters. After 2 s of exposure, the carrier mobility increases over ten-fold in illuminated gate curves, as the laser power is turned up. We find no clear relationship between the mobility and the laser power for the untreated sample. However, we obtain a good power law fit to the mobility scaling as $\mu_{fe} \propto P^{0.64}$ above laser powers of 10^{-3} mW. The dependence of the photocurrent on the laser power is sub-linear, although the power law response is enhanced by the plasma treatment from $\mu_{fe} \propto P^{0.13}$ for the unexposed sample, to $\mu_{fe} \propto P^{0.29}$ for the treated sample (**Fig. 7.2(d)**).

7.3 Photoresponsivity and temporal characteristics after plasma treatment

We plot the DC photoresponsivity, R_{ph}, for the pristine and treated cases at different gate biases as a function of irradiation power in **Figs. 7.3(a-b)**. R_{ph} is the current generated in the device (I_{ph}) per unit of input laser power (P_{in}) in the photo-active region [308], and is a crucial parameter that quantifies the sensitivity of photodetectors:

$$R_{ph} = \frac{I_{ph}}{P_{in}} \tag{7.1}$$

We obtain good linear fits of R_{ph} as a function of power, P, across the whole gate bias range, before and after plasma treatment. The negative slope in the log-log plot indicates the saturation of trap states in the material with increasing incident optical power [288, 290, 302]. In **Fig. 7.3(a)**, we see the 0 V and 60 V gate bias trends exhibiting similar levels of R_{ph}, especially at higher laser powers. Upon plasma treatment, in **Fig. 7.3(b)**, we observe an enhancement of R_{ph} for all tested gate biases and a notable separation of the responsivity as a function of V_g. As V_g is increased, the device becomes more responsive to laser illumination. The slope of this relationship depends on the charge trapping rate in the MoS_2 FET channel [307, 311]. Our results suggest that the presence of plasma-created oxides on the surface inhibits photo-generated pair recombination via defect sites. When compared at V_g = 60 V where the FET moves into depletion, i.e. the majority carrier concentration in MoS_2 induced by gating begins to approach that of the photo-generated carrier density [312], the dependence on laser power is stronger for the treated sample. This also serves as a measure of the photo-gating effect seen in the power-graded transfer curves (V_{ds}= 1 V) in **Fig. 7.2(a-b)**. An increased response after plasma treatment is thus a direct consequence of the additional charge present in the device, as demonstrated by the higher current levels in the gate curves.

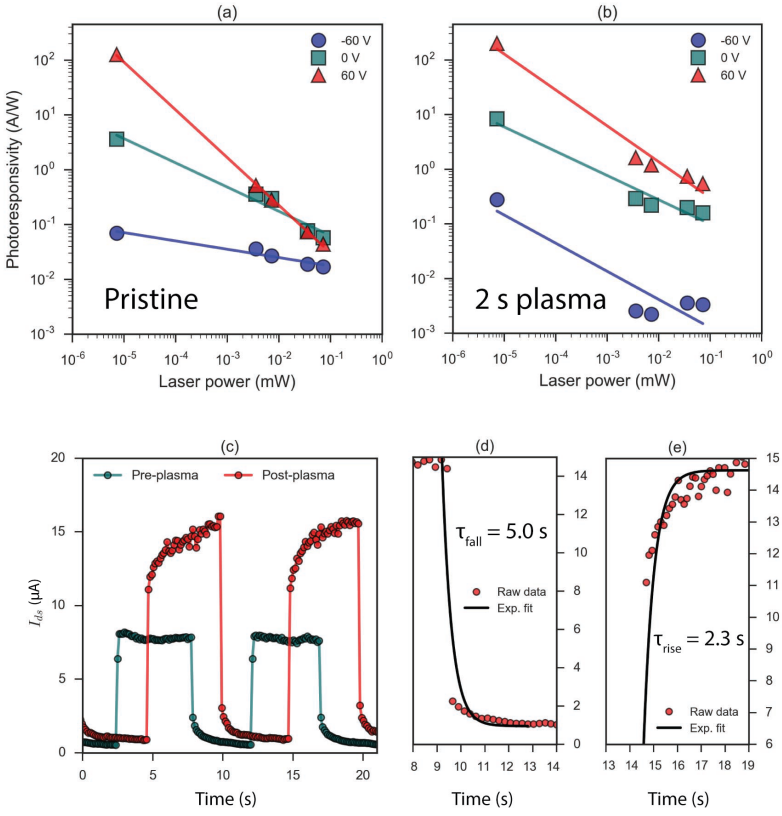

Figure 7.3: **(a)** R_{ph} trends for the untreated MoS_2 sample. **(b)** Increased responsivity of the MoS_2 phototransistor after 2 s of O_2:Ar plasma treatment. **(c)** Comparison of the temporal photocurrent response over laser irradiation cycles lasting 5 s. **(d)** Exponential fit of the fall component of the photoresponse for the treated device. **(e)** Exponential fit of the rise component from the next cycle. Data acquired with the assistance of Gen Li and Dr. Jing-Jing Wang.

In addition, a curious phenomenon seems to occur where a single incident photon ends up generating more than one charge carrier, i.e.. looking at **Figs. 7.3(a-b)**, it seems that we are getting $\sim 1\ \mu$A of current when the laser power is 10^{-8} W at V_g = 60 V. A single photon of this wavelength has an energy of $4.07 \cdot 10^{-19}$ J. This power of the laser hence produces $2.46 \cdot 10^{10}$ photons per second. A single charge carrier has a charge of $1.6 \cdot 10^{-19}$ C. Thus, in order to produce a current of 1 μA, we need to have $6.25 \cdot 10^{13}$ charge carriers flowing per second. Thus, ostensibly, we are producing 254 carriers for every photon that is put into the system. This is the case in both pristine and plasma-exposed MoS_2. This apparent incongruity is known as the so-called photodetector *gain*, G, and is formalised as:

$$G = \frac{\tau}{\tau_e} \tag{7.2}$$

where τ is the time taken for electrons and holes to recombine, while τ_e is the electron transit time across the device [313]. In short; if electrons travel faster than holes in a semiconductor, they will transit outside of the sample into the contact faster than the holes. To conserve charge, the external circuit will inject charge on the opposite side into the device. These quickly-moving electrons can effectively lap the transit time of the heavy hole before recombination even occurs. G quantifies this lapping outcome, ultimately delivering a charge to the circuit equal to:

$$q = Ge > e \tag{7.3}$$

where e is the electronic charge, leading to the gain observed in the photocurrent response. As this effect is entirely tunable by the gate field, we have to assume that it is also sensitive to the fluctuation of the carrier mobility, which is inaccurately probed in this two-contact system. As the current density is the product of available charge carriers and their mobility, we cannot decouple the two together in this sort of device; as is also evidenced in other works on 2D photodetectors which are reporting these superlative photocurrents.

The temporal response of the device pre- and post-plasma treatment is charted in **Fig. 7.3(c)**. The photocurrent is seen to improve two-fold for the tested device when the laser irradiation is modulated through 5 s on/off cycles at a power of 36 μW and V_{ds} = 5 V. The post-sensitisation fall (τ_{fall}) and rise (τ_{rise}) times are extracted from single exponential fits in **Figs. 7.3(d) and 7.3(e)**, respectively. The time-resolved photoresponses compare favourably with the evaporated MoO_x overlayer report [296], where our rise time at a much lower irradiation power is 35% shorter. However, the response time of the photo-FET has been sacrificed to achieve favourable responsivity. This is a well-known issue in sensitised MoS_2 photo-FETs arising from carrier trapping [314, 315], and needs to be addressed in future research on these devices.

7.4 Spectroscopic characterisation of the surface and proposed R_{ph} enhancement mechanism

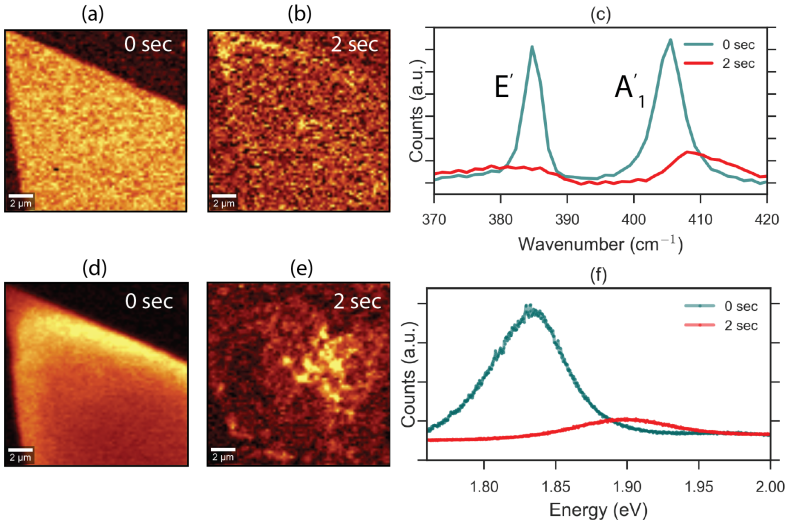

Figure 7.4: Raman maps of a monolayer flake **(a)** before and **(b)** after 2 s of plasma treatment, filtered for the in-plane mode at 385 cm^{-1}. **(c)** Raman spectra averaged from the flake area. PL maps of the same flake **(d)** before and **(e)** after treatment, tracking the direct *A* exciton emission. **(e)** Averaged PL spectra from the same flake area. Data acquired by Conor Cullen.

Spectroscopic mapping of the samples allows for a closer inspection of the chemical state of the CVD MoS_2 surface pre- and post-plasma treatment. **Figures 7.4(a-b)** show the spatially-resolved Raman maps of the material corresponding to the in-plane vibrational mode at 385 cm^{-1}. We notice a drastic drop in the intensity of the signal at this frequency, indicating a change in the MoS_2 lattice which alters the Raman-active modes in the sample. The flake-averaged spectra are presented in **Fig. 7.4(c)**, demonstrating the quenching effect of plasma treatment on the monolayer CVD MoS_2 Raman peaks. From the spectral component fits, the monolayer nature of the sample is confirmed with a wave number separation of 20.5 cm^{-1} between the A'_1 and E′ peaks [263]. Upon plasma treatment, the intensity of both Raman modes is severely reduced after 2 s of exposure, while the peak position also shifts and the FWHM increases. Both the downshift of the E′ peak and upshift of the A'_1 peak are consistent with reports on molybdenum oxide formation on MoS_2, as is the asymmetric broadening of both peaks [156, 174, 134]. PL maps of the neutral *A* exciton emission (1.84 eV) of the same flake are presented before and after 2 s of plasma treatment in **Figs. 7.4(d-e)**. Accompanying spectra averaged across the whole sample are shown in **Fig. 7.4(f)**. We observe significant quenching of direct excitonic recombination in the sample after the plasma introduces the oxide

species on the surface, as evidenced in microscopic data from previous chapters. The emission is also largely blue-shifted to higher energies by ~ 0.1 eV. These observations are also in line with previous studies of oxidised MoS_2, where the monolayer PL emission intensity is reduced and blue-shifts due to the presence of sub-stoichiometric oxides on the surface as a function of exposure time [134, 264].

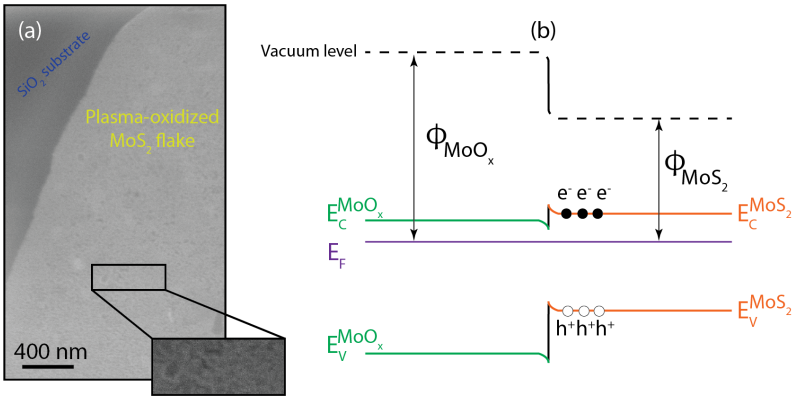

Figure 7.5: **(a)** SEM micrograph of plasma-treated MoS_2 showing dark contrast areas of MoO_x. The inset shows a magnified region with the contrast increased, highlighting the presence of the dark regions. **(b)** Representative band diagram of the equilibrated MoS_2/MoO_x heterojunction, visualising the trapping of photo-generated holes at the interface. E_C; bottom of the conduction band, E_V; top of the valence band, E_F; Fermi level, Φ; work function, e^-; electrons, h^+; holes.

We suggest that the observed photoresponsivity improvement results from carrier trapping at the lateral MoS_2/MoO_x heterojunction interface. The electron affinity and band gap of monolayer MoS_2 are ~ 4.3 eV and 1.8 eV, respectively [14, 316]. After the rapid plasma treatment, MoO_x is generated on the device surface as demonstrated in the previous discussions. In **Fig. 7.5(a)**, we present a SEM image of plasma-treated MoS_2, where small regions of high work function material (dark contrast) are seen nested on the MoS_2 surface. Oxides of molybdenum are commonly known as high work function materials (6.8 eV) with a band gap of 3 eV [296, 264] and hence appear darker in SE micrographs than the lower work function MoS_2 at this electron beam energy (15 keV). Uniformly distributed plasma-generated oxides spanning tens of nanometres form an effective medium with the unreacted MoS_2 in the FET channel, as observed more clearly in the contrast-adjusted inset on the micrograph in **Fig. 7.5(a)**. As the Fermi level of the donor MoS_2 is higher than that of MoO_x, significant band bending will occur at the equilibrated interface of the heterojunction [317]. Photo-generated holes in MoS_2 will become trapped at the junction interface [318], inhibiting radiative recombination and thereby enhancing the photocurrent with electrons as majority carriers, as previously pointed out by

Yoo *et al.* [296], and outlined in the band diagram sketch in **Fig. 7.5(b)**. This observation is also supported by the suppressed radiative recombination observed in the PL data and the strong photogating effect [308] mediated by the electron-rich FET channel. The improved responsivity at higher back-gate fields is a direct consequence of Fermi level alignment which also facilitates easier photocarrier injection into the contacts [16, 319, 320] and hence primes the device for photon detection levels exceeding those of the pristine MoS_2.

7.5 Conclusions and outlook

We have demonstrated that the photoresponsivity of CVD MoS_2 monolayer FETs can be enhanced ten-fold by the introduction of surface-bound molybdenum oxides. The effect of the mobility and photoresponsivity enhancement depends on laser power and is more prominent at powers exceeding several μWatts. Additional work ought to be carried out to study the effect of light absorption on the observed phenomenon, i.e. to correct for the actual absorbed laser power. If the material film is getting thicker, as we saw in the AFM results in previous sections, it may largely affect the absorbance of the device. However, the surface-formed oxide has a relatively high band gap ($\sim$ 3 eV), while the incident photon energy for this experiment was 2.54 eV, so the absorption may not be so efficient.

Thus, in **Chapters 5-7**, we have established plasma treatment as a viable means for tuning the optoelectronic properties of layered semiconductors on a large scale. We now shift gears for **Chapters 8-10**, where we will focus on a site-specific and highly-controlled inclusion of defects into MoS_2 with the helium ion beam.

Chapter 8

Effect of varying the irradiation area on the conductance of monolayer MoS_2

> "You know what radiation at that
> level does to transistors,
> for instance."
>
> - Poul Anderson,
> *Tau Zero*, 1970.

In this chapter, we examine the effects of irradiating a monolayer MoS_2 FET with a charged helium beam as a function of increasing exposure area. Subsequent chapters will focus greatly on the effect of exposing the channel in a one-dimensional limit; where the irradiation pattern mimics the presence of a grain boundary in a MoS_2 crystal. For now, we need to establish what the effect of irradiation is between those extreme limits of a synthetic line fault and the full-channel irradiation explored in depth in Fox *et al.* [192]. We also take a look at the effect of irradiating the MoS_2/electrode interface with the helium ion beam by means of experiment and simulation, and how that compares to channel-confined irradiations in terms of device performance.

8.1 Device fabrication and experimental design

A series of devices was fabricated for these experiments from the same batch of CVD-grown MoS_2. For this study in particular, we focus solely on single-layer MoS_2 devices of the same FET channel length, in order to obtain a good performance comparison between devices, where the only parameter we want to vary is the area of the channel which is exposed to the He^+ beam. These monolayer MoS_2 samples were grown using the CVD microreactor method described in detail in **Chapter 4** on 285 nm SiO_2/Si substrates which served as the back-gate. The flakes were contacted with 5 nm Ti/35 nm Au electrodes using EBL.

Following metal film lift-off, the devices were tested electrically in the vacuum to gauge their initial electrical characteristics and prioritise well-performing devices with a high initial conductance for helium ion irradiations. Example *I-V* and gate

curves of the same devices (with on-chip locations labelled) before any helium exposures are presented in **Fig. 8.1** and **Fig. 8.2** respectively.

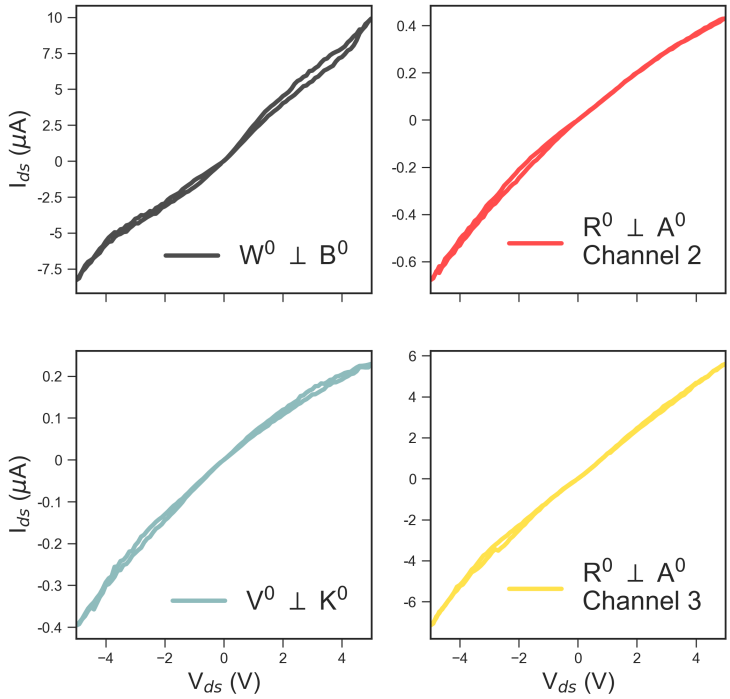

Figure 8.1: Low-bias output characteristics of fabricated monolayer CVD MoS_2 FETs, showing good ohmic behaviour with negligible I_{ds} hysteresis on the return sweep. Labels on each plot identify sample locations, e.g. column W, 0^{th} period, perpendicular to row B, 0^{th} period.

The low-bias *I-V* response of the FETs is largely ohmic, indicating good contacts to the Ti/Au electrodes. A negligible degree of hysteresis is present in the *I-V* curves on return sweeps, indicating no mobile charges in the FET channel in the as-grown flakes. The transfer characteristics reveal standard depletion mode n-type functionality of the FETs, although the exact V_{th}, on/off ratio, subthreshold swing and current saturation values can differ from device to device. This is a function of the degree of intrinsic n-dopants (sulfur vacancies) present in the device, highlighting the importance of consistent fabrication of such TMD FETs for future electronics.

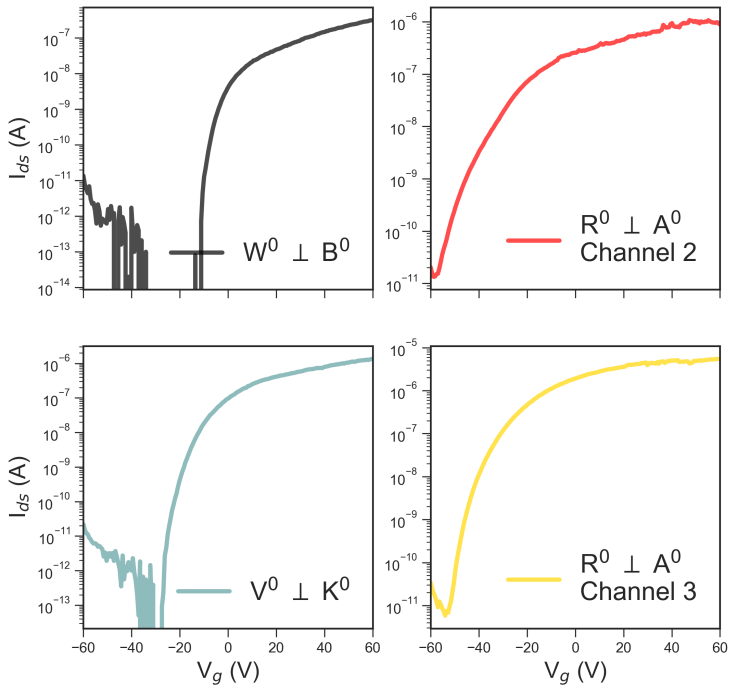

Figure 8.2: Transfer characteristics of fabricated monolayer CVD MoS_2 FETs, showing standard depletion n-type functionality. V_{th} may vary between devices due to the degree of intrinsic doping in as-grown flakes.

The areal ion dose delivered to each sample was maintained at $\sim 10^{17}$ He^+ ions cm^{-2} in order to study the effect of changing the exposure area at the same dose (the *pseudo-metallic* dose from our group's previous work [192], described in **Fig. 3.9**). The step size, dwell time and delivery time parameters of each pattern are shown in **Table 8.1** below:

Chip	Location	Designated ratio	Beam current (pA)	Step size (nm)	Dwell time (μs)	Dose delivered (ions cm^{-2})	Time taken to deliver
1	X ⊥ M	**0.05**	37.8	1	4.3	1.02×10^{17}	**0 m 16 s**
1	X ⊥ M	**0.1**	37.8	1	4.3	1.02×10^{17}	**0 m 34 s**
2	R ⊥ A	**0.2**	37.7	1	4.3	1.01×10^{17}	**2 m 22 s**
1	V ⊥ K	**0.3**	37.9	1	4.3	1.02×10^{17}	**1 m 36 s**
2	T ⊥ A	**0.4**	37.5	1	4.3	1.01×10^{17}	**2 m 17 s**
1	V ⊥ K	**0.5**	36.7	1	4.5	1.03×10^{17}	**2 m 12 s**
2	T ⊥ A	**0.6**	37.3	1	4.3	1.00×10^{17}	**5 m 29 s**
1	V ⊥ K	**0.7**	37.5	1	4.3	1.01×10^{17}	**3 m 00 s**
2	T ⊥ A	**0.75**	38.0	1	4.3	1.02×10^{17}	**11 m 28 s**
1	W ⊥ L	**1.0**	37.4	1	4.3	1.00×10^{17}	**4 m 18 s**
2	W ⊥ B	**0.001**	37.4	1	4.3	1.00×10^{17}	**0 m 500 ms**
2	Z ⊥ A	**0.25**	36.9	1	4.3	9.90×10^{16}	**3 m 04 s**
2	W ⊥ B	**0.35**	37.4	1	4.3	1.00×10^{17}	**3 m 11 s**
2	Z ⊥ A	**0.55**	37.0	1	4.4	1.02×10^{17}	**9 m 48 s**
2	R ⊥ A	**0.75**	38.0	1	4.3	1.02×10^{17}	**6 m 02 s**
2	W ⊥ B	**0.9**	37.2	1	4.3	9.98×10^{16}	**3 m 25 s**

Table 8.1: **Summary of exposure parameters used to make patterns for different I_R exposures.** Column 2 gives the column/row locations of markers where the sample is located on each chip. Column 3 is the *designated ratio*, discussed in detail in the next paragraph.

The effect of changing the scan area on the total delivery time can clearly be seen

from the way values in the last column (in green) scale as we vary the ratios in the third column (in blue). Recalling our dose discussion in **Chapter 4**, we need to consider that all of our ion beam irradiations are done in a single-scan unidirectional manner, i.e. no dwell site is ever met again by the beam throughout the areal dose delivery. Due to this, the dwell time is quite long (several μs), and for μm^2-sized patterns this adds up significantly (up to 10 hours of irradiation) if the beam current were to be kept in the usual sub-pA range used for imaging. Hence, we need to increase the beam current by choosing a larger-than-usual aperture (20 μm, spot control = 1). This leads to a few drawbacks on our He^+ ion work:

1. the probe size of the beam is increased from ~ 1.5 nm to ~ 7 nm on the larger aperture. This means a larger beam spread and a guaranteed overlap of dwell sites.

2. the beam current is less stable in this higher pA range. This may lead to slight dose variations, as evident in the final calculated doses in **Table 8.1**.

3. these factors at such a high dose delivery over the course of minutes will lead to inevitable drift of the target pattern, i.e. the edges of the pattern may be shifted by tens of nanometres or more in some cases. Hence, when the irradiations were finished, an SEM analysis was performed to calculate the exact I_R value achieved for each device. This means that a designated I_R = 0.1 ratio may have changed to an absolute I_R = 0.07 ratio, etc. The electrical results will hence be discussed in the context of these more accurate I_R values evaluated from post-irradiation imaging.

A collection of SEM images of example post-irradiation devices with their chip locations noted is presented in **Fig. 8.3**.

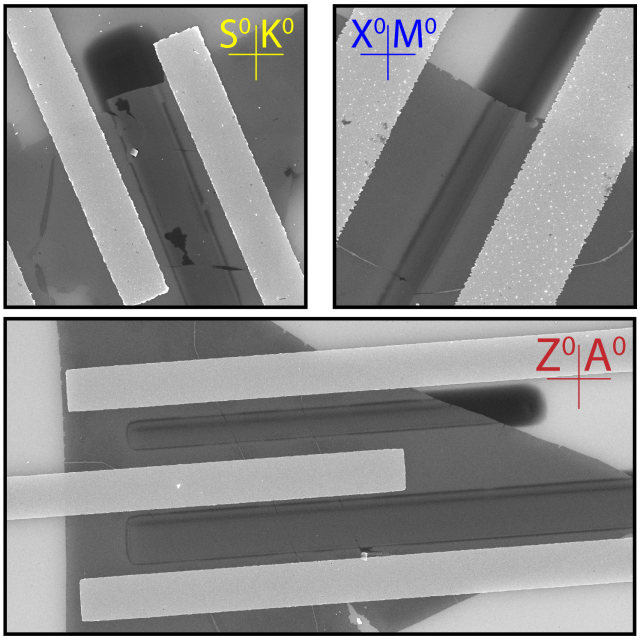

Figure 8.3: **Examples of irradiated devices with their chip locations marked on the SEM image. The electrode-electrode distance in each is 5 μm. SEM beam energy = 5 keV.**

8.2 Electrical performance as a function of I_R

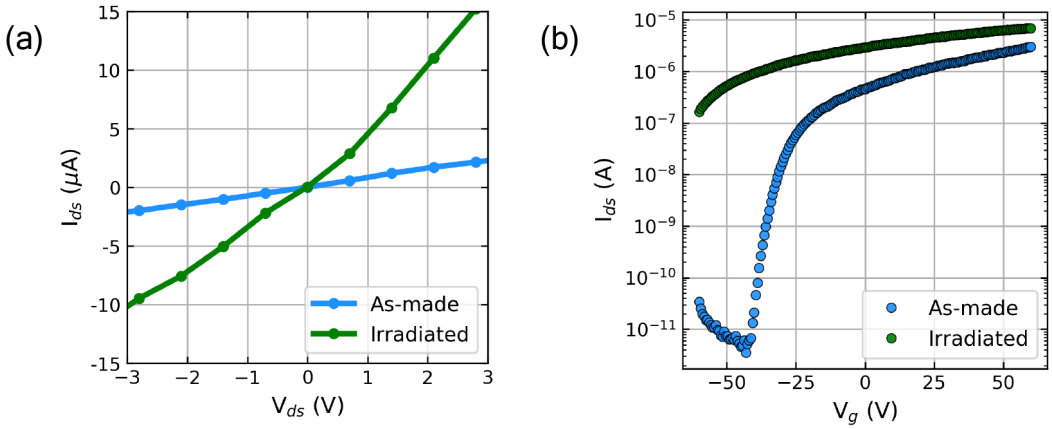

Figure 8.4: **Effect of irradiating the device at I_R = 0.07.** **(a)** Output curves before and after irradiation, showing the emergence of higher conductance in the material. **(b)** Transfer curves before and after irradiation, highlighting the higher degree of n-type doping and increased conductivity.

As shown in **Fig. 8.4(a)**, localised irradiation in the small I_R regime (7%) causes a notably higher electrical conduction to emerge in the monolayer MoS_2. I_{ds} increases $\sim$ 5-fold for the same V_{ds} compared with the as-made device. After the irradiation, the transfer characteristics (**Fig. 8.4(b)**) reveal a much-reduced gate response. The FET channel cannot be effectively turned off in the tested bias range, with significant

drain current persistent at $V_g = -60$ V, indicating a sharp increase in the subthreshold swing and a large shift of V_{th} to negative gate biases ($> \Delta 10$ V); deepening the depletion-mode n-type device functionality noted for the MoS_2 channel prior to the irradiation.

The observed results resemble bilayer MoS_2 behaviour following full-channel irradiations at this dose, reported by our group in 2015 [192]. However, the irradiations performed in that work also included the modification of the electrode/MoS_2 interface, as the exposure pattern overlapped the electrode. The pseudo-metallic transition observed in Fox *et al.* was characterised by a completely flat gate curve, i.e. a near-total lack of conductance tunability by the field effect, suggesting the Fermi level was beyond the bottom of the conduction band. Herein, some tunability is still present, which may originate from the preservation of the pristine metal/semiconductor interface and how gating modulates the carrier injection at that interface. We will examine the effects of irradiating one of the MoS_2/electrode interfaces in our devices in an upcoming section in this chapter.

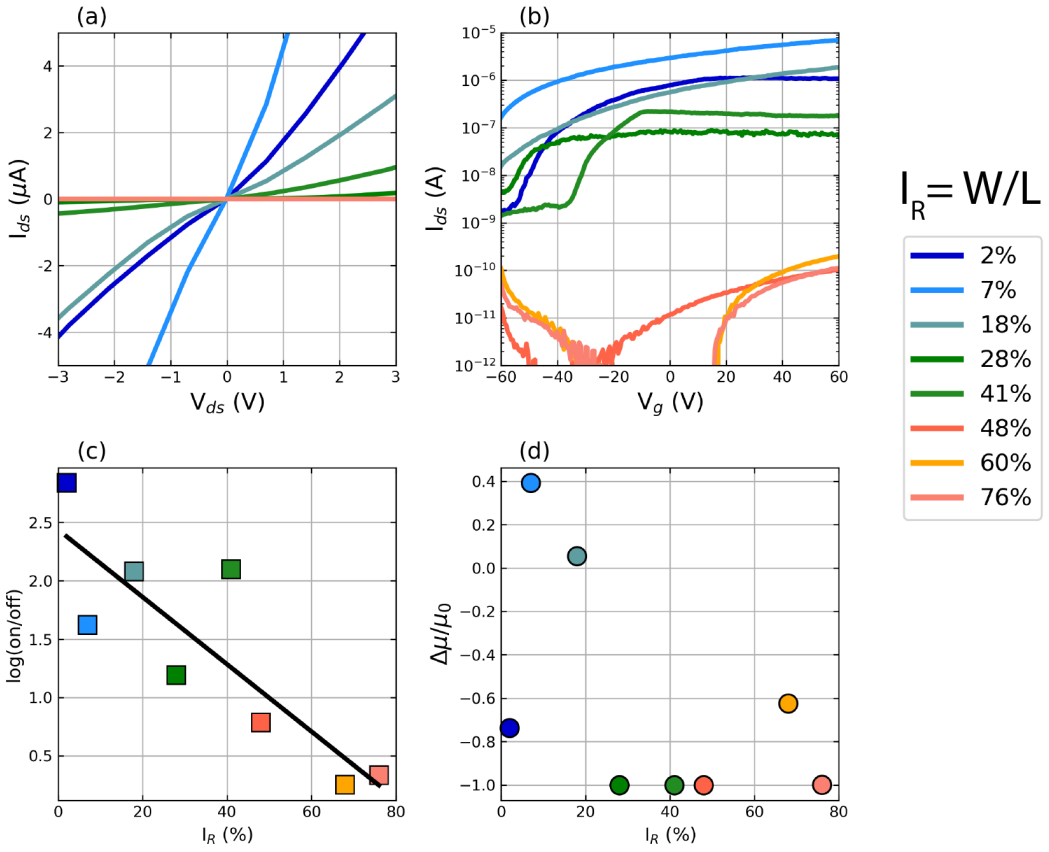

Figure 8.5: **Electrical characteristics as a function of increasing I_R.** Note that all the plots share the same colour legend on the right. **(a)** *I-V* and **(b)** gate sweeps of different devices with varying I_R. **(c)** Semi-log plot of the extracted electron branch on/off ratios corresponding to each gate curve in **(b)**. The black line is a linear fit to the semi-log data. **(d)** Change in the field-effect mobility relative to as-made device mobilities extracted from transfer curves in **(b)**.

The effects of increasing I_R are evident from changes to the output and transfer characteristics in **Fig. 8.5(a,b)**. The data are organised into 3 groups marked by blue, green and red shades, corresponding to small (2-18%), medium (28-41%) and large (48-76%) I_R values, respectively. The output curves, taken at V_g= 0 V, demonstrate an increase in conductance between the I_R = 2% and I_R = 7% irradiations followed by a continuing drop when I_R > 18%. For a small I_R (blue curves), the FET experiences large V_{th} shifting (> Δ 10 V) to negative biases, a lowered on/off ratio ($\sim 10^2$), and an increased conductance relative to the untreated device. As I_R is increased into the green (28-41%) and red (48-76%) groups, the device conductance drops heavily, accompanied by positive bias V_{th} shifts, while the on/off ratio is also seen to decrease roughly exponentially. This is demonstrated in **Fig. 8.5(c)**, which tracks the log-transformed on/off ratio as a function of I_R with

a good linear correlation ($R = -0.85$) from the semi-logarithmic fit. This suggests that an optimal ion irradiation for a conductance increase occurs when the areal channel exposure is close to 10%.

At high I_R values (red group), we see the emergence of a weak ambipolar response in our transfer curves. At these ratios, the device starts to enter a regime where more than half of the channel has been treated with the ion beam. Thus, we expect a dominant contribution of oxygen-containing atmospheric adsorbates (known p-type dopants) in saturating the vacancy sites created by the ion beam, allowing for residual hole conduction in the newly-formed effective medium channel [133]. For a given dose, the ion beam provides a high concentration of effective adsorption sites for atmospheric p-type dopants within the area defined by the FWHM of the Gaussian probe extension. This is accompanied by lowered-dose probe tails, whose damage extends to > 20 nm and may induce additional n-doping with no complementary adsorbent saturation, due to the dose variation. A larger irradiation area will thus provide more effective p-doping sites while stifling the n-doping response due to probe tails extending past the FET channel; leading to the observed ambipolar gate response for large I_R.

Fig. 8.5(d) charts the effect of I_R on the change in μ_{fe} of the irradiated device relative to its as-made mobility, μ_0. Extracted from the linear region of the transfer curve, μ_{fe} is seen to improve by up to a factor of 0.4 in 2 out of 3 devices in the blue region. For the green and red regions of I_R, μ is always seen to worsen as the area of the irradiated channel is increased. μ_{fe} is expected to drop heavily as the rate of scattering rises with an increased defective channel area. The improved mobility at $I_R \sim 10\%$ indicates the screening of scattering centres by the increased carrier concentration, which corroborates the increase in conductance observed in **Fig. 8.5(a)**.

8.3 Effect of irradiating the MoS_2/electrode interface

We now consider the effects of irradiating the metal/semiconductor interface. We treated two FETs within each I_R regime, but for one of the devices in each pair, a single electrode interface was also irradiated. SEM images in **Fig. 8.6** show examples of patterns overlapping both the channel (leading to a given I_R) and one of the electrode interfaces.

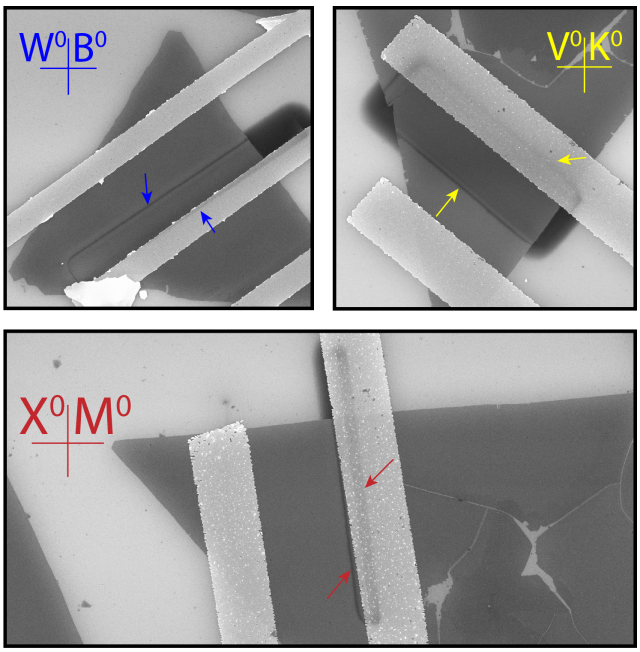

Figure 8.6: **SEM images of example devices where one of the electrode/MoS_2 interfaces was irradiated.** The chip locations are marked on the images. The exposed regions are the dark contrast areas in the micrographs. Arrows mark the edges of the exposed patterns in the images. FET channels in all panels are 5 μm. SEM beam energy = 5 keV.

In all three I_R regimes, allowing one of the electrode/MoS_2 interfaces to be damaged by the beam leads to a drop in the device conductance, as evident in **Fig. 8.7**. Moreover, the conductance of the devices where the electrode/MoS_2 interface was treated with the ion beam is lower than the conductance of the as-grown device. The transfer curves in **Fig. 8.7** indicate that as the device approaches the strong inversion regime, the electrode/channel interface damage (green curves) inhibits high drain currents in the FET relative to the case of no electrode damage (purple curves).

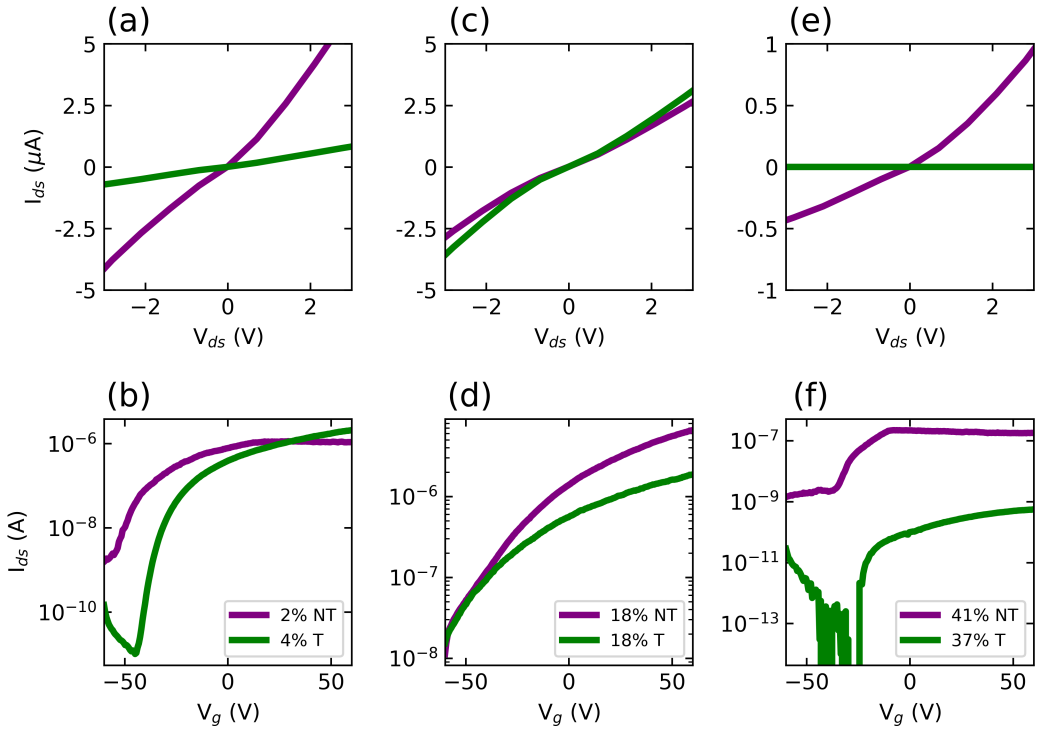

Figure 8.7: Three sets of *I-V* and output curves corresponding to the low I_R **(a,b)**, medium I_R **(c,d)** and high I_R **(e,f)** regimes, respectively. The purple curves are samples where only the channel had been irradiated (NT; *not touching* the electrode interface), while the green curves are devices where the MoS_2/electrode interface had been irradiated (T; *touching* the electrode interface).

8.4 SRIM simulation of interface damage

We simulated the atomic vacancy yield per each delivered ion as a function of target penetration depth on the 35 nm-Au/5 nm-Ti/0.7 nm-MoS_2/285 nm-SiO_2 stack using stopping range of ions in matter (SRIM) software [321]. As evident from **Fig. 8.8**, the sputtering yield at the Ti/MoS_2 interface is very close to that of unencapsulated MoS_2 [322], indicating notable damage to the interface at this delivered dose. It may be expected that an increase in the Schottky barrier height will occur if the usually-pinned Fermi level [91] is now a function of the beam-altered metal-semiconductor interface.

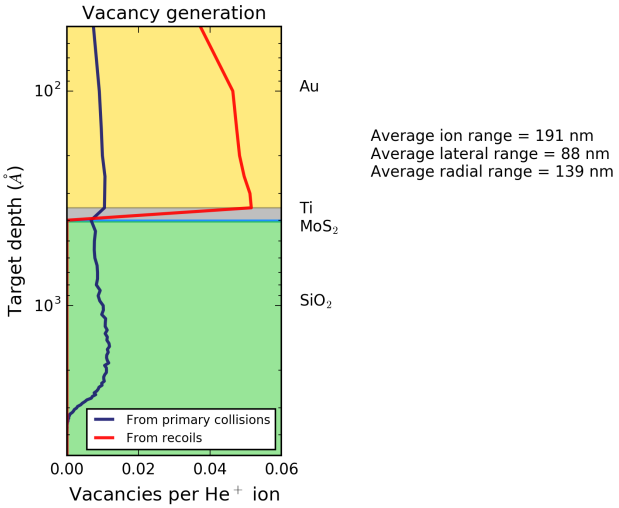

Figure 8.8: **SRIM simulation of the vacancy yield** generated as the He^+ beam penetrates the device stack, indicating damage to the metal-semiconductor interface. Simulation performed by Dr. Pierce Maguire.

Ion beam pre-treatment of the interface before metal deposition increases the concentration of dangling bonds available for hybridisation [87] when the contact is deposited. Pre-treatments of the contact interface with an energetic Ar^+ ion beam have already been employed in this manner to reduce the contact resistance to MoS_2 FET channels for nickel electrodes [323, 324]. As in our case we are treating an already-hybridised interface, we suspect that the formation of point defects therein, such as migrated interstitials and antisite defects, will serve to trap carriers at the interface and will reduce the crowded injection current at the contact interface [325]. This may be experimentally confirmed with a combination of low-temperature electrical characterisation and capacitance measurements [326, 327] in future work.

8.5 Correlating I_R, grain boundaries and interface damage with electrical performance

We have collected a large data set of similar devices, whose electrical performance has been altered by ion beam irradiation. We have varied only two parameters: **(1)** I_R and **(2)** whether or not we have irradiated the metal/semiconductor interface. In addition, we need to consider the effect of naturally-occurring GBs on the electrical performance of the MoS_2 FETs. This is of particular importance in the case of resistive switching, as synthetic monolayer MoS_2 has in recent years been shown to have memristive properties when biasing across grain boundaries, as we have seen in **Chapter 2** [107, 108, 109, 110].

8.5.1 On the nature of flake growth and device geometry

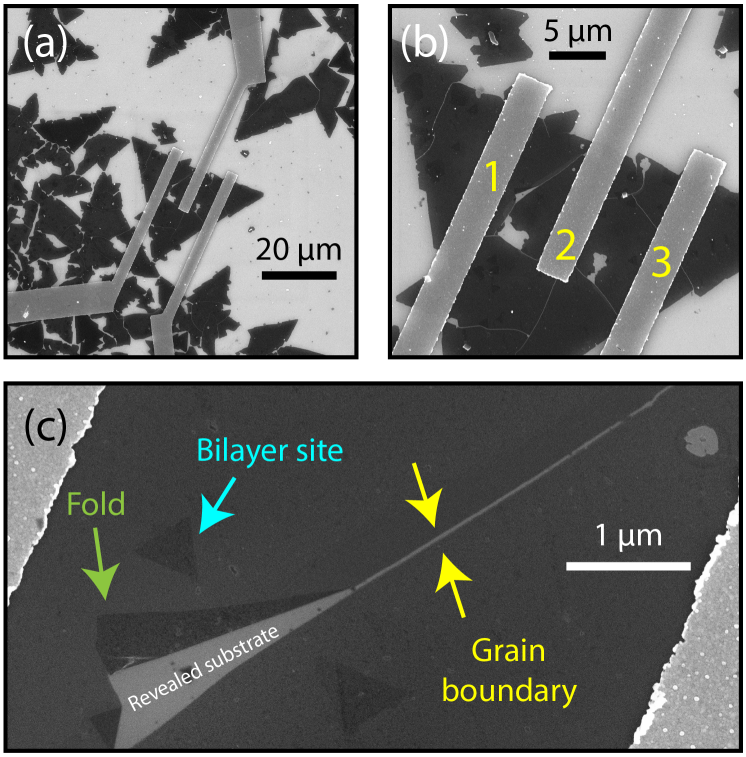

Figure 8.9: **Three SEM images of the same as-made MoS_2 FET device.** On the optical microscope scale like in **(a)**, it is difficult to identify whether the channel contains any GBs. A higher magnification image in **(b)** reveals discontinuities in the crystal lattice of the FET channel. Electrodes are labelled as 1, 2, and 3. **(c)** A closer look at the channel region shows multiple impurities labelled with arrows. SEM beam energy = 5 keV.

Some of our MoS_2 triangles used in this study already contain cracked GBs/line defects in the FET channel before any He^+ irradiation. These are too small to be identified with an optical microscope before patterning and would need to be screened with an SEM before making every device, if they turn out to affect transport properties adversely. This may occur through inducing hysteresis in the *I-V* curve, or by artificially upping the delivered ion dose by acting as nucleation sites for vacancy seeding for the incoming ion irradiation [328]. This would be a significant drawback for using CVD-grown monolayers for industrial-grade applications. Example SEM images of a device containing extended GBs are presented in **Fig. 8.9**. As visible in the high-magnification image in **(c)**, multiple sources of impurities can be present in the FET channel on what otherwise seems a perfect isosceles triangle of MoS_2. We see regions of nucleation for bilayer growth, stripping of the monolayer off the substrate and subsequent folding, as well as wide trenches separating crystallites

within the channel between the contacts. Note that these are at 60° to the edge of the triangle and are thus along crystallographic directions.

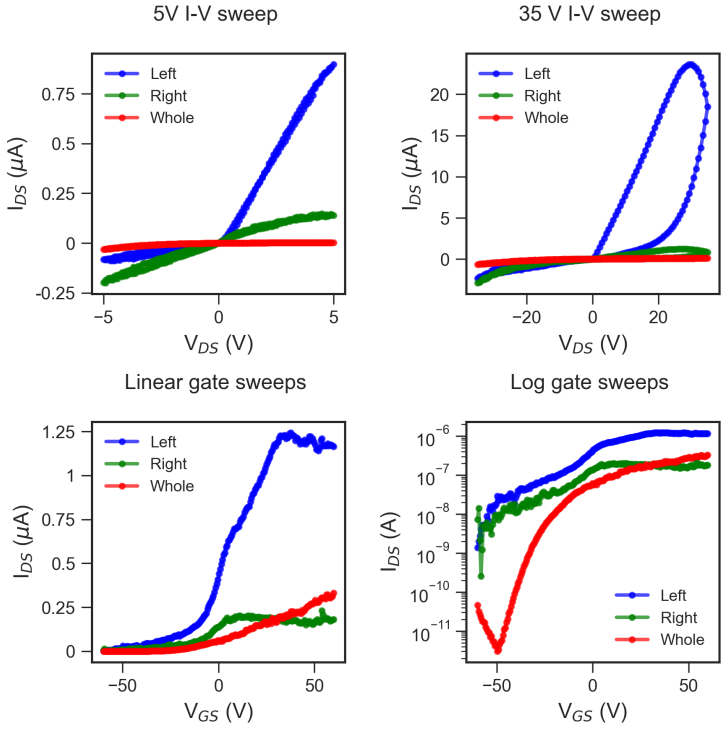

Figure 8.10: **Electrical characterisation of the three channels on the device in Fig. 8.9**. **(a)** ± 5 V *I-V* sweeps on the three channels. **(b)** ± 35 V *I-V* sweeps on the three channels. **(c)** ± 60 V gate sweeps on the three channels on the linear scale. **(d)** ± 60 V gate sweeps on the three channels on the semi-log scale.

We performed electrical tests of this device (**Fig. 8.10**) in various configurations: **Left**: between electrodes 1 & 2; **Right**: between electrodes 2 & 3; and **Whole**: between electrodes 1 & 3. **Figure 8.10** shows the low and high-bias *I-V* sweeps, as well as gate sweeps on both the linear and semi-log scales for these testing configurations. Somewhat unexpectedly, the **Whole** channel seems to retain ideal n-type MoS_2 functionality with a healthy subthreshold swing and no hysteresis in the *I-V* curve, despite obvious GBs and defects present in the whole channel area. In contrast, both the **Left** and **Right** channels show sub-par gating stability despite an increased conductivity. In addition, the **Left** device harbours significant hysteresis in the high-bias *I-V* curve, indicating that the presence of defects in that channel mediates resistive switching behaviour, even before any helium ion beam irradiation is performed.

Looking closely at the images in **Fig. 8.9**, we see that the inter-digitation of

electrodes on the triangle leads to a straddling of electric field containment between electrodes 1/3 & 2, while electrodes 1 & 3 are quite parallel. This electrode width ratio on the FET channel may help to explain the difference in device performance and needs to be considered in all devices when comparing electrical parameters in this section. As the same types of defects are present in the **Left** channel as in the **Whole** channel, but the electrical performance is drastically different, the design of electrodes on these defective CVD films is crucial to maintain reliable FET functionality.

As polycrystalline films are expected to be memristive circuit components only when the sulfur gas supply is throttled during deposition [107, 108], we may not see resistive switching in geometries where the MoS_2 sample is an isosceles triangle. In the case of sulfur-restricted growth, the samples tend to contain visible strain on the triangle edges and look more like starfish (see comparison in **Fig. 8.11**). Nevertheless, we go on to study the effects of both GB-containing starting material and the electrode width ratio on the device performance, while varying I_R and irradiating the metal/semiconductor interface in some devices.

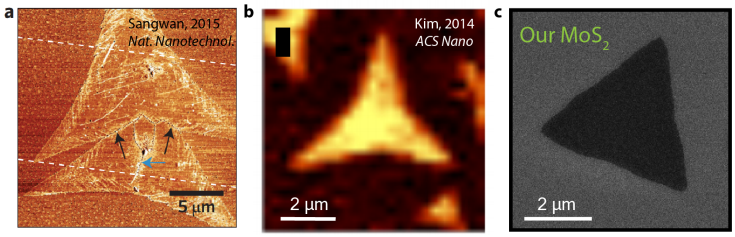

Figure 8.11: **Examples of strained MoS_2 CVD growth achieved by restricting sulfur gas supply, compared with our CVD flakes.** **(a)** AFM image of a starfish-shaped flake growing out of the grain boundary of another flake [107] and **(b)** a Raman map of a sub-stoichiometric MoS_{2-x} starfish-shaped flake [329]. **(c)** SEM image of an individual as-grown single-crystal triangle from our process, exhibiting an isosceles geometry.

8.5.2 Statistical analysis

When we carry out the He^+ irradiation on devices with different I_R, it becomes clear that some samples exhibit resistive switching in their *I-V* curves. However, no clear trend can be observed with regards to the nature of the noted *I-V* hysteresis as a function of I_R. Hence, other considerations need to be weighed in order to determine what causes the abrupt resistance change in some devices. As we have delved deep into the effects of grain boundaries on this phenomenon in the literature review, we need to consider whether GBs existing in our device channel pre-irradiation have any impact on resistive switching. In addition, the effect of

irradiating the electrode/MoS_2 interface impedes current injection into the channel as we discussed recently. If the height of the Schottky barrier at the interface can be additionally tuned by modulation doping [330] due to sulfur vacancy drift from grain boundaries [107, 108, 110, 109], one may also expect a different resistance state to emerge when the interface is altered by the beam.

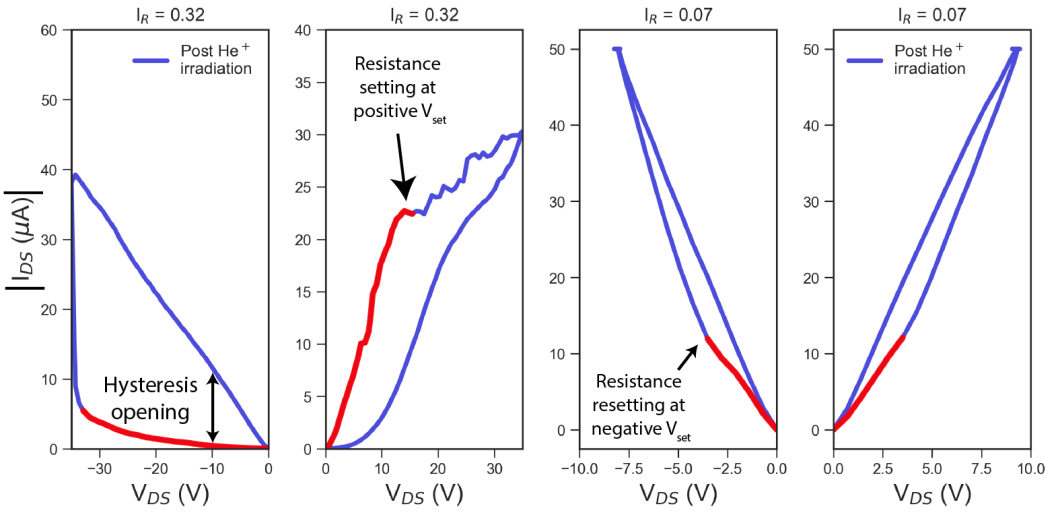

Figure 8.12: **Examples of hysteretic *I-V* curves in two devices after He^+ ion irradiation.** The red traces mark the point at which resistance states switch, and hence the data point around which linear fits were performed to the *I-V* curves. The quotient of the curve slopes was then evaluated to obtain the resistance ratio in case of hysteresis.

Figure 8.12 presents example hysteretic *I-V* curves observed for the cases of I_R = 0.32 and 0.07. In the 0.32 device, a large hysteretic window opens on both sweep polarities, with a significant resistance shift at V_{ds} ≈ -34 V on the negative polarity sweep and V_{ds} ≈ 15 V on the positive polarity sweep. The red lines signify the sweep up to the point of resistance change on both sides. The two devices have strikingly different features, as the sweeps are more symmetric in the 0.07 device, with mirrored set bias (V_{set}) magnitudes on either side of the sweep (≈ ± 4 V) and similar current magnitudes, indicating a more ohmic device behaviour. The ratio of the resistances is reduced however, when compared with the 0.32 loops.

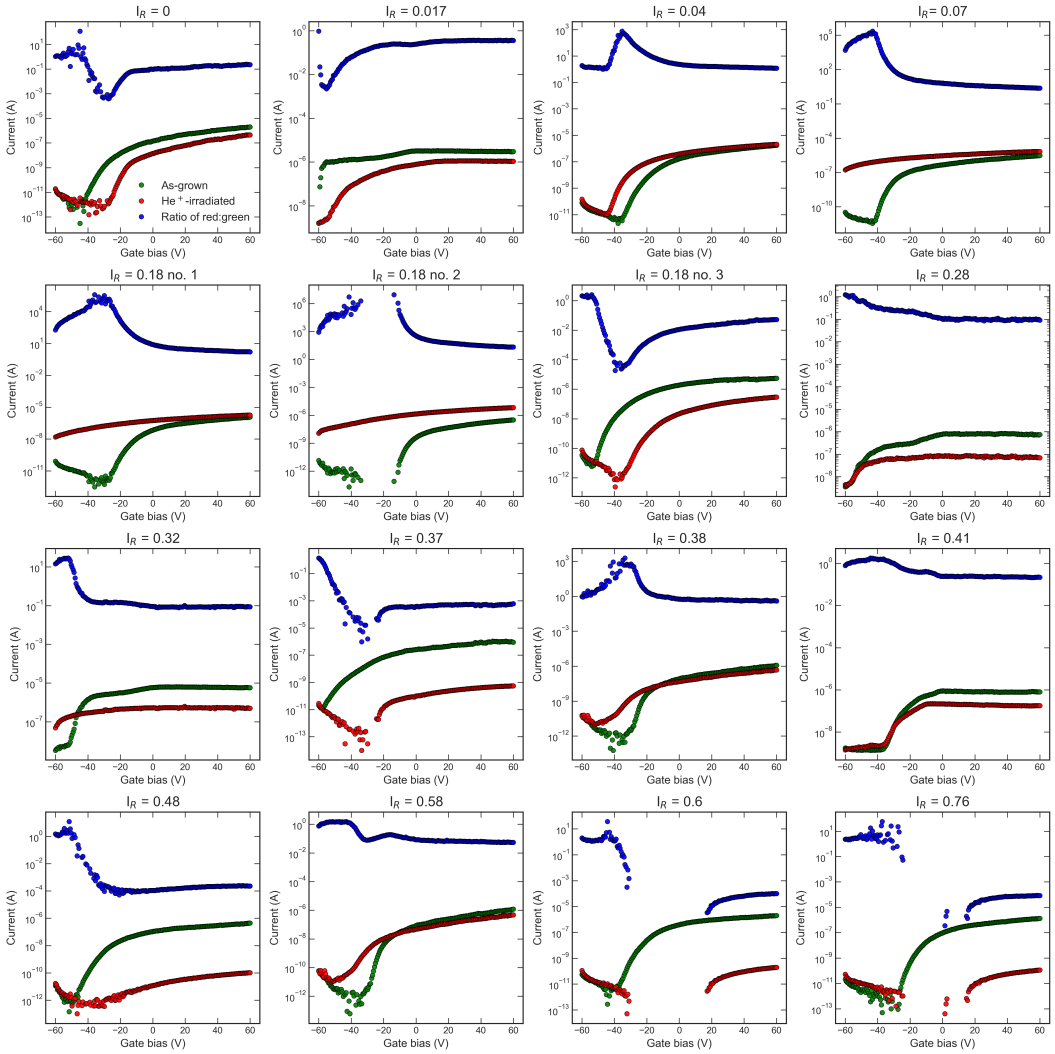

Figure 8.13: **A series of gate curves for each tested device, demonstrating the transfer characteristics before and after helium beam irradiation.** The blue curve traces out the quotient of the gate sweeps values after (red) and before (green) ion beam exposure at a given I_R.

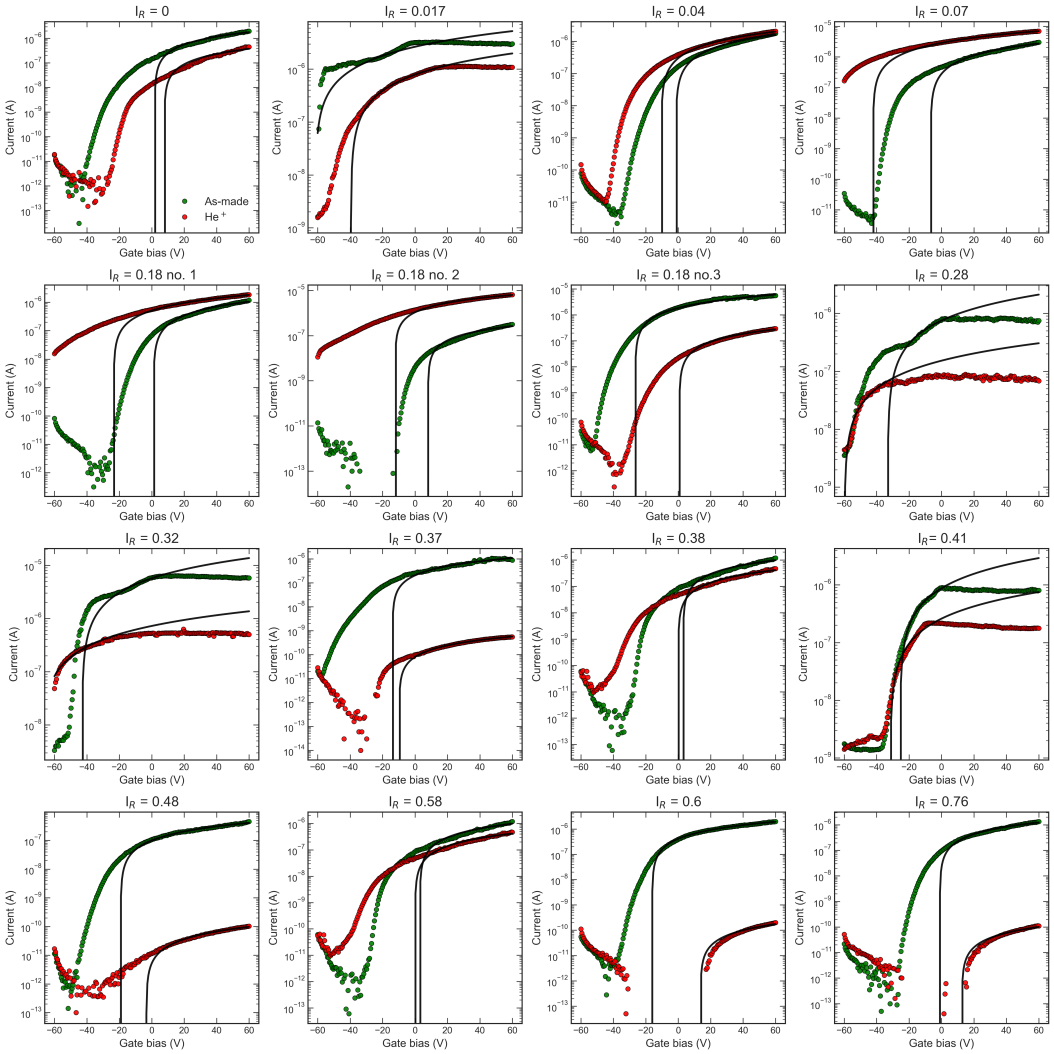

Figure 8.14: **Extraction of threshold biases from gate curves before and after helium ion beam irradiation.** The black solid lines are linear fits on the linear scale. The intercept on the x-axis is taken to be V_{th}.

Figure 8.13 and **Figure 8.14** collate the raw gate curves before and after irradiation for each tested I_R. We plot the after:before quotient of the curves at each gate voltage in blue in **Fig. 8.13** which allows us to obtain an on/off ratio from before to after irradiation. We also trace out fits (on a semi-log scale) to the linear region of each transfer curve in **Fig. 8.14**, which helps us extract the threshold voltage in each case. We can then use these parameters to evaluate the performance of the devices before and after ion treatment, but also account for group differences in the categories of GB-containing channels and electrode/MoS_2 interface-irradiated devices.

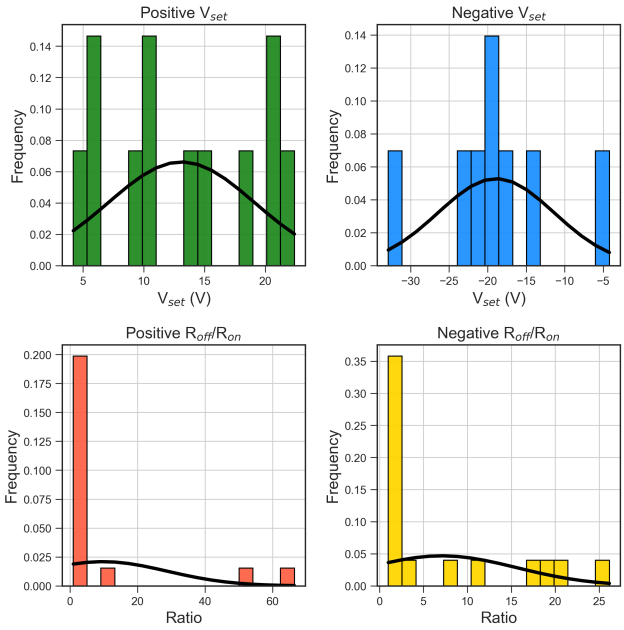

Figure 8.15: **Distributions of extracted parameters from any hysteretic *I-V* curves in the data set as a function of irradiation-to-channel ratio.** The V_{set} on the negative half of the sweep, on average, has a larger voltage magnitude, i.e. a larger electric field is necessary to switch resistance on that side of the sweep. The resistance ratio, R_{on}/R_{off}, as evaluated on both sides of the sweep does not, on average, exceed 10.

Figure 8.15 shows the distributions of key parameters from *I-V* curves, which may correlate the resistive switching behaviour to any experimentally-controlled variables such as I_R. The V_{set} on the negative half of the sweep (blue histogram), on average, has a larger voltage magnitude, i.e. a larger electric field necessary to switch resistance, than the positive polarity of the sweep (green histogram). The resistance ratio, R_{on}/R_{off}, as evaluated on both sides of the sweep does not, on average, exceed 10. This indicates an asymmetry in the device functionality, i.e. a possible domination of one of the flake sides on device performance. Spontaneously large hysteresis loops appear on the positive side of the sweep (red histogram) with ratios in excess of 60, while the negative side of the sweep (yellow histogram) tends to have a lower ratio, with the maximum resistance ratio noted on that side not exceeding 30.

Table 8.2 categorises some extracted parameters to be used for statistical tests to help us determine if there is a significant difference between samples containing GBs and/or where the electrode interface had been irradiated with regards to resistive switching. In addition, we can study the effect on device conductance post-irradiation at different stages of the transfer curve, the change in V_{th} and the effect of asymmetric electrode widths.

8.5.3 Correlations between experimentally-evaluated parameters

True area of channel (μm^2)	True area of cut (μm^2)	True I_R	Larger electrode width (μm)	Smaller electrode width (μm)	Electrode width ratio	Electrode cut	GBs	I_{ds} quotient at V_R = -60 V	I_{ds} quotient at V_R = 60 V	Max. I_{ds} quotient	Min. I_{ds} quotient
63.65	43.46	0.682796544	14.6	12.8	0.876712329	0	1				
60.64	29.06	0.479221636	13.8	9.87	0.715217391	0	0	0.000226	1.485061511	12.214	-0.828571428
36.26	27.58	0.76061761	8.52	7.02	0.823943662	0	1	2.336512262	8.24E-05	57.4	-70.66666667
52.12	31.28	0.600153492	13.28	7.47	0.5625	1	1	2.033559509	0.00010093	36.85714286	-10.89189189
51.14	9.1	0.177942902	11.88	6.96	0.585858586	1	1	188.2242306	1.578124336	39146.875	-554956
56.14	9.94	0.177057357	11.66	11.03	0.945969125	0	1	830.0441176	21.02974252	100000	-9956990
70.43	2.8	0.039755786	14.59	12.67	0.868403016	1	0	1.873374139	1.177135508	754.9145299	1.026101142
135.38	0	0	27.81	27.69	0.995685005	1	0	1.068638393	0.227342263	118.3333333	-8.272727273
133.88	51.18	0.382282641	20.18	19.85	0.983647175	1	0	0.917683933	0.397886332	1877.733333	-7815.333333
99.55	6.91	0.069412356	19.04	12.2	0.640756303	1	0	4852.30408	2.300042636	224527.095	2.300042636
166.13	30.19	0.181725155	31.65	21.43	0.677093207	1	0	2.162797532	0.053849513	2.596912521	-1.20E-05
228.85	84.6	0.369674459	31.62	28.92	0.914611006	1	1	1.385714286	0.000622961	1.385714286	-0.000193438
144.38	46.06	0.319019255	21.17	19.3	0.911667454	1	0	14.43131378	0.086192279	28.51228353	0.077430103
79.29	1.32	0.016647749	15.07	9.4	0.623755806	0	0	0.95839086	0.360646733	9.58E-01	0.002212888
53.64	14.89	0.27759135	9.77	8.45	0.864892528	1	0	1.242273223	0.091326447	1.242273223	0.085179161
139.61	57.42	0.411288859	28.85	28.16	0.976083189	0	1	0.796814508	0.220049642	1.779326391	0.21180901
160.07	93.57	0.584556756	45.64	28.62	0.627081507	0	1	0.764174288	0.054265501	1.535318117	0.054186441

Table 8.2: Summary of different qualifiers extracted from the data presented in the figures above. Note that **1** is a binary `yes` and **0** a binary `no` when considering the presence of GBs or electrode interface irradiation in the device.

Figure 8.16 is a correlation heat map of Pearson's r relationship between the variables listed on the x and y axes. Pearson's r is a measure of the linear correlation between two variables (1 for a total positive linear correlation, - 1 for a total negative linear correlation). It can be represented with the following equation:

$$r_{x,y} = \frac{\mathrm{cov}(x, y)}{\sigma_x \sigma_y} \tag{8.1}$$

where cov denotes the *covariance* between x and y, while σ is the standard deviation. The covariance is a measure of the joint variability of x and y, i.e. if x increases as y increases and vice versa, the covariance is positive. If x increases while y decreases, or vice versa, the covariance would be negative. We can apply the $r_{x,y}$ calculation using the `numpy` package in *Python* to cross-test the trends of each variable against that of any other in this heat map set.

From **Fig. 8.16**, we can see that no very strong r dependencies emerge between any of the tested variables. The values are mirrored about the self-correlating diagonal, with dark pink squares signifying strong negative r correlations, while the dark green squares signify strong positive r correlations (with the numerical values mapped to the colour bar on the right). White squares indicate no linear correlation. The strongest trends emerge between:

1. the electrode width ratio & the positive sweep polarity resistance ratio ratio (*positive r*).
2. the negative sweep polarity resistance ratio & V_{set} on the negative side of the sweep. (*negative r*)
3. I_R & the V_{set} on the negative side of the sweep. (*negative r*)
4. V_{set} on the negative side of the sweep & V_{set} on the positive side of the sweep. (*negative r*)

From points **(2)** and **(4)** above, we can surmise that most of the instances of resistive switching occur such that the *I-V* curve is asymmetric like in the 0.32 device in **Fig. 8.12**. Meanwhile, for most devices, the resistance ratio is also larger on the negative side of the sweep at lower voltages. This suggests that the fundamental mechanism of resistive switching in these MoS_2 devices depends on the asymmetry of the back-to-back diode with the He^+-created fissure bisecting the structure. The finding in

(3) tells us that as the defective area of the channel increases, we need a lower set bias to switch the device. This is a supporting piece of evidence for the fact that the switching characteristics of the device are highly sensitive to the concentration or absolute number of available mobile defects. From **(1)** we can see that the more symmetric the device is in terms of electrode positioning, the more likely we are to obtain hysteretic *I*-*V* curves. This suggests that we need to electrostatically confine the electric field which is to drive the mobile vacancies as much as we can in order to migrate the defective front effectively between the contacts.

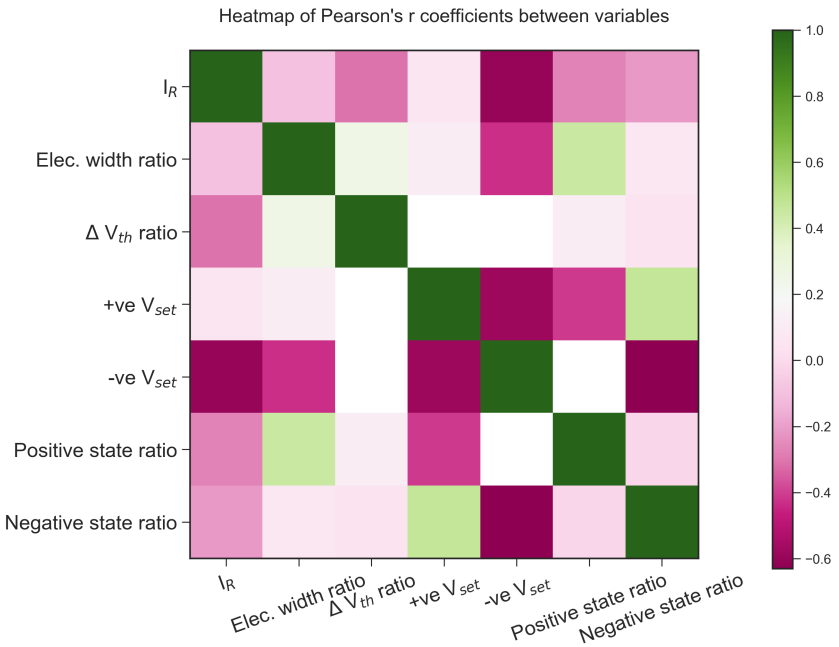

Figure 8.16: **Coloured statistical correlation heat map between various parameters examined in this study**. The darker green colours signify a larger positive correlation between parameters (hence the diagonal self-correlation of 1), while the darker pink colours indicate a stronger negative correlation, i.e. the larger the input, the smaller the output.

8.5.4 *t*-tests on the effects of GBs and interface irradiation

In order to examine the effects of initial GB inclusion in the FET channel, and that of irradiating the MoS_2/electrode interface on the electrical performance, we can carry out Welch's *t*-test (otherwise known as the *unequal variances t-test*), which can help us test whether or not two data set populations have equal means. We propose the following *alternative* hypothesis (as opposed to the *null* hypothesis):

- *Is it true that the difference in means of the two populations is not equal to 0?*

In simpler terms: are the means of these two populations different precisely because they belong to those different populations?

Welch's t-test is defined by the statistic t represented by:

$$t = \frac{\bar{X}_1 - \bar{X}_2}{\sqrt{\frac{s_1^2}{N_1} + \frac{s_2^2}{N_2}}} \tag{8.2}$$

where $\bar{X}_1$, s_1^2 and N_1 are the first sample mean, variance and size, respectively; with analogous notation with different subscripts for the second sample. Running the `t.test` function in the statistical package `R` across the categorised data sets allows us to check t against p-values on a two-tailed distribution. The lower the p-value, the larger the margin of confidence that any difference between the resulting means is not the result of a meaningless statistical fluctuation.

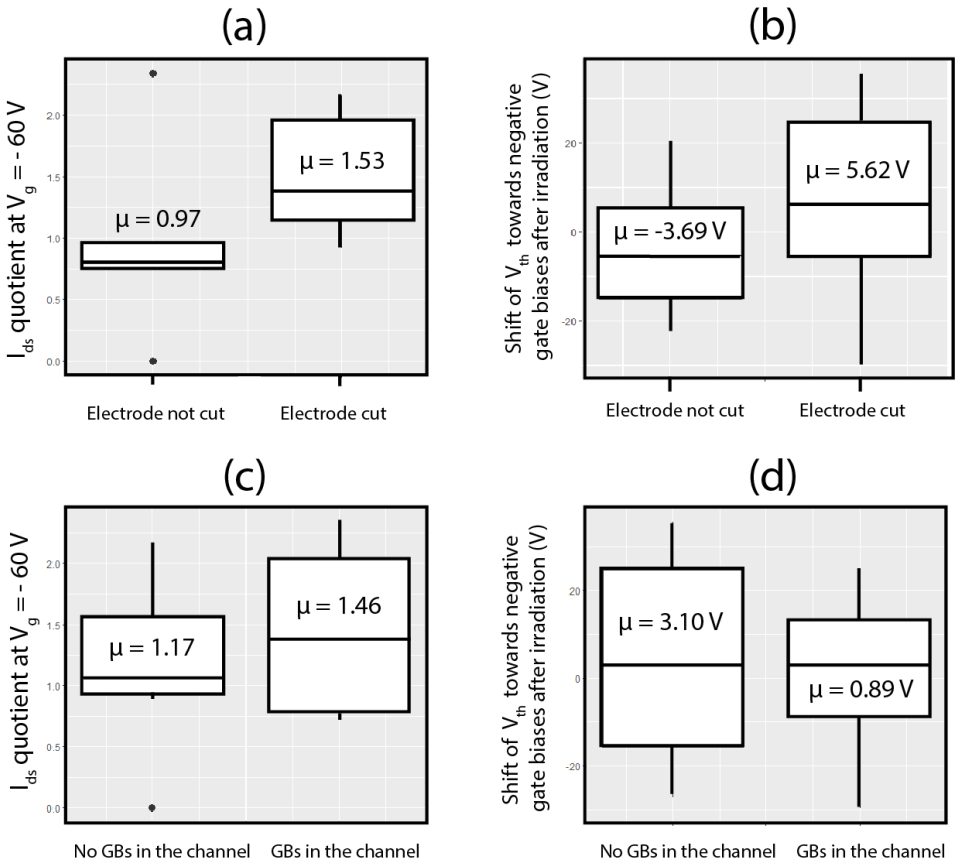

Figure 8.17: **(a)** Box plots of the data distributions of the I_{ds} ratio (extracted in the subthreshold transfer curve regime) before and after He^+ ion irradiation, categorised by whether or not the electrode/MoS_2 interface had been cut by the beam. **(b)** The shift in V_{th} after ion irradiation categorised by whether or not the electrode/MoS_2 interface had been cut by the beam. **(c)** I_{ds} ratio (extracted in the subthreshold transfer curve regime) before and after He^+ ion irradiation, categorised by whether or not the initial FET channel contained GBs. **(d)** The shift in V_{th} after ion irradiation categorised by whether or not the initial FET channel contained GBs.

In **Fig. 8.17** we show categorised box plots of the distributions of the I_{ds} ratio evaluated in the subthreshold regime of the gate curve before and after helium treatment as delineated by:

1. whether or not the device had the electrode/MoS_2 interface irradiated.
2. whether or not the device contained GBs in the FET channel prior to any irradiation.

From the box plots, it is clear that the effect of cutting the electrode is significant. In the case of not cutting the electrode, the conductance of the device always decreases

(quotient < 1), while in the case of irradiating the interface, the mean conductance always increases. At the same time, the population of devices with irradiated electrodes, on average, experience an average V_{th} shift to negative gate biases by Δ5.62 V, while devices that experience channel-only irradiations show shifts to positive gate biases by Δ3.69 V. This is easily understood in terms of saturation of V_S sites by oxygen-containing adsorbates. When vacancies are created by the beam in the atmosphere-exposed FET channel, they provide rich adsorption sites for atmospheric adsorbates such as O_2, H_2O and N_2. These are known electron-withdrawing species, which will shift the V_{th} to more positive gate biases [69]. In the case of knock-on damage underneath the Ti/Au electrode stack, the V_S sites created in MoS_2 cannot readily be saturated by these atmospheric chemical species, and the observed V_{th} shift is in the opposite direction, as mediated only by electron donation to the MoS_2 channel from unsaturated vacancy sites.

The GB tests, in turn, show negligible effects on both the I_{ds} ratio and V_{th} shift before and after irradiation. The conductance increase is slightly higher when GBs are initially present in the channel, which we can read as the availability of an additional concentration of nucleation sites for defect creation by the ion beam. Meanwhile, V_{th} always shifts to negative biases slightly, regardless of GB presence in the channel, indicating that saturation of beam-created V_S sites happens in both data sets.

We note that the power of our statistical tests is relatively weak. Although experimentally extensive, the data set is statistically not hugely significant (16 samples) and the obtained p-values from each of the plots in **Fig. 8.17** are respectively: **(a)** 0.24 **(b)** 0.35 **(c)** 0.50 and **(d)** 0.83. Although some of these values are approaching 0.05, they are still significantly higher and the alternative hypothesis may not be confidently confirmed. However, the trends seen in the gate curves from sample to sample and the electrode irradiation data are comprehensive enough to indicate that the physical phenomena observed upon carrying out the same device modification method are consistent.

8.6 Conclusions

In conclusion, thus far we have studied the effects of varying the irradiated channel area of helium ion-treated monolayer MoS_2 FETs. The main takeaways from this chapter are:

- The presence of GBs in our initial CVD MoS_2 devices has no impact on the

electrical properties of our FETs after helium ion irradiation. This gives us confidence that the effect of ion beam irradiation is the dominant modification mechanism in the tested devices.

- Introducing a small number of defects into the material ($\sim$ 10% of irradiated-to-pristine channel area) can serve to improve the carrier mobility and material conductance.
- Irradiating the electrode/MoS_2 interface is deleterious to the performance of the FET, with a conductance drop noticed for each of the areal irradiation regimes.
- In addition, the threshold voltage can be shifted to negative biases by irradiating the electrode, and to positive gate voltages by containing the irradiations to the FET channel only. This gives us a significant means for tuning the electrical properties of monolayer TMD transistors.
- Varying I_R has no meaningful effect on the resistive switching phenomena which were observed in some cases.

We have demonstrated that by tuning the irradiation strategy and localising the damage to specific sites, the electronic characteristics of on-dielectric MoS_2 FETs can be well-controlled in the monolayer limit. We will build on this knowledge in the next chapter where we will fabricate and study a hybrid MoS_2 device known as the *memtransistor* by confining our channel-bisecting irradiations to quasi-one dimensional line scans.

Chapter 9

Neuromorphic MoS_2 memtransistors fabricated by localised helium ion beam irradiation

We have discussed in the introductory sections that 2D layered semiconductors have recently emerged as attractive building blocks for next-generation low-power non-volatile memories. However, the down-scaling of lateral *memtransistors* is ultimately limited by the grain boundary distribution; restricting large-scale device implementation due to the intrinsic difficulty in fabricating GBs with a high density, uniformity and organisation. The ability to locally modify the structure of TMDs by scalable and industry-compatible top-down methods so that resistive switching is induced in these materials has remained a challenge. The HIM is a relatively novel scientific instrument whose functionality allows for the targeted, localised introduction of defects into layered semiconductors. As such, it is an ideal candidate for *prototype* studies where high spatial resolution and fluence control is required to manipulate the structure and properties of 2D materials. One of the main achievements of this thesis is the experimental realisation of lateral on-dielectric memtransistors from monolayer single-crystal MoS_2 utilising a focused helium ion beam. Site-specific irradiation with the focused probe of the HIM allows for the creation of charged defects in the MoS_2 lattice. The reversible drift of these locally-seeded defects in the applied electric field modulates the resistance of the semiconducting channel, enabling versatile memristive functionality on the nanoscale. The device can reliably retain its resistance ratios and set/reset biases for 1180 switching cycles, while a range of optimal ramping speeds was also investigated. Long-term potentiation and depression with sharp habituation that is demanded by future neuromorphic architectures is demonstrated in individual components. This work establishes the feasibility of ion irradiation for the controllable fabrication of 2D memristive devices with promising key performance parameters such as low power consumption. The applicability of these devices for synaptic emulation may address the demands of future neuromorphic architectures.

9.1 Memtransistor fabrication with the helium ion microscope

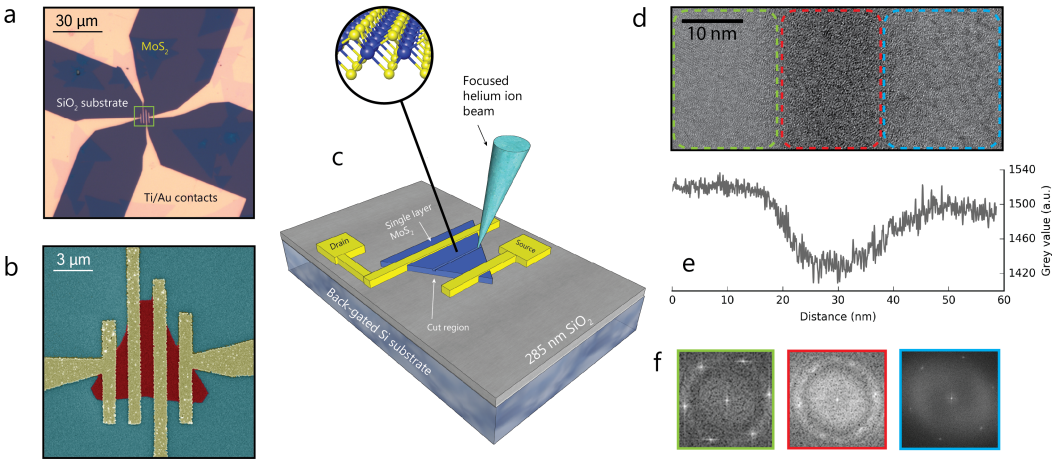

Figure 9.1: **Device fabrication and characterisation of the irradiated region.** **(a)** Optical micrograph of monolayer CVD MoS_2 flakes grown on a SiO_2 substrate contacted with EBL-deposited Ti/Au electrodes. **(b)** False-colour SEM image of the region marked with the green square in **(a)**, showing a single-crystal device contacted with multiple terminals. **(c)** Illustration of the irradiation strategy. **(d)** TEM image of the fissure region on a mechanically-exfoliated few-layer sample. We observe a defect-rich region in the MoS_2 laterally spanning > 10 nm. Areas immediately adjacent to the fissure show different levels of defectivity (*blue*: higher, *green*: lower), suggesting that the ion beam preferentially introduces an asymmetric defect distribution into the sample, as outlined by the intensity line scan in **(e)** and the FFTs evaluated from each region in **(f)**.

We once again employ the close-proximity CVD method to grow large single-crystal triangles of monolayer MoS_2. **Figure 9.1(a)** is an optical micrograph of a typical device, which can contain multiple channels on the same flake. The area marked with the green frame is shown magnified in the false colour SE micrograph in **Fig. 9.1(b)**. The irradiation strategy for inducing memristive behaviour in MoS_2 involves tracing out a unidirectional single pixel-wide line scan of dose 1.6 pC μm^{-1} to bisect the whole FET channel, i.e. parallel to the source and drain electrodes (see geometry in **Fig. 9.1(c)**). This introduces a *fissure* region in the middle of the channel. The irradiation is performed once a sub-3 nm probe size is obtained by focusing elsewhere close-by on the SiO_2 chip. Exposure to the MoS_2 channel at this beam energy will introduce sulfur vacancies into the material, as studied previously with nanoscale EDX [192] and predicted by simulations [204]. For additional SEM and HIM images of the fissure region see also **Fig. 9.2**. The irradiated region shows darker contrast on the SiO_2 substrate due to differing SE yield.

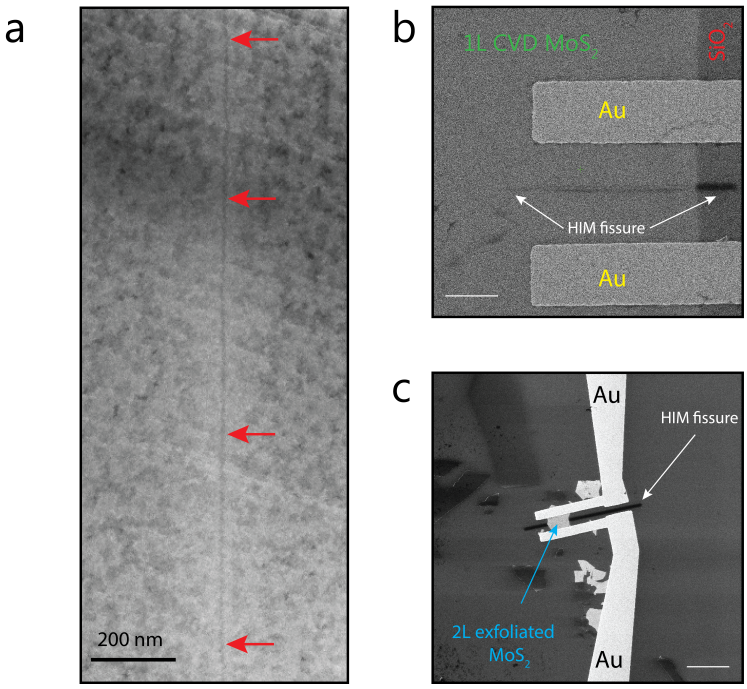

Figure 9.2: **SEM and HIM images of irradiated devices.** **(a)** High-magnification SEM image (5 keV) of the fissure region with minimal beam-induced deposition built up on the surface. The ion-damaged region is faintly seen running from top to bottom of the image; its right edge is marked by the red arrows. **(b)** HIM image (30 keV) of an irradiated monolayer CVD device, showing darker contrast of the cut on the SiO_2 substrate due to differing SE yield. Scale bar is 3 μm. **(c)** HIM image (30 keV) of a bilayer MoS_2 memtransistor, showing the fissure region extending out onto the substrate on both sides of the device to ensure complete channel bisection. Scale bar is 5 μm.

Figure 9.1(d) shows a TEM image of the fissure region on a suspended few-layer sample irradiated at 1.6 pC μm^{-1}. We observe damage extension in the fissure area (red) to > 10 nm and a visible difference in the level of defectivity on either side of the helium-introduced cut. This asymmetry - which is induced by the irradiation - is crucial to the functionality of this resistive switch, as we will go on to explain in the coming sections. Its origin may come from either the astigmatism of the ion probe or the natural tilt of the sample on the substrate. **Figure 9.1(e)** is an averaged intensity line scan across the regions shown in the TEM image, demonstrating the increased intensity variation in the fissure and the blue region, relative to the green region. **Figure 9.1(f)** collates the FFTs taken from each colour-coded area, showing a varying degree of MoS_2 crystallinity across all three regions. More plan-view micrographs of irradiated MoS_2 samples are shown in **Figs. 9.3(a-c)**.

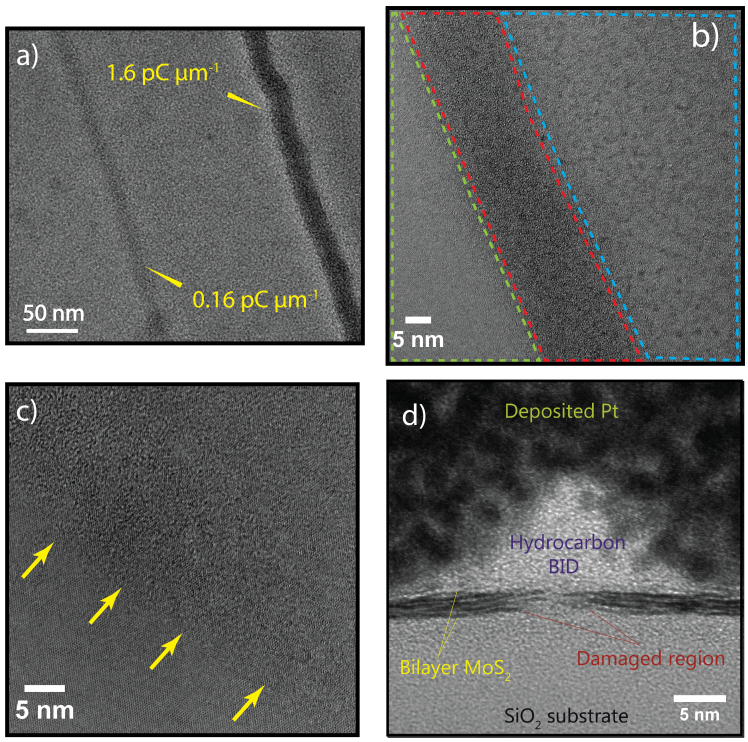

Figure 9.3: **Plan-view TEM images of ion beam cuts performed on suspended MoS_2 at doses of 0.16 and 1.6 pC μm^{-1}, and a cross-sectional TEM image of the fissure region after a FIB lift-out.** **(a)** Side-by-side exposures at different doses on the same sample, showing visible differences in phase contrast due to larger BID buildup on the higher-dose cut. **(b)** Fissure region (red) showing clear asymmetry of the defectivity level about the irradiated area. The green area has suffered less damage from ion irradiation than the area in blue. **(c)** Closer look at the interface between the green and red regions from **(b)**. The boundary between the irradiated region and pristine MoS_2 extends only a few atomic rows and is demarcated by the yellow arrows. Data in **(a)**-**(c)** was acquired by Dr. Danny Fox. **(d)** Cross-sectional TEM image of the fissure region of an irradiated device lamella (mechanically-exfoliated bilayer), prepared by FIB lift-out (lamella prepared by Dr. Pierce Maguire, imaging by Clive Downing). We note that the extent of true lattice damage to the MoS_2 flake is obscured from plan view by the hydrocarbon BID mound, and in actuality extends to just under 10 nm, where it interfaces abruptly with the pristine lattice. TEM beam energy = 300 keV.

We note that the true extension of the MoS_2 lattice modification is obscured from plan view by the ion beam-induced deposition (BID) which forms on the MoS_2 surface due to the highly-charged beam exposure. In **Fig. 9.3(d)** we present a cross-sectional TEM image of the fissure lamella prepared by lift-out in the FIB. The observed MoS_2 lattice damage extension from the centre of the Gaussian probe is in agreement with the range estimated from simulations for the beam energy of 30 keV employed in our experiments [204]. The edge of the damaged region in this work functions as a rich source of charged mobile defects, i.e. sulfur vacancies. Their drift in the applied electric field modulates the carrier concentration in the fissure area, which ultimately governs the memristive behavior of the device. We note that ion implantation doping schemes in the semiconductor industry are also site and

dose specific, while our method provides rapid prototyping and device optimisation for the scalable ion-based fabrication of 2D memristive devices.

The ion BID observed on top of the fissure in SEM, HIM and TEM is a by-product of the fabrication process. A charged focused probe will cross-link adventitious surface-adsorbed organic molecules at the irradiation site, and attract further molecules to diffuse towards the charged impact site [331]. These hydrocarbons will continue to cross-link and pile up on the beam impact site, as long as a reservoir of foreign molecules is present in the microscope chamber (be it from the chamber itself [332] or the sample surface). Their deposition rate, S, depends on the incoming beam energy, E, such that:

$$S \propto \ln\left(\frac{J/E}{E}\right) \approx E^{-0.8} \tag{9.1}$$

where J is the mean ionisation energy. Thus, a sub-second scan necessary to perform our irradiation on a single device leads to the formation of a BID mound from residual organic molecules in the chamber that can be anywhere from 1 to 10 nanometres in height. This mound is a mostly sp^2-hybridised [333], amorphous electrical insulator which is notoriously difficult to fully remove; rendering standard solvent washes (IPA, acetone, water) unhelpful [334]. Harsher methods such as sample annealing and *in-situ* plasma cleaning of the microscope chamber [335] degrade MoS_2 samples [336, 124] and hence are not suitable for this work. As the ion BID deposit is chemically inert and electrically insulating, currently we have no reason to believe that its presence is detrimental to the device performance in this work.

We find that the height of this mound is dependent on the delivered dose of the helium ion beam. This is expected, as the dwell time is increased when increasing the dose, thus allowing more time for adventitious hydrocarbons to be attracted to the beam impact site. AFM maps of the irradiated monolayer MoS_2 area as a function of increasing ion dose, close to the memristive dose, are presented in **Fig. 9.4**, while a high resolution map of the area irradiated at exactly 1.6 pC μm^{-1} is presented in **Fig. 9.5**. A set of data showing the mound heights after irradiation on samples of different layer number are also shown in **Table 9.1**.

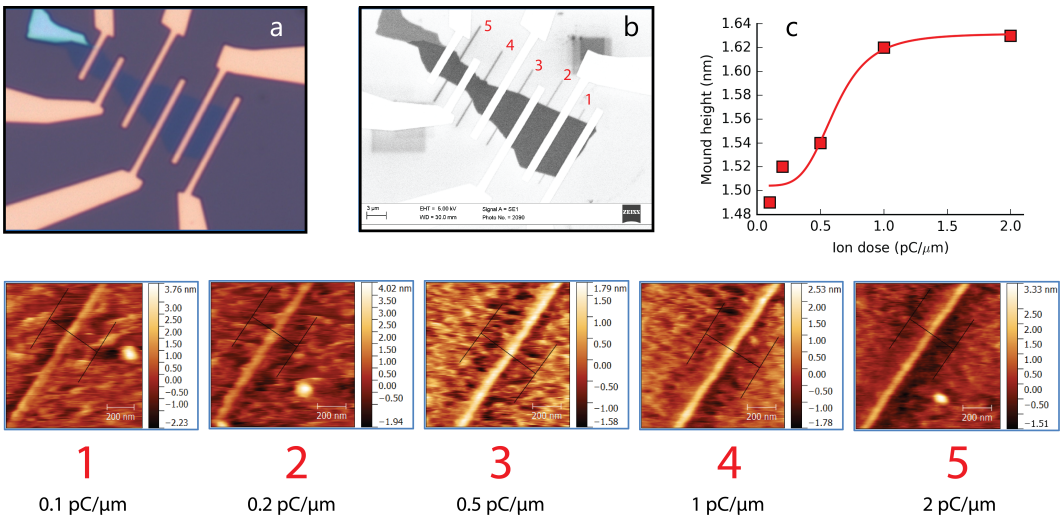

Figure 9.4: **Dependence of hydrocarbon BID mound height on the delivered ion dose. (a,b)** Optical and SEM images of a monolayer device irradiated at different helium ion doses. The 1-5 labels correspond to the AFM maps presented below. **(c)** Extracted mound heights from the regions marked in AFM maps at each respective dose. The solid line is a saturating fit scaling as $\propto \frac{1}{1+d^{\alpha}}$ where d is the dose and α is a fitting exponent. Data taken by Darragh Keane.

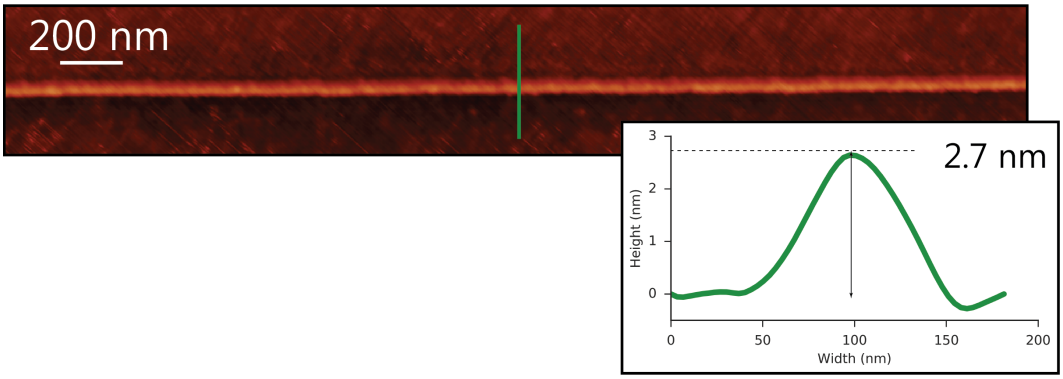

Figure 9.5: **AFM of a device irradiated at the memristive dose.** AFM scan of an irradiated line fissure on monolayer CVD MoS_2. At the delivered ion dose of 1.6 pC μm^{-1}, the build-up of the hydrocarbon BID is observed to average out at $\sim$ 2.7 nm along the length of the fissure on this particular sample. Inset: thickness line profile taken from the green line marked on the AFM map. Data taken by Darragh Keane.

Sample	Thickness	Height increase on fissure	Flake RMS surface roughness
CVD	1L	2.6 nm	0.38 nm
CVD	1L	1.7 nm	0.46 nm
Mech.	1L	1.6 nm	0.39 nm
Mech.	2L	2.3 nm	0.8 nm
Mech.	4L	1.3 nm	0.25 nm
CVD	1L	2.7 nm	0.33 nm

Table 9.1: **Summary of ion BID heights on different samples mapped with AFM.** The average height increase noted from the AFM measurements is 2.03 nm. The RMS surface roughness of each flake around the fissure is also listed. *Mech.* - mechanically-exfoliated.

Considering the TEM cross-section in **Fig. 9.3(d)**, we can evaluate the actual ion dose distribution about the centre of the fissure. **Figure 9.6** shows a simulated areal helium ion dose distribution for a line scan with overlapping beam probes (spacing 1 nm), extending into the page.

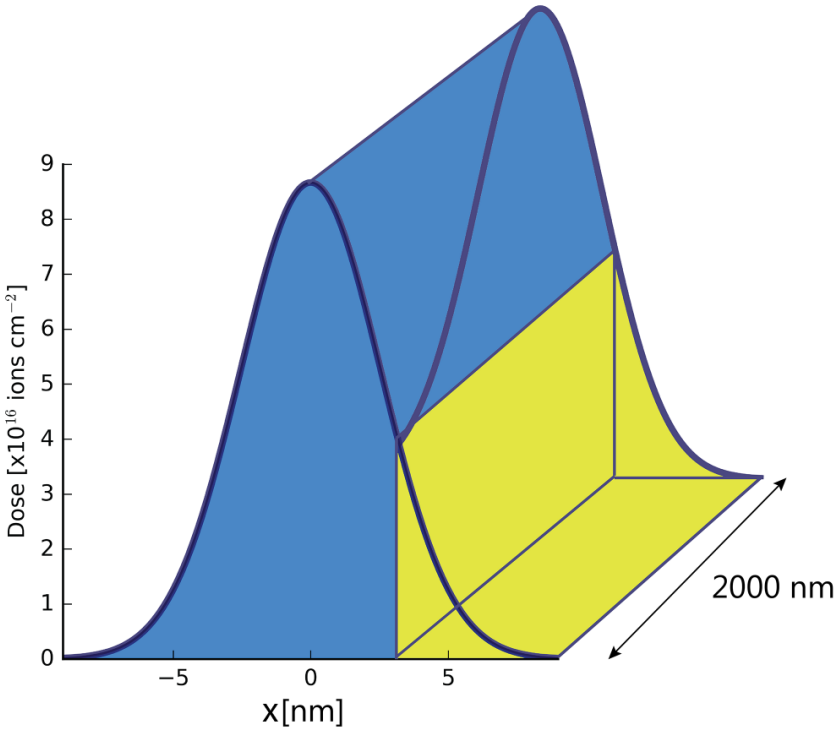

Figure 9.6: **Sketch of simulated dose delivery** along a line scan of probe size 6 nm, as based on the TEM cross-section from **Fig. 9.3(d)**.

The Gaussian distribution of the ion dose is smeared by a 6 nm probe size, as estimated by the spread of the highly-damaged lattice area in the cross-sectional micrograph. We assume that any ions delivered to the MoS_2 lattice integrated under

the blue region cannot cross or leave the fissure, effectively not contributing to the creation of mobile V_S species. The region shaded in yellow marks the concentration of delivered ions that will be able to sputter sulfur atoms and leave behind potential mobile vacancies on one side of the device.

The integrated areal dose in the yellow portion of the curve was calculated to be 6.4 $\times$ 10^{16} ions cm^{-2}. As the sputter yield of S per helium ion is $\approx$ 0.007 [322], the final higher bound for the available V_S concentration sourced from the yellow strip is therefore 4.2 $\times$ 10^{14} V_S cm^{-2}.

9.2 Resistive switching in He^+-irradiated MoS_2

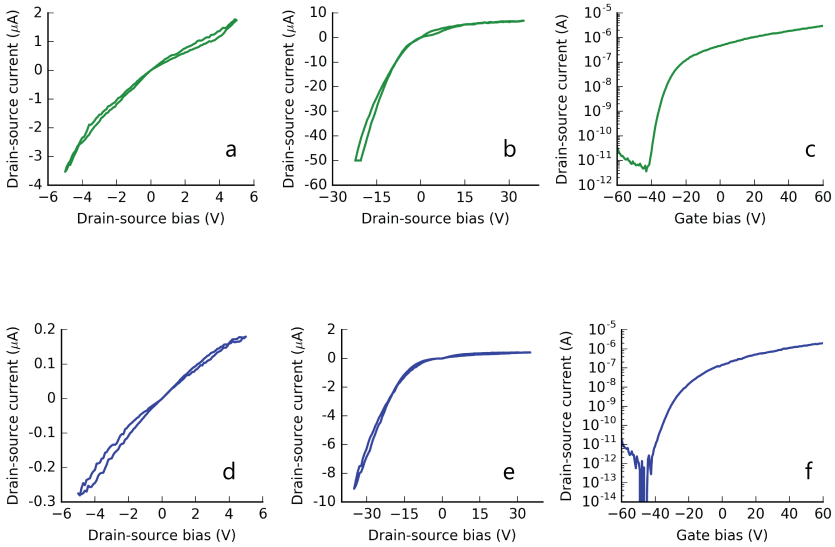

Figure 9.7: **Typical *I-V* and gate curves of non-irradiated CVD devices. (a,b,c)** *I-V* curves between ± 5 V, ± 35 V and gate curve, respectively, for the same device. **(d,e,f)** *I-V* curves between ± 5 V, ± 35 V and gate curve, respectively, for another device on the same chip. In both cases, no significant hysteresis opens up in the output characteristics even at large V_{ds}. Transfer curves are typical of n-type MoS_2 with μ_{fe} in the linear region not exceeding 10 cm^2 V^{-1} s^{-1}.

The starting materials in this study do not possess grain boundaries, and their initial electrical performance is typical of pristine n-type MoS_2 FETs, with no hysteresis observed in the *I-V* characteristics (see **Fig. 9.7**).

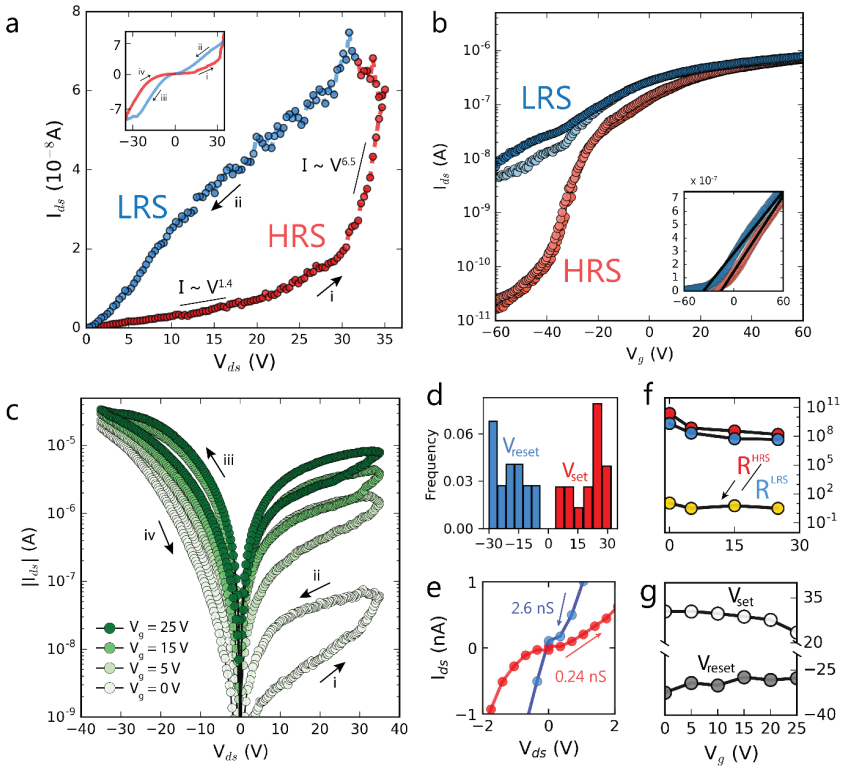

Figure 9.8: **Gate-tunable resistive switching in the helium ion beam-fabricated memtransistor.** *Note*: where they appear, arrows with Roman numerals mark subsequent parts of the *I-V* sweep. **(a)** Positive-bias sweep region of an irradiated monolayer memtransistor device (L = 1 μm, W = 6 μm) recorded at V_g = 0 V. Inset: full range of the sweep with labelled trace directions. A sharp emergence of non-linearity in the *I-V* sweep marks the set point from HRS to LRS. The device stays in LRS until a reset bias of negative polarity is reached on the reverse sweep. **(b)** Gate curves of the memtransistor taken alternately at V_{ds} = 1 V in both LRS (*blue*) and HRS (*red*). Sweeps in the same state are marked by different shades of blue or red. Inset: same plot on the linear scale, with fits to the linear FET region in black extending to the threshold gate bias, V_{th}. **(c)** Gate-modulated *I-V* sweeps of the same device. Each full cycle was recorded at the labelled V_g value. **(d)** Histograms of V_{set} and V_{reset} values recorded in 16 monolayer CVD memtransistor devices at V_g = 0 V. Switching can occur at biases as low as 3 V in some devices. **(e)** Magnified look at the zero-bias pinched region of the *I-V* curve from **(a)**, demonstrating the disparate conductances of the two states as V_{ds} is ramped up at low bias. **(f)** Resistances of each state as a function of gate bias (in units of Ω), with the resistance ratio (R_{HRS}/R_{LRS}), no units) plotted in yellow. **(g)** Set/reset biases (in V) as a function of gate voltage. Increasing positive gate fields bring about an earlier onset of resistive switching for both polarities. Note that **(d,e)** and **(f,g)** share the same x-axis units.

Upon the creation of the fissure with the helium ion beam, a significant hysteresis opens up in the output curve of the device as shown in **Fig. 9.8(a)**. This particular device sets into HRS when first irradiated. As V_{ds} is swept from 0 V to 35 V (red trace), we observe a sudden highly non-linear increase in the current, as the device switches into the LRS. The memtransistor remains in LRS as the bias is decreased back to 0 V (blue trace), until a change in bias polarity is introduced and the device is reset into the high resistance state. HRS persists then as the bias is swept back

up to 0 V (see full sweep on linear scale in the inset of **Fig. 9.8(a)**). For this device, the set (V_{set}) and reset (V_{reset}) biases, defined here as the biases at which a sharp non-linearity emerges in the *I-V* curve, are 31 V and -32.5 V, respectively. The zero-bias pinching of the loop, and the requirement of polarity change for resetting are hallmarks of bipolar resistive switching. The opening of this hysteresis is accompanied by a significant drop in the drain current (three orders of magnitude relative to the non-irradiated device I_{ds}), and the output curve is more symmetric with respect to the origin. This indicates the fissure region exhibits the largest resistivity compared with other elements in the device, i.e. the contact interfaces, the non-irradiated regions. The fissure area therefore is the *current-limiting resistor* in this lateral stack and is responsible for the opening of the *I-V* hysteresis.

Figure 9.8(b) shows the transfer curves of the device in the respective resistance states. Significant shifting of V_{th} is observed from -19 V in HRS to -37 V in LRS, with V_{th} remaining stable through alternating gate sweeps in each state. The different shades of blue and red respectively in **Fig. 9.8(b)** represent gate sweeps (- 60 V to 60 V) taken immediately after two consecutive switches between states, i.e. HRS gate sweep → *I-V* switch to LRS → LRS gate sweep → *I-V* switch to HRS → HRS gate sweep → *I-V* switch to LRS → LRS gate sweep. High output current levels at V_g = -60 V suggest the presence of surplus donors in the channel in LRS. The opening of this hysteresis is accompanied by a drop in μ_{fe} relative to the non-irradiated device (6.2 $cm^2\ V^{-1}\ s^{-1}$ before irradiation to < 1 $cm^2\ V^{-1}\ s^{-1}$ afterwards). No major change in mobility at V_g = 0 V is observed between states (0.14 $cm^2\ V^{-1}\ s^{-1}$ and 0.16 $cm^2\ V^{-1}\ s^{-1}$ in HRS and LRS respectively), despite a tenfold difference in conductivity. This suggests a fundamentally similar transport mechanism in both states, with the major differentiating factor between states being the level of available donors in the channel. The difference in n_{2D} between states detected by gating is $\approx 1.57 \times 10^{12}\ cm^{-2}$. The estimated V_S concentration induced by sputtering at this delivered dose is thus comfortably above the experimentally-detected carrier concentration difference between LRS and HRS, suggesting that even more vacancies get trapped in the fissure region; possibly due to back-scattered and secondary atom sputtering events extending the fissure region beyond the assumed probe size confinement.

Application of the field effect through the back-gate oxide allows for the tuning of the onset of switching, as well as the resistance ratio of the memtransistor. **Figure 9.8(c)** shows *I-V* sweeps on a semi-log scale taken at multiple gate biases, while **Fig. 9.8(d)** collates the set and reset biases recorded in 16 different monolayer CVD

memtransistor devices (average V_{set} = 21.3 V, average V_{reset} = - 19.5 V). **Figure 9.8(e)** shows a magnified look at the zero-bias pinched region, with disparate conductance values of both states shown on the plot. The degree of hysteresis and the resulting resistance ratios (**Fig. 9.8(f)**) can be manipulated by the gate bias, with values in the subthreshold regime of the transistor resulting in greater quotients. **Figure 9.8(g)** tracks the effect of the gate bias on V_{set} and V_{reset} of the device, with increasing gate fields reducing the bias necessary to switch between states. Our irradiation strategy makes it possible to write multiple memristive circuit elements in specified locations on a single chip. Their carrier concentrations can then be controlled at the same time by the global back-gate, opening new possibilities for novel circuit design. Similar data from another monolayer device are presented in **Figure 9.9**.

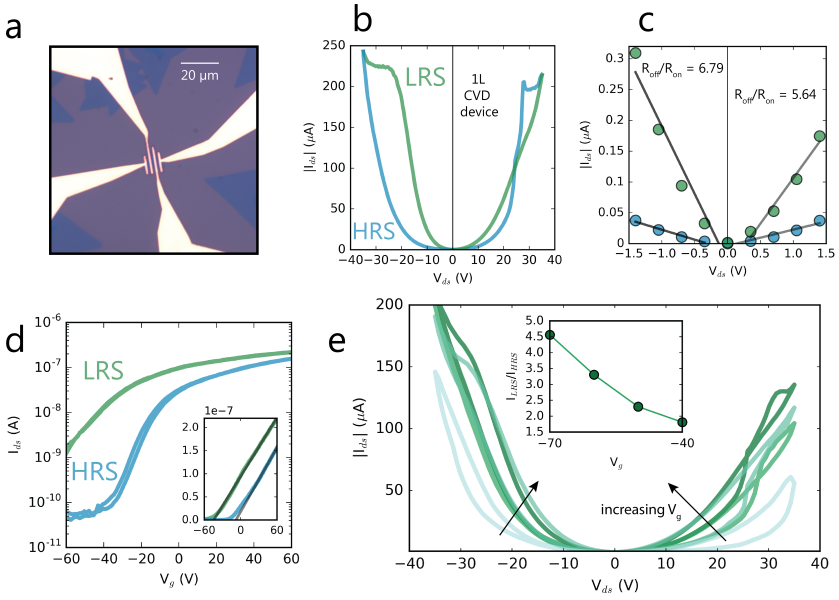

Figure 9.9: **Example of switching on another 1L CVD device.** **(a)** Optical image of the memtransistor. **(b)** *I-V* curves showing distinct resistance states with an additional crossover in the positive-bias section of the hysteretic loop. **(c)** Resistance ratios fitted in the low bias regime. **(d)** Gate sweeps of the device demonstrating LRS V_{th} shifting to negative V_g. Inset is the same plot on the linear scale. Data taken at V_{ds} = 1 V. **(e)** Gate-tunable looping behaviour of the device. The black arrow marks the direction of increasing V_g. Inset: Dependence of resistance ratios on the applied gate bias. The ratio increases with increasing negative polarity.

We note that some devices start in LRS, exhibit multiple crossovers during the sweep and show NDR. The V_{set} will also vary from device to device, subject to channel non-uniformity and the intrinsic level of defects present in the pristine flake. However, the underlying mechanism of dopant drift, which we will discuss in detail in the spectroscopy section, remains consistent. To demonstrate the effectiveness of the helium beam in inducing resistive switching in layered materials, we repeated

the experiments on MoS_2 devices of various thicknesses (2, 4, 8 and 10 layers) and we also observed similar gate-tunable memristive functionality allowing our methodology to be extended to devices of larger layer thickness. We present this data in **Fig. 9.10** and **Fig. 9.11** below.

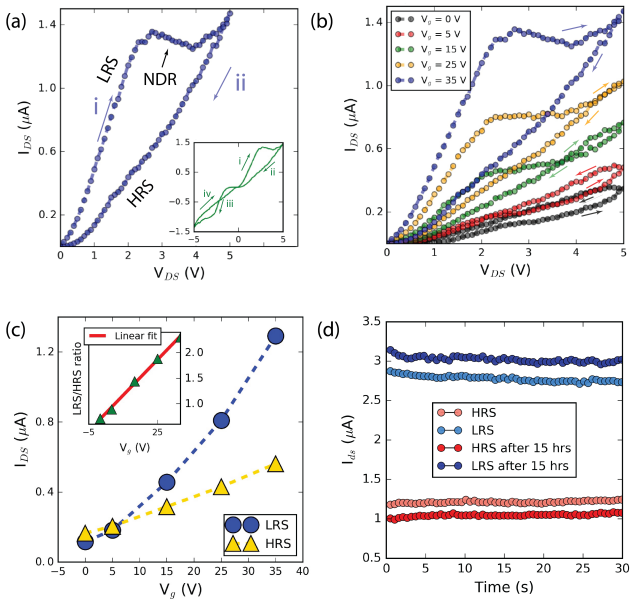

Figure 9.10: **Switching behaviour in mechanically-exfoliated bilayer MoS_2.** **(a)** *I-V* curve of a bilayer device, starting in LRS and demonstrating NDR before switching to HRS. Inset is the full range curve, with an additional resistance crossover on the negative side of the sweep. **(b)** Gate field tunability of the hysteretic loop; higher positive biases reduce the resistance ratio. **(c)** Resistance state read currents at different values of the back-gate bias, extracted at the largest discrepancy point between states in the *I-V* loop. Inset shows the linear scaling of this absolute largest resistance ratio with increasing gate bias; which follows from the scaling of V_{set} with V_g discussed previously. **(d)** Retention times of resistance states in a bilayer device, showing current levels in each state after cutting off power supply for 15 hours. V_{ds} during readout was 1 V.

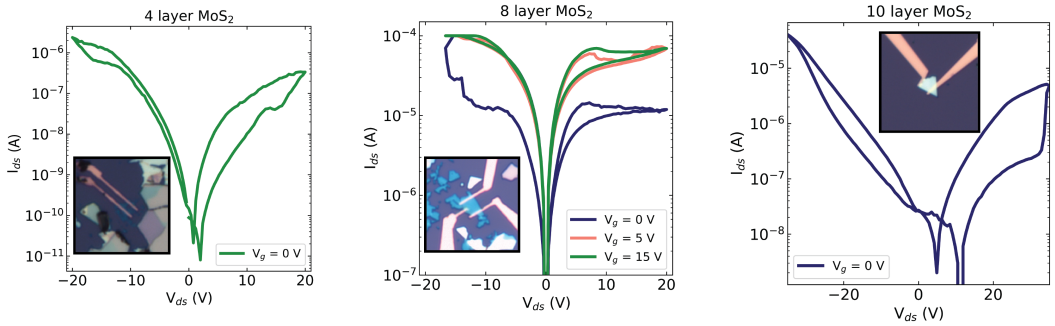

Figure 9.11: **Examples of resistive switching on mechanically-exfoliated samples of different layer number.** Optical images of each are attached as insets. All were irradiated at a He^+ ion dose of ~ 1.6 pC μm^{-1}, demonstrating the generalisability of this method to TMDs of larger layer number. Data acquired by Darragh Keane.

9.3 Performance metrics of the HIM-enabled MoS_2 memtransistor

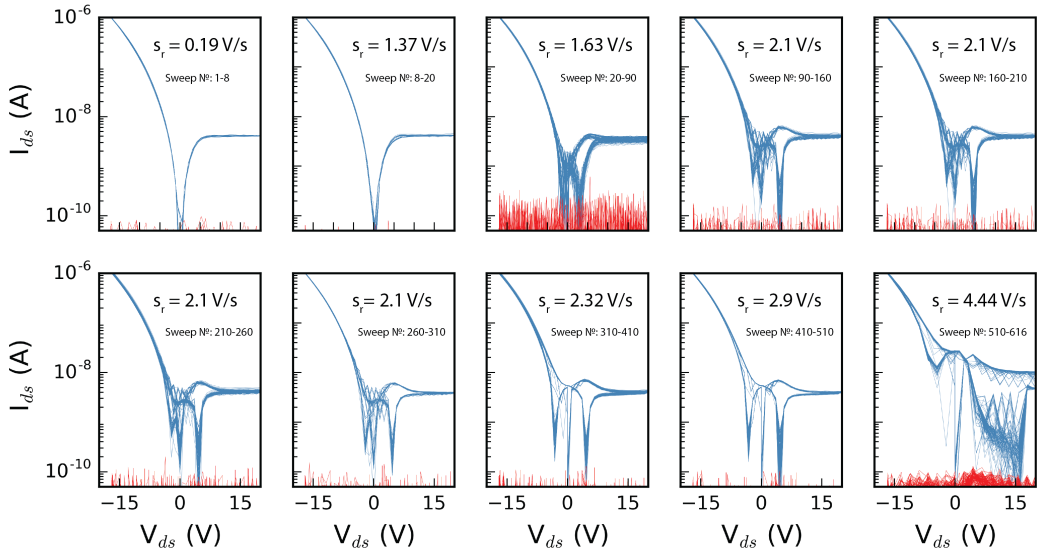

Figure 9.12: **Consecutive switching cycles of a monolayer CVD memtransistor device.** The graphs are organised in order of consecutive testing, with the ramping speed and cycle numbers labelled on each plot. Blue traces are the I_{ds} recorded on sweeps of V_{ds} = ± 20 V. The red trace is the recorded gate leakage current for each cycle, showing negligible leakage close to the noise floor of the SMU.

We evaluate the switching parameters of a well-performing monolayer device (L = 8.5 μm, V_g = 5 V, measured at ~ 10 mbar) as a function of ramping speed, s_r. With a given s_r, the V_{ds} was ramped between ± 20 V, as this ensures the switching between HRS and LRS on this device. The resistances were read off at V_{ds} = 4 V (see evolution of epochs in **Fig. 9.12**). We make a note here on the unusual shape of some of the curves when hysteresis opens on this particular device. The NDR region observed between ~ 5-10 V and the instances of more complementary-like switching [337] may be indicative of tunnelling diode-like behaviour across the insulating tails of the fissure region sandwiched between regions of more conductive MoS_2. In **Fig. 9.13(a)**, each coloured portion of the plot indicates the s_r at which the *I-V* characteristics were swept, with s_r values marked on each portion. The black data points in the bottom part of the plot trace out the R_{HRS}/R_{LRS} ratio for each cycle. The HRS and LRS resistances exhibit negligible temporal variation between cycles when tested in the optimal s_r range of 2.1-2.9 V s^{-1}. Sub-optimal ramping speeds on either side of this range overdamp/underdamp the ionic drift process resulting in the loss of stability or no switching of resistance at all.

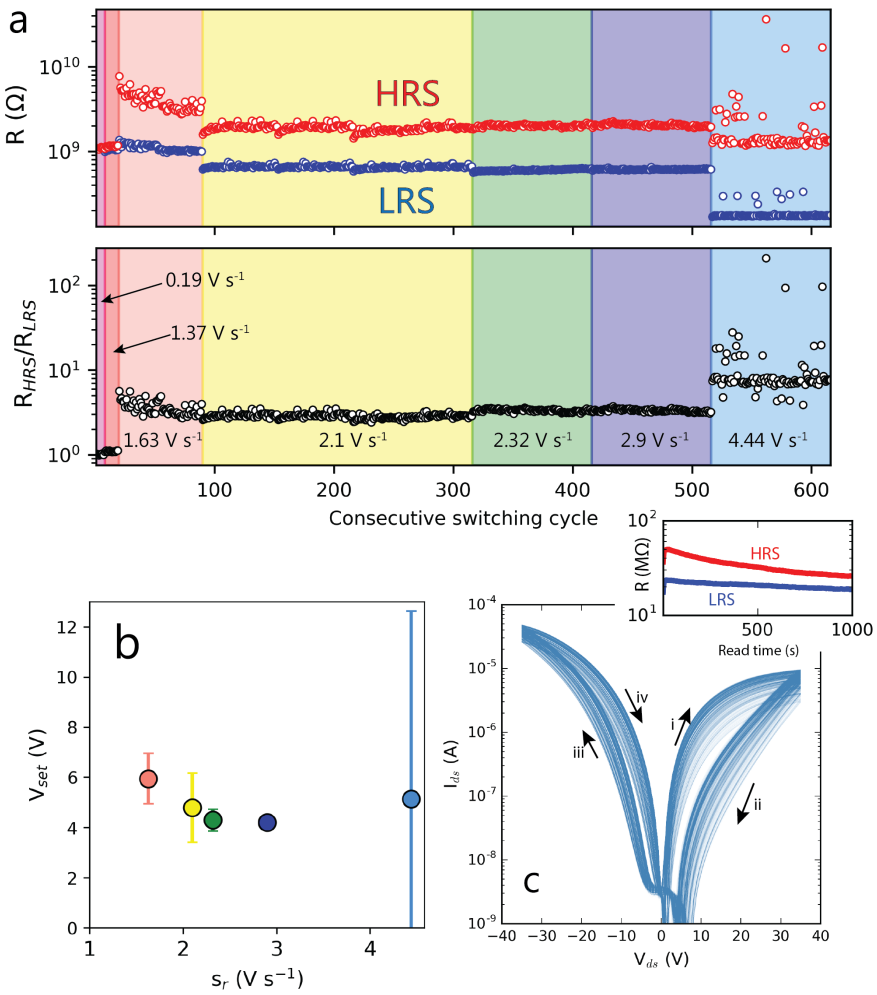

Figure 9.13: **Cycling endurance and stability of resistance states.** **(a)** Endurance (top) and resistance ratios (bottom) of resistance states read off at V_{ds} = 4 V and V_g = 5 V across more than 600 consecutive ± 20 V switching cycles at different ramping speeds, s_r. Each coloured portion of the plot corresponds to the s_r used to evaluate device performance, as labelled on the graph. **(b)** Dependence of V_{set} on ramping speed, showing the device instability at higher-than-optimal s_r. **(c)** 1180 consecutive *I-V* epochs of another monolayer CVD memtransistor device (L = 9 μm) recorded over 7 hours and 56 minutes. The retention of each state resistance (R) for > 10^3 s at V_{read} = 5 V is shown in the inset in the upper right corner.

Figure 9.13(b) visualises the distribution of set biases as s_r changes. Set/reset bias stability is a crucial parameter that governs accurate learning in neuromorphic devices, with low stochastic variations between epochs necessary for the optimal performance of resistive random-access memory hardware [338, 339]. The V_{set} is extracted based on a reached current threshold and is noted to drop with increasing s_r, from 5.95 V at s_r = 1.63 V s^{-1} to 4.21 V at s_r = 2.9 V s^{-1}. Meanwhile, the standard deviation (error bars in the plot) of the V_{set} distributions at each ramping speed tends to fall with rising s_r, with negligible deviations on a ± 20 V sweep

range at s_r = 2.9 V s^{-1}. At the more extreme s_r of 4.44 V s^{-1}, the V_{set} becomes unstable, with the mean value rising again with a very high deviation at this high ramping speed. We note that for large-scale implementations of neuromorphic architectures, it is preferable to operate memtransistors at a low V_{set} to reduce power consumption, while retaining a high resistance ratio. Seeking this trade off needs to be the goal of future work in this area, while the device-to-device variability ought to be standardised by consistent material growth, yielding a comparable intrinsic defect concentration between individual devices.

Figure 9.13(c) presents 1180 consecutive *I-V* traces on another monolayer CVD device, collected over a period of 7 hours and 56 minutes of constant cycling, demonstrating excellent endurance of the He^+ ion-fabricated memtransistor. The inset of **Fig. 9.13(c)** shows the retention characteristics of currents in both resistance states on the same device, read out at V_{ds} = 5 V for > 10^3 seconds. The resistance of the HRS tends to collapse with increasing readout time, as is also the case in the polycrystalline MoS_2 memtransistors [108], suggesting that the ionic species in the device are quite mobile. Future temperature-dependent studies ought to shed light on the activation energy of these mobile species and how they contribute to the switching dynamics. The stability of V_{set} and V_{reset} is also looked at more closely in **Fig. 9.14(a-c)**.

A unique feature of this device is the rise of the R_{HRS}/R_{LRS} ratio and the conductance increase of both resistance states at higher-than optimal s_r, which is unusual for resistive switches [340]. The short migration range of the vacancies in the fissure region (< 10 nm) may facilitate sudden resistance state switching at high sweep rates (effectively pulsing the voltage input), while the current in both HRS and LRS is seen to increase; most likely due to the non-negligible parallel capacitor AC component of the metal-insulator-metal device structure at this s_r. The sketch in **Fig. 9.14(d)** demonstrates a simplified circuit diagram of the effective device structure. As MoS_2 is quite resistive, it may be considered as a dielectric sandwiched between metal contacts (*left*); in parallel with a memristor (*right*). When a high frequency AC voltage is applied to the circuit, the current flowing through the capacitor becomes non-negligible, increasing the I_{ds} recorded in both HRS and LRS.

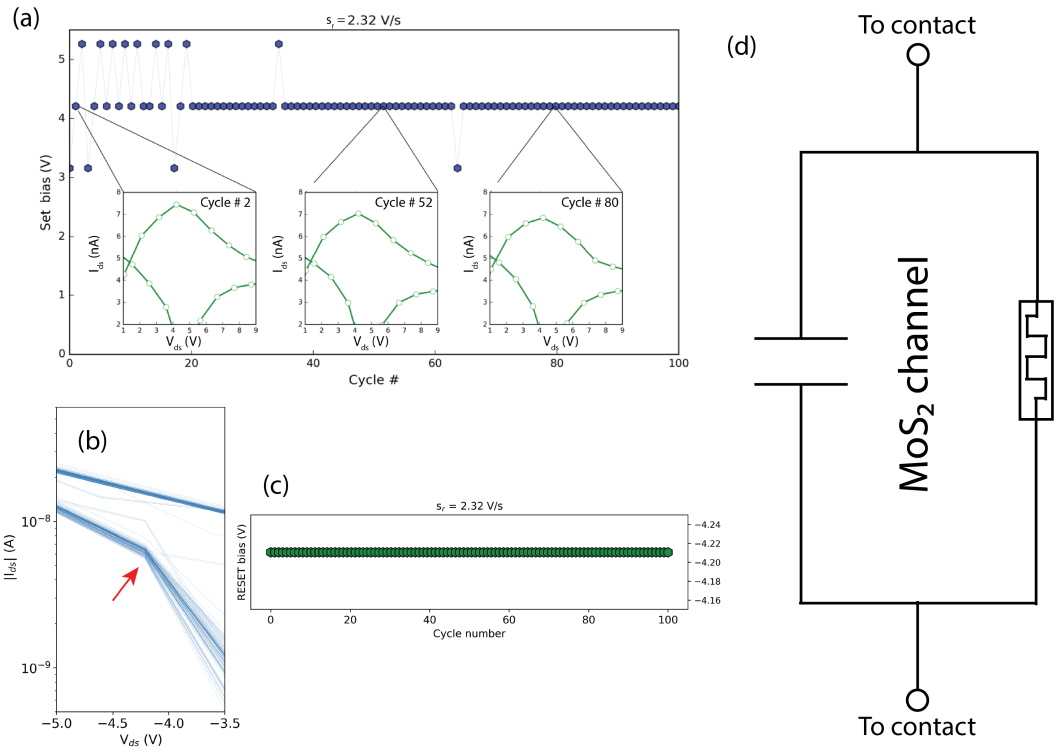

Figure 9.14: V_{set} **&** V_{reset} **stability, and a simplified circuit diagram of the device.** **(a)** Set bias stability over 100 switching cycles at s_r = 2.32 V s^{-1} from **Fig. 9.13(a)**. The shape of the hysteretic loop varies around the V_{set} as the device is stabilised by consecutive switching cycles, and the maximum current level drops slightly. The insets in green are the V_{set} portions of the n^{th} labelled s_r = 2.32 V s^{-1} graph from **Fig. 9.12**. **(b)** Evolution of *I-V* curves swept at s_r = 2.32 V s^{-1} on the negative portion of the sweep (reset). Red arrow points to the bias at which the resistance branches switch. **(c)** Extracted V_{reset} as a function of cycle number at the same ramping speed. **(d)** Circuit diagram of the simplified structure of the metal/highly-resistive MoS_2/metal device. It consists of parallel capacitor and memristor components. At high s_r the current flowing through the capacitor becomes non-negligible.

Meanwhile, the collapse of HRS seen in the time retention data in **Fig. 9.13(d)** suggests that its faltering is the cause for *I-V* loop collapse; ostensibly due to non-zero V_S drift in HRS, even at low read V_{ds}. Our devices are bipolar resistive switches and ought to show a hallmark of this type of functionality, i.e. the dependence of the zero-bias pinched hysteresis loop on the frequency of its input AC signal. When supplied with alternating voltage, the Lissajous figure *I-V* trace of a bipolar memristor will tend to approach that of a linear resistor as the input frequency is increased [341]. In the case of resistive switches, this may be due to over-damping of ionic drift in the device at high frequencies, driving the governing state function (the distribution of vacancies) towards its initial state; in line with pioneering memristor theories proposed by L. Chua and S. Kang [93] in 1976. In **Fig. 9.15** we present the

AC frequency dependence of the device from **Fig. 9.8(a)**, with a clear compression of the hysteresis loop when s_r is increased to 7.33 V s^{-1} (1.65 times faster than the 4.44 V s^{-1} portion of the graph in **Fig. 9.13(a)**). The *I-V* loop starts collapsing entirely, indicating that operations above 10 Hz for the memtransistor do not result in resistive switching at all, as the process of V_S drift is ultimately rate-limited. We will discuss these switching dynamics in more detail in the coming sections.

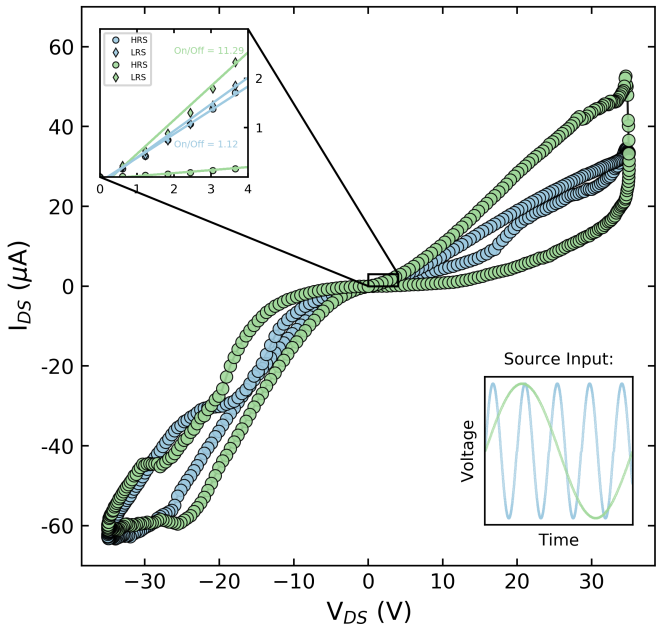

Figure 9.15: **Lissajous figure of the memtransistor at high s_r.** When the device is subjected to extremely fast ramping speeds at V_g = 0 V, the *I-V* loop is seen to shrink. Data taken by Darragh Keane.

For a comparison of other performance parameters between our devices and the latest MoS_2 resistive switches from the literature, see **Table 9.2** below:

Material (thickness, growth)	Electr-ode	G	V_{set} (V)	$\frac{R_{HRS}}{R_{LRS}}$	τ_r (s)	C	t_s (s)	P (μW)	Ref
1/few, CVD+HIM	Ti/Au	Planar	3.5-32	~ 10	$> 10^3$	1180	> 0.1	0.01-0.64	This
15nm, Printed	Ti/Au		12-20	< 10	> 30	> 5	10^{-3}	200-1200	[111]
82% 1L, CVD MoS_2	Ti/Au		~5	~ 11	N/A	500	N/A	5	[109]
1L, CVD MoS_2	Ti/Au		<12	10^4	N/A	160	N/A	0.5	[110]
CVD	Ti/Au		10-80	$\sim 10^2$	$\sim 10^5$	~ 500	10^{-3}	0.005-1	[108]
CVD	Ti/Au		8.4	10^3	120	15	N/A	2.5-2000	[107]
CVD	Cr/Au	Vertical	1-3.3	$> 10^4$	$> 10^6$	150	1	0.002-500	[112]
40nm, $MoS_{2-x}O_x$	Gra		0.45-3	~ 10	$\sim 10^6$	$>10^7$	10^{-7}	45-450	[118]
few, 92% 1T	Ag		0.066	$\sim 10^3$	N/A	10^3	N/A	20-96	[117]
few, MoS_2/MoO_x	Ag		0.1	10^4	10^3	$> 10^4$	10^{-3}	0.12	[342]
1-2, MoS_2	Cr/Au		1-1.2	10^4	$> 10^4$	20	$< 10^{-8}$	< 1	[116]

Table 9.2: **A summary of various performance parameters from relevant MoS_2 memory devices in the literature.** The presently-discussed work is highlighted in blue. The V_{set} covers ranges reported in each paper, while power consumption for the write operation is extracted at V_{set} explicitly ($P = V_{set} \times I_{ds}$). *Note*; G: device geometry, τ_r: retention time, C: endurance cycles, t_s: switching time, P: writing power, Gra: graphene.

9.4 Remark on the definition of set voltage

Let us here make a brief comment on our definition of V_{set} and the physics of what that arbitrary parameter even means. The V_{set} needs to be defined carefully for the gradual LRS-HRS transition seen in these devices. For comparison, we adopt the definition of V_{set} used by Sangwan *et al.* in the GB-enabled 2D MoS_2 memtransistors [107], where the V_{set} is the point of abrupt current increase in the *I-V* curve. This is a somewhat loose definition, which may be nonetheless empirically appropriate. We have fitted our HRS data from the device in **Fig. 9.8(a)** to the space-charge limited current (SCLC) model [343] and the trap limited current (TLC) model [344] with similar carrier mobilities to MoS_2, as shown in **Fig. 9.16**. The expressions for the current density in the two respective models are given as:

$$J_{SCLC} = \frac{A\mu\varepsilon\varepsilon_0}{d^3} V^2 \exp\left[\left(\frac{0.891}{k_B T}\sqrt{\frac{q^3}{d\pi\varepsilon\varepsilon_0}}\right)\sqrt{V}\right] \tag{9.2}$$

where J is the current density (in A m^{-2}), V the applied voltage, μ the carrier mobility, ε the device dielectric constant, ε_0 the permittivity of free space, d the device thickness, k_B the Boltzmann constant, T the temperature, q the electronic charge and A is a fitting constant;

and:

$$J_{\mathrm{TLC}} = q^{1-l}\mu N_c \left(\frac{2l+1}{l+1}\right)^{l+1} \left(\frac{l}{l+1}\frac{\varepsilon\varepsilon_0}{H_{\mathrm{t}}}\right)^{l} \frac{V^{l+1}}{d^{2l+1}} \tag{9.3}$$

where N_c is the density of states in the conduction band, H_{t} is the volumetric trap density in the device, $l > 1$ is a constant, and all other variables have the same meaning as defined above.

Taking into account the converted volumetric trap density, $\mathrm{H_t}$, observed from the threshold voltage shifts between LRS and HRS, and assuming a density of states of 10^{14} $\mathrm{eV^{-1}\ cm^{-2}}$ in the conduction band [42], we can fit the two models to our raw HRS data as it approaches the switching regime. The large deviations in both fittings are evidence that the sharp non-linearity in the *I-V* curve cannot be attributed to either SCLC or TLC alone. The SCLC regime (where the injected charge density exceeds the intrinsic free carrier density) occurs only briefly right before V_{set} is reached, while TLC-like behaviour (due to the presence of exponentially distributed trap states) can be observed shortly after the beginning of the large non-linear increase in current. Both models may not be accurate in our situation, however, as both the trap state population and available intrinsic carrier concentration varies highly between LRS and HRS as vacancies drift in and out of the fissure, respectively. Further theoretical studies need to be carried out to model the behaviour of such hybrid 2D devices to determine the exact nature of carrier transport around the point of resistance setting/resetting, such as the recent work by Wang *et al.* [345] on modelling SCLC-like transport and taking into account energy barriers associated with the presence of GBs, or alternatively the ion beam-created fissure. However, the sharp non-linearity occurs near the crossover between the SCLC-like and TLC-like regimes at ≈ 32 V. The V_{set} may thus be thought of as the crossover. In our case, the two definitions give the same value, so the approximate method employed by Sangwan *et al.* may be used here too.

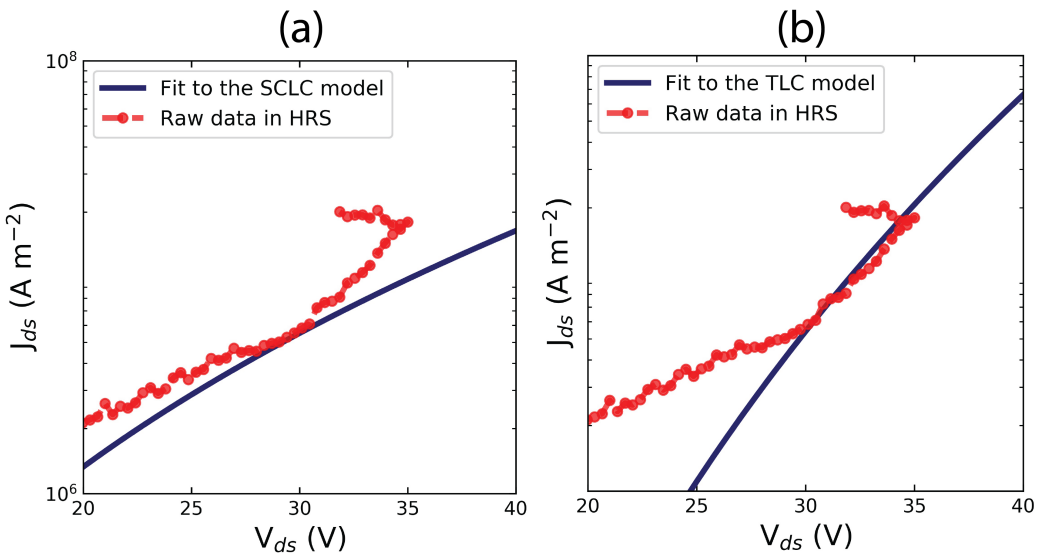

Figure 9.16: The same traces of the HRS sweep data from the device in **Fig. 9.8(a)**, up to the spike into LRS, fitted with **(a)** the SCLC model from [343] and **(b)** the TLC model from [344]. The two regimes cross over at $\approx$ 32 V.

This observed sharp non-linearity is induced by the ion movement, which is voltage-driven. At low voltages, the diffusion energy barrier for a V_S in MoS_2 is $\sim$ 2.3 eV [328]. The vacancies tend to form row structures and the lowest energy barrier for the diffusion of V_S in these row structures through the exchange of V_S with a nearby sulfur atom is 0.79 eV [346]. These row structures can hence act as metallic conducting filaments, enhancing the conductivity and lowering the potential difference. The formation of such row structures thus marks the start of the setting process, leading to the sharp non-linearity. We note that the electric field magnitudes needed for our devices to switch resistance states range from 0.42 to 24.2 V μm^{-1} in this study. Usually for MoS_2 memristors, these magnitudes are in the 1 V μm^{-1} range [107, 108, 111]. This highlights the necessity for a large voltage drop across the ion beam-created fissure in order to migrate the vacancies and to start setting the device.

9.5 Neuromorphic memtransistor performance

The success of 2D materials in future neuromorphic architectures will largely depend on their ease of implementation with on-dielectric integrated circuits, as well as their ability to mimic synaptic processes with good accuracy. Training pulses which simulate neuronal input activity were used to demonstrate the neuromorphic applicability of our devices. Voltage spikes past the V_{set} and V_{reset} were applied to

the device in order to make it learn or forget to be of a resistance, i.e. habituate to incoming stimuli by "remembering" what state it should be in by the next time it receives said stimulus. Consecutive cycles of LTP and LTD were recorded (**Fig. 9.17(a)**) by stressing the device into HRS or LRS, respectively, with a train of 16 evenly-spaced action potential pulses between electrodes 1 and 2. The post-excitation current was read out at V_{ds} = 6 V following each pulse and is fitted well with a sharp exponential rise/decay function (**Fig. 9.17(b)**), into saturation. The memtransistor was always back-gated at V_g = 5 V throughout this testing. We note that the lowest power consumption (disregarding gating) in standby is $P = I_{HRS} \times V_{read} = 16$ nW, while the write operation can be carried out at powers below 0.64 μW for all devices we have tested. This is comparable with the previously-reported polycrystalline films [108, 110, 109] and favourable when contrasted against printed multi-layer devices [111] (mW range). With optimisations, such as the reduction of channel length and contact area, our devices should start approaching the ballistic transport regime in MoS_2 [248], immunising them against further power losses upon down-scaling.

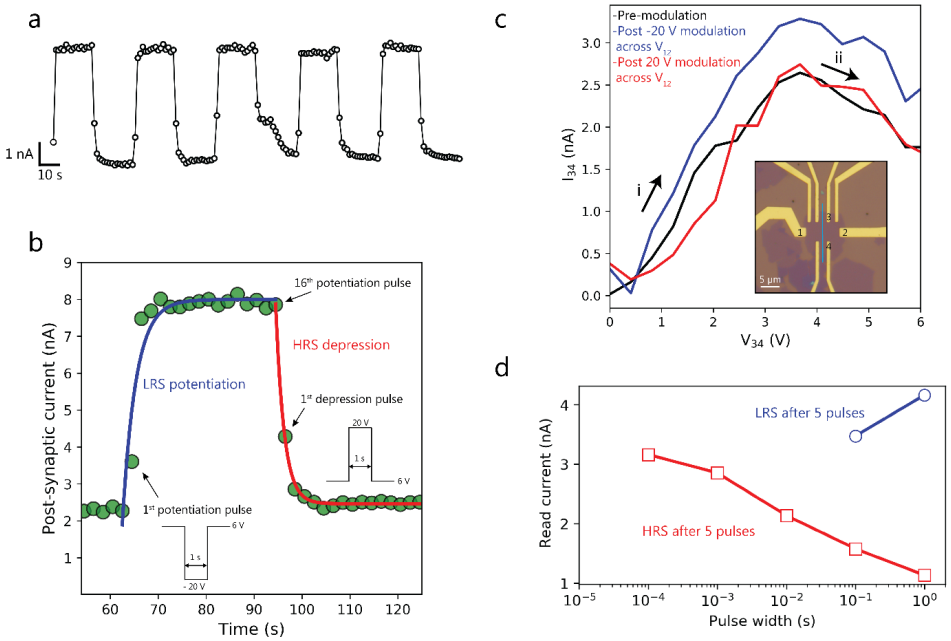

Figure 9.17: **Neuromorphic memtransistor performance, cross-terminal conductance modulation and pulsed input response. (a)** Trace of post-synaptic current recorded during 5 sequential LTP/LTD training cycles. Trains of 16 pulses were applied past the V_{reset} into LRS and V_{set} into HRS. **(b)** Closer look at the second potentiation/depression cycle from **(a)**. Both the rise and decay readouts are fitted well with single exponentials and habituate to saturated resistance values in each state within < 5 pulses. **(c)** Memtransistor cross-terminal modulation enabled by the lateral drift of defects sourced from the fissure region. Arrows indicate direction of sweep. Inset is an optical micrograph of the device with the particular terminals labelled and the cut region marked in blue. V_{34}; voltage across terminals 3 and 4, I_{34}; current across terminals 3 and 4. **(d)** Dependence of read current on the width of the pre-synaptic learning pulse. Shorter timescales inhibit complete habituation to LRS below 0.1 s at the applied read voltage of 5 V.

As demonstrated recently by Sangwan *et al.* [108], planar MoS_2 memtransistors enable the emulation of hetero-synaptic plasticity through seamless incorporation of multi-terminal architectures. **Figure 9.17(c)** presents low-bias *I-V* traces recorded between terminals 3 and 4 of the device in the inset optical image. By stressing the channel across the He^+ ion fissure (between contacts 1 and 2), defects can migrate between the fissure region and electrode 2. This modulates the conductance of the MoS_2 channel on the right-hand side of the artificial defect source, significantly altering the output current between perpendicular terminals 3 and 4. This also directly demonstrates that the resistance of the channel is a function of mobile defect concentration. The output current of the 3-4 junction is modulated multi-fold only by stressing the perpendicular 1-2 junction, even below its V_{set}.

The logic and switching applications of any memristive device will ultimately be limited by the frequency at which states can be accessed and read out, as discussed

in the earlier discussion about fast s_r regimes. Functionalities such as pattern recognition rely on effective thresholding of output currents [347, 100] and smearing of state conductivities at high binary switching frequencies will lower the tolerance required for multi-level operations [342]. Our devices maintain state distinguishability below switching rates of 10 Hz in a 8.5 μm-long channel containing a single sub-10 nm fissure. **Figure 9.17(d)** tracks the dependence of read currents on the width of the applied 5-pulse train used to stress the device into the different resistance states. HRS can be reliably accessed down below the millisecond range, and down to 0.1 s for LRS.

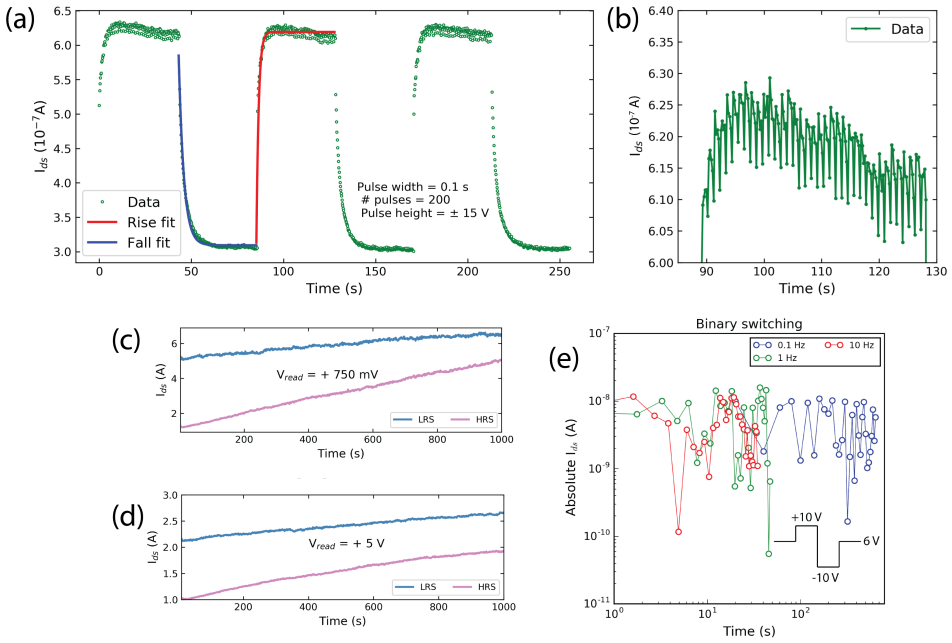

Figure 9.18: **Higher impulse response, retention characteristics at different read biases and binary switching characteristics.** **(a)** Trace of post-synaptic current recorded using trains of 5 pulses, 40 times with pulse width = 0.1 s and pulse magnitude = ± 15 V. **(b)** Closer look at the saturation region of the LRS potentiation. Retention characteristics of both states in the same device read off at V_{ds} = **(c)** 750 mV and **(d)** 5 V. **(e)** On-off switching between binary states as a function of pulse width.

Another set of LTP and LTD habituations on a different monolayer CVD device (L = 9 μm) is presented in **Fig. 9.18(a)**. This time, shorter pulses of higher magnitude were used (0.1 s, ± 15 V) and the device was observed to require more pulses to achieve habituation into a given resistance state. In addition, it was possible to still modulate the resistance of the LRS after exponential habituation from HRS by continuing the pulsing. This transient response is presented in **Fig. 9.18(b)**, where the first of the 5 pulses is able to spike the I_{ds} momentarily, before decaying

upon further pulsing, with the general envelope of the state conductance decaying with incoming pulses. No such behaviour was noted when depressing into HRS, suggesting a fundamental asymmetry of functionality in the device - a concept which we will explore in more detail in the coming sections. **Figures 9.18(c,d)** show the readout of state currents over 1000 s at read biases of V_{ds} = 750 mV and 5 V, respectively. In both cases, the current is seen to rise over time in LRS and HRS. Thus, some degree of ionic migration still occurs at very low electric fields even before hard state switching; suggesting that in order to detect such a notable resistance change, the distance across which the V_S concentration is modulated must be very short. **Figure 9.18(e)** presents the binary switching characteristics of the device from **Fig. 9.17** as a function of applied pulse width. Alternating pulses of ± 10 V were used to continually force the device into LRS or HRS with state readout performed at V_{ds} = 6 V. As the width of the pulses narrows, a frequency-dependent smearing of states emerges above 1 Hz, where the on/off states are hard to distinguish (green & red traces) and the readout currents are no longer consistent. Defect migration is hence rate-limited and the operational frequency needs to be well-paired with device geometry to achieve optimal performance.

We may want to consider whether or not the physical values we are seeing in these switching events match the physical picture we are trying to present here. Let us consider the device whose micrograph is presented in the inset of **Fig. 9.17(c)**. *Note*: we define the pulse polarity as $V_{12} = V_1 - V_2 < 0$. This means electrode 2 is the drain and the setting happens when $V_{ds} = V_2 - V_1 > 0$. This is required for the 3-4 electrode pair on the drain side of the channel to detect any resistance change at all. See the sketch in **Fig. 9.19** for reference.

From **Fig. 9.17(b)**, we can see that the resistance difference between terminals 1 and 2 is $\Delta R_{12} = R_{12}^{H} - R_{12}^{L} \approx 2.35 \times 10^7\ \Omega$, while between terminals 3 and 4 it is $\Delta R_{34} = R_{34}^{H} - R_{34}^{L} \approx 6.8 \times 10^9\ \Omega$. To clarify the physical magnitudes of these observed differences, we estimate the variation in the vacancy concentration that leads to the switching between HRS and LRS across these two sets of electrodes.

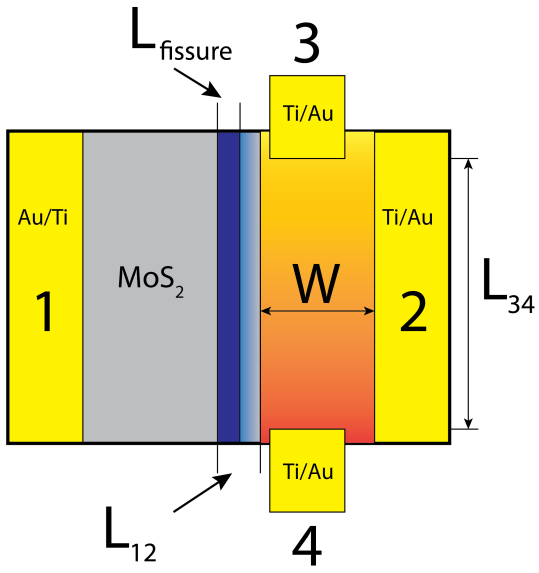

Figure 9.19: **Representative sketch (not to scale) outlining the device geometry from Fig. 9.17(b).** L_{12} marks out the extension of the V_S drift that modulates the resistive switching between terminals 1 and 2.

As discussed in detail in the introduction, our group's previous work [192] relates MoS_2 resistance, R, to the ion dose Φ, i.e. the empirical relationship $R(\Phi)$ holds. Meanwhile, the concentration of generated V_S is approximately proportional to the dose via the sulfur sputtering yield of 0.007, i.e. $V_S \simeq 0.007 \cdot \Phi$. ΔR_{12} and ΔR_{34} correspond to the dose difference ranges for the insulating-to-metallic and semiconducting-to-insulating regions respectively (although it is difficult to know which side of the resistivity-dose curve the device happens to fall on). During the setting (i.e. transition from HRS to LRS, as defined by the polarity of the pulses relative to the fissure asymmetry), a number of vacancies migrate from the drain-side channel to the fissure, which lowers the concentration of vacancies in the drain-side channel (i.e. $C_{34}^{H} < C_{34}^{L}$) and hence increases its resistance (i.e. $R_{34}^{H} > R_{34}^{L}$). Accordingly, the fissure undergoes an increase in vacancy concentration, leading to $C_{12}^{H} > C_{12}^{L}$ and $R_{12}^{H} > R_{12}^{L}$.

Let us think about the necessary vacancy concentration change that results in the measured resistance discrepancy between states. The number of mobile vacancies, N_{34}, that causes the resistance variation between electrodes 3-4 can be estimated from the fact that we know the change in vacancy concentration necessary to induce switching between states between electrodes 3 and 4, i.e. $(C_{34}^{L} - C_{34}^{H})$, and we know the area over which this concentration change happens (the length and width of the

channel between electrodes 3 and 4). Thus, the number of mobile vacancies ought to be:

$$N_{34} = L_{34} \cdot W \cdot (C_{34}^{\mathrm{L}} - C_{34}^{\mathrm{H}}) \simeq 4\ \mu\mathrm{m} \cdot 4.5\ \mu\mathrm{m} \cdot 5 \cdot 10^{11}\ \mathrm{cm}^{-2} \simeq 1.8 \times 10^{6} \quad (9.4)$$

where L_{34}, W are the length and width of the channel in between electrodes 3 and 4. As a first-order approximation, we can assume that the total number of mobile vacancies that accumulate (dispatch) in (from) the fissure region in the setting (resetting) process, N_{12}, is roughly equal to N_{34}. We can then estimate the extension of the region, L_{12}, that is responsible for the resistive switching between electrodes 1 and 2:

$$L_{12} = \frac{W \cdot \Delta C_{34}}{\Delta C_{12}} \simeq 200\ \mathrm{nm} \quad (9.5)$$

This means that in order to account for the observed resistance discrepancy between the perpendicular terminals, the resistance modulation must occur largely across an area at most 200 nm in width on one side of the fissure. This is in line with our theory that the resistance is modulated largely at the fissure interface, and that any variations in the V_S concentration in that small area will have a large effect on the electric potential drop across the fissure. This ultimately bottle-necks the electron transport and governs the resistance states of the device. Hence, the fissure is *necessary* to modulate the resistance in the observed consistent manner across different devices in this work, and its physical confinement is the deciding factor in controlling the resistance ratio of the memtransistor.

9.6 Spectroscopic studies

Figure 9.20 shows Raman and PL spectroscopy mapping of a contacted monolayer CVD MoS_2 memtransistor. The channel length of the presented device is $\approx 1\ \mu$m, extending from 0.5 μm to 1.5 μm on the x-axes in the figures. Raman and PL maps were collected in each resistance state using the *WITec Alpha 300R* system in ambient conditions. The device was switched between resistance states *ex-situ* between each map acquisition, and the maps were acquired within minutes of switching states. The excitation wavelength was 532 nm, with a diffraction grating of 1800 grooves mm^{-1} and a 100× objective lens (NA = 0.95, spot size $\sim 0.3\ \mu$m). Mapping was carried out at low incident powers ($< 100\ \mu$W) to avoid altering the sample with the laser,

with the beam refocused manually every time between each scan to ensure accurate comparisons. The 4 μm^2 areas scanned in 60 lines in the maps were sampled at a resolution of 60 pixels per line, with an integration time of 0.21 s. We remark that our devices were mapped and electrically switched in ambient conditions.

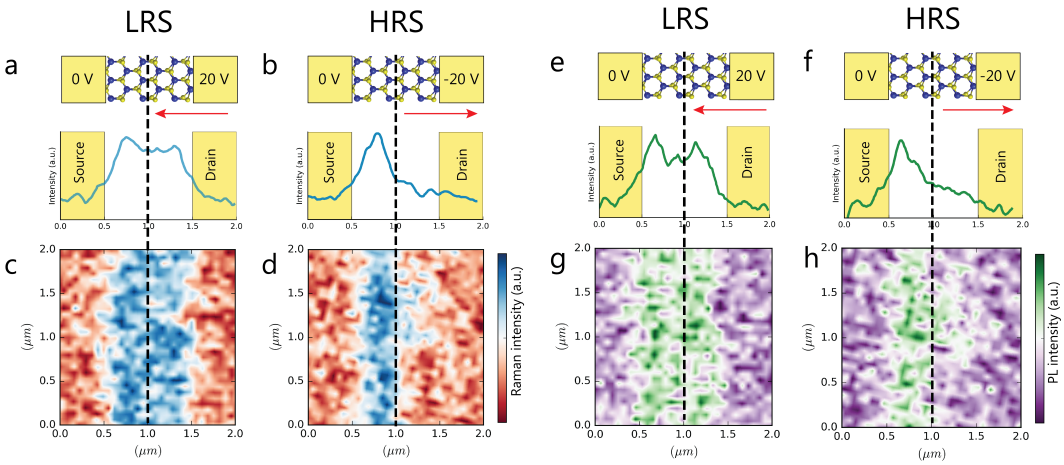

Figure 9.20: **Raman and PL spectroscopic characterisation of the device in different resistance states. (a, b)** Line profiles of Raman intensities across the He$^+$ ion cut in LRS and HRS respectively. The sketches above show the bias on the electrodes used to switch *into* the presented state, while the red arrows show the direction of V_S drift to achieve the given resistance state. **(c, d)** Spatially-resolved Raman intensity maps of the E′ mode of monolayer MoS_2, normalised to the colour bar on the right. Severe quenching of signal is observed on the drain-side in HRS. **(e-h)** Analogous *B* exciton PL data from the same device. Mapping data processed by Dr. Pierce Maguire.

To visualise the mapping results, the E′ Raman mode at 386 cm^{-1} was summed over a spectral window of ± 5 cm^{-1} on either side of the peak, while the PL intensity of the *B* exciton, at 2.01 eV, was summed over a spectral window of 0.1 eV. **Figures 9.20(a,b)** show line profile intensities of the E′ Raman mode and *B* exciton PL intensity averaged across the device channel; alternating between LRS and HRS. The source and drain electrodes are represented in yellow on either side of the MoS_2 channel. We thus distinguish the drain and source sides of the device, which are separated by the He$^+$-created fissure of our standard dose of 1.6 pC μm^{-1}. The location of the He$^+$ cut is indicated in the figures by the dotted black lines. In LRS, the spatial distribution of the Raman intensity on either side of the black line is roughly uniform, as represented by the blue colour in **Fig. 9.20(c)**. The red areas represent low signal intensity regions from the MoS_2 hidden by the electrodes. In HRS (**Fig. 9.20(d)**), the intensity drops off strongly on the drain side and is distributed non-uniformly in the material. **Figures 9.20(e,f)** show analogous PL line profiles of the *B* exciton intensity. The green signal in the PL maps in **Figs.**

9.20(g,h) indicates areas where contributions of the *B* exciton are strongest. As seen from the line profiles, the uniformity of the *B* exciton emission across the fissure changes significantly by switching from LRS to HRS, roughly tracking the observed Raman trends. The emission on the drain side declines in intensity for both *A* and *B* excitons; with particular quenching of the *B* exciton (factor of ~ 7) in the PL maps. The spatial uniformity of the emission on the drain side of the fissure is disrupted in HRS, with most of the signal from the top and bottom regions of the channel quenching drastically between states. See **Fig. 9.21** for explicit comparison of the device halves between LRS and HRS in the Raman and PL spectra.

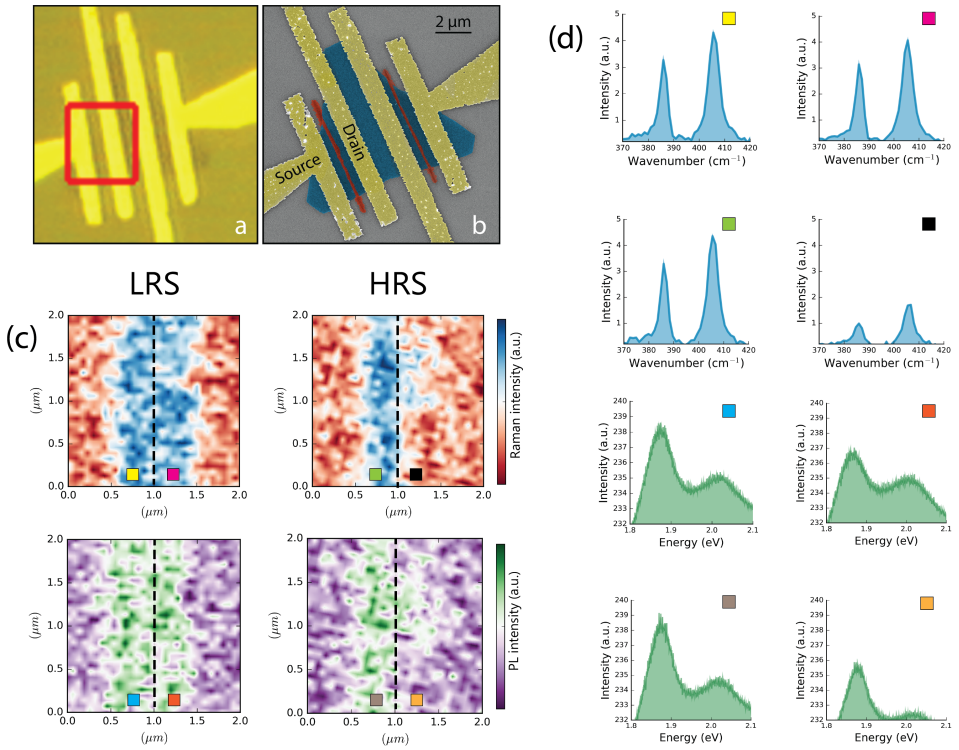

Figure 9.21: **Raman and PL spectra averaged from each side of the fissure on the switched device.** **(a)** Optical micrograph (100× lens), showing the square area which was mapped, outlined in red. **(b)** False-colour SEM image of the same device post-irradiation, with the helium ion fissures marked in red and the source and drain electrodes labelled as used in the experiment. **(d)** Raman and PL spectra extracted from the maps in **(c)**. Each coloured square indicates the fissure side from which the corresponding spectrum was averaged (900 spectra per each average in the region spanning 0-0.5 μm or 1-1.5 μm on the x-axis, and 0-2 μm on the y-axis). Quenching of both Raman and PL intensities is visible on the drain-side (right hand side) in HRS, as seen on the spectra marked with the black and orange squares. Mapping data processed by Dr. Pierce Maguire.

We observe no significant shifts or broadening of the E′ and A_1' Raman peaks on the drain-side, despite a large drop in intensity of both (see **Table 9.3** below). The separation of the in-plane E′ (386 cm^{-1}) and out-of-plane A_1' (405 cm^{-1}) first-order

modes is $\simeq 20\ \mathrm{cm}^{-1}$, consistent with single-layer MoS_2 [233] as we switch between states, thus maintaining good integrity of the crystal structure.

Resistance state	**LRS**		**HRS**	
Area relative to fissure	*Source*	*Drain*	*Source*	*Drain*
$\omega_{A_1'}$ (cm^{-1})	405.8	405.4	405.6	405.8
$I_{A_1'}$ (a.u.)	3.89	3.69	4.12	1.6
$\Gamma_{A_1'}$ (cm^{-1})	5.1	5.3	5.3	5.1
$\omega_{E'}$ (cm^{-1})	386.2	386.2	386.1	385.8
$\Gamma_{E'}$ (cm^{-1})	3.2	3.2	3.3	4
$I_{E'}$ (a.u.)	2.67	2.72	2.78	0.75
A_1'/E' intensity ratio	1.46	1.36	1.48	2.13

Table 9.3: **Summary of fitting parameters to spectra presented in Fig. 9.21**. No major peak shifts are noted, but the intensity of both peaks decreases on the drain side of the channel in HRS. That region is also the only one where the E′ peak is more intense than the A_1' peak, suggesting reduced out-of-plane vibration intensities due to lattice rearrangement.

The drop in Raman intensity suggests a large decrease in electron-phonon coupling as defects migrate out from the centre of the fissure region towards the drain side. PL emission from the direct-recombination *A* exciton and the spin-orbit split *B* exciton is centred at 1.89 eV and 2.01 eV, respectively, throughout the switching events with no energy shifts. This range is usually reported for typical monolayer MoS_2 [15, 348], also confirming the relative structural integrity of the material in both LRS and HRS.

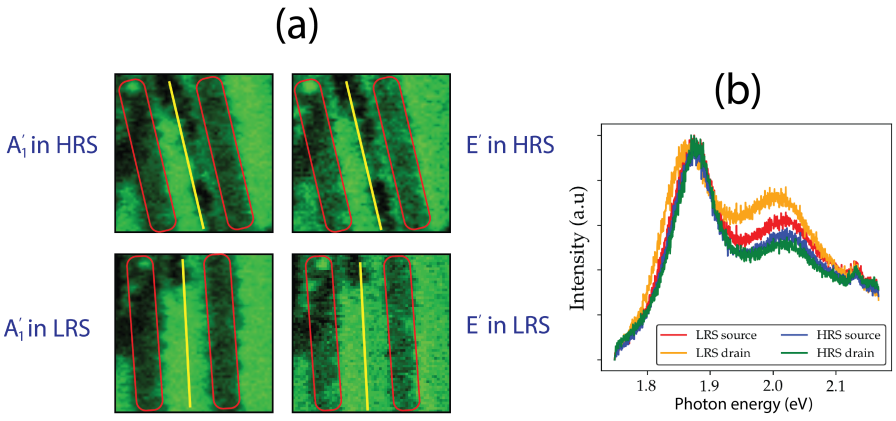

Figure 9.22: **Additional Raman maps and normalised PL spectra. (a)** Comparison of Raman maps of the A_1' and E′ monolayer MoS_2 modes between HRS and LRS. Both modes are affected by state switching and track the MoS_2 intensity nearly identically. Yellow lines are locations of the He^+ fissures, red outlines mark the device electrodes. **(b)** Normalised PL spectra, showing the quenching of the emission on the drain-side of the device, with a severe drop in intensity of the *B* exciton. Mapping data processed by Dr. Pierce Maguire.

Based on these observations, we propose that when switching the device from LRS into HRS, the defects are forced to migrate towards the drain electrode, out from the centre of the fissure. Their movement attenuates the PL intensity (see normalised spectra in **Fig. 9.22**), whose quenching has been associated with the presence of V_S in MoS_2 [349]. Helium ion irradiation above doses of 1 pC μm^{-1} results in V_S concentrations [192] that far exceed sub-stoichiometries achieved naturally by CVD growth [329]. As sulfur vacancies are defects with the lowest formation energy in MoS_2 [350], are stable on substrates when charged [351], and also have a lowered energy barrier for diffusion when in clusters [328, 346] and when charged [352], we propose that they are the majority species responsible for resistive switching in our devices. However, computational works have challenged the role of V_S in donating electrons to the MoS_2 lattice [350, 353] so we cannot rule out Mo interstitials or antisite defects, inevitably introduced by the helium beam, as also contributing to the mechanism.

We note that a downshift of E′ is expected if the V_S concentration is higher than 1% [354]. As the difference in V_S concentration between LRS and HRS in our case is less than 1% when averaged across the area sampled by the laser spot, we do not detect any peak shifts in the Raman spectra. The exact nature of the switching process at the fissure interface needs to be elucidated in future characterisation work. The optical properties of our device in this experiment show complementary symmetries in HRS and LRS between the Raman and PL maps. We thus propose that defects from the drain-side are not able to readily pass the beam-created fissure when moving towards the source electrode upon bias polarity reversal - hence forming the asymmetric material structure necessary to activate the bipolar resistive switching.

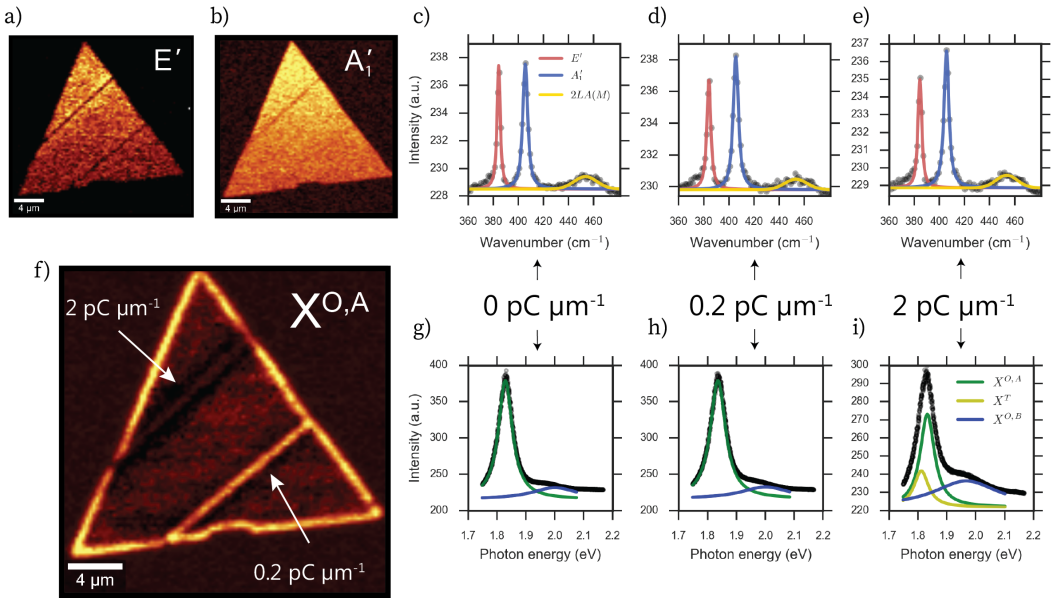

Figure 9.23: **Raman and PL spectroscopic characterisation of helium ion fissures created at doses of 0.2 pC μm^{-1} and 2 pC μm^{-1}. (a,b)** Raman maps filtered for the E′ and A$_1^{\prime}$ monolayer modes, showing an effect of peak shifting (red-shift of 0.2 cm^{-1} and further 0.6 cm^{-1} after 0.2 pC μm^{-1} and 2 pC μm^{-1}, respectively for E$^{\prime}$; and blue-shift of 0.7 cm^{-1} and further red-shift of 0.6 cm^{-1} after 0.2 pC μm^{-1} and 2 pC μm^{-1}, respectively for A$_1^{\prime}$). Spectra in **(c-e)** are extracted from a pristine middle region (0 pC μm^{-1}) and the fissure regions from edge-to-edge of the flake, parallel to the fissure. Different ion dose spectra are marked with arrows in the figure. **(f)** PL map of the *A* exciton intensity, showing enhanced emission at the site of the lower dose delivery. **(i)** The higher dose destroys the material significantly, quenching the PL emission relative to **(g)** and **(h)**, and introduces a defect-associated trion peak [236] as seen in yellow on the spectrum in **(i)**. Mapping data processed by Dr. Pierce Maguire. $2LA(M)$ stands for the second-order longitudinal acoustic mode.

We can also study the effects of different He$^+$ ion doses on the Raman and PL response of the damaged MoS_2 region. We are limited by the resolution of the laser used for the mapping, but the effects of the helium ion beam-induced defect generation spread far out from the centre of the fissure; detectable to more than 1 μm at the higher doses (most likely due to residual lattice strain and/or some substrate buckling). No obvious emergence of defect-related peaks is observed in the Raman spectra. Raman intensity quenching of the E$^{\prime}$ mode due to ion irradiation of the material in the tested area is stronger than that of the A$_1^{\prime}$ mode, however, suggesting possible exposed MoS_2 lattice edges in the region (see also the similarity between helium fissures and edges of the as-grown CVD flake in both the Raman and PL). No significant peak shifting is observed, even at the high 2 pC μm^{-1} dose, but the intensity is reduced. The PL emission intensity of the *A* exciton is seen to be enhanced at the site of the lower dose delivery. This is likely due to an increased concentration of available adsorption sites for molecular

oxygen and nitrogen, which have been shown to boost the quantum yield of PL in monolayer MoS_2 [355, 356, 357]. By using this lower irradiation dose, the modified lattice contains enough V_S sites to facilitate the physisorption of ambient species that enhance PL emission, but not enough scattering centres to facilitate non-radiative recombination which would quench the PL, as is the case for the higher dose. The highly-localised and directional ability to write enhanced PL patterns into these monolayer semiconductor films with the helium ion microscope may find future applications in nanoscale cryptographic primitives [358], but this avenue has not been explored deeply in this thesis. The higher dose of 2 pC μm^{-1} (**Fig. 9.23(i)**) destroys the material significantly, quenching the PL emission relative to **Fig. 9.23(g)** and **Fig. 9.23(h)**, while introducing a defect-associated trion peak [236], as seen in yellow on the spectrum in **Fig. 9.23(i)**.

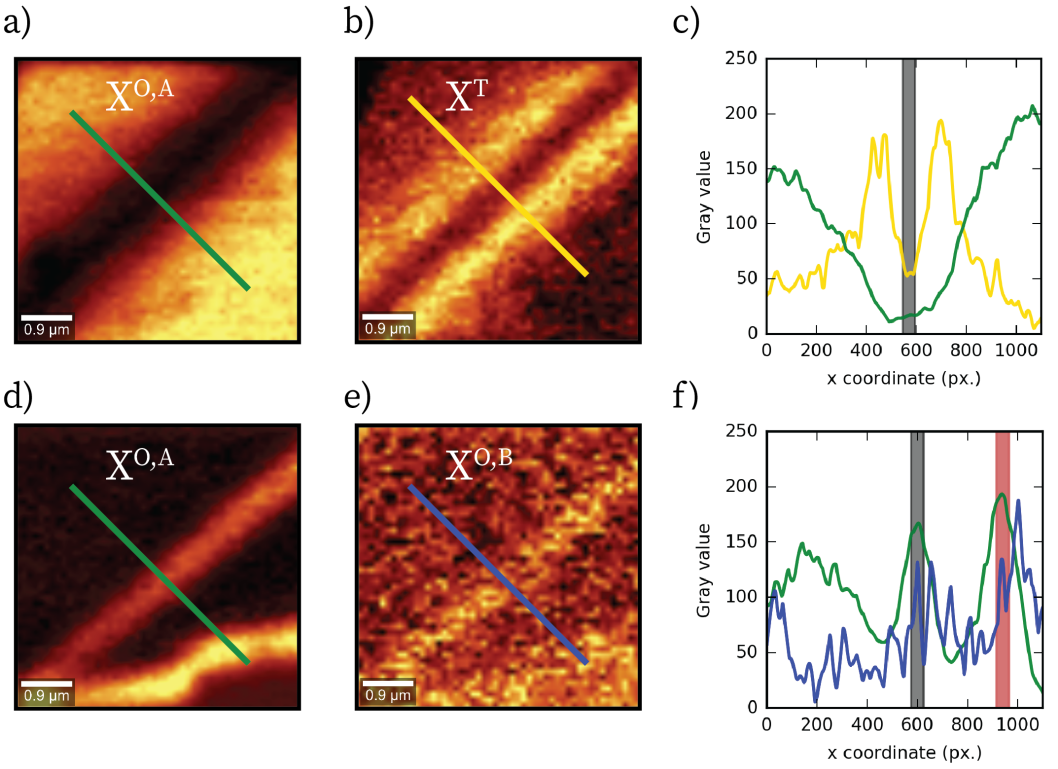

Figure 9.24: **PL line profiles of fissure regions at different ion doses and emission energies.** **(a,b)** The 2 pC μm^{-1} fissure region filtered for the *A* exciton and A^- trion energies, respectively. **(c)** Line profiles across the fissure showing the spatial variation in those respective emissions. **(d,e)** The 0.2 pC μm^{-1} region showing the *A* and *B* exciton maps, respectively. **(f)** Line profiles taken from the lines marked on the maps in **(d,e)**, demonstrating the increased emission yield of both the *A* and *B* signals in the low-dose fissure (grey shading in the plot) and the flake edge (red shading in the plot). *px.*; pixels.

We can filter the maps for the energies associated with each exciton to see how their recombination is spatially localised around the defective MoS_2 regions. In **Fig. 9.24(a)**, the *A* emission is clearly quenched in the high-dose fissure, with the intensity dropping significantly even a few microns out from the centre of the irradiation site. The emission of the trion peak is heavily localised to edges of the fissure region on both sides (**Fig. 9.24(b)**), suggesting that the recombination of the charged exciton occurs close to the interface of the damaged and the pristine MoS_2 lattice. Intensity line profiles across the fissure are presented in **Fig. 9.24(c)** for both. Analogous data for the low-dose fissure is presented in **Figs. 9.24(d,e)**, with the edge of the as-grown flake also visible in the bottom right corner of the maps. Both the *A* and *B* excitons are seen to be enhanced at the site of the 0.2 pC μm^{-1} irradiation (grey shading in **Fig. 9.24(f)**), as well as on the edge of the flake itself (red shading in **Fig. 9.24(f)**).

Thus, we see that some nuanced dynamics regarding charge recombination and defect concentration occur at the site of the irradiation itself, before any biasing. In addition, the emission profiles are not entirely symmetric as we traverse the fissure region. This agrees with our TEM images from earlier, which also showed a non-uniform defect generation in the fissure region. We contend that this feature is a key characteristic of our devices and enables the observed bipolar resistive switching. Let us now introduce this idea in the penultimate section of this chapter, before diving deeper into it in the last chapter of the thesis.

9.7 Considerations of asymmetry

The asymmetry observed in the Raman and PL maps after resistive switching suggests that the cause of bipolar switching is the asymmetric distribution of vacancies in the device. In this picture, HRS occurs when the V_S distribution around the fissure is highly asymmetric, while LRS occurs when the V_S distribution around the fissure is more symmetric. This skewed vacancy distribution in the material may originate from either the nature of the helium beam irradiation or the initial *I-V* sweep. To elucidate which of these is the dominant process, we purposely introduced a skewed V_S distribution into our device by tilting the microscope stage during helium ion irradiation. We fabricated two FET channels on the same monolayer CVD MoS_2 flake (designated as *left* and *right* channels) and tilted the stage by 15° when creating the fissures. The source and drain terminals were then exchanged when sweeping the *I-V* curves on the two channels, inverting the initial electric field direction relative to

the skewed V_S distribution, i.e. forcing vacancies in the defect-rich side to migrate away from the fissure in one channel, and across the fissure in the other channel.

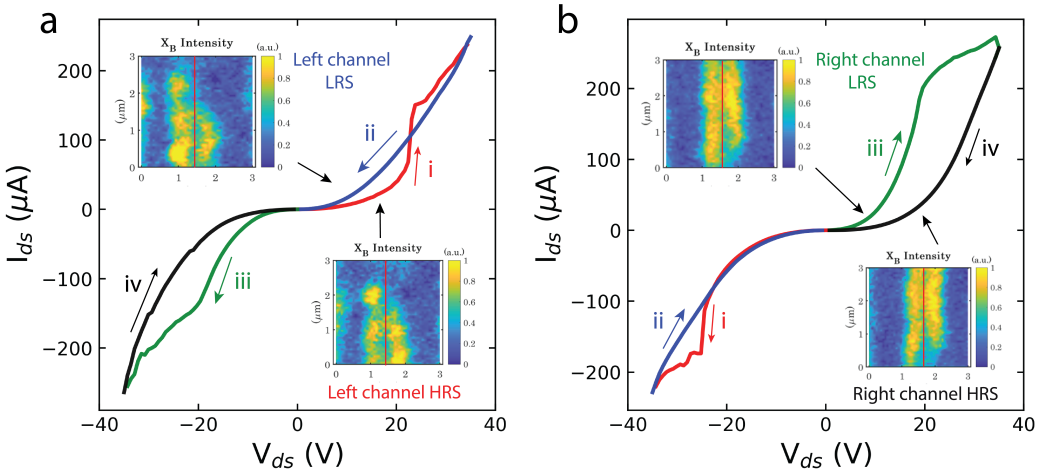

Figure 9.25: **Effects of asymmetric irradiations on initial resistance state setting.** Roman numerals indicate sequential *I-V* sweep portions in both plots. **(a)** The *left channel* device had the source electrode tilted 15° away from the incident helium beam. In this case, the memtransistor is initiated into HRS (red trace, *i*). PL maps of the device in LRS and HRS are included as insets, showing a clear asymmetry emerging in the recorded signal across the helium-created fissure (red line on maps). **(b)** The *right channel* device had the source electrode tilted 15° towards the incident helium beam. In this case, He^+ ion irradiation initiates the device into LRS for the virgin sweep (red trace, *i*). PL maps reveal a more symmetric defect distribution after initial biasing (just as in LRS in **Fig. 9.20**), suggesting that the asymmetric vacancy arrangement introduced by the tilted irradiation is the dominant variable for device functionality over the initial sweep polarity. Blue areas in the PL maps are the device electrodes obscuring the MoS_2 signal.

Figures 9.25(a,b) show the virgin *I-V* sweeps of the asymmetric devices with the source electrode tilted away and towards the helium beam, respectively. Insets are PL intensity maps of the *B* exciton around the fissure area (marked in the map as a red line) taken in HRS and LRS for each device. Note that *positive* drain current is defined here relative to the bias polarity of the device, thus the reflection about the origin between **(a)** and **(b)**, when we flip the electrode bias polarity between devices. We will explore this in more detail in the next chapter. As evident from the relative magnitude of the red and blue sweep portions on both plots, the resistance state initially obtained by each device from the helium irradiation depends on the direction of bias relative to the asymmetric vacancy distribution introduced by the tilted exposure. The PL maps of the left channel device exhibit significant intensity variations on both sides of the fissure in the two resistance states, suggesting a more prominent defect migration in this device, i.e. the skewed V_S distribution is closer to the attracting electrode. In the right channel PL maps, the asymmetry between

resistance states is not as pronounced, hinting that vacancies cannot move as readily through the fissure towards the attracting electrode. Hence, we observe the flip from LRS to HRS as the bias is increased and more vacancies are forced away from the fissure region. Both FET channels retain similar levels of current, set biases and resistance ratios despite the differing switching dynamics.

Thus, we propose that the bipolar nature of this resistive switch is largely dependent on the initial V_S distribution introduced by the ion beam and it is the fissure that ultimately governs the switching behaviour of the device. We will go on to study this hypothesis in more detail in the final chapter of the dissertation.

Another question which arises when considering device non-uniformity is the asymmetry of the starting material itself. Upon azimuthal rotation, an ideal isosceles triangle monolayer flake of MoS_2 capped with S atoms along each edge has 120° rotational symmetry when viewed along the [0001] direction. This means that fissures created by irradiating at angles between 0-120° relative to some base of the triangle will always yield a different atomic termination to the (here assumed to be crystallographically perfect) fissure edge. Thus, there will always be a crystal asymmetry, where in a certain configuration a row of S capping atoms may be the terminating border, while a row of Mo is exposed on the other side of the fissure, creating an asymmetry to the device structure. This non-equivalent reconstruction of fissure edges (disregarding adventitious oxygen, etc.) might make it easier for one side of the fissure to mediate the motion mobile vacancies depending on biasing polarity, as we have discussed the low energetics of vacancy hopping along S row structures in **section 9.4**. As we know that electronic transport across grain boundaries is affected by crystallographic orientation [42, 53], this is a hypothesis that needs further study, though it will always have downsides due to the non-ideal spread of the ion beam probe. Results of initial experimental outcomes of changing this fissure direction relative to the crystal symmetry will be discussed in the next chapter.

9.8 *In-situ* TEM biasing

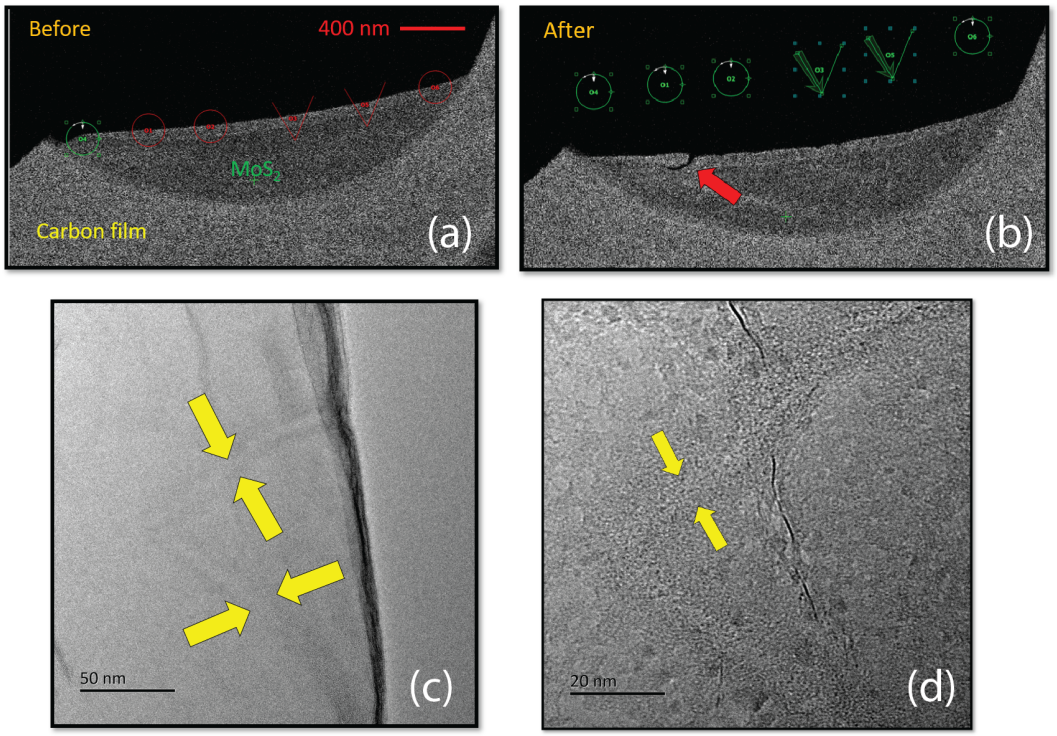

Figure 9.26: **Irradiations of suspended monolayer CVD MoS_2 for *in-situ* biasing in the TEM.** **(a)** HIM image of suspended monolayer MoS_2 sticking out from the edge of a sliced TEM grid. The sequential patterns irradiated with the ion beam are marked on the plot. **(b)** The same sample after suffering HIM irradiations over the suspended regions. **(c)** Low magnification TEM image of an irradiated area near the edge of the sample. The yellow arrows point to the edges of the fissures (note the irradiations enclose a pristine MoS_2 region from edge to edge). **(d)** Higher magnification TEM image of the same region, showing visible damage to the lattice in the irradiated line scan regions. Beam energy for all images was 120 keV. Images taken by Mingqiang Li.

In order to visualise the migration of V_S species in our monolayer MoS_2 devices, we fabricated helium ion-irradiated samples for *in-situ* electrical biasing in the TEM. A series of chips containing our CVD monolayers were subjected to oxide dissolution in ambient potassium hydroxide (KOH) solution overnight after spin-coating in PMMA. The films were then fished out of solution using several copper TEM grids, dissolved with an acetone & IPA wash and dried off on a hotplate at 130°C. This usually results in large-area monolayer flakes distributed randomly across the grid. The grids are then sliced in half with a razor blade, with the hope that some of the flakes will end up hanging over the exposed edge of the carbon film. **Figure 9.26(a)** shows a HIM image of such an area, where the MoS_2 sample is found to extend past the edge of the grid, leaving a free-standing area that is also available for approach by the sharp tungsten tip of the *in-situ* biasing holder.

The flake was line-irradiated with the HIM in such a way that the beam-created V_S-rich boundary enclosed a pristine MoS_2 area in a semi-circle, or in a V-shaped trough, from edge to edge. This ensures that the electric field, which is applied between the W tip and the copper grid itself, would always drop across a V_S-containing boundary region; hopefully leading to visible defect migration during TEM imaging. As such, multiple cuts were made on the suspended flake as seen in **Fig. 9.26(b)**. **Figures 9.26(c,d)** present TEM micrographs of the irradiated regions, showing a boundary ~ 10 nm in width, enclosing a region of MoS_2 fully, available for contacting. On the approach to the sample, it was important not to touch the overhanging carbon film on the side of the MoS_2 (**Fig. 9.27(a)**), as that would short the circuit around the helium-created boundary, potentially leading to no observable V_S drift.

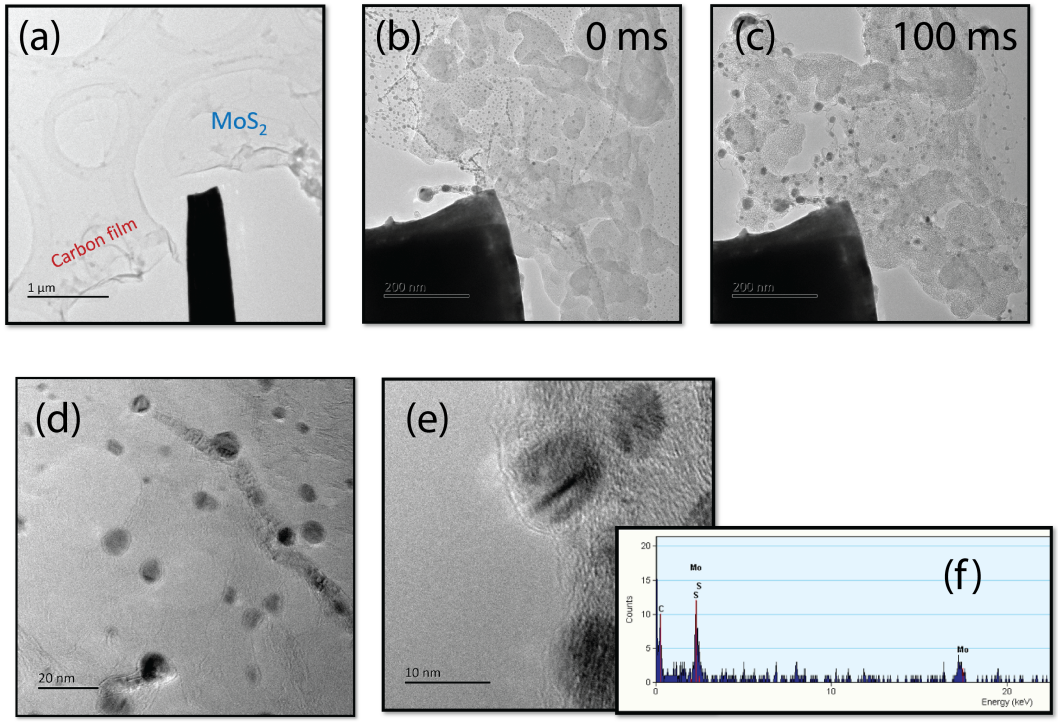

Figure 9.27: **Effects of biasing the sample *in-situ* in the TEM. (a)** W tip on the approach to the suspended MoS_2 sample in the irradiated region. **(b)** Image of an already-electrically stressed MoS_2 sample before the second round of biasing at 1 V. **(c)** The same sample region 100 ms after applying 1 V on the tip. **(d)** Streaks of nanoparticles precipitated in the MoS_2 matrix after the biasing. **(e)** Closer look at the particles, mostly containing Mo and S, as seen on the EDX spectrum in **(f)**. Beam energy for all images was 120 keV. Images taken by Mingqiang Li.

The biasing set-up only worked in steps of 1 V, thus limiting the ability to raise the potential slowly across the device during imaging. Unfortunately, an initial try of

biasing once contact was made led to the sample suffering nearly-instant electrical discharge and crumpling up, before any high-resolution images of the sample could be taken. Thus, the image seen in **Fig. 9.27(b)** is an already-discharged and distorted flake to begin with. A potential of 1 V was applied again to the device seen in **Fig. 9.27(b)**, while a video recording of the TEM console was taken to catch the evolution of the sample under bias *in-situ*. **Figure 9.27(c)** presents the same sample after 100 ms under biasing (highest frame rate resolution on the system), with massive changes to the flake structure happening virtually instantly when the field is dropped across it. This may not be so surprising, as we are biasing a monolayer crystal across a contact region of tens of nanometres, leading to a relatively high electric field at this step size of 1 V - enough to effectively blow up the flake in the TEM. The crumpling was accompanied by the formation of many metal-rich nanoparticles embedded in an amorphous MoS_2 matrix, as visible in **Fig. 9.27(d)**. A closer look at these electro-deposited particles in **Fig. 9.27(e)** reveals a dense, semi-crystalline structure, rich in both Mo and S, as monitored by EDX (**Fig. 9.27(f)**).

Thus, unfortunately, limitations both to do with equipment and some physical considerations (such as the magnitude of the electric field at the point of contact) meant that the drift of sulfur vacancies could not be directly observed in a monolayer memtransistor inside the microscope. The evolution of metal-rich particles under electrical stressing from the CVD material matrix was interesting in itself, but beyond the scope of this thesis. Thus, in order for the V_S drift to be directly imaged in these monolayer devices, a much smaller electric field needs to be applied, or else the samples need to be deposited on a coil-like biasing holder over an electron-transparent Si_3N_4 window, where the set-up mimics a standard EBL-deposited device. This work may be carried out in the future by incoming PhD students in the group.

9.9 Conclusions and outlook

In this chapter, we have demonstrated how the helium ion microscope can be employed to create atomically-thin gate-tunable resistive switching components. We have presented complementary evidence from microscopic and spectroscopic studies that sulfur vacancies are introduced into the material and govern the memristive properties of the device. Our memtransistors perform well when contrasted against most 2D memristive devices in the literature, comfortably reaching state-of-the-art benchmarks in the power consumption for the write operation, the cycling endurance and the retention times of states for atomically-thin resistive switches. We have also

hinted at the role of the fissure asymmetry in the resistance switching process. Hence, we go on to explore this idea now in more depth in the final chapter of the thesis.

Chapter 10

On the nature of resistance states in the MoS_2 memtransistor

Our demonstration of lateral resistive switching in defect-rich monolayer MoS_2 in the last chapter is the latest instalment in the community's efforts to advance the field of nanoscale memories. As non-volatile switching devices emerge in the atomic limit, it becomes crucial to obtain a good understanding of the physical nature of the operational principles of the presiding resistance states. In this chapter, we focus on the electrical properties of the low and high resistance states of the monolayer MoS_2 memtransistor fabricated by helium ion beam irradiation. Firstly, we consider the asymmetry of the ion beam-created fissure and how the introduction of a skewed sulfur vacancy distribution into the device governs its switching behaviour. We then probe and characterise each resistance state by means of cryogenic charge transport down to 1.5 K. We uncover the impact of sulfur vacancy drift on the device operation; parametrised by large differences in V_{th}, μ_{fe} scaling with temperature, the electron localisation lengths, the amplitude of 1/f noise and current density saturation between the two resistance states. Moreover, we discover that an early onset metal-insulator transition in LRS is mediated by the reversible doping brought about by the bi-directional drift of sulfur vacancies. Our method of inducing resistive switching in monolayer MoS_2 thus also demonstrates the utility of field-controllable dopant drift in facilitating exotic physical phenomena in two dimensions. We hence go on to propose a picture for the mechanism of resistive switching that occurs in our devices.

10.1 Effect of asymmetric irradiations on device performance

We have alluded to the importance of irradiation asymmetry on memtransistor characteristics in the last chapter. We have also described the change of the dose distribution (and by extension V_S concentration) in the irradiated region with increasing stage tilt in **Fig. 4.14**. This will inevitably affect the local resistance of the material and the current flow through those regions. We refer to **Appendix D**, where we establish a passive convention for the direction of positive current flow through our memtransistor fissure. As we exchange electrode polarities on some

devices in this chapter, it is necessary to adjust our data interpretation/visualisation to keep a consistent convention throughout testing.

10.1.1 TEM imaging of asymmetrically-irradiated suspended monolayers

We have tested our assertion that increasing the stage tilt leads to the creation of wider fissures by irradiating polymer-transferred CVD MoS_2 monolayers on a TEM grid at different tilt angles. The samples were moved onto Si_3N_4 grids by dissolution of PMMA-covered chips in NaOH. Each angled irradiation was performed on the same monolayer MoS_2 flake in a cluster of 6 fissures, separated vertically from each other by 600 nm. The irradiation parameters for each run were identical, other than the tilt angle of the HIM stage (see **Table 10.1**). Once eucentric height was obtained, the stage was tilted after each cluster was made and rotated so that the scan direction was always perpendicular to the tilt axis of the stage, and also parallel to the raster direction of the ion beam. Thus, the beam never has to refresh or retrace its path as it makes the line scan on the MoS_2, ensuring a higher degree of control over the irradiated area.

Dose (pC μm^{-1})	Step size (nm)	Beam current (pA)	Dwell time (μs)	Repeats	Aperture (μm)	Tilt angle (°)	Fissure length (μm)	Probe size (nm)
1.6	1	1	1600	1	5	*0*	1.5	1.4
1.6	1	1	1600	1	5	*30*	1.5	1.3
1.6	1	1	1600	1	5	*50*	1.5	0.9

Table 10.1: **Asymmetric irradiation parameters for TEM imaging.**

Figures 10.1(a-c) collates high magnification micrographs of cuts made on the same monolayer MoS_2 flake at three different angles (0° and the exaggerated tilt cases of 30° and 50°). For each angle, we also present FFTs taken from the regions marked in the corresponding colours on the micrograph, i.e. the irradiated region in yellow and the non-irradiated regions just outside of the fissure on either side (*green* closer to the beam, *red* further away from the beam). The direction of the tilt axis away from the normal beam incidence is as marked by the blue arrow in **Fig. 10.1(b)**. Each data set also contains the spatial plot of the second derivative of the line scan intensity across the fissures, to more clearly outline the terminations of the fissure region, which are not readily seen from the faint phase contrast in the HRTEM images on this monolayer sample.

From the FFTs it is clear that the helium-irradiated region has suffered significant amorphisation relative to the non-irradiated areas. In fact, large perforations spanning several nanometres begin to form on these three atom-thin bombarded areas. We note that there is polymer residue from the transfer process present on the surface,

which makes discerning the edges of the fissure by eye difficult. An FFT analysis of the image on the approach to the irradiated region did not reveal a pronounced asymmetry in the spatial extent of amorphisation preferably on either side of the cut, suggesting that the suspended monolayer sample may not suffer such an exaggerated asymmetric bombardment as in the case of thicker or substrate-supported samples. This is strongly linked to how far away we are from the focal point at the time of irradiation, as evident from **Equation 4.3**. From the probe size being sub-1.5 nm in all three cases, we can hence expect the tilt exaggeration to not be as pronounced. From the plot in **Fig. 10.1(d)**, however, it is clear that tilting the stage away from the ion beam landing location increases the observed width of the created fissure, at the same ion dose and similar probe size. The spatial extent of the fissure increases by as much as 32% between 0° and 50°. This suggests that the available area from which vacancies can be sourced to facilitate resistive switching on contacted samples also increases if the stage is tilted.

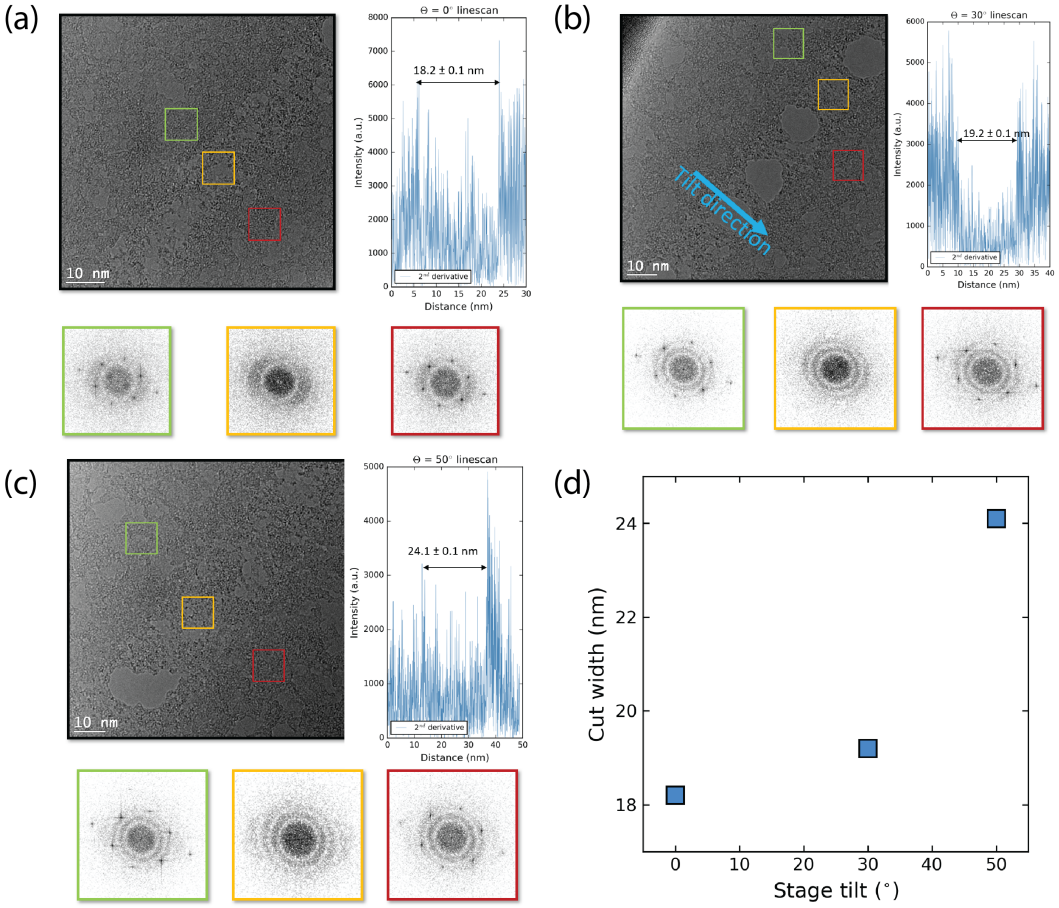

Figure 10.1: **TEM images of asymmetric HIM irradiations on the same monolayer MoS_2 flake as a function of stage tilt, Θ.** **(a)** Micrograph of the 0° line irradiation, showing increased amorphisation in the FFT from the fissure region (*yellow*) relative to those from the regions outside the fissure (*green* and *red*). The blue plot on the right is a second derivative of an intensity line scan across the fissure, highlighting the approximate width of the damaged region. **(b)** and **(c)** are analogous data for the 40° and 50° irradiations. The tilt direction of the stage is marked on the micrograph in **(b)** and is the same for all three cases. **(d)** Plot of the changing width of the irradiated fissure with increasing stage tilt angle. As expected, the observed extension of the damage in monolayer MoS_2 is widened by tilting the stage away from the beam by exaggerated angles.

10.1.2 Electrical characterisation of asymmetrically-irradiated monolayer mem-transistors

We proceed to evaluate the switching performance of monolayer CVD MoS_2 mem-transistors when asymmetrically-irradiated on a substrate. **Table 10.2** below collates the key parameters for this experiment. Note that the dwell time for all irradiations was always 1600 μs and the dose was 1.6 pC μm^{-1}. Images of the same device (chip location: A^L-B^L) undergoing fabrication and irradiation are presented in **Fig. 10.2**; starting from the optical lithography step, through the metal deposition to the ion

beam irradiation. **Figure 10.3** presents a schematic of the device fabrication and a HRTEM image of the fissure, exhibiting a clear asymmetry after irradiation.

Location	Tilt angle (°)	Probe size (nm)	Patterning time (s)	Length of fissure (μm)	FET channel length (μm)
2^T-3^T	50	2.3	53	37	46.8
A^L-B^L	50	2.3	37	23	8.6
A^R-B^R	50	2.3	80	50	8.7
B^L-C^L	40	2.3	38	29.7	11.3
C^R-B^R	40	2.3	107	66	9.5
1^T-2^T	0	1.2	82	51	18.3
3^B-4^B	0	1.2	120	50	13.9
B^L-C^L	0	1.2	75	46.8	9.0
1^B-2^B	30	0.5	174	109	18.6
2^B-3^B	30	0.5	75	47	22.6
A^L-B^L	30	0.5	113	71	11.4

Table 10.2: **Asymmetric irradiation parameters employed for electrical testing.**

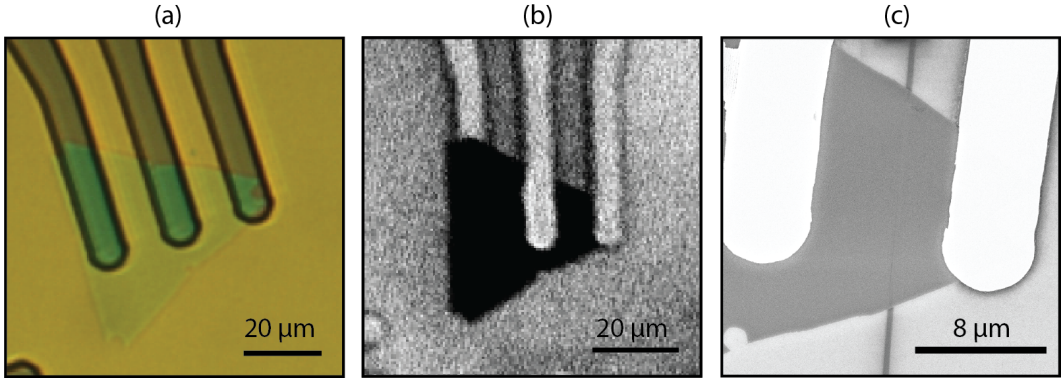

Figure 10.2: **Images of a memtransistor device irradiated at 50°. (a)** Optical micrograph of a monolayer flake after optical lithography exposure before film deposition. **(b)** SEM image of the device post-metallisation before He^+ ion exposure. **(c)** SEM of the device after ion exposures incident at 50°, also extending out onto the SiO_2 substrate.

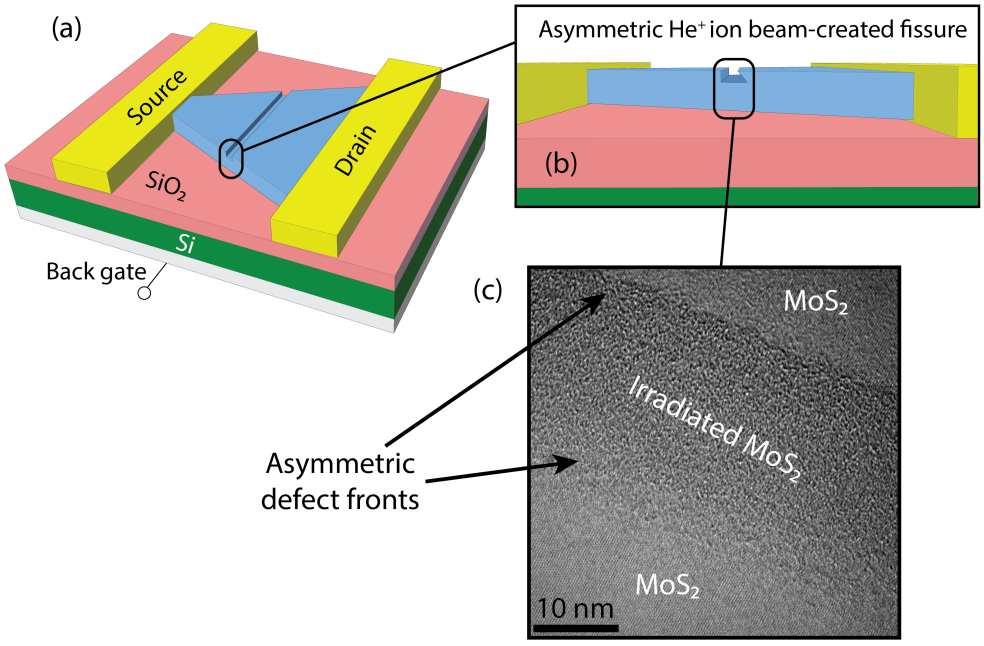

Figure 10.3: **(a,b)** Schematics of the asymmetrically-irradiated memtransistor device and **(c)** a HRTEM image of the fissure region showing clear asymmetry.

Figure 10.4 collates the hysteretic *I-V* loops for each set of irradiation tilts. In each figure panel **(a)**-**(d)**, we present two plots: the *left* shows the output characteristics recorded when the high-voltage electrode is on the side closer to the asymmetric extension of the fissure, while the *right* panel shows the *I-V* curve when the polarity of the electrodes is reversed, i.e. when the high-voltage electrode is across the fissure, away from the centre of the skewed V_S distribution. With increasing tilt angle (and by extension width of the fissure) we observe a severe increase in the asymmetry of the *I-V* curves, i.e. a suppression of conductance for one polarity of the sweep relative to the 0° tilt data. We have already introduced this idea before in **Chapter 9**, where the creation of the close-to-symmetric fissure at 0° tilt yielded more mirrored output characteristics about the zero-bias point. The introduction of a more non-localised V_S distribution into the helium-created fissure affects the symmetry of the device and its distribution of local resistances.

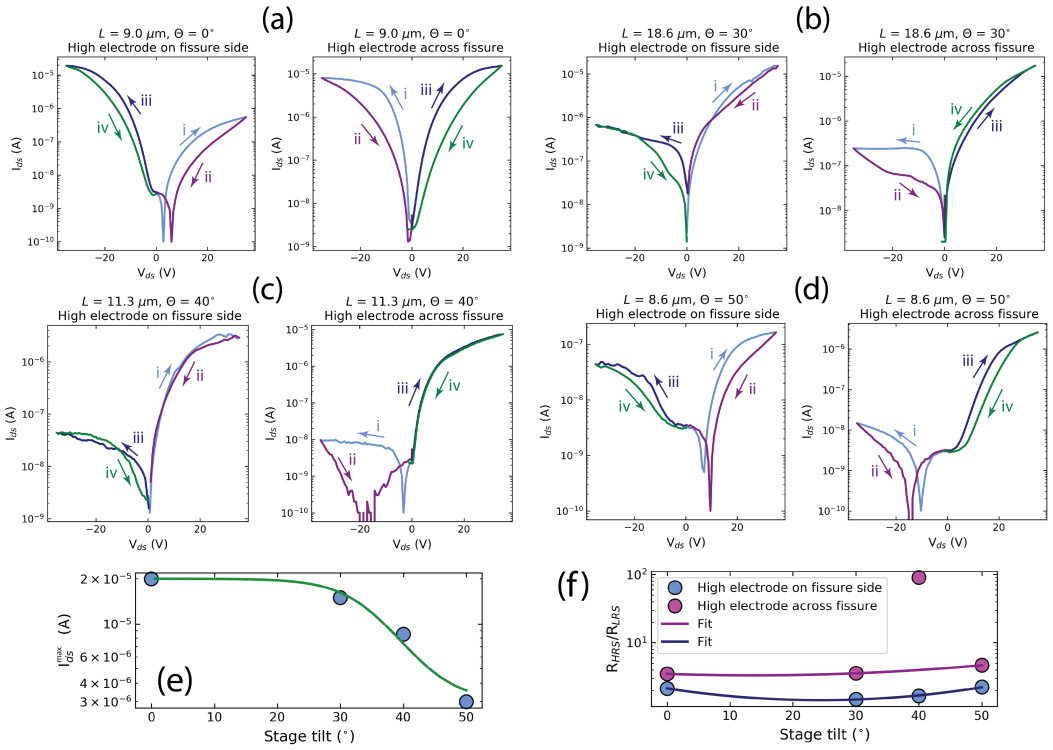

Figure 10.4: **Electrical characteristics of MoS_2 memtransistors relative to the asymmetry of the ion beam-created fissure.** The *left* plot in each set is for case **i** from **Appendix D**; the *right* plot in each set is for case **ii**. **(a)** Data set for 0° stage tilt. **(b)** Data set for 30° stage tilt. **(c)** Data set for 40° stage tilt. **(d)** Data set for 50° stage tilt. Each data set has the respective channel lengths, high electrode locations and tilt angles labelled above the graphs. **(e)** Change in reached I_{ds}^{max} in LRS with increasing stage tilt angle. **(f)** Evolution of the resistance ratio (evaluated at V_{ds} = ± 20 V) as a function of tilt angle for the two asymmetric biasing cases. R_{HRS}/R_{LRS}; resistance ratio at V_{ds} = ± 20 V.

Skewing the V_S concentration towards one of the electrodes increases the resistance of the material and modulates the voltage drop on the reverse sweep in such a way that the original levels of material resistance in LRS seen in the 0° irradiations cannot be recovered for higher tilt angles. This is visualised in the drop of the maximum output current levels that the devices are able to reach in LRS for the same sweep range of ± 35 V. This plot is shown in **Fig 10.4(e)**. The decrease in I_{ds}^{max} with increasing stage tilt is fitted reasonably well with a sigmoidal dose response Hill-like curve of the form:

$$I_{ds}^{max} = \frac{A}{1 + p \cdot 10^{\log(x_0) - x}} \tag{10.1}$$

where p and A are fitting constants, and x is the stage tilt. This suggests that the

stage tilt can serve as a proxy parameter for the delivered ion dose in the fissure region which modulates the injection current between flake halves in LRS.

In addition, we can track the R_{HRS}/R_{LRS} ratio of the initial sweep states in the device (marked **i** and **ii** on the plots) as a function of angle. In **Fig 10.4(f)**, we see that the ratio is always higher for the case of the high electrode being placed across the fissure, away from the extended V_S spread. This can be understood when one considers our proposed reference scheme. In that case, the device starts in a given resistance state and $\Delta V_{RL} < 0$. V_S species begin to drift towards the high electrode and refill the sub-stoichiometric lattice in the central part of the fissure. However, the dose distribution in the fissure has been skewed by tilting the stage (**Fig. 4.14(b)**). We now have a gradient of the V_S concentration and of the local material resistance. As V_S species drift towards the centre of the fissure, they shrink the spatial extent of the switching region, setting the device into LRS. Thus, for the reverse polarity sweep, the voltage drop encountered by the electric field is more abrupt, leading to an increased resistance ratio as the device is reset into HRS. For the case where the high electrode is on the side of the V_S extension, biasing the device spreads the V_S species even further out into that half of the flake. On the reverse polarity sweep, as the device sets into LRS, the voltage drop is already more gradual as the field encompasses a much more extended switching region - resulting in a lower R_{HRS}/R_{LRS} ratio for the initial **i** and **ii** sweep portions. In addition, the previously observed asymmetry of state writing upon irradiation at mirrored tilts is observed in the case of the 30° *I-V* curves, suggesting once again that the beam shape may be a key contributor to the switching behaviour. A more systematic study on more samples is necessary to elucidate the exact effects of irradiations performed at negative tilts, rather than at opposite bias polarities.

The effect of increasing the stage tilt in general is to slightly raise the resistance ratio for both cases, by exaggerating this V_S skewness discussed above. The two trends can be fitted with rising polynomials towards higher angles (discounting a high ratio outlier at 40°); with the increase in R_{HRS}/R_{LRS} from 30° to 50° registered at 31% for the high electrode across the fissure, and 50% for the high electrode on the side of the V_S extension. However, we have found no meaningful trends with stage tilt for the set/reset biases, nor for the gating behaviour with regards to the resistance ratio or any other standard parameters as the stage tilt is increased. Thus, the gate modulation of the resistive switching process in these memtransistor devices requires further study. It is yet unclear whether gating modulates the injection current at the

fissure/pristine flake interface by equalising Fermi levels in the asymmetric lateral stack, or whether it has a pronounced effect on the physical drift of V_S species in the device. In addition, the suggestions from Sangwan *et al.* that gate-controlled resistance switching is modulated at the contact/channel interface in GB-mediated devices [108] may not hold true in our case, as we have shown that introducing the fissure drops the conductance of the device by at least an order of magnitude - highlighting its importance for throttling the electron transport across the channel. We go on to explore this assertion in later sections of this chapter with cryogenic charge transport experiments.

The physical effects of biasing these asymmetric memtransistors can be seen for some devices using the *in-lens* SE detector in the SEM. **Figure 10.5(a)** presents an example micrograph of a device which was irradiated at 40° and cycled 16 times (11 times with the *high* electrode on the side of V_S extension, 5 times with the *high* electrode across the fissure). A visible fissure (bright contrast) is seen bisecting the CVD MoS_2 FET channel. A visible defect extension is present on both sides of the fissure as dark contrast. The grey scale values of the SE intensity are plotted in **Figure 10.5(b)**, as extracted from a line profile spanning from electrode to electrode across the irradiated MoS_2 channel.

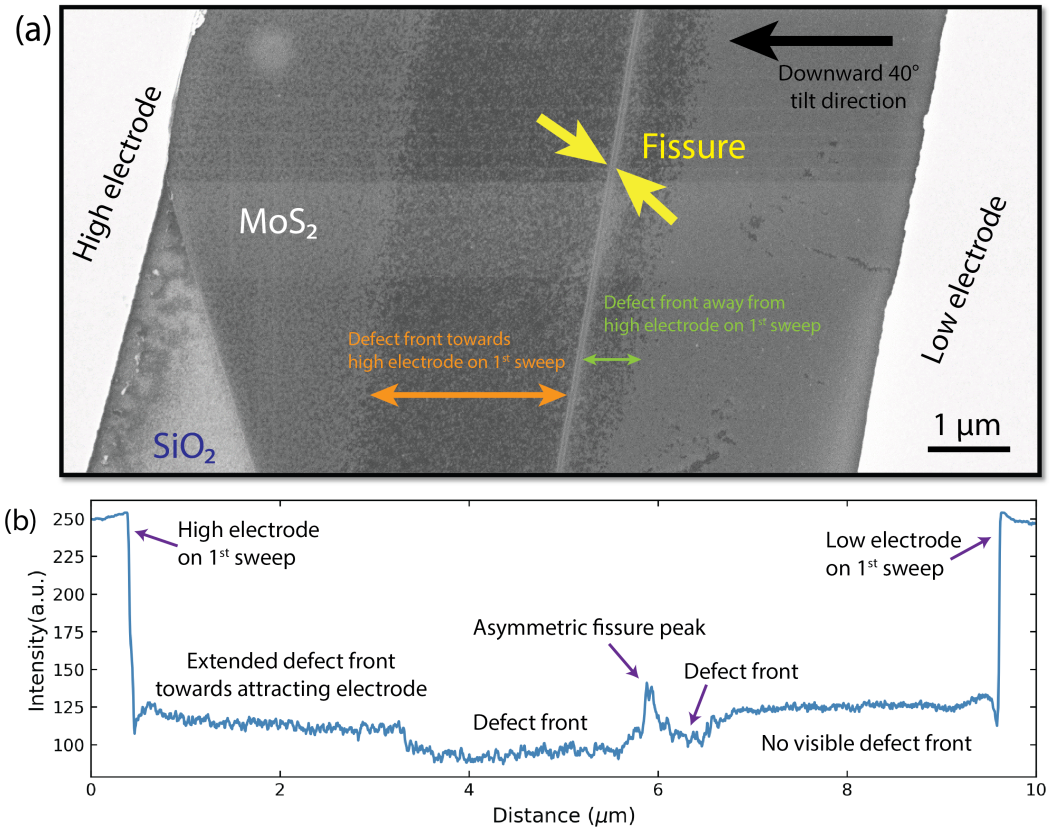

Figure 10.5: **(a)** SEM micrograph of a CVD monolayer MoS_2 memtransistor device irradiated at 40° and cycled 16 times (11 times with the *high* electrode on the side of V_S extension, 5 times with the *high* electrode across the fissure). **(b)** Intensity line scan across the device channel, showing clear changes in contrast due to the migration of defects in a preferential direction. Note that the bright peak around the fissure is asymmetric.

It is evident that the defect extension towards the electrode designated as *high* on the initial sweep is much wider ($\sim$ 2.5 μm, compared to $\sim$ 1 μm on the other side), as that was also the side of the extended V_S distribution during the 40° tilt irradiation. Meanwhile, the drift of defects to the other side of the device is much less expansive, considering most of the V_S species had to cross the fissure fully after polarity change, i.e. when attracted towards the electrode designated as *low* on the first sweep. As we found no experimental evidence in the SEM of visible defect drift towards the high electrode upon polarity reversal in devices tilted during irradiation, a potential check in future work should involve irradiations at physically negative tilt angles to ensure that beam shape has the purported effect on electrical performance as claimed in this chapter.

These exaggerated cases of asymmetric fissures provide additional evidence for our

theory that the driving force for ion migration in these devices is voltage-mediated and the polarity of the applied bias is key to the device functionality. The modulation of resistance states by the local change of the V_S concentration, and the associated effect on the voltage drop across the device when biased, becomes more pronounced when the V_S distribution is skewed about the central portion of the irradiated pattern. We go on to describe the proposed mechanism of resistive switching in these bisected MoS_2 devices in the following section.

10.2 Effects of crystal orientation

As mentioned previously in **Chapter 9**, the direction of the fissure trace relative to the crystal orientation of MoS_2 will introduce an asymmetry to the atomic termination of the irradiated fissure edges, possibly allowing for the easier migration of vacancies, leading to an observed asymmetry in the *I-V* hysteresis. **Figure 10.6** shows the electrical response of monolayer CVD devices from the same growth batch, where electrodes had been deposited in the same geometry (perpendicular to the base of the MoS_2 triangle), but the angle of the fissure trace had been rotated to the angle given in the figure legend. The trend observed in **Figure 10.6(a)** (for this admittedly limited range of tested angles) is the increased asymmetry of the *I-V* response at angles which are not divisors of the nearest high-symmetry rotation of 30°, i.e. the 4° and 17° cuts. The cases of 0°, 5° and 30° itself have a much more symmetric response and show much higher conductance levels, suggesting a larger resistance at the fissure interface for the slightly lattice-offset irradiations. In addition, the largest hystereses open for the 4° and 17° cases, suggesting that the drift of vacancies out of these interfaces is more prominent in HRS. Transfer curves of the same devices presented in **Figure 10.6(b)** highlight how the carrier density of the device/fissure region can be tuned by the field effect as a function of this changing symmetry of channel bisection. In all cases but the 17° irradiation, the device conductance at saturation notably increases, suggesting that irradiations close to multiples of the high-symmetry rotation of 30° (including 0°) allow for increased current flow, presumably due to favourable interfacial reconstruction due to a "cleaner" cut down a high-symmetry lattice orientation (see difference between these in **Figure 10.6(c)**). In addition, the 5° and 30° cases show a higher degree of n-type doping upon irradiation, initially setting into LRS, which may suggest zig-zag and armchair edges allow for higher vacancy mobility across the interface than mixed edges (the 17° case). As this asymmetry emerges in the *I-V* response, additional experiments will be needed in the future to elucidate whether the crystallographic

direction is the dominant factor over the beam shape across a range of azimuthal rotations, as we have seen that both affect the switching characteristics of monolayer memtransistors.

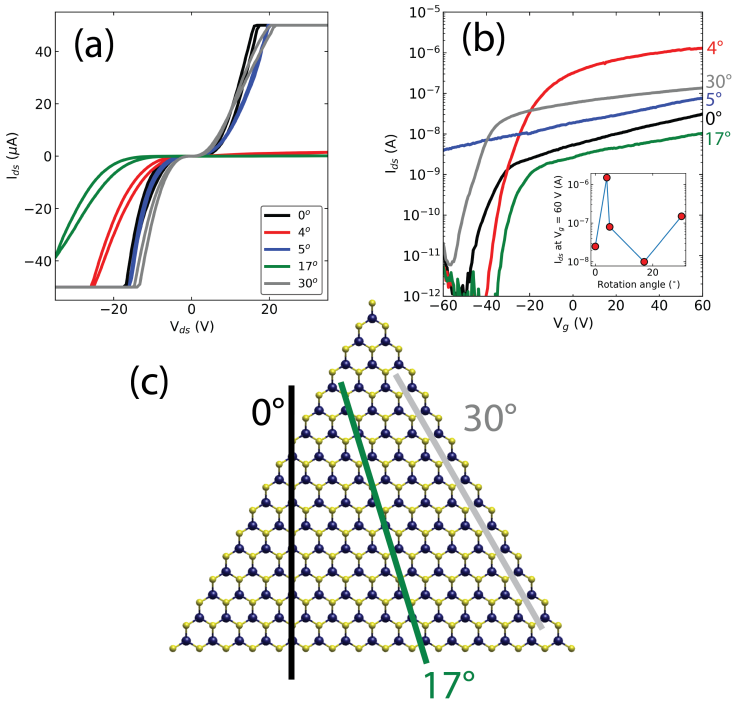

Figure 10.6: **(a)** *I-V* curves of monolayer devices (V_g = 0 V) irradiated at different fissure angles relative to the base of the MoS_2 triangular flake. **(b)** Gate curves (V_{ds} = 1 V) of the same devices with the inset showing the change in the maximum I_{ds} noted for each device as the fissure orientation changes (blue lines are guides to the eye). **(c)** Sketch of the fissure orientations relative to the MoS_2 crystal structure. Visible asymmetries emerge due to irradiations at different angles. Data taken by Darragh Keane.

In addition, characterisation of devices irradiated at various azimuthal rotations relative to the base of the MoS_2 triangle may reveal differing atomic terminations on either side of the fissure. Work carried out so far did not follow a systematic approach with regards to azimuthal rotations, as tilt dependence (and by proxy beam shape) was the focus of the first half of this chapter. The most applicable method for this investigation ought to be TEM, as previous freestanding irradiations have revealed defect front asymmetry across a fissure irradiation at an unknown azimuthal rotation (**Figure 10.3**).

10.3 Proposed switching mechanism

Let us outline a simple picture for what may be happening when we change resistance states. The key pieces of experimental evidence contributing to this model are summarised below:

1. Raman and PL intensities from **Fig. 9.20** vary more on one side of the fissure than the other when switching between LRS/HRS. The spread of defects is also visibly asymmetric in the SEM image in the previous figure. *This is the asymmetry argument*.

2. the intensity of E' and A_1' modes decreases at doses of 10^{16} ions cm^{-2}. *This shows we are, in fact, generating* V_S.

3. both E' and A_1' mode intensity is quenched on one half of the flake in HRS relative to LRS. Meanwhile the PL intensity is also higher in LRS. This is in line with established evidence in the literature for MoS_2 with increasing defect concentration. *Thus, LRS is the* V_S*-rich state in the fissure, while HRS is the* V_S*-rich state outside the fissure on one side of the flake*.

4. conductivity regimes as a function of dose (in ions cm^{-2}, from our previous work [192]) are established as: 10^{14}- semiconducting; 10^{15} - insulating; 10^{17} - metallic - see visual guide in **Fig. 10.7**. *Hence, changes to the* V_S *concentration will tune the metallicity of a given region, changing the voltage drop across it*.

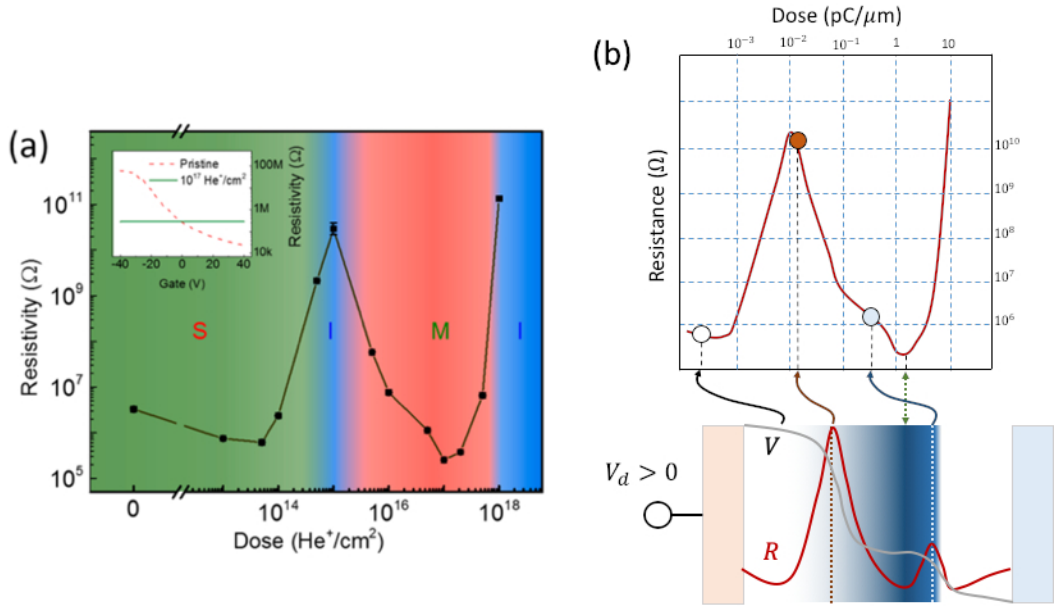

Figure 10.7: **Switching mechanism basis. (a)** Resistivity-dose plot from Fox *et al.* [192]. **(b)** The graph from **(a)** re-drawn in terms of linear ion dose and mapped to a sketch of the device structure after irradiation. The dark blue band is the centre of the delivered dose distribution (at $\sim 10^{17}$ ions cm^{-2}), which is naturally asymmetric about the middle of the ion probe. By applying a bias and drifting vacancies into the non-irradiated MoS_2 channel, its conductivity, the associated voltage drop and the electric field magnitude needed to drift the vacancies all change. The grey curve symbolises the voltage drop across the device when $V_{ds} < 0$.

Implications of the above are as follows: the drain-side has better crystallinity in LRS. The *setting* process enables V_S migration from the drain-side of the flake to the fissure; enriching the V_S concentration in the cut region. This establishes conducting paths in the drain-side of the fissure region, lowering its resistance. *Note*; the voltage drops mainly across the drain-side of the flake, on the approach to the fissure, since it has the largest serial resistance. Following the diagrams in **Fig. 10.8**, when the V_S drift is *towards* the fissure, the device is set into LRS at positive bias, shrinking the extent of the V_S spread on the drain-side of the channel. This means the concentration of V_S is now localised to a narrower band in the channel. When the applied bias is negative, the device is *reset* into HRS. This happens because vacancies move out of the fissure towards the drain electrode and expand the defective band in the channel, changing the voltage drop across it. This causes the V_S concentration and associated MoS_2 conductivity to change. The resistance is increased precisely because the spread of V_S into MoS_2 enters the resistance-dose peak empirically established in our previous work [192]. Sliding up and down this

resistivity-dose curve (and by proxy the resistivity-V_S concentration curve) is the fundamental physical origin of the resistance changes observed in the device.

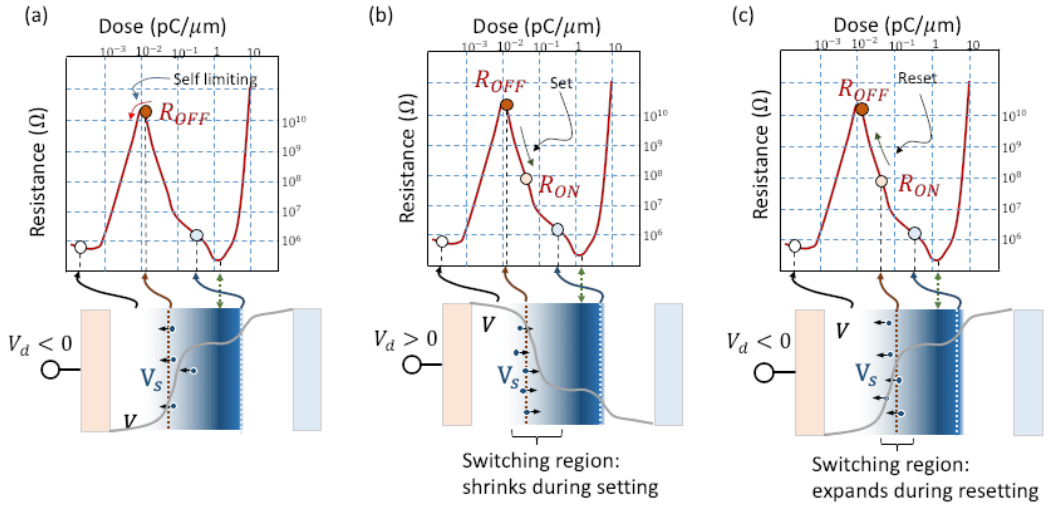

Figure 10.8: **Switching between states.** In the MoS_2 channel cartoons, the grey line tracks the voltage drop across the channel as the V_S distribution and associated conductivity change with the applied electric field. The black dots with arrows symbolise the movement of V_S. **(a)** Initial state of the device immediately after irradiation. The beam sets the device into HRS upon fabrication as the delivered dose is naturally asymmetric (equivalent to electroforming by applying $V_{ds} < 0$). **(b)** Setting into LRS happens when the spatial extent of the V_S spread shrinks into a more confined region in the centre of the fissure (occurs when $V_{ds} < 0$). The voltage drop across the fissure is more gradual, as the spread of V_S is more extensive when starting in the HRS configuration from **(a)**. **(c)** Resetting into HRS occurs when the spatial extent of the switching region physically expands (when $V_{ds} < 0$). The voltage is mostly dropped across the confined highly-metallic region in the fissure. R_{OFF}; HRS, R_{ON}; LRS.

10.4 Low temperature electrical characterisation of the MoS_2 memtransistor

We go on to describe the outcome of cryogenic transport measurements on our memtransistor device when switched into each individual resistance state (on a nominally 0° tilt-irradiated device). These measurements were carried out in the bath cryostat in the lab of Prof. Zhi-Min Liao at Peking University, China, as described in more detail in **Chapter 4**. Briefly; the samples were wire-bonded using aluminium leads to large-area Ti/Au pads, and globally back-gated through a silver paint-connected terminal underneath the highly-doped Si substrate. The cryogenic transport measurements were carried out in an *Oxford Instruments* bath cryostat with no applied magnetic field, pressure of $\approx$ 10 mbar and temperature equilibration to within $\pm$ 1 K 5 $mins^{-1}$. The electrical measurements, including data for 1/f noise analysis, were obtained using a semiconductor analyser (*Agilent B2912A*) interfaced with `Keysight` software. All switching of resistance states was

undertaken at room temperature, with each device remaining in LRS or HRS for respective testing as the temperature was varied up from 1.5 K to 280 K. For each temperature point, gate curves were collected first with V_{ds} = 0.5, 1, 2 and 5 V, in that order. *I-V* sweeps were then collected between ± 20 V with the gate bias held at -60, -40, -20, 0, 20, 40, 60 V, in that order. The noise data were collected for ≈ 5 minutes at V_{ds} = ±1 V, with the gate voltage held at V_g = 30 V for the low temperatures until V_{th} had shifted enough at higher temperatures to hold it at values of V_g = 0, 5, 10 V, in that order.

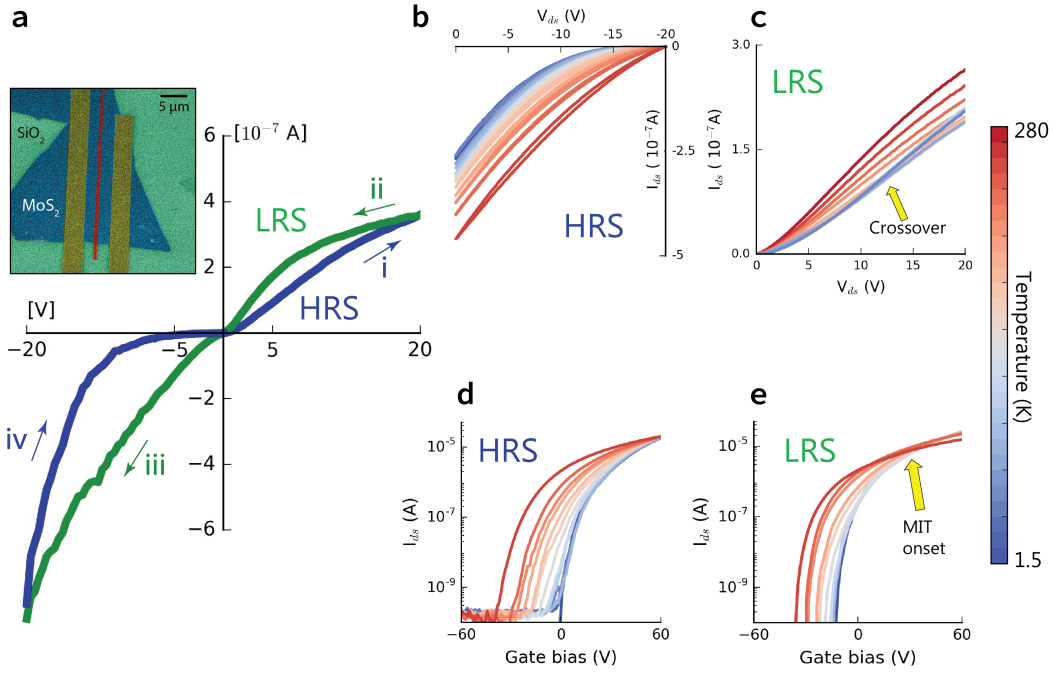

Figure 10.9: **Temperature-dependent output and transfer characteristics of the monolayer MoS_2 memtransistor in the high and low resistance states.** **(a)** Initial bipolar *I-V* sweep of the device after fabrication, with the resistance branches of the switching cycle highlighted on the plot (V_g = 0 V). Inset is a false-colour HIM image of the fabricated device, with the fissure region marked in red. **(b)** Temperature-graded *I-V* curves of the negative-polarity branch of the high resistance state. **(c)** Temperature-graded *I-V* curves of the positive-polarity branch of the low resistance state. The yellow arrow marks a conductance crossover below 100 K. **(d)** Temperature-dependent transfer curves in HRS. **(e)** Temperature-dependent transfer curves in LRS, with the carrier density-dependent metal-insulator transition marked with the yellow arrow. Note the colour bar on the right applies to **(b)**, **(c)**, **(d)** and **(e)**. V_{ds} = 5 V for the gate sweeps.

Figure 10.9(a) presents the typical hysteretic bipolar resistive switching *I-V* curve of the monolayer MoS_2 memtransistor. The inset shows a false-colour He^+ ion micrograph of a contacted device (electrodes in gold), with the irradiated region marked in red. LRS is marked in green, while HRS is marked in blue. Each consecutive quarter-sweep of the switching cycle is marked with sequential Roman

numerals on the plot. **Figures 10.9(b,c)** show the drain-source *I-V* sweeps, locked in the negative-polarity branch of HRS and the positive-polarity branch of LRS respectively; recorded at various temperatures corresponding to the colour bar on the right of the figure. We measured the unipolar *I-V* sweeps from 0 V to ∓ 20 V in each resistance state starting from the lowest temperature. We only switched the device from HRS to LRS once room temperature was reached between **Fig. 10.9(b)** and **Fig. 10.9(c)**. The switching was carried out at room temperature to ensure standard device functionality and to control for the unknown effects of ionic drift at cryogenic temperatures. In both cases, the sweeps were carried out in the active range of the MoS_2 FET (V_g = 20 V). In HRS, as the temperature is decreased, the device outputs less current for the same applied voltage; suggesting typical semiconducting behavior. In LRS, as the temperature is lowered to below 100 K, the output current of the device compared to that at intermediate temperatures begins to increase - a sign of emergent metallic-like behaviour. This crossover is marked on the plot with the yellow arrow.

Figure 10.9(d) demonstrates the temperature-dependent gate characteristics of MoS_2 in HRS evaluated at V_{ds} = 5 V . Typical n-type MoS_2 behaviour is noted at all temperatures, with an observable V_{th} shift to positive biases as the temperature is lowered; a phenomenon previously observed in MoS_2 FETs [281, 37, 108, 46, 305]. **Figure 10.9(e)** presents analogous data collected in LRS after the device was resistively switched at room temperature. The LRS transfer characteristics show a large deviation from their HRS counterparts. The device V_{th} shifts by $\approx \Delta 12$ V to negative gate biases at 1.5 K, indicating a considerable increase of electron doping in LRS as compared with HRS at the same gate bias. Both states demonstrate relatively sharp subthreshold swings for a back-gated device, in the range of 0.5 - 1 V dec^{-1}, with no notable dependence on temperature. The collected data is also less noisy in LRS at the same sampling rate. Importantly, a temperature-dependent conductance crossover, indicated by the yellow arrow in **Fig. 10.9(e)**, is observed in the LRS gate curves at $\approx V_g$ = 43 V. As discussed in the literature overview, this crossover has been reported in both mechanically-exfoliated and CVD-grown MoS_2 devices of various layer thickness [46, 37, 281, 359], and is proposed to have its origin in the MIT due to disorder-dominated electron correlation effects in the monolayer limit [32, 38]. This suggests that we are crowding electrons into a very confined 2D area in LRS - which agrees with the picture of V_S being squeezed into the fissure region in LRS.

10.5 Electron mobility scaling with temperature

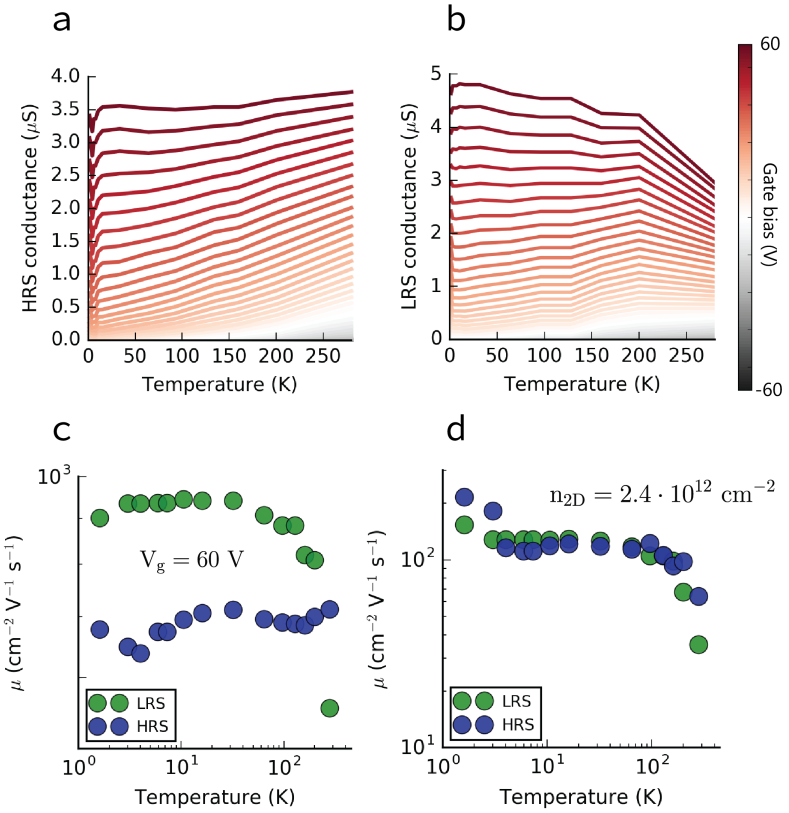

Figure 10.10: **Impact of device resistance states on electron transport.** **(a)** Device conductance in HRS as a function of temperature extracted at different gate biases. **(b)** Analogous data for LRS. Gate biases are mapped to the colour bar on the right for both **(a)** and **(b)**. **(c)** Temperature dependence of the electron μ_{fe} for both LRS and HRS, extracted at V_g = 60 V. **(d)** Mobility as a function of temperature in both states when evaluated at the same carrier concentration of n_{2D} = 2.4 · 10^{12} cm^{-2}. Data taken at V_{ds} = 5 V.

To examine this more closely, we can analyse the temperature dependence of the device conductance at various carrier concentrations, as controlled by the gate bias. **Figures 10.10(a)** and **10.10(b)** track the conductance of the device (G) in HRS and LRS as a function of temperature respectively, graded for the gate bias at which G was evaluated (between V_g = ± 60 V). Gray colour in the plots represents negative gate biases and hence lower carrier concentrations. Dark red colours signify higher gate biases and a rising two-dimensional carrier concentration, n_{2D}, which ultimately is the key factor for the onset of the MIT in both the quantum criticality [38] and percolation-driven models [360].

As evident from the plot in **Fig. 10.9(a)**, the conductance of MoS_2 in HRS drops as the device is cooled across all tested carrier concentrations (up to n_{2D}^{HRS} = 3.5 ·10^{12} cm^{-2} at 1.5 K). In contrast to this, when the system is in LRS (**Fig. 10.10(b)**),

we observe the onset of the carrier density-dependent MIT at a much lower gate bias and temperature, with the conductance manifesting metallic-like behaviour as it rises visibly with dropping temperature. The controllable drift of sulfur vacancies in the memtransistor fissure allows for the dynamic tuning of the electron donor concentration in the current-limiting section of the FET channel. The same n_{2D} is achieved in the device in LRS at V_g = 43 V as at V_g = 60 V in HRS. This allows us to cross the MIT threshold at smaller operating transistor powers in LRS, highlighting the direct impact of vacancy motion on the electron doping of the device.

As temperature-dependent electron-phonon scattering events are governed by the concentration of charged impurities, we evaluate the temperature scaling of the electron mobility across both resistance states at the same gate bias (**Fig. 10.10(c)**) and at the same n_{2D} (**Fig. 10.10(d)**). As the transistor V_{th} shifts drastically between states, a correct evaluation of n_{2D} induced by the field effect must take this into account. Upon the introduction of the V_S source by the ion beam, the effect on carrier mobility scaling evaluated at V_g = 60 V is seen in **Fig. 10.10(c)**. In LRS (green), it is evident that the electron mobility increases at lower temperatures. This is a rare phenomenon in monolayer MoS_2 FETs [37], usually requiring encapsulation with a high-κ top gate dielectric [32, 38] or encasing in hexagonal boron nitride [36]. Meanwhile, at the same gate bias, the HRS mobility (blue) generally trends downwards below $\sim$ 80 K. When evaluated at the same n_{2D} of 2.4 $\cdot 10^{12}$ cm^{-2}, the mobility of the carriers in both LRS and HRS rises as the temperature drops, as is typical for a metallic material (**Fig. 10.10(d)**). Despite its increased disorder ($>$ 1% of V_S concentration, as we have seen in the previous chapter), the vacancy-rich memtransistor can be doped into a strongly interacting state in LRS, that allows for dominant electron-electron interactions to cause a mobility upturn at low temperatures. Conceivably, carrier concentrations of the order of 10^{14} cm^{-2} can be achieved by seeding vacancies with the ion beam in MoS_2 devices grown on a thinner gate dielectric [361]. This method may provide a new platform for more fundamental studies of quantum phase transitions and/or superconductivity that does not require gating the material with an ionic gel, which is the standard approach as of today.

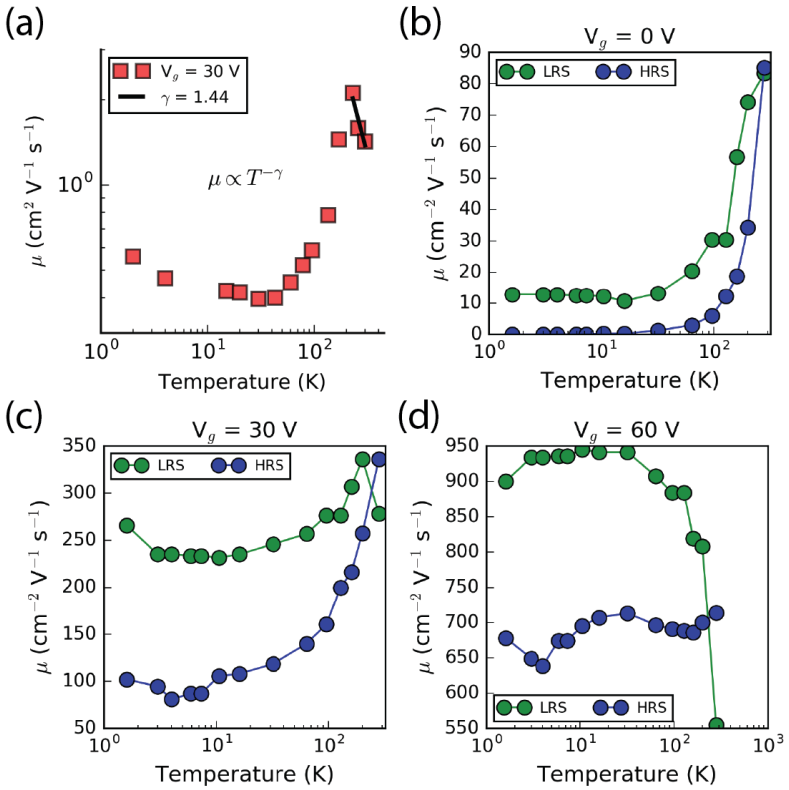

Figure 10.11: **Electron mobility scaling with temperature, before and after irradiation at different gate biases. (a)** μ_{fe} of the monolayer CVD MoS_2 device before ion irradiation. The black line is a fit to the high temperature regime of the $\mu(T)$ relationship shown on the plot. **(b)**-**(d)** Electron mobilities extracted from an irradiated device in LRS and HRS, at three different gate voltages. Data taken at V_{ds} = 5 V.

Explicit comparisons of the mobility scaling with temperature at various gate biases, and the $\mu(T)$ relationship in our pristine monolayer CVD MoS_2 device before ion irradiation, are presented in **Fig. 10.11**. Theory-compliant scaling of μ as $T^{-1.44}$ is observed in the high temperature regime [362], followed by a mobility decrease with falling temperatures, as is standard for semiconducting 2H-MoS_2. A slight upturn at liquid helium temperatures is noticed in the data, probably arising from extended metallic-like states from intrinsic V_S in the CVD-grown film [185] or the approach of the superconducting regime for monolayer MoS_2 at these temperatures [363, 364, 365]. Once activated, the resistance states of the memtransistor are clearly differentiated in their mobility scaling with temperature when evaluated at the same gate bias. The extracted mobility in LRS is always higher, as expected, and both states retain the semiconducting scaling at low carrier densities (V_g = 0 V and 30 V). As n_{2D} is increased at higher gate fields, the states visibly separate out, with LRS mobilities now exceeding those in HRS by factors of > 2.5 at V_g = 30 V and ~ 1.5 at V_g = 60 V. The LRS trend is also visibly metallic-like at V_g = 60 V, and

the extracted μ_{fe} (though overestimated in absolute terms as mentioned before [68]) is very high for MoS_2 samples (especially defective ones) at low temperatures.

10.6 Conductance mechanisms in the two resistance states

We now analyse the temperature dependence of the conductivity in both states as a function of the applied gate bias in **Figs. 10.12(a,b)**. We first tested the appropriate fitting exponent of the temperature dependence using the Zabrodskii formalism [44, 40, 39] and obtained a closest agreement to the VRH model with $T^{-1/3}$ scaling in both HRS and HRS:

$$G = G_0 \exp\left[-\left(\frac{T_0}{T}\right)^{1/3}\right] \tag{10.2}$$

where G is the conductance, T the measured temperature and T_0 is the correlation energy scale. This model has previously successfully described electronic transport in polymorphic (metallic-like) MoS_2 [40] and across grain boundaries in CVD-grown monolayer MoS_2 [42]. From the slopes of the data fits at each extraction V_g (not shown here for clarity), we observe a sharper conductance drop-off in HRS as the temperature decreases, suggesting a larger degree of carrier localisation in HRS than LRS for a given extraction gate bias. The VRH model describes the transport mechanism in both states reasonably well, even down to temperatures below 50 K, where the fit normally collapses due to the insulating nature of semiconducting MoS_2 [286].

From the VRH fits to our data, we obtained the correlation energy scale:

$$T_0 = \frac{\beta}{k_B \zeta^2 N(E_F)} \tag{10.3}$$

where k_B is the Boltzmann constant, $\beta \approx 13.8$ is a numerical constant, $N(E_F) \approx 10^{14}$ eV^{-1} cm^{-2} is the density of states at the Fermi level [42], and ζ is the electron localisation length. $N(E_F)$ may be overestimated in the case of our defective samples due to the presence of a larger trap density in the channel, although for a micron-sized sample it ought to be of the right order of magnitude around the bottom of the conduction band [366]. When evaluated explicitly in the linear region of the transfer curve, the hopping distance of carriers in the two resistance states is revealed to vary significantly at the same gate bias (**Fig. 10.12(c)**). ζ in HRS is in keeping with previously reported distances of < 5 nm for MoS_2 [40, 42, 41]. The localisation

is weakened in LRS, however, where carriers achieve twofold the hopping distance of HRS for the same gate bias. The strong localisation regime persisting in HRS at these gate biases suppresses carrier transport across the irradiated region and lowers the device conductivity. The onset of weakened localisation in LRS is a fine balancing act between doping levels brought about by the V_S concentration and the applied field effect. A parameter of crucial consequence is the large threshold voltage shift induced by V_S electron donation in the device. As the field effect begins to invert the channel, hopping through defective states is the dominant mode of transport in HRS. Due to V_{th} shifting to higher negative biases in the dopant-rich LRS, extraction of ζ at the same gate bias probes the channel in the active transistor region in LRS (shaded in with violet), where extended states begin to form and allow for increased hopping distances between defective sites [37].

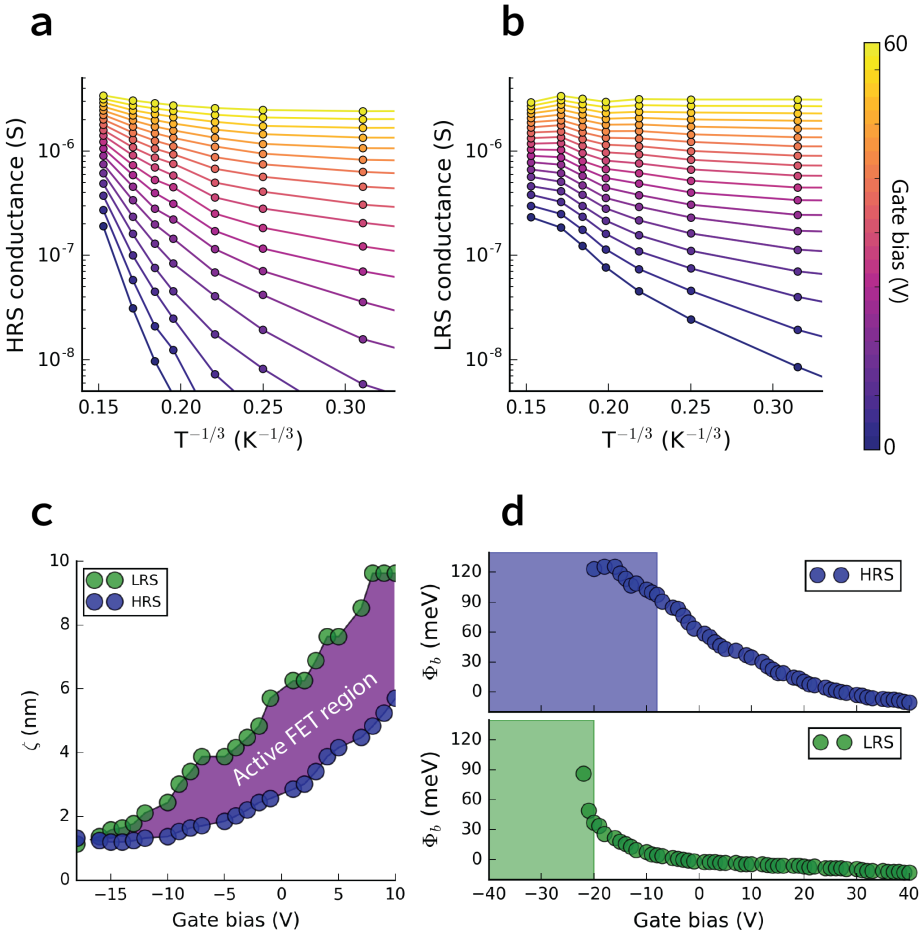

Figure 10.12: **Conductance mechanisms, carrier localisation lengths and carrier injection barrier heights in the two resistance states.** **(a)** and **(b)** show the conductivity on a semi-log scale plotted against $T^{-1/3}$ across the active gate bias range (colour bar on right) for the MoS_2 memtransistor in HRS and LRS respectively. Lines are guides to the eye. **(c)** Extracted electron localisation lengths for carriers in the two states in the linear region of the FET. **(d)** Effective carrier injection barrier heights for both resistance states across a range of gate biases. The shaded coloured areas extend to the approximate flatband condition ($V_g = V_{fb}$) necessary for carriers to overcome the barrier in both states. Data taken at $V_{ds} = 5$ V.

Just as in our low-temperature study of plasma-treated MoS_2 in **Chapter 6**, we can employ the 2D Richardson equation to extract the effective carrier injection barrier heights (Φ_b) of the device in the two resistance states from curves of $\ln(I/T^{3/2})$ vs $1000/T$ around the flatband condition (V_{fb}). Where the linearity breaks in the relationship of Φ_b and V_g, as V_g approaches V_{fb}, emission across the barrier is no longer largely thermionic and the effective barrier height can be extracted.

Note; we stray from calling Φ_b the *Schottky* barrier height. The introduction of the ion beam-created fissure into the channel increases the resistance of MoS_2 by

$\sim$ 1 order of magnitude. Thus, the current-limiting interface in the device in both states is no longer the semiconductor/metal interface, but rather the fissure itself (or more precisely, the interface of the fissure edge with the pristine flake). Hence, we are calling the barrier height an *effective barrier height* for carrier injection to differentiate it from the metal/contact interface. The conductance mechanism analysis thus is also limited precisely to the current-limiting fissure region (as we have shown, at most 200 nm) in both states. As the temperature scaling remains the same in LRS and HRS ($G \propto T^{-1/3}$, Mott VRH due to the heavy presence of vacancies), we can assume the physics of the trap-limited transport in the fissure region is roughly the same in both states; supported by the fact that the n_{2D} difference between LRS and HRS is at most $\sim 10^{12}$ cm^{-2}. Thus, we can analyse the injection-limited transport at the interface in terms of energy barriers above a certain gate voltage where both states enter a similar conductance scaling with temperature.

Figure 10.12(d) presents this data with shaded coloured regions approaching the flatband condition from the side of the thermionic emission. The difference in V_{fb} between LRS and HRS approximately matches that of the gate V_{th} difference, though the break in the linearity in HRS is less pronounced. This is a direct consequence of the physical state of the defective MoS_2/pristine MoS_2 interface as vacancies drift out of the fissure in HRS. In our proposed picture, the interface is more gradual and spread out in HRS, while the LRS interface is more spatially-confined. Thus, the break in linearity of Φ_b with V_g is sharp in LRS, as it effectively mimics the standard metal/semiconductor interface, while the extended V_S states across the gradual interface in HRS lead to no discernible break in this relationship in the energy landscape as V_g is ramped up. The barrier height in LRS is extracted at $\approx$ 40 meV, while Φ_b in HRS is $\approx$ 100 meV. This barrier height ratio is in good agreement with the extracted Schottky barrier heights of the polycrystalline MoS_2 memtransistors, where Φ_b were reported as 80 meV and 125 meV for LRS and HRS, respectively, for the V_S-rich Au/MoS_2 interface [108].

10.7 1/f noise and carrier velocity saturation in LRS and HRS

A study of pink noise in the memtransistor as a function of temperature unveils the impact of the defective FET channel on carrier transport in the two resistance states. **Figures 10.13(a-b)** present the raw temporal current traces taken in each resistance state across a range of different temperatures at V_g = 30 V and V_{ds} = $\pm$ 1 V, respectively, for LRS and HRS. Meanwhile, **Figs. 10.13(c-d)** show the transformed power spectral densities of each I_{ds} trace in the low-frequency regime. Each of the

$\frac{S}{I^2}(f)$ plots was fitted with a linear relationship in β to determine the magnitude of the noise amplitude A from the Hooge law: $S = \frac{AI^\gamma}{f^\beta}$, with $\gamma = 2$. The ratio of these noise amplitudes between the two resistance states, A_{HRS}/A_{LRS}, is plotted against temperature in **Fig. 10.13(e)**. A visible trend emerges where A_{HRS}/A_{LRS} increases by orders of magnitude as the temperature decreases (with an outlier datum at 32 K) and saturates off at liquid helium temperatures. Thus, it is clear that the noise amplitude in HRS is much higher than that in LRS at the same gate and drain-source voltage. The effect is more pronounced at low temperatures where thermal components contributing to the noise, be it phonons or activated carrier populations, do not play a major role.

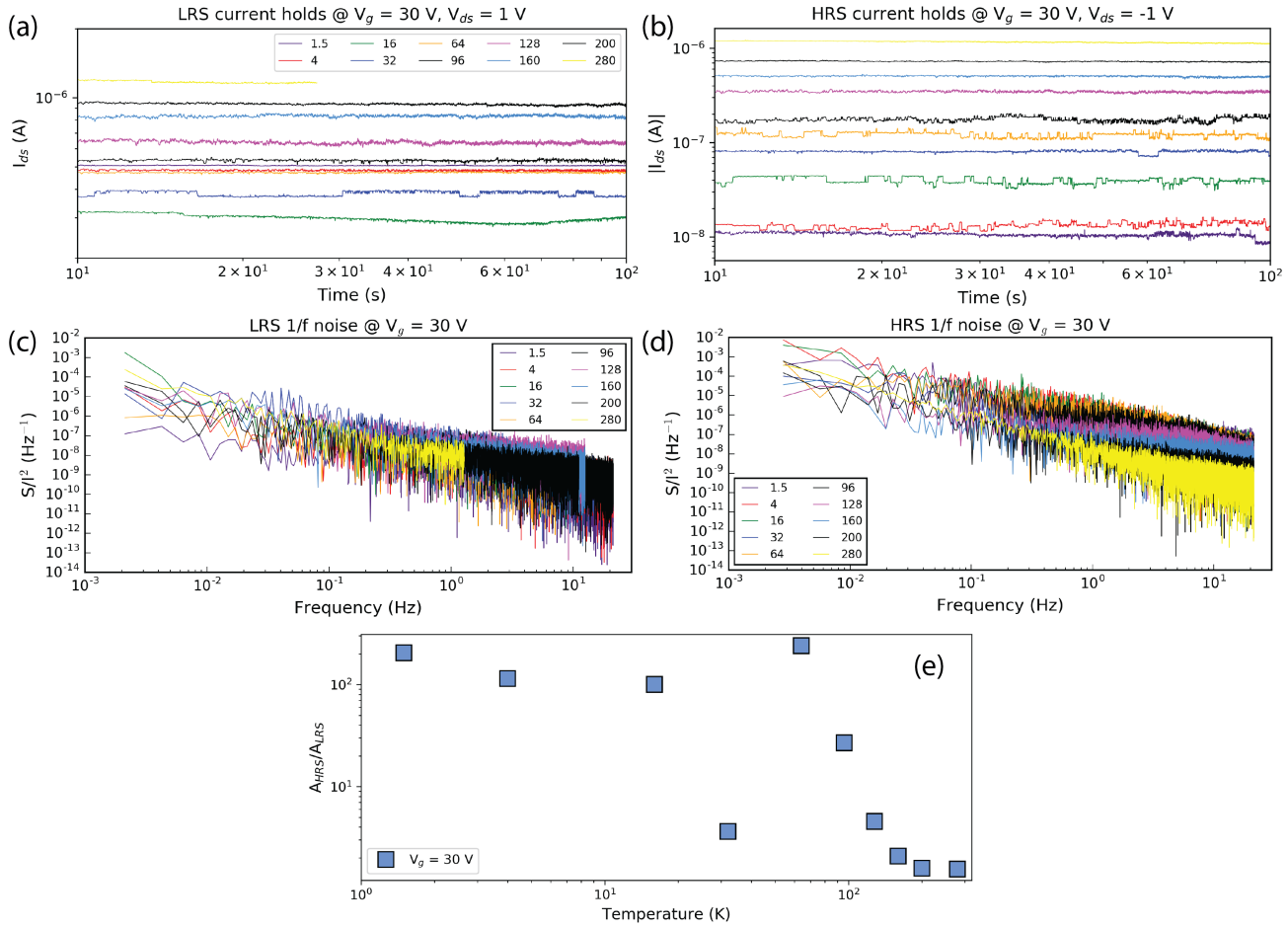

Figure 10.13: **1/f noise in the temporal traces of current in each resistance state. (a,b)** Current temporal traces in LRS and HRS of the MoS_2 memtransistor held at V_g = 30 V and V_{ds} = ± 1 V, respectively, recorded across a range of temperatures between 1.5 K and 280 K. Note the HRS currents are absolute values. **(c,d)** Noise spectral density plots of the traces in **(a)** and **(b)** at low frequencies. **(e)** Plot of the ratio of noise magnitude between states (from fits of $S = \frac{AI^\gamma}{f^\beta}$, with $\gamma = 2$ and $\beta = 1$).

Figure 10.14(a) presents a closer look at the temporal traces of the drain current in both LRS and HRS, biased at V_{ds} = ±1 V and V_g = 30 V. Insets give a magnified look at the data across the same time frame in both states. As expected, I_{ds} has a significantly lower magnitude in HRS at the same V_{ds} and gate bias. Even on the logarithmic scale, one observes strong fluctuations in the time series of I_{ds} in HRS, with multiple occurrences of RTN which, as we have seen in the literature overview, has been linked explicitly to the presence of single carrier traps in MoS_2 FETs [49]. The LRS trace, in turn, exhibits a smaller degree of fluctuations and RTN spikes originating from the random de-trapping of charge carriers in the channel.

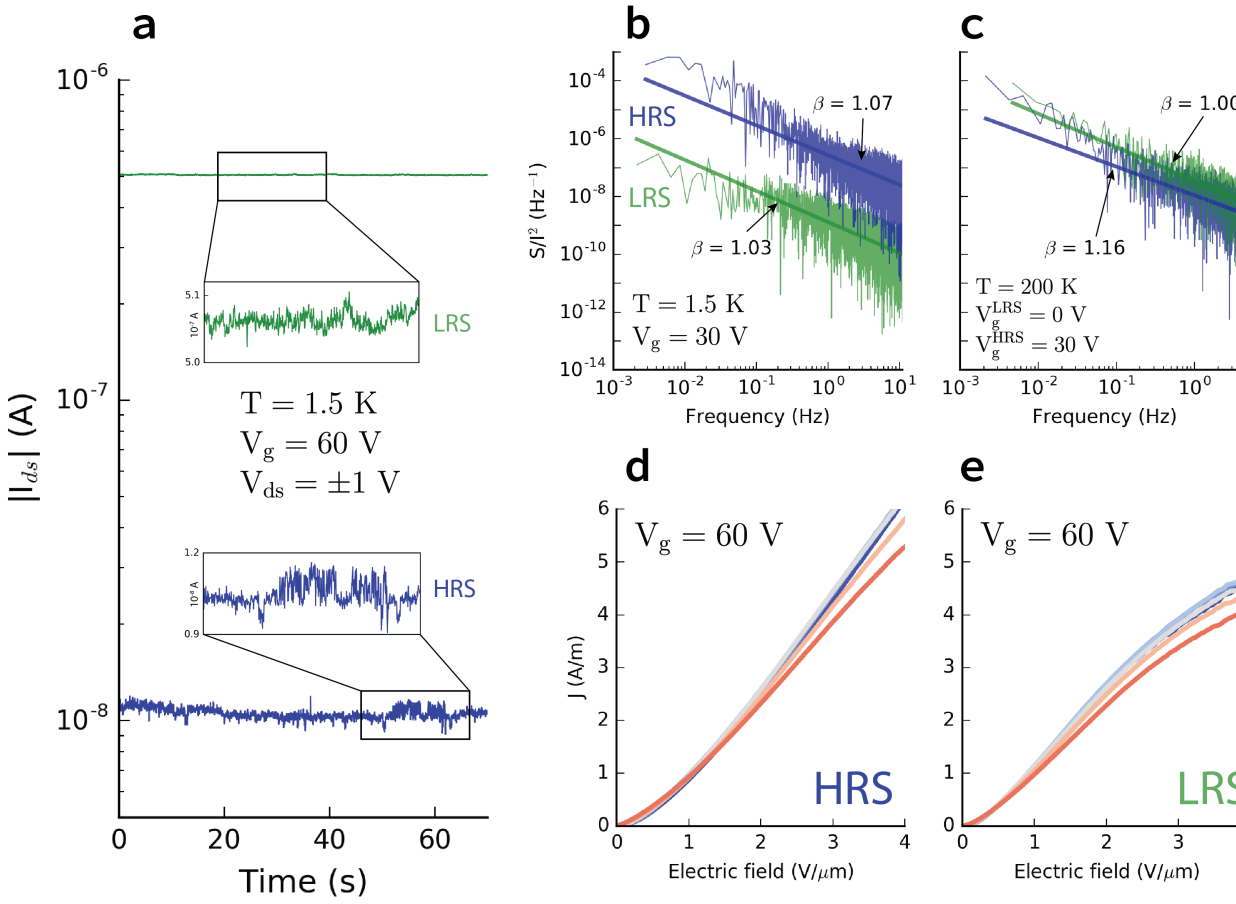

Figure 10.14: **Pink noise spectra and the current density saturation response of the memtransistor states at different carrier concentrations.** **(a)** Current temporal traces for both resistance states of the MoS_2 memtransistor held at V_g = 30 V and V_{ds} = ± 1 V, recorded at T = 1.5 K. Insets show magnified regions of the plot across 20 seconds. **(b)** Noise spectral density of the traces in **(a)** at low frequencies. Both show $f^{-\beta}$ scaling with respective β values marked on the plot. **(c)** Analogous plot for data taken at T = 200 K and at different gate biases for the two resistance states, to correct for the V_{th} shift between LRS and HRS. Note that **(b)** and **(c)** share the same y-axis. **(d)** Current density as a function of lateral electric field in HRS, showing a linear response with increasing field. **(e)** Current density saturation as observed at high electric fields in LRS. Note that **(d)** and **(e)** were both taken at V_g = 60 V.

Both signals are obtained at the same gate bias (meaning different carrier concentrations), with true carrier number differing mainly due to the varied V_S concentration in the fissure in the two resistance states. The discrepancy in noise magnitude therefore arises from both the fluctuation in the carrier mobility due to the different stages of channel inversion sampled between states [275, 46], as well as CNF due to the V_S concentration, as studied previously in ultra-thin MoS_2 [47, 42]. As we are always operating below annealing temperatures which begin to affect surface traps

in MoS_2 [47], we do not attribute the large difference between LRS and HRS at 1.5 K to factors other than the intrinsic traps already present in the device fissure. Our memtransistor is switched between LRS and HRS in vacuum between consecutive state testing, so the origin of noise is inherent to the FET channel, i.e. the change in the concentration of mobile sulfur vacancies.

Analysis of the power density spectrum of the time domain fluctuations (**Fig. 10.14(b)**) reveals a stark contrast in the noise amplitude (ratio of 204) between the two states when measured at the same temperature, gate bias and V_{ds}. Both transforms are fitted well by the Hooge law in the low frequency regime, with β values extracted from the fit shown on the plot. As the device is gated well past the threshold in both states and good fits are obtained when $\gamma = 2$, the contribution to 1/f noise from the contact resistance and effective drain-source biasing in MoS_2 is negligible [48], as would be expected for our devices whose transport is governed by the central fissure in the channel. When compared at a similar n_{2D}, i.e. different gate biases, the noise spectral densities for LRS and HRS show comparable amplitudes (**Fig. 10.14(c)**). We note that this evaluation was carried out at a higher temperature (200 K) to account for the V_{th} shifts that make it impossible to evaluate data at the same carrier density in both states at low temperatures. The LRS spectrum, which is now acquired in the linear region of the transfer curve, shows a higher noise magnitude than the HRS data acquired past the linear region of the FET. As the FET just enters the linear region past V_{th} in HRS, the noise amplitude will be much larger than in the approach to the strong inversion regime at higher gate biases. This has its origin in the nature of the field effect and how its centroid envelops the MoS_2 channel with increasing gate bias [275, 47]. In LRS, in turn, the large V_{th} shift to negative V_g values means that the channel is saturated at the same gate bias for which the channel in HRS is not. For the presently discussed case, LRS and HRS will differ in trap density and mobility fluctuation as the gate field is ramped up. Due to the V_{th} shift and the increased electron doping in LRS, the conductive hot spot will form at a lower gate voltage, allowing the CNF contribution from actively-doping vacancies to overcome the mobility fluctuation from the field effect in the active region of the FET. This will result in LRS noise amplitudes exceeding those of HRS when evaluated at similar n_{2D} values, as evident in **Fig. 10.14(c)**.

The previously established discrepancy in carrier hopping distance will directly affect the trapping and de-trapping rate and thus the velocity with which electrons drift across the channel. A measure of this effect can be established by analysing the

current density saturation in both states at maximum carrier densities (V_g = 60 V), in response to the applied electric field. **Figures 10.14(d,e)** present the current density (J) in HRS and LRS, respectively, as a function of the lateral electric field applied to the channel at temperatures varying between 280 K (red) and 1.5 K (blue). At low fields (< 1 V μm^{-1}), we observe a similar linear increase in J in both states across all temperatures, in keeping with the mobility-proportional scaling also observed in 2D black phosphorus [64] and graphene [61] (see the linear increase in the low-field data at all temperatures in **Fig. 10.15**). As the field strength increases, the linearity remains largely unaffected in HRS, especially at low temperatures, while an observable saturation is approached in LRS at all temperatures. Notably, the LRS current at low fields exceeds that of HRS at low fields, where the memtransistor is usually operational, but the trend is reversed once LRS currents roll off at high fields. A cross-over is also noted in the current density at low temperatures in LRS at V_g = 60 V, even in the low-field regime.

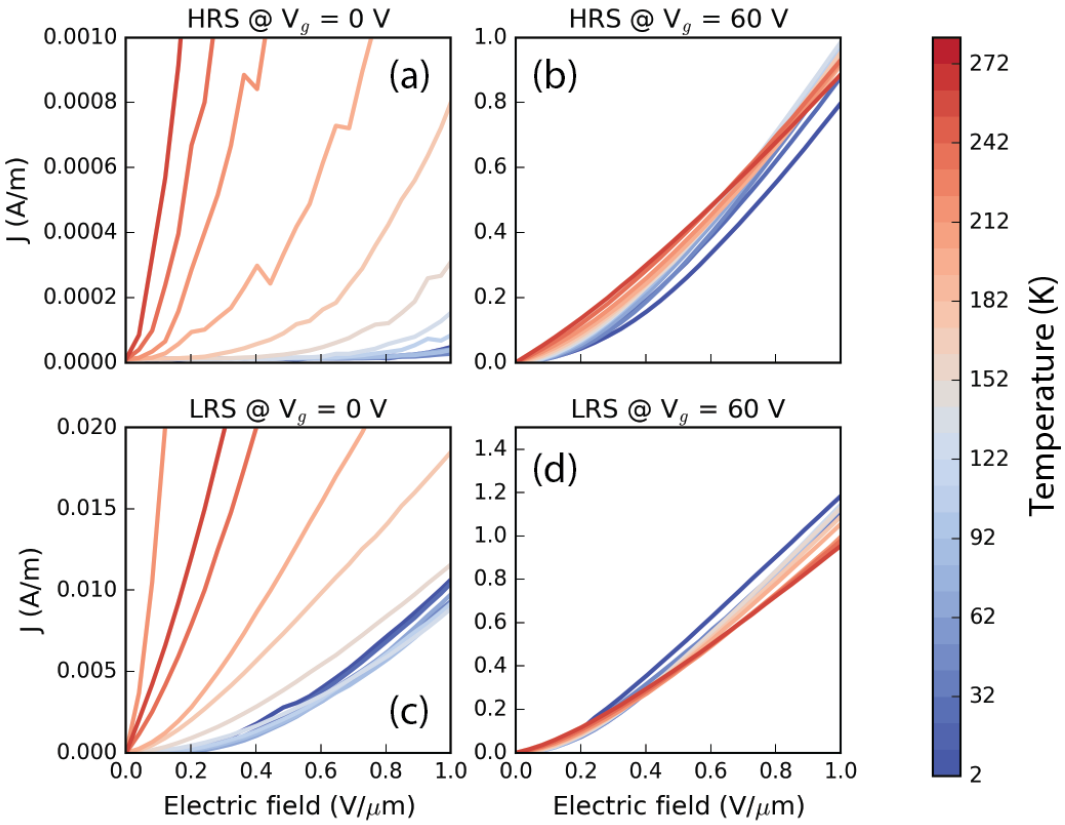

Figure 10.15: **Low-field current density saturation as a function of temperature in the two resistance states at different carrier concentrations.** **(a)** Low-field current densities in HRS at V_g = 0 V. **(b)** Low-field current densities in HRS at V_g = 60 V. **(c)** Low-field current densities in LRS at V_g = 0 V. **(d)** Low-field current densities in LRS at V_g = 60 V. All curves are mapped to the same temperature colour bar on the right.

This observed high-field saturation behaviour is a direct consequence of the concentration of scattering centres present in the device channel. In the case of the vacancy-rich fissure state in LRS, a significant dampening of drift velocity will occur due to the increased frequency of scattering events. The observed saturation here occurs at lateral field strengths much lower than in pristine devices [63], as would be expected. As both states are probed at carrier densities approaching high 10^{12} cm^{-2}, significant electrostatic screening alleviates charged impurity-scattering. The dominant scattering mechanism for this defective 2D system in the high-field regime is thus electron-phonon scattering, whose effectiveness is known to scale with carrier density and is reflected in sharper saturations for lower current densities [64], as is the case in our devices in LRS. As the memtransistor hosts more sulfur vacancies (and by extension scattering events) in the current-limiting channel in LRS

than in HRS, a more pronounced current saturation will be observed, especially at higher temperatures where phonon occupancy is higher. These cryogenic charge transport data thus confirm our theory that LRS is the V_S-rich state in the fissure.

10.8 Conclusions and outlook

In this final chapter, we have outlined our proposed mechanism for the resistive switching phenomenon occurring in He^+ ion beam-irradiated CVD monolayer MoS_2 FETs. We propose that the switching behaviour is governed by the introduced amorphous fissure interface and provide evidence for this hypothesis with measurements of devices which had undergone purposefully-skewed irradiations. In addition, cryogenic charge transport studies revealed several measurable physical differences between LRS and HRS when it comes to electron transport across the fissure region. We have compared and contrasted the two states in terms of their charge transport mechanisms, current injection across the beam-created fissure, the impact of mobile defects on 1/f noise and the current density saturation. We have thus revealed the contribution of sulfur vacancies to controllable and reversible FET channel doping in these neuromorphic devices. In addition, we observed the carrier concentration-dependent metal-insulator transition in the low resistance state of the defective material due to electron dopant crowding in the beam-created fissure region. This novel method of site-specific seeding of mobile dopants may serve to open up the field to innovative device design for the fundamental study of defective two-dimensional systems.

Chapter 11

Conclusions and future work

In the beginning of this dissertation we set out to study the effects of introducing defects into nano-electronic MoS_2 devices by means of plasma treatment and helium ion beam irradiation. We have demonstrated that both are viable methods for activating new electronic functionalities in down-scaled molybdenite. Let us here summarise the outcomes of each chapter and give an outlook for the future work that can follow up these studies:

Plasma treatment

Oxide-mediated recovery of field-effect mobility in plasma-treated MoS_2

In this chapter, we showed extensively how we can tune the electron mobility in MoS_2 by the surface inclusion of a sub-stoichiometric molybdenum oxide. In the case of 4L samples, μ_{fe} can improve from ~ 20 cm^2 V^{-1} s^{-1} to ~ 30 cm^2 V^{-1} s^{-1} after only 6 s of plasma processing. Meanwhile, the threshold gate voltage shifts to negative biases by $\sim \Delta 19$ V. Spectroscopic and microscopic analyses have revealed the role of the oxide as a function of increasing plasma exposure and unveiled its volatility under high vacuum. The height of the MoS_2 thin film increases by as much as 30% due to the surface insertion of oxygen into the sample, corresponding to at least 61% of the bilayer of 2D MoO_3, as studied by XPS, while no S-O bond formation was detected. The nanoscale formation of oxide pits and voids in the crystal was monitored by high-resolution microscopy. Importantly, we showed that the effect of the formed oxide on the properties of the MoS_2 FET channel is directly controlled by the thickness of the semiconducting crystal - highlighting its importance in screening the underlying transistor channel. In addition, we demonstrated with a robust simulation of resistor networks how the conductance of the lattice evolves in the presence of an ever-increasing concentration of conductive and insulating oxide phases forming concurrently.

The key finding of this study was that oxides of Mo do not always exclusively lead to p-type doping in MoS_2. Hence, the electronic properties of MoS_2 FETs can be locally modified to turn on at negative gate biases, opening up new architecture possibilities for 2D heterostructure circuits. The next step to avail of this new-found

tunability would be to protect areas of a MoS_2 film with a polymer and open up treatment windows with EBL to expose only specific areas of the material to the plasma. By tuning the amount of time required for exposure, p-n junctions could feasibly be fabricated, while the whole circuit could be contained to a single large MoS_2 flake.

Low-temperature electrical conduction in plasma-treated bilayer MoS_2

Electrical testing of plasma-treated bilayer MoS_2 carried out at liquid N_2 temperatures revealed severe changes to the observed transport mechanisms in the crystal as a function of increasing plasma exposure. The ES hopping mechanism was found to govern the electron conduction in the pristine device, while below the critical temperature of $T^* \approx 181$ K, the defective plasma-treated MoS_2 system was discovered to undergo an additional crossover to a mixed Arrhenius-like regime. V_{th} of the device was found to linearly shift to positive gate biases with the lowering temperature; independent of plasma treatment time. The layer-number normalised exponential drop in the conductance of the device was found to depend on the rate of change of the conductance. Emission currents were seen to drop severely with increasing plasma exposure, while the metal/contact interface was affected such that the Schottky barrier heights could be modulated by hundreds of meV.

The natural next step would be to extend this study down to liquid He temperatures, which could not be done at the time these experiments were performed. This would allow for more accurate fittings in the low-temperature regime and a closer study of the dependence of the electron mobility on the temperature in these heavily-defective systems.

Photoresponsivity enhancement in monolayer MoS_2 by rapid O_2:Ar plasma treatment

This chapter explored the effects of plasma treatment on the optoelectronic performance of synthetic MoS_2 monolayers. We demonstrated the ten-fold enhancement of the photoresponsivity of the material in back-gated devices only after 2 s of exposure to the O_2:Ar (1:3) plasma. This led to output current enhancements from 9 μA to 25 μA at $V_{\text{ds}} = 5$ V, and an improved generated photocurrent scaling with laser power from $\propto P^{0.13}$ to $\propto P^{0.29}$. The observed temporal responsivities exceeded those of other reports of oxide-sensitised MoS_2 photodetectors by $\sim 35\%$ at the same laser power. Meanwhile, the gain in the system was estimated at ≈ 254. The proposed mechanism of hole trapping at the MoO_x/MoS_2 heterojunction interface in the FET

channel matches well with the observed transfer characteristics as a function of increasing laser irradiation power.

Future work on this system should focus on the role of light absorption on the observed enhancement phenomena. The noted increase in material thickness needs to be cross-correlated with absorption/reflection experiments to determine how much laser power is actually contributing to charge carrier generation in the semiconductor. This large-scale functionalisation method for the tuning of the optoelectronic properties of monolayer semiconductors ought to be utilised in light-activated circuit components and/or lateral heterojunction devices combining multiple TMDs.

Helium ion beam irradiation

Effect of varying the irradiation area on the conductance of monolayer MoS_2

In this chapter, we examined the effects of irradiating a monolayer MoS_2 FET with a charged helium beam as a function of increasing exposure area. Some irradiations in the low irradiated area-to-channel area regime improved the conductance of the MoS_2 device, presumably due to the light doping with electron donors in the form of sulfur vacancies. Output currents were found to increase as much as 4-fold for the same applied V_{ds}, while V_{th} was shifted heavily to negative gate biases, indicating the increased V_S concentration. At higher irradiated area-to-channel area regimes, ambipolar conductance emerged, with a large decrease in the on-off ratio of the FET and a substantial drop in electron mobility (up to 100%). The effect of irradiating the contact interface was also studied and revealed a reduced current injection in devices where the interface had been damaged by the ion beam. SRIM simulations confirmed that the vacancy generation in irradiated MoS_2 at the contact interface is in the ≈ 0.007 V_S per He ion range; same as for unencapsulated MoS_2. In addition, it was found with statistical analyses that the presence of GBs in the starting MoS_2 material had no impact on the electrical properties of the FET after ion irradiation, and varying the irradiation area had no meaningful impact on the resistive switching phenomena which were observed in some cases.

The following chapters expand on the observed results by delving deeper into the low irradiation ratio regime case and the resistive switching phenomena. Thus, this chapter served as a good platform study for the development of a more specialised research approach. However, the high irradiation ratio cases remain an interesting system to study due to the increased trade-off between V_S sites and adsorbed p-dopants. A balance may be reached where ambipolar conduction occurs in a channel whose mobility has not yet so drastically deteriorated, if the FET is much smaller than the 5 μm dimensions used herein.

Neuromorphic MoS_2 memtransistors fabricated by localised helium ion beam irradiation

Chapter 9 is undoubtedly the most exciting achievement of this thesis work. The top-down fabrication of atomically-thin gate-tunable memristive components is a world-first, and is competitive in terms of certain benchmarks with other lateral 2D memristive devices reported in the literature. This includes power consumption (as low as 16 nW for read operations), cycling endurance (1180 cycles over 7 hours and 56 minutes) and V_{set} stability (± 410 mV on a ± 20 V sweep). We have explored in

detail the fabrication methodology and highlighted the advantages of the helium ion microscope in writing localised, site-specific memristive components in 2D MoS_2. The method is not limited to synthetic monolayers, as we have shown it also works on thicker samples - up to at least 10 molecular layers. Individual devices were shown to exhibit neuromorphic behaviour and the time scales of optimal switching behaviour were extracted. Spectroscopic mapping revealed the role of V_S drift on the asymmetric device functionality, while high-resolution microscopic studies revealed the physical state of the irradiated interface.

Future work on these systems ought to focus on up-scaling the device fabrication. As the advantages of the HIM are its high precision and dose-controlled doping control, as well as its potential synergy with already-established lithographic systems, this scalability needs to be exploited. Work has already begun in our group on fabricating large-area arrays of MoS_2 devices, whose memristive functionality could then be activated wherever necessary on a chip, with ease. For a sneak peek of the ongoing work see **Fig. 11.1** below:

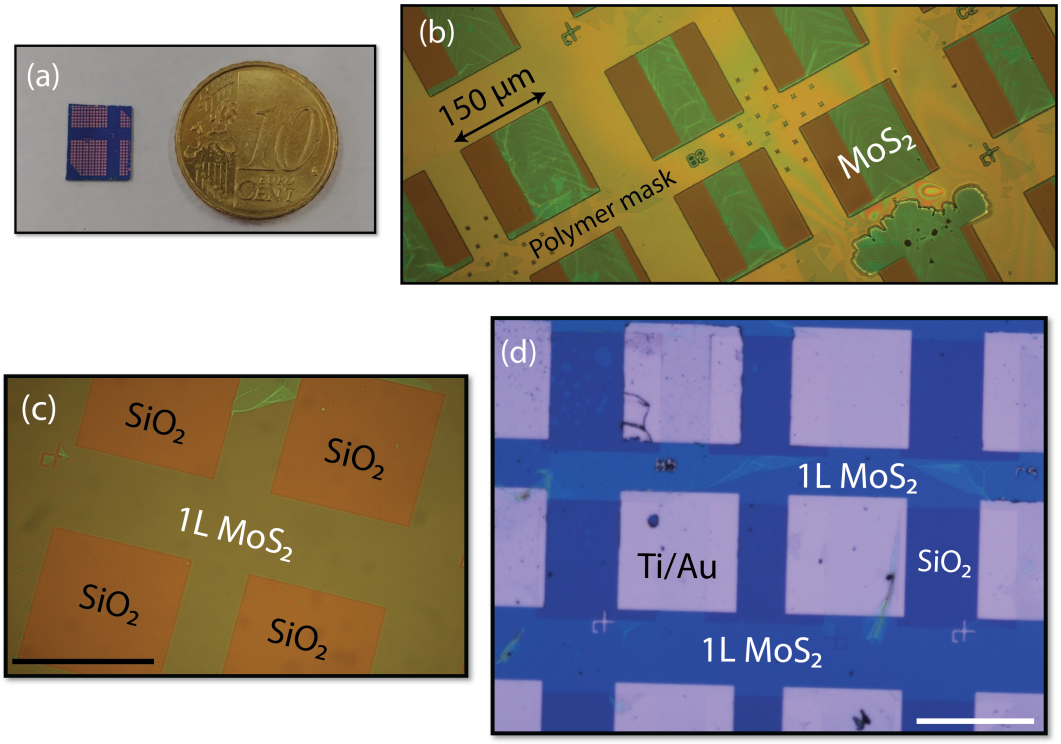

Figure 11.1: **Large-scale device fabrication.** **(a)** A fabricated chip next to a 10 euro cent coin, for scale. The electrodes are clearly visible to the eye, deposited in four clusters. **(b)** Optical micrograph of a polymer mask shifted by half a period from the previous exposure and etching step. **(c)** Etched MoS_2 regions shaped into channels on the SiO_2 substrate. **(d)** Channels after depositing the metal contacts. Scale bars in **(c,d)** are 150 μm.

Using the same square-array mask for optical lithography allows for the opening of windows in a large-area MoS_2 film. The material can then be etched away with SF_6 plasma, and the pattern shifted appropriately in a subsequent lithography step to define contact areas for film deposition. This results in the creation of 384 MoS_2 FET channels on a ~ 1 cm^2 chip in the same time that it would take to make a few devices by EBL, and does not require the pre-deposition of lithography markers. The HIM can then be utilised to irradiate a given channel to make a memtransistor. This work is currently ongoing.

On the nature of resistance states in the MoS_2 memtransistor

In the final chapter of the thesis we outlined the proposed switching mechanism which occurs in our ion beam-enabled memtransistors. We highlighted the importance of the definition of conventional current in these asymmetric devices and studied the change in the switching dynamics as a function of increasing asymmetry; as informed by simulated dose delivery variations for different stage tilt angles. We found evidence of asymmetric defect drift in cycled devices and characterised the asymmetry with changing figures of merit such as the drive current and on/off ratio of the devices. Cryogenic charge transport measurements revealed a substantial difference in the physical properties of the device between LRS and HRS. These include large differences in V_{th}, μ_{fe} scaling with temperature, the electron localisation lengths, the amplitude of 1/f noise and the current density saturation. Moreover, we discovered that an early onset metal-insulator transition in LRS is mediated by the reversible doping brought about by the bi-directional drift of sulfur vacancies in the fissure region.

In early proof-of-concept work for certain classes of devices, the approaches presented in this dissertation are acceptable. However, now is the time that we take advantage of the similarity between an emerging device and a biological counterpart, and use it for energy-efficient computing. The missing link to achieve this integration is of course the analogue-to-digital algorithm. Priorities in memristive device research should thus be given to deeper understanding of device physics that may lead to better devices, e.g. improved uniformity and the integration of large-scale arrays that can solve real world problems. Along each of these directions, there exist many practical challenges that need to be addressed in order to really make advancements in either the scientific aspect or the engineering challenges. Knowledge of the switching physics of MoS_2 memristive devices is still lacking in the community. Limits of physical characterisation need to be pushed in order to fully

understand how these mobile defects are governing the observed switching. True breakthroughs will only occur if the consistent uniformity of fabrication exists, so that sneak paths and cross-talk between cells in functional arrays are suppressed. In the meantime, researchers can work to fine-tune the fabrication process at each step - starting from the growth, moving through the modification process, and finishing with universal standard criteria for device testing.

References

[1] J. Bardeen and W. H. Brattain, "The transistor, a semi-conductor triode," *Physical Review*, vol. 74, no. 2, p. 230, 1948.

[2] M. M. Waldrop, "The chips are down for Moore's law," *Nature*, vol. 530, pp. 144–147, 2 2016.

[3] IEEE, "International Roadmap for Devices and Systems." `https://irds.ieee.org/`, 2019. Accessed: 2019-07-31.

[4] K. S. Novoselov, A. K. Geim, S. V. Morozov, D. Jiang, Y. Zhang, S. V. Dubonos, I. V. Grigorieva, and A. A. Firsov, "Electric field effect in atomically thin carbon films," *Science*, vol. 306, no. 5696, pp. 666–669, 2004.

[5] S. V. Morozov, K. S. Novoselov, M. I. Katsnelson, F. Schedin, D. C. Elias, J. A. Jaszczak, and A. K. Geim, "Giant intrinsic carrier mobilities in graphene and its bilayer," *Phys. Rev. Lett.*, vol. 100, 1 2008.

[6] K. Novoselov, A. K. Geim, S. Morozov, D. Jiang, M. Katsnelson, I. Grigorieva, S. Dubonos, and A. Firsov, "Two-dimensional gas of massless Dirac fermions in graphene," *Nature*, vol. 438, no. 7065, pp. 197–200, 2005.

[7] C. Lee, X. Wei, J. W. Kysar, and J. Hone, "Measurement of the elastic properties and intrinsic strength of monolayer graphene," *Science*, vol. 321, no. 5887, pp. 385–388, 2008.

[8] A. A. Balandin, S. Ghosh, W. Bao, I. Calizo, D. Teweldebrhan, F. Miao, and C. N. Lau, "Superior thermal conductivity of single-layer graphene," *Nano Letters*, vol. 8, no. 3, pp. 902–907, 2008.

[9] "Graphene Flagship - Funding Systems." `http://graphene-flagship.eu/project/fundingsystem/`. Accessed: 2016-10-13.

[10] M. Peplow, "UK graphene inquiry reveals commercial struggles," *Nature*, 5 2016.

[11] F. Schwierz, "Graphene transistors," *Nature Nanotechnology*, vol. 5, no. 7, pp. 487–496, 2010.

[12] F. Schwierz, "Graphene transistors: status, prospects, and problems," *Proceedings of the IEEE*, vol. 101, no. 7, pp. 1567–1584, 2013.

[13] C. R. Dean, L. Wang, P. Maher, C. Forsythe, F. Ghahari, Y. Gao, J. Katoch, M. Ishigami, P. Moon, M. Koshino, T. Taniguchi, K. Watanabe, K. L. Shepard, J. Hone, and P. Kim, "Hofstadter's butterfly and the fractal quantum Hall effect in moiré superlattices," *Nature*, vol. 497, pp. 598–602, 5 2013.

[14] K. F. Mak, C. Lee, J. Hone, J. Shan, and T. F. Heinz, "Atomically thin MoS_2: a new direct-gap semiconductor," *Physical Review Letters*, vol. 105, no. 13, p. 136805, 2010.

[15] A. Splendiani, L. Sun, Y. Zhang, T. Li, J. Kim, C.-Y. Chim, G. Galli, and F. Wang, "Emerging photoluminescence in monolayer MoS_2," *Nano Letters*, vol. 10, pp. 1271–1275, 4 2010.

[16] Z. Yin, H. Li, H. Li, L. Jiang, Y. Shi, Y. Sun, G. Lu, Q. Zhang, X. Chen, and H. Zhang, "Single-layer MoS_2 phototransistors," *ACS Nano*, vol. 6, no. 1, pp. 74–80, 2011.

[17] B. Radisavljevic, A. Radenovic, J. Brivio, V. Giacometti, and A. Kis, "Single-layer MoS_2 transistors," *Nature Nanotechnology*, vol. 6, pp. 147–150, 1 2011.

[18] L. O. Chua, "How we predicted the memristor," *Nature Electronics*, vol. 1, pp. 322–322, May 2018.

[19] L. Chua, "Memristor - the missing circuit element," *IEEE Transactions on Circuit Theory*, vol. 18, no. 5, pp. 507–519, 1971.

[20] D. B. Strukov, G. S. Snider, D. R. Stewart, and R. S. Williams, "The missing memristor found," *Nature*, vol. 453, no. 7191, p. 80, 2008.

[21] D. O. Hebb, *The organization of behavior: a neuropsychological theory*. Science Editions, 1962.

[22] K. S. Novoselov, D. Jiang, F. Schedin, T. J. Booth, V. V. Khotkevich, S. V. Morozov, and A. K. Geim, "Two-dimensional atomic crystals," *Proceedings of the National Academy of Sciences*, vol. 102, pp. 10451–10453, 7 2005.

[23] N. Mounet, M. Gibertini, P. Schwaller, D. Campi, A. Merkys, A. Marrazzo, T. Sohier, I. E. Castelli, A. Cepellotti, G. Pizzi, and N. Marzari, "Two-dimensional materials from high-throughput computational exfoliation of experimentally known compounds," *Nature Nanotechnology*, vol. 13, pp. 246–252, 2 2018.

[24] Y. Hernandez, V. Nicolosi, M. Lotya, F. M. Blighe, Z. Sun, S. De, I. T. McGovern, B. Holland, M. Byrne, Y. K. Gun'Ko, J. J. Boland, P. Niraj, G. Duesberg, S. Krishnamurthy, R. Goodhue, J. Hutchison, V. Scardaci, A. C. Ferrari, and J. N. Coleman, "High-yield production of graphene by liquid-phase exfoliation of graphite," *Nature Nanotechnology*, vol. 3, pp. 563–568, 8 2008.

[25] V. Nicolosi, M. Chhowalla, M. G. Kanatzidis, M. S. Strano, and J. N. Coleman, "Liquid Exfoliation of Layered Materials," *Science*, vol. 340, pp. 1226419–1226419, 6 2013.

[26] P. Chen, Z. Zhang, X. Duan, and X. Duan, "Chemical synthesis of two-dimensional atomic crystals, heterostructures and superlattices," *Chemical Society Reviews*, vol. 47, no. 9, pp. 3129–3151, 2018.

[27] R. G. Dickinson and L. Pauling, "The crystal structure of molybdenite," *Journal of the American Chemical Society*, vol. 45, no. 6, pp. 1466–1471, 1923.

[28] Y.-C. Lin, D. O. Dumcenco, Y.-S. Huang, and K. Suenaga, "Atomic mechanism of the semiconducting-to-metallic phase transition in single-layered MoS_2," *Nature Nanotechnology*, vol. 9, pp. 391–396, 4 2014.

[29] E. S. Kadantsev and P. Hawrylak, "Electronic structure of a single MoS_2 monolayer," *Solid State Communications*, vol. 152, pp. 909–913, 5 2012.

[30] A. Molina-Sanchez and L. Wirtz, "Phonons in single-layer and few-layer MoS_2 and WS_2," *Physical Review B*, vol. 84, no. 15, p. 155413, 2011.

[31] N. Wakabayashi, H. Smith, and R. Nicklow, "Lattice dynamics of hexagonal MoS_2 studied by neutron scattering," *Physical Review B*, vol. 12, no. 2, p. 659, 1975.

[32] B. Radisavljevic and A. Kis, "Mobility engineering and a metal–insulator transition in monolayer MoS_2," *Nature Materials*, vol. 12, 2013.

[33] N. Ma and D. Jena, "Carrier statistics and quantum capacitance effects on mobility extraction in two-dimensional crystal semiconductor field-effect transistors," *2D Materials*, vol. 2, p. 015003, 1 2015.

[34] M. J. Mleczko, A. C. Yu, C. M. Smyth, V. Chen, Y. C. Shin, S. Chatterjee, Y.-C. Tsai, Y. Nishi, R. M. Wallace, and E. Pop, "Contact engineering high performance n-type $MoTe_2$ transistors," *arXiv:1907.02587*, 2019.

[35] M. R. Graham, C. Adkins, H. Behar, and R. Rosenbaum, "Experimental study of the Ioffe-Regel criterion for amorphous indium oxide films," *Journal of Physics: Condensed Matter*, vol. 10, no. 4, p. 809, 1998.

[36] X. Cui, G.-H. Lee, Y. D. Kim, G. Arefe, P. Y. Huang, C.-H. Lee, D. A. Chenet, X. Zhang, L. Wang, F. Ye, F. Pizzocchero, B. S. Jessen, K. Watanabe, T. Taniguchi, D. A. Muller, T. Low, P. Kim, and J. Hone, "Multi-terminal transport measurements of MoS_2 using a van der waals heterostructure device platform," *Nature Nanotechnology*, vol. 10, pp. 534–540, 4 2015.

[37] D. Jariwala, V. K. Sangwan, D. J. Late, J. E. Johns, V. P. Dravid, T. J. Marks, L. J. Lauhon, and M. C. Hersam, "Band-like transport in high mobility unencapsulated single-layer MoS_2 transistors," *Applied Physics Letters*, vol. 102, no. 17, p. 173107, 2013.

[38] B. H. Moon, J. J. Bae, M.-K. Joo, H. Choi, G. H. Han, H. Lim, and Y. H. Lee, "Soft coulomb gap and asymmetric scaling towards metal-insulator quantum criticality in multilayer MoS_2," *Nature Communications*, vol. 9, 5 2018.

[39] N. Papadopoulos, G. A. Steele, and H. S. J. van der Zant, "Efros-Shklovskii variable range hopping and nonlinear transport in 1T/1T′-MoS_2," *Physical Review B*, vol. 96, 12 2017.

[40] J. S. Kim, J. Kim, J. Zhao, S. Kim, J. H. Lee, Y. Jin, H. Choi, B. H. Moon, J. J. Bae, Y. H. Lee, and S. C. Lim, "Electrical transport properties of polymorphic MoS_2," *ACS Nano*, vol. 10, pp. 7500–7506, 8 2016.

[41] H. Qiu, T. Xu, Z. Wang, W. Ren, H. Nan, Z. Ni, Q. Chen, S. Yuan, F. Miao, F. Song, *et al.*, "Hopping transport through defect-induced localized states in molybdenum disulphide," *Nature Communications*, vol. 4, p. 2642, 2013.

[42] K. Hsieh, V. Kochat, X. Zhang, Y. Gong, C. S. Tiwary, P. M. Ajayan, and A. Ghosh, "Effect of carrier localization on electrical transport and noise at individual grain boundaries in monolayer MoS_2," *Nano Letters*, vol. 17, no. 9, pp. 5452–5457, 2017.

[43] H. Liu, A. Pourret, and P. Guyot-Sionnest, "Mott and Efros-Shklovskii variable range hopping in CdSe quantum dots films," *ACS Nano*, vol. 4, pp. 5211–5216, 8 2010.

[44] A. Zabrodskii, "The Coulomb gap: the view of an experimenter," *Philosophical Magazine B*, vol. 81, no. 9, pp. 1131–1151, 2001.

[45] A. Yildiz, N. Serin, T. Serin, and M. Kasap, "Crossover from nearest-neighbor hopping conduction to Efros-Shklovskii variable-range hopping conduction in hydrogenated amorphous silicon films," *Japanese Journal of Applied Physics*, vol. 48, no. 11R, p. 111203, 2009.

[46] V. K. Sangwan, H. N. Arnold, D. Jariwala, T. J. Marks, L. J. Lauhon, and M. C. Hersam, "Low-frequency electronic noise in single-layer MoS_2 transistors," *Nano Letters*, vol. 13, no. 9, pp. 4351–4355, 2013.

[47] X. Xie, D. Sarkar, W. Liu, J. Kang, O. Marinov, M. J. Deen, and K. Banerjee, "Low-frequency noise in bilayer MoS_2 transistor," *ACS Nano*, vol. 8, pp. 5633–5640, 5 2014.

[48] J.-W. Wang, Y.-P. Liu, P.-H. Chen, M.-H. Chuang, A. Pezeshki, D.-C. Ling, J.-C. Chen, Y.-F. Chen, and Y.-H. Lee, "Controlled low-frequency electrical noise of monolayer MoS_2 with ohmic contact and tunable carrier concentration," *Advanced Electronic Materials*, vol. 4, p. 1700340, 12 2017.

[49] B. Stampfer, F. Zhang, Y. Y. Illarionov, T. Knobloch, P. Wu, M. Waltl, A. Grill, J. Appenzeller, and T. Grasser, "Characterization of single defects in ultrascaled MoS_2 field-effect transistors," *ACS Nano*, vol. 12, no. 6, pp. 5368–5375, 2018.

[50] D. Sharma, M. Amani, A. Motayed, P. B. Shah, A. G. Birdwell, S. Najmaei, P. M. Ajayan, J. Lou, M. Dubey, Q. Li, *et al.*, "Electrical transport and low-frequency noise in chemical vapor deposited single-layer MoS_2 devices," *Nanotechnology*, vol. 25, no. 15, p. 155702, 2014.

[51] T. Paul, S. Ghatak, and A. Ghosh, "Percolative switching in transition metal dichalcogenide field-effect transistors at room temperature," *Nanotechnology*, vol. 27, p. 125706, 2 2016.

[52] M. Ghorbani-Asl, A. N. Enyashin, A. Kuc, G. Seifert, and T. Heine, "Defect-induced conductivity anisotropy in MoS_2 monolayers," *Physical Review B*, vol. 88, 12 2013.

[53] S. Najmaei, M. Amani, M. L. Chin, Z. Liu, A. G. Birdwell, T. P. O'Regan, P. M. Ajayan, M. Dubey, and J. Lou, "Electrical transport properties of polycrystalline monolayer molybdenum disulfide," *ACS Nano*, vol. 8, pp. 7930–7937, 7 2014.

[54] X. Zou, Y. Liu, and B. I. Yakobson, "Predicting dislocations and grain boundaries in two-dimensional metal-disulfides from the first principles," *Nano Letters*, vol. 13, pp. 253–258, 12 2012.

[55] Y. Ma, H. C. Diaz, J. Avila, C. Chen, V. Kalappattil, R. Das, M.-H. Phan, T. Čadež, J. M. P. Carmelo, M. C. Asensio, and M. Batzill, "Angle resolved photoemission spectroscopy reveals spin charge separation in metallic $MoSe_2$ grain boundary," *Nature Communications*, vol. 8, 2 2017.

[56] H. Liu, L. Jiao, F. Yang, Y. Cai, X. Wu, W. Ho, C. Gao, J. Jia, N. Wang, H. Fan, W. Yao, and M. Xie, "Dense network of one-dimensional midgap metallic modes in monolayer $MoSe_2$ and their spatial undulations," *Physical Review Letters*, vol. 113, 8 2014.

[57] A. Sanne, R. Ghosh, A. Rai, M. N. Yogeesh, S. H. Shin, A. Sharma, K. Jarvis, L. Mathew, R. Rao, D. Akinwande, and S. Banerjee, "Radio frequency transistors and circuits based on CVD MoS_2," *Nano Letters*, vol. 15, pp. 5039–5045, 7 2015.

[58] S. M. Sze, *Semiconductor devices: physics and technology*. John Wiley & Sons, 2008.

[59] C. Jacoboni, C. Canali, G. Ottaviani, and A. A. Quaranta, "A review of some charge transport properties of silicon," *Solid-State Electronics*, vol. 20, pp. 77–89, 2 1977.

[60] D. Caughey and R. Thomas, "Carrier mobilities in silicon empirically related to doping and field," *Proceedings of the IEEE*, vol. 55, no. 12, pp. 2192–2193, 1967.

[61] M. A. Yamoah, W. Yang, E. Pop, and D. Goldhaber-Gordon, "High-velocity saturation in graphene encapsulated by hexagonal boron nitride," *ACS Nano*, vol. 11, pp. 9914–9919, 9 2017.

[62] V. E. Dorgan, M.-H. Bae, and E. Pop, "Mobility and saturation velocity in graphene on SiO_2," *Applied Physics Letters*, vol. 97, p. 082112, 8 2010.

[63] K. K. H. Smithe, C. D. English, S. V. Suryavanshi, and E. Pop, "High-field transport and velocity saturation in synthetic monolayer MoS_2," *Nano Letters*, vol. 18, pp. 4516–4522, 6 2018.

[64] X. Chen, C. Chen, A. Levi, L. Houben, B. Deng, S. Yuan, C. Ma, K. Watanabe, T. Taniguchi, D. Naveh, X. Du, and F. Xia, "Large-velocity saturation in thin-film black phosphorus transistors," *ACS Nano*, vol. 12, pp. 5003–5010, 5 2018.

[65] M. Chhowalla, D. Jena, and H. Zhang, "Two-dimensional semiconductors for transistors," *Nature Reviews Materials*, vol. 1, no. 11, p. 16052, 2016.

[66] S.-L. Li, K. Tsukagoshi, E. Orgiu, and P. Samorí, "Charge transport and mobility engineering in two-dimensional transition metal chalcogenide semiconductors," *Chemical Society Reviews*, vol. 45, no. 1, pp. 118–151, 2016.

[67] J. Kang, W. Cao, X. Xie, D. Sarkar, W. Liu, and K. Banerjee, "Graphene and beyond-graphene 2D crystals for next-generation green electronics," in *Micro- and Nanotechnology Sensors, Systems, and Applications VI* (T. George, M. S. Islam, and A. K. Dutta, eds.), SPIE, 6 2014.

[68] H. H. Choi, K. Cho, C. D. Frisbie, H. Sirringhaus, and V. Podzorov, "Critical assessment of charge mobility extraction in FETs," *Nature Materials*, vol. 17, pp. 2–7, 1 2018.

[69] W. S. Leong, Y. Li, X. Luo, C. T. Nai, S. Y. Quek, and J. T. Thong, "Tuning the threshold voltage of MoS_2 field-effect transistors via surface treatment," *Nanoscale*, vol. 7, no. 24, pp. 10823–10831, 2015.

[70] J. Guo, B. Yang, Z. Zheng, and J. Jiang, "Observation of abnormal mobility enhancement in multilayer MoS_2 transistor by synergy of ultraviolet illumination and ozone plasma treatment," *Physica E: Low-dimensional Systems and Nanostructures*, vol. 87, pp. 150–154, 3 2017.

[71] J. Shu, G. Wu, Y. Guo, B. Liu, X. Wei, and Q. Chen, "The intrinsic origin of hysteresis in MoS_2 field effect transistors," *Nanoscale*, vol. 8, no. 5, pp. 3049–3056, 2016.

[72] K. Cho, W. Park, J. Park, H. Jeong, J. Jang, T.-Y. Kim, W.-K. Hong, S. Hong, and T. Lee, "Electric stress-induced threshold voltage instability of multilayer MoS_2 field effect transistors," *ACS Nano*, vol. 7, no. 9, pp. 7751–7758, 2013.

[73] K. Bhattacharya and R. Sharma, *Solid state electronic devices*. Oxford University Press, USA, 2013.

[74] H. Schmidt, F. Giustiniano, and G. Eda, "Electronic transport properties of transition metal dichalcogenide field-effect devices: surface and interface effects," *Chemical Society Reviews*, vol. 44, no. 21, pp. 7715–7736, 2015.

[75] C. R. Dean, A. F. Young, I. Meric, C. Lee, L. Wang, S. Sorgenfrei, K. Watanabe, T. Taniguchi, P. Kim, K. L. Shepard, and J. Hone, "Boron nitride substrates for high-quality graphene electronics," *Nature Nanotechnology*, vol. 5, pp. 722–726, 8 2010.

[76] C. R. Woods, L. Britnell, A. Eckmann, R. S. Ma, J. C. Lu, H. M. Guo, X. Lin, G. L. Yu, Y. Cao, R. V. Gorbachev, A. V. Kretinin, J. Park, L. A. Ponomarenko, M. I. Katsnelson, Y. N. Gornostyrev, K. Watanabe, T. Taniguchi, C. Casiraghi, H.-J. Gao, A. K. Geim, and K. Novoselov, "Commensurate–incommensurate transition in graphene on hexagonal boron nitride," *Nature Physics*, vol. 10, pp. 451–456, 4 2014.

[77] D. Jariwala, V. K. Sangwan, L. J. Lauhon, T. J. Marks, and M. C. Hersam, "Emerging device applications for semiconducting two-dimensional transition metal dichalcogenides," *ACS Nano*, vol. 8, no. 2, pp. 1102–1120, 2014.

[78] J. Pu, Y. Yomogida, K.-K. Liu, L.-J. Li, Y. Iwasa, and T. Takenobu, "Highly flexible mos_2 thin-film transistors with ion gel dielectrics," *Nano Letters*, vol. 12, no. 8, pp. 4013–4017, 2012.

[79] M. M. Perera, M.-W. Lin, H.-J. Chuang, B. P. Chamlagain, C. Wang, X. Tan, M. M.-C. Cheng, D. Tománek, and Z. Zhou, "Improved carrier mobility in few-layer mos_2 field-effect transistors with ionic-liquid gating," *ACS Nano*, vol. 7, no. 5, pp. 4449–4458, 2013.

[80] F. Wang, P. Stepanov, M. Gray, C. N. Lau, M. E. Itkis, and R. C. Haddon, "Ionic liquid gating of suspended mos_2 field effect transistor devices," *Nano Letters*, vol. 15, no. 8, pp. 5284–5288, 2015.

[81] W. Bao, X. Cai, D. Kim, K. Sridhara, and M. S. Fuhrer, "High mobility ambipolar MoS_2 field-effect transistors: Substrate and dielectric effects," *Applied Physics Letters*, vol. 102, no. 4, p. 042104, 2013.

[82] D. Lembke, A. Allain, and A. Kis, "Thickness-dependent mobility in two-dimensional MoS_2 transistors," *Nanoscale*, vol. 7, no. 14, pp. 6255–6260, 2015.

[83] G.-H. Lee, X. Cui, Y. D. Kim, G. Arefe, X. Zhang, C.-H. Lee, F. Ye, K. Watanabe, T. Taniguchi, P. Kim, *et al.*, "Highly stable, dual-gated MoS_2 transistors encapsulated by hexagonal boron nitride with gate-controllable contact, resistance, and threshold voltage," *ACS Nano*, vol. 9, no. 7, pp. 7019–7026, 2015.

[84] D. Lembke and A. Kis, "Breakdown of high-performance monolayer MoS_2 transistors," *ACS Nano*, vol. 6, no. 11, pp. 10070–10075, 2012.

[85] D. Krasnozhon, D. Lembke, C. Nyffeler, Y. Leblebici, and A. Kis, "MoS_2 transistors operating at gigahertz frequencies," *Nano Letters*, vol. 14, no. 10, pp. 5905–5911, 2014.

[86] D. Lembke, S. Bertolazzi, and A. Kis, "Single-layer MoS_2 electronics," *Accounts of Chemical Research*, vol. 48, no. 1, pp. 100–110, 2015.

[87] A. Allain, J. Kang, K. Banerjee, and A. Kis, "Electrical contacts to two-dimensional semiconductors," *Nature Materials*, vol. 14, no. 12, pp. 1195–1205, 2015.

[88] E. Rhoderick, "Transport processes in Schottky diodes," *Metal-Semiconductor Contacts. Institute of Physics, London. 1974, 3-19*, 1974.

[89] F. Padovani and R. Stratton, "Field and thermionic-field emission in Schottky barriers," *Solid-State Electronics*, vol. 9, no. 7, pp. 695 – 707, 1966.

[90] F. Léonard and J. Tersoff, "Role of Fermi-level pinning in nanotube Schottky diodes," *Physical Review Letters*, vol. 84, no. 20, p. 4693, 2000.

[91] C. Kim, I. Moon, D. Lee, M. S. Choi, F. Ahmed, S. Nam, Y. Cho, H.-J. Shin, S. Park, and W. J. Yoo, "Fermi level pinning at electrical metal contacts of monolayer molybdenum dichalcogenides," *ACS Nano*, vol. 11, no. 2, pp. 1588–1596, 2017.

[92] L. Wang, I. Meric, P. Huang, Q. Gao, Y. Gao, H. Tran, T. Taniguchi, K. Watanabe, L. Campos, D. Muller, *et al.*, "One-dimensional electrical contact to a two-dimensional material," *Science*, vol. 342, no. 6158, pp. 614–617, 2013.

[93] L. Chua and S. M. Kang, "Memristive devices and systems," *Proceedings of the IEEE*, vol. 64, no. 2, pp. 209–223, 1976.

[94] S. Vongehr and X. Meng, "The missing memristor has not been found," *Scientific Reports*, vol. 5, p. 11657, 2015.

[95] J. J. Yang, D. B. Strukov, and D. R. Stewart, "Memristive devices for computing," *Nature Nanotechnology*, vol. 8, pp. 13–24, 12 2012.

[96] R. Waser, R. Dittmann, G. Staikov, and K. Szot, "Redox-based resistive switching memories - nanoionic mechanisms, prospects, and challenges," *Advanced Materials*, vol. 21, no. 25-26, pp. 2632–2663, 2009.

[97] D. Ielmini and H.-S. P. Wong, "In-memory computing with resistive switching devices," *Nature Electronics*, vol. 1, no. 6, p. 333, 2018.

[98] M. A. Zidan, J. P. Strachan, and W. D. Lu, "The future of electronics based on memristive systems," *Nature Electronics*, vol. 1, no. 1, p. 22, 2018.

[99] Y. Yang and R. Huang, "Probing memristive switching in nanoionic devices," *Nature Electronics*, vol. 1, no. 5, p. 274, 2018.

[100] P. M. Sheridan, F. Cai, C. Du, W. Ma, Z. Zhang, and W. D. Lu, "Sparse coding with memristor networks," *Nature Nanotechnology*, vol. 12, no. 8, p. 784, 2017.

[101] R. Hall, "The synapse." `http://www.rhsmpsychology.com/Handouts/synapse.htm`, 2019. Accessed: 2019-07-08.

[102] Q. Xia and J. J. Yang, "Memristive crossbar arrays for brain-inspired computing," *Nature Materials*, vol. 18, no. 4, p. 309, 2019.

[103] R. Sarpeshkar, "Brain power," *IEEE Spectrum*, vol. 43, pp. 24–29, 5 2006.

[104] M. F. Bear, "A synaptic basis for memory storage in the cerebral cortex," *Proceedings of the National Academy of Sciences*, vol. 93, pp. 13453–13459, 11 1996.

[105] Y. Lee and T.-W. Lee, "Organic synapses for neuromorphic electronics: From brain-inspired computing to sensorimotor nervetronics," *Accounts of Chemical Research*, vol. 52, pp. 964–974, 3 2019.

[106] S. H. Jo, T. Chang, I. Ebong, B. B. Bhadviya, P. Mazumder, and W. Lu, "Nanoscale memristor device as synapse in neuromorphic systems," *Nano Letters*, vol. 10, pp. 1297–1301, 4 2010.

[107] V. K. Sangwan, D. Jariwala, I. S. Kim, K.-S. Chen, T. J. Marks, L. J. Lauhon, and M. C. Hersam, "Gate-tunable memristive phenomena mediated by grain boundaries in single-layer MoS_2," *Nature Nanotechnology*, vol. 10, no. 5, p. 403, 2015.

[108] V. K. Sangwan, H.-S. Lee, H. Bergeron, I. Balla, M. E. Beck, K.-S. Chen, and M. C. Hersam, "Multi-terminal memtransistors from polycrystalline monolayer molybdenum disulfide," *Nature*, vol. 554, no. 7693, p. 500, 2018.

[109] L. Wang, L. Chen, S. L. Wong, X. Huang, W. Liao, C. Zhu, Y.-F. Lim, D. Li, X. Liu, D. Chi, and K.-W. Ang, "Electronic devices and circuits based on wafer-scale polycrystalline monolayer MoS_2 by chemical vapor deposition," *Advanced Electronic Materials*, p. 1900393, 6 2019.

[110] L. Wang, W. Liao, S. L. Wong, Z. G. Yu, S. Li, Y.-F. Lim, X. Feng, W. C. Tan, X. Huang, L. Chen, L. Liu, J. Chen, X. Gong, C. Zhu, X. Liu, Y.-W. Zhang, D. Chi, and K.-W. Ang, "Artificial synapses based on multiterminal memtransistors for neuromorphic application," *Advanced Functional Materials*, p. 1901106, 4 2019.

[111] D. Li, B. Wu, X. Zhu, J. Wang, B. Ryu, W. D. Lu, W. Lu, and X. Liang, "MoS_2 memristors exhibiting variable switching characteristics toward biorealistic synaptic emulation," *ACS Nano*, vol. 12, no. 9, pp. 9240–9252, 2018.

[112] R. Ge, X. Wu, M. Kim, J. Shi, S. Sonde, L. Tao, Y. Zhang, J. C. Lee, and D. Akinwande, "Atomristor: Nonvolatile resistance switching in atomic sheets of transition metal dichalcogenides," *Nano Letters*, vol. 18, no. 1, pp. 434–441, 2018.

[113] Y. Shi, X. Liang, B. Yuan, V. Chen, H. Li, F. Hui, Z. Yu, F. Yuan, E. Pop, H.-S. P. Wong, *et al.*, "Electronic synapses made of layered two-dimensional materials," *Nature Electronics*, vol. 1, no. 8, p. 458, 2018.

[114] H. Zhao, Z. Dong, H. Tian, D. DiMarzi, M.-G. Han, L. Zhang, X. Yan, F. Liu, L. Shen, S.-J. Han, S. Cronin, W. Wu, J. Tice, J. Guo, and H. Wang, "Atomically thin femtojoule memristive device," *Advanced Materials*, vol. 29, no. 47, p. 1703232, 2017.

[115] R. Xu, H. Jang, M.-H. Lee, D. Amanov, Y. Cho, H. Kim, S. Park, H. jin Shin, and D. Ham, "Vertical MoS_2 double-layer memristor with electrochemical metallization as an atomic-scale synapse with switching thresholds approaching 100 mV," *Nano Letters*, vol. 19, pp. 2411–2417, 3 2019.

[116] M. Kim, R. Ge, X. Wu, X. Lan, J. Tice, J. C. Lee, and D. Akinwande, "Zero-static power radio-frequency switches based on MoS_2 atomristors," *Nature Communications*, vol. 9, no. 1, 2018.

[117] P. Cheng, K. Sun, and Y. H. Hu, "Memristive behavior and ideal memristor of 1T phase MoS_2 nanosheets," *Nano Letters*, vol. 16, no. 1, pp. 572–576, 2015.

[118] M. Wang, S. Cai, C. Pan, C. Wang, X. Lian, Y. Zhuo, K. Xu, T. Cao, X. Pan, B. Wang, S.-J. Liang, J. J. Yang, P. Wang, and F. Miao, "Robust memristors based on layered two-dimensional materials," *Nature Electronics*, vol. 1, no. 2, pp. 130–136, 2018.

[119] M. Chen, H. Nam, S. Wi, L. Ji, X. Ren, L. Bian, S. Lu, and X. Liang, "Stable few-layer MoS_2 rectifying diodes formed by plasma-assisted doping," *Applied Physics Letters*, vol. 103, no. 14, p. 142110, 2013.

[120] S. Wi, H. Kim, M. Chen, H. Nam, L. J. Guo, E. Meyhofer, and X. Liang, "Enhancement of photovoltaic response in multilayer MoS_2 induced by plasma doping," *ACS Nano*, vol. 8, no. 5, pp. 5270–5281, 2014.

[121] N.-Y. Cui, N. M. Brown, and A. McKinley, "An AFM study of the topography of natural MoS_2 following treatment in an RF-oxygen plasma," *Applied Surface Science*, vol. 151, no. 1-2, pp. 17–28, 1999.

[122] P. D. Fleischauer, "Fundamental aspects of the electronic structure, materials properties and lubrication performance of sputtered MoS_2 films," *Thin Solid Films*, vol. 154, no. 1-2, pp. 309–322, 1987.

[123] J. B. Park, C. B. France, and B. A. Parkinson, "Scanning tunneling microscopy investigation of nanostructures produced by Ar^+ and He^+ bombardment of MoS_2 surfaces," *Journal of Vacuum Science & Technology B: Microelectronics and Nanometer Structures*, vol. 23, no. 4, p. 1532, 2005.

[124] M. R. Islam, N. Kang, U. Bhanu, H. P. Paudel, M. Erementchouk, L. Tetard, M. N. Leuenberger, and S. I. Khondaker, "Tuning the electrical property via defect engineering of single layer MoS_2 by oxygen plasma," *Nanoscale*, vol. 6, no. 17, pp. 10033–10039, 2014.

[125] S. I. Khondaker and M. R. Islam, "Bandgap Engineering of MoS_2 Flakes via Oxygen Plasma: A Layer Dependent Study," *The Journal of Physical Chemistry C*, vol. 120, pp. 13801–13806, 6 2016.

[126] P. Zhao, D. Kiriya, A. Azcatl, C. Zhang, M. Tosun, Y.-S. Liu, M. Hettick, J. S. Kang, S. McDonnell, S. KC, J. Guo, K. Cho, R. M. Wallace, and A. Javey, "Air stable p-doping of WSe_2 by covalent functionalization," *ACS Nano*, vol. 8, no. 10, pp. 10808–10814, 2014.

[127] M. Yamamoto, S. Dutta, S. Aikawa, S. Nakaharai, K. Wakabayashi, M. S. Fuhrer, K. Ueno, and K. Tsukagoshi, "Self-limiting layer-by-layer oxidation of atomically thin WSe_2," *Nano Letters*, vol. 15, no. 3, pp. 2067–2073, 2015.

[128] D. Kiriya, M. Tosun, P. Zhao, J. S. Kang, and A. Javey, "Air-stable surface charge transfer doping of MoS_2 by benzyl viologen," *Journal of the American Chemical Society*, vol. 136, pp. 7853–7856, 5 2014.

[129] W. Su, N. Kumar, S. J. Spencer, N. Dai, and D. Roy, "Transforming bilayer MoS_2 into single-layer with strong photoluminescence using UV-ozone oxidation," *Nano Research*, vol. 8, no. 12, pp. 3878–3886, 2015.

[130] H. I. Yang, S. Park, and W. Choi, "Modification of the optoelectronic properties of two-dimensional MoS_2 crystals by ultraviolet-ozone treatment," *Applied Surface Science*, vol. 443, pp. 91–96, 2018.

[131] K. Bazaka, O. Baranov, U. Cvelbar, B. Podgornik, Y. Wang, S. Huang, L. Xu, J. Lim, I. Levchenko, and S. Xu, "Oxygen plasmas: a sharp chisel and handy trowel for nanofabrication," *Nanoscale*, vol. 10, no. 37, pp. 17494–17511, 2018.

[132] T. Saburi, H. Murata, T. Suzuki, Y. Fujii, and K. Kiuchi, "Oxygen plasma interactions with molybdenum: Formation of volatile molybdenum oxides," *Journal of Plasma and Fusion Research*, vol. 78, no. 1, pp. 3–4, 2002.

[133] P. R. Pudasaini, A. Oyedele, C. Zhang, M. G. Stanford, N. Cross, A. T. Wong, A. N. Hoffman, K. Xiao, G. Duscher, D. G. Mandrus, T. Z. Ward, and P. D. Rack, "High-performance multilayer WSe_2 field-effect transistors with carrier type control," *Nano Research*, vol. 11, no. 2, pp. 722–730, 2017.

[134] J. Jadwiszczak, C. O'Callaghan, Y. Zhou, D. S. Fox, E. Weitz, D. Keane, C. P. Cullen, I. O'Reilly, C. Downing, A. Shmeliov, *et al.*, "Oxide-mediated recovery of field-effect mobility in plasma-treated MoS_2," *Science Advances*, vol. 4, no. 3, p. eaao5031, 2018.

[135] M. G. Stanford, Y.-C. Lin, M. G. Sales, A. N. Hoffman, C. T. Nelson, K. Xiao, S. McDonnell, and P. D. Rack, "Lithographically patterned metallic conduction in single-layer MoS_2 via plasma processing," *npj 2D Materials and Applications*, vol. 3, no. 1, 2019.

[136] S. M. Rossnagel, J. J. Cuomo, and W. D. Westwood, *Handbook of plasma processing technology: fundamentals, etching, deposition, and surface interactions*. William Andrew, 1990.

[137] H. Conrads and M. Schmidt, "Plasma generation and plasma sources," *Plasma Sources Science and Technology*, vol. 9, no. 4, p. 441, 2000.

[138] A. Ganguli and R. Tarey, "Understanding plasma sources," *CURRENT SCIENCE-BANGALORE-*, vol. 83, no. 3, pp. 279–290, 2002.

[139] J. Hopwood, "Review of inductively coupled plasmas for plasma processing," *Plasma Sources Science and Technology*, vol. 1, no. 2, p. 109, 1992.

[140] A. R. Chadwick, G. Herdrich, M. Kim, and B. Dally, "Transient electromagnetic behaviour in inductive oxygen and argon-oxygen plasmas," *Plasma Sources Science and Technology*, vol. 25, p. 065025, 11 2016.

[141] D. Toneli, R. Pessoa, M. Roberto, and J. T. Gudmundsson, "On the formation and annihilation of the singlet molecular metastables in an oxygen discharge," *Journal of Physics D: Applied Physics*, vol. 48, no. 32, p. 325202, 2015.

[142] S. Wu, Y. Zeng, X. Zeng, S. Wang, Y. Hu, W. Wang, S. Yin, G. Zhou, W. Jin, T. Ren, Z. Guo, and J. Lu, "High-performance p-type MoS_2 field-effect transistor by toroidal-magnetic-field controlled oxygen plasma doping," *2D Materials*, vol. 6, no. 2, p. 025007, 2019.

[143] J. T. Gudmundsson, D. Lundin, N. Brenning, M. A. Raadu, C. Huo, and T. M. Minea, "An ionization region model of the reactive Ar/O_2 high power impulse magnetron sputtering discharge," *Plasma Sources Science and Technology*, vol. 25, no. 6, p. 065004, 2016.

[144] J. T. Gudmundsson and E. G. Thorsteinsson, "Oxygen discharges diluted with argon: dissociation processes," *Plasma Sources Science and Technology*, vol. 16, no. 2, pp. 399–412, 2007.

[145] D. Lundin, J. T. Gudmundsson, N. Brenning, M. A. Raadu, and T. Minea, "A study of the oxygen dynamics in a reactive Ar/O_2 high power impulse magnetron sputtering discharge using an ionization region model," *Journal of Applied Physics*, vol. 121, no. 17, p. 171917, 2017.

[146] J. R. Lince, "$MoS_{2-x}O_x$ solid solutions in thin films produced by RF-sputter-deposition," *Journal of Materials Research*, vol. 5, no. 1, pp. 218–222, 1990.

[147] V. Buck, "Lattice parameters of sputtered MoS_2 films," *Thin Solid Films*, vol. 198, no. 1-2, pp. 157–167, 1991.

[148] E. Schmidt, F. Weill, G. Meunier, and A. Levasseur, "New amorphous molybdenum oxysulfides obtained in the form of thin films and their characterization by TEM," *Thin Solid Films*, vol. 245, no. 1-2, pp. 34–39, 1994.

[149] N.-Y. Cui, N. M. Brown, and A. McKinley, "An AFM study of a laboratory-grown single-crystal MoS_2 surface following radio-frequency oxygen plasma treatment," *Applied Surface Science*, vol. 158, no. 1-2, pp. 104–111, 2000.

[150] N. M. Brown, N. Cui, and A. McKinley, "An XPS study of the surface modification of natural MoS_2 following treatment in an RF-oxygen plasma," *Applied Surface Science*, vol. 134, no. 1-4, pp. 11–21, 1998.

[151] A.-Y. Lu, H. Zhu, J. Xiao, C.-P. Chuu, Y. Han, M.-H. Chiu, C.-C. Cheng, C.-W. Yang, K.-H. Wei, Y. Yang, Y. Wang, D. Sokaras, D. Nordlund, P. Yang, D. A. Muller, M.-Y. Chou, X. Zhang, and L.-J. Li, "Janus monolayers of transition metal dichalcogenides," *Nature Nanotechnology*, vol. 12, no. 8, p. 744, 2017.

[152] S. Xiao, P. Xiao, X. Zhang, D. Yan, X. Gu, F. Qin, Z. Ni, Z. J. Han, and K. K. Ostrikov, "Atomic-layer soft plasma etching of MoS_2," *Scientific Reports*, vol. 6, p. 19945, 2016.

[153] M. H. Jeon, C. Ahn, H. Kim, K. N. Kim, T. Z. LiN, H. Qin, Y. Kim, S. Lee, T. Kim, and G. Y. Yeom, "Controlled MoS_2 layer etching using CF_4 plasma," *Nanotechnology*, vol. 26, no. 35, p. 355706, 2015.

[154] Y. Liu, H. Nan, X. Wu, W. Pan, W. Wang, J. Bai, W. Zhao, L. Sun, X. Wang, and Z. Ni, "Layer-by-layer thinning of MoS_2 by plasma," *ACS Nano*, vol. 7, no. 5, pp. 4202–4209, 2013.

[155] K.-C. Chen, C.-W. Liu, C. Chen, and S.-Y. Lin, "The atomic layer etching of molybdenum disulfides using low-power oxygen plasma," *Semiconductor Science and Technology*, vol. 34, no. 4, p. 045007, 2019.

[156] T. Y. Ko, A. Jeong, W. Kim, J. Lee, Y. Kim, J. E. Lee, G. H. Ryu, K. Park, D. Kim, Z. Lee, *et al.*, "On-stack two-dimensional conversion of MoS_2 into MoO_3," *2D Materials*, vol. 4, no. 1, p. 014003, 2016.

[157] L. Zhao, Y. Wei, R. Zhang, and Y. Peng, "Controlled surface oxidation of $HfSe_2$ via oxygen-plasma treatment," *Materials Letters*, vol. 243, pp. 96–99, 2019.

[158] Z. Li, S. Yang, R. Dhall, E. Kosmowska, H. Shi, I. Chatzakis, and S. Cronin, "Layer control of WSe_2 via selective surface layer oxidation," *ACS Nano*, vol. 10, no. 7, p. 6836, 2016.

[159] Y. Huang, J. Wu, X. Xu, Y. Ho, G. Ni, Q. Zou, G. K. W. Koon, W. Zhao, A. C. Neto, G. Eda, C. Shen, and Ózyilmaz Barbaros, "An innovative way of etching MoS_2: Characterization and mechanistic investigation," *Nano Research*, vol. 6, no. 3, pp. 200–207, 2013.

[160] H. Zhu, X. Qin, L. Cheng, A. Azcatl, J. Kim, and R. M. Wallace, "Remote plasma oxidation and atomic layer etching of MoS_2," *ACS Applied Materials & Interfaces*, vol. 8, no. 29, pp. 19119–19126, 2016.

[161] S. Kim, M. S. Choi, D. Qu, C. H. Ra, X. Liu, M. Kim, Y. J. Song, and W. J. Yoo, "Effects of plasma treatment on surface properties of ultrathin layered MoS_2," *2D Materials*, vol. 3, no. 3, p. 035002, 2016.

[162] C. H. Lee, E. W. Lee II, W. McCulloch, Z. Jamal-Eddine, S. Krishnamoorthy, M. J. Newburger, R. K. Kawakami, Y. Wu, and S. Rajan, "A self-limiting layer-by-layer etching technique for 2H-MoS_2," *Applied Physics Express*, vol. 10, no. 3, p. 035201, 2017.

[163] K.-C. Chen, T.-W. Chu, C.-R. Wu, S.-C. Lee, and S.-Y. Lin, "Atomic layer etchings of transition metal dichalcogenides with post healing procedures: equivalent selective etching of 2D crystal hetero-structures," *2D Materials*, vol. 4, no. 3, p. 034001, 2017.

[164] T. Lin, B. Kang, M. Jeon, C. Huffman, J. Jeon, S. Lee, W. Han, J. Lee, S. Lee, G. Yeom, and K. Kim, "Controlled layer-by-layer etching of MoS_2," *ACS Applied Materials & Interfaces*, vol. 7, no. 29, pp. 15892–15897, 2015.

[165] K. S. Kim, K. H. Kim, Y. Nam, J. Jeon, S. Yim, E. Singh, J. Y. Lee, S. J. Lee, Y. S. Jung, G. Y. Yeom, and D. W. Kim, "Atomic layer etching mechanism of MoS_2 for nanodevices," *ACS Applied Materials & Interfaces*, vol. 9, no. 13, pp. 11967–11976, 2017.

[166] W. Lu, H. Nan, J. Hong, Y. Chen, C. Zhu, Z. Liang, X. Ma, Z. Ni, C. Jin, and Z. Zhang, "Plasma-assisted fabrication of monolayer phosphorene and its Raman characterization," *Nano Research*, vol. 7, no. 6, pp. 853–859, 2014.

[167] J. Jia, S. K. Jang, S. Lai, J. Xu, Y. J. Choi, J.-H. Park, and S. Lee, "Plasma-treated thickness-controlled two-dimensional black phosphorus and its electronic transport properties," *ACS Nano*, vol. 9, no. 9, pp. 8729–8736, 2015.

[168] J. Pei, X. Gai, J. Yang, X. Wang, Z. Yu, D.-Y. Choi, B. Luther-Davies, and Y. Lu, "Producing air-stable monolayers of phosphorene and their defect engineering," *Nature Communications*, vol. 7, no. 1, 2016.

[169] S. KC, R. C. Longo, R. M. Wallace, and K. Cho, "Surface oxidation energetics and kinetics on MoS_2 monolayer," *Journal of Applied Physics*, vol. 117, no. 13, p. 135301, 2015.

[170] F. Giannazzo, G. Fisichella, G. Greco, S. Di Franco, I. Deretzis, A. La Magna, C. Bongiorno, G. Nicotra, C. Spinella, M. Scopelliti, *et al.*, "Ambipolar MoS_2 transistors by nanoscale tailoring of Schottky barrier using oxygen plasma functionalization," *ACS Applied Materials & Interfaces*, vol. 9, no. 27, pp. 23164–23174, 2017.

[171] Y.-D. Lim, D.-Y. Lee, T.-Z. Shen, C.-H. Ra, J.-Y. Choi, and W. J. Yoo, "Si-compatible cleaning process for graphene using low-density inductively coupled plasma," *ACS Nano*, vol. 6, no. 5, pp. 4410–4417, 2012.

[172] P. Bolshakov, C. M. Smyth, A. Khosravi, P. Zhao, P. K. Hurley, C. L. Hinkle, R. M. Wallace, and C. D. Young, "Contact engineering for dual-gate MoS_2 transistors using O_2 plasma exposure," *ACS Applied Electronic Materials*, vol. 0, no. 0, p. null, 2019.

[173] M. Kang, S. Rathi, I. Lee, L. Li, M. A. Khan, D. Lim, Y. Lee, J. Park, S. J. Yun, D.-H. Youn, C. Jun, and G.-H. Kim, "Tunable electrical properties of multilayer $HfSe_2$ field effect transistors by oxygen plasma treatment," *Nanoscale*, vol. 9, no. 4, pp. 1645–1652, 2017.

[174] N. Choudhary, M. R. Islam, N. Kang, L. Tetard, Y. Jung, and S. I. Khondaker, "Two-dimensional lateral heterojunction through bandgap engineering of MoS_2 via oxygen plasma," *Journal of Physics: Condensed Matter*, vol. 28, p. 364002, 7 2016.

[175] R. Dhall, Z. Li, E. Kosmowska, and S. B. Cronin, "Charge neutral MoS_2 field effect transistors through oxygen plasma treatment," *Journal of Applied Physics*, vol. 120, no. 19, p. 195702, 2016.

[176] M. Chen, S. Wi, H. Nam, G. Priessnitz, and X. Liang, "Effects of MoS_2 thickness and air humidity on transport characteristics of plasma-doped MoS_2 field-effect transistors," *Journal of Vacuum Science & Technology B Nanotechnology & Microelectronics Materials Processing Measurement & Phenomena*, vol. 32, no. 6, pp. 06FF02–06FF02–5, 2014.

[177] J. Shim, A. Oh, D.-H. Kang, S. Oh, S. K. Jang, J. Jeon, M. H. Jeon, M. Kim, C. Choi, J. Lee, S. Lee, G. Y. Yeom, Y. J. Song, and J.-H. Park, "High-performance 2d rhenium disulfide (res_2) transistors and photodetectors by oxygen plasma treatment," *Advanced Materials*, vol. 28, no. 32, pp. 6985–6992, 2016.

[178] P. Mishra, M. Tangi, T. K. Ng, M. N. Hedhili, D. H. Anjum, M. S. Alias, C.-C. Tseng, L.-J. Li, and B. S. Ooi, "Impact of N-plasma and Ga-irradiation on MoS_2 layer in molecular beam epitaxy," *Applied Physics Letters*, vol. 110, no. 1, p. 012101, 2017.

[179] B. J. Lee, B. J. Lee, J. Lee, J. W. Yang, and K. H. Kwon, "Effects of plasma treatment on the electrical reliability of multilayer MoS_2 field-effect transistors," *Thin Solid Films*, vol. 637, 2017.

[180] A. Azcatl, X. Qin, A. Prakash, C. Zhang, L. Cheng, Q. Wang, N. Lu, M. J. Kim, J. Kim, K. Cho, R. Addou, C. L. Hinkle, J. Appenzeller, and R. M. Wallace, "Covalent nitrogen doping and compressive strain in MoS_2 by remote N_2 plasma exposure," *Nano Letters*, vol. 16, no. 9, pp. 5437–5443, 2016.

[181] K.-C. Chen, C.-R. Wu, X.-R. Chang, S.-W. Chang, S.-C. Lee, and S.-Y. Lin, "Enhancement of field-effect mobility in molybdenum-disulfide transistor through the treatment of low-power oxygen plasma," *Japanese Journal of Applied Physics*, vol. 55, p. 090302, 8 2016.

[182] S. Yim, D. M. Sim, W. I. Park, M. Choi, J. Choi, J. Jeon, K. H. Kim, and Y. S. Jung, "Surface-shielding nanostructures derived from self-assembled block copolymers enable reliable plasma doping for few-layer transition metal dichalcogenides," *Advanced Functional Materials*, vol. 26, no. 31, pp. 5631–5640, 2016.

[183] B. Huang, F. Tian, Y. Shen, M. Zheng, Y. Zhao, J. Wu, Y. Liu, S. J. Pennycook, and J. T. L. Thong, "Selective engineering of chalcogen defects in MoS_2 by low-energy helium plasma," *ACS Applied Materials & Interfaces*, 6 2019.

[184] J. Zhu, Z. Wang, H. Yu, N. Li, J. Zhang, J. Meng, M. Liao, J. Zhao, X. Lu, L. Du, R. Yang, D. Shi, Y. Jiang, and G. Zhang, "Argon plasma induced phase transition in monolayer MoS_2," *Journal of the American Chemical Society*, vol. 139, no. 30, pp. 10216–10219, 2017.

[185] V. K. Sangwan and M. C. Hersam, "Electronic transport in two-dimensional materials," *Annual Review of Physical Chemistry*, vol. 69, pp. 299–325, 2018.

[186] M. Tosun, L. Chan, M. Amani, T. Roy, G. H. Ahn, P. Taheri, C. Carraro, J. W. Ager, R. Maboudian, and A. Javey, "Air-stable n-doping of WSe_2 by anion vacancy formation with mild plasma treatment," *ACS Nano*, vol. 10, no. 7, pp. 6853–6860, 2016.

[187] T.-H. Su and Y.-J. Lin, "Effects of nitrogen plasma treatment on the electrical property and band structure of few-layer MoS_2," *Applied Physics Letters*, vol. 108, no. 3, p. 033103, 2016.

[188] G. Hlawacek and A. Gölzhäuser, eds., *Helium Ion Microscopy*. Springer International Publishing, 2016.

[189] G. Hlawacek, V. Veligura, R. van Gastel, and B. Poelsema, "Helium ion microscopy," *Journal of Vacuum Science & Technology B, Nanotechnology and Microelectronics: Materials, Processing, Measurement, and Phenomena*, vol. 32, p. 020801, 3 2014.

[190] D. C. Joy, *Helium Ion Microscopy: Principles and Applications*. Springer, 2013.

[191] M. Nastasi, N. Michael, J. Mayer, J. K. Hirvonen, and M. James, *Ion-solid interactions: fundamentals and applications*. Cambridge University Press, 1996.

[192] D. S. Fox, Y. Zhou, P. Maguire, A. O'Neill, C. Ó'Coileáin, R. Gatensby, A. M. Glushenkov, T. Tao, G. S. Duesberg, I. V. Shvets, M. Abid, M. Abid, H.-C. Wu, Y. Chen, J. N. Coleman, J. F. Donegan, and H. Zhang, "Nanopatterning and electrical tuning of MoS_2 layers with a subnanometer helium ion beam," *Nano Letters*, vol. 15, no. 8, pp. 5307–5313, 2015.

[193] V. Iberi, L. Liang, A. V. Ievlev, M. G. Stanford, M.-W. Lin, X. Li, M. Mahjouri-Samani, S. Jesse, B. G. Sumpter, S. V. Kalinin, *et al.*, "Nanoforging single layer $MoSe_2$ through defect engineering with focused helium ion beams," *Scientific Reports*, vol. 6, p. 30481, 2016.

[194] M. G. Stanford, P. R. Pudasaini, E. T. Gallmeier, N. Cross, L. Liang, A. Oyedele, G. Duscher, M. Mahjouri-Samani, K. Wang, K. Xiao, *et al.*, "High conduction hopping behavior induced in transition metal dichalcogenides by percolating defect networks: toward atomically thin circuits," *Advanced Functional Materials*, vol. 27, no. 36, p. 1702829, 2017.

[195] M. G. Stanford, P. R. Pudasaini, N. Cross, K. Mahady, A. N. Hoffman, D. G. Mandrus, G. Duscher, M. F. Chisholm, and P. D. Rack, "Tungsten diselenide patterning and nanoribbon formation by gas-assisted focused-helium-ion-beam-induced etching," *Small Methods*, vol. 1, no. 4, p. 1600060, 2017.

[196] G. Nanda, G. Hlawacek, S. Goswami, K. Watanabe, T. Taniguchi, and P. F. Alkemade, "Electronic transport in helium-ion-beam etched encapsulated graphene nanoribbons," *Carbon*, vol. 119, pp. 419–425, 2017.

[197] M. G. Stanford, P. D. Rack, and D. Jariwala, "Emerging nanofabrication and quantum confinement techniques for 2D materials beyond graphene," *npj 2D Materials and Applications*, vol. 2, no. 1, p. 20, 2018.

[198] J. Klein, A. Kuc, A. Nolinder, M. Altzschner, J. Wierzbowski, F. Sigger, F. Kreupl, J. J. Finley, U. Wurstbauer, A. W. Holleitner, *et al.*, "Robust valley polarization of helium ion modified atomically thin MoS_2," *2D Materials*, vol. 5, no. 1, p. 011007, 2017.

[199] J. Klein, M. Lorke, M. Florian, F. Sigger, J. Wierzbowski, J. Cerne, K. Müller, T. Taniguchi, K. Watanabe, U. Wurstbauer, *et al.*, "Atomistic defect states as quantum emitters in monolayer MoS_2," *arXiv:1901.01042*, 2019.

[200] Z. Li and F. Chen, "Ion beam modification of two-dimensional materials: Characterization, properties, and applications," *Applied Physics Reviews*, vol. 4, no. 1, p. 011103, 2017.

[201] M. G. Stanford, B. B. Lewis, K. Mahady, J. D. Fowlkes, and P. D. Rack, "Advanced nanoscale patterning and material synthesis with gas field helium and neon ion beams," *Journal of Vacuum Science & Technology B, Nanotechnology and Microelectronics: Materials, Processing, Measurement, and Phenomena*, vol. 35, no. 3, p. 030802, 2017.

[202] M. G. Stanford, P. R. Pudasaini, A. Belianinov, N. Cross, J. H. Noh, M. R. Koehler, D. G. Mandrus, G. Duscher, A. J. Rondinone, I. N. Ivanov, *et al.*, "Focused helium-ion beam irradiation effects on electrical transport properties of few-layer WSe_2: enabling nanoscale direct write homo-junctions," *Scientific Reports*, vol. 6, p. 27276, 2016.

[203] D. Fox, Y. Zhou, A. O'Neill, S. Kumar, J. J. Wang, J. Coleman, G. Duesberg, J. Donegan, and H. Zhang, "Helium ion microscopy of graphene: beam damage, image quality and edge contrast," *Nanotechnology*, vol. 24, no. 33, p. 335702, 2013.

[204] S. Kretschmer, M. Maslov, S. Ghaderzadeh, M. Ghorbani-Asl, G. Hlawacek, and A. V. Krasheninnikov, "Supported two-dimensional materials under ion irradiation: The substrate governs defect production," *ACS Applied Materials & Interfaces*, vol. 10, no. 36, pp. 30827–30836, 2018.

[205] S. Bertolazzi, S. Bonacchi, G. Nan, A. Pershin, D. Beljonne, and P. Samorí, "Engineering chemically active defects in monolayer MoS_2 transistors via ion-beam irradiation and their healing via vapor deposition of alkanethiols," *Advanced Materials*, vol. 29, no. 18, p. 1606760, 2017.

[206] Z. G. Yu, Y.-W. Zhang, and B. I. Yakobson, "An anomalous formation pathway for dislocation-sulfur vacancy complexes in polycrystalline monolayer MoS_2," *Nano Letters*, vol. 15, no. 10, pp. 6855–6861, 2015.

[207] M. O'Brien, N. McEvoy, T. Hallam, H.-Y. Kim, N. C. Berner, D. Hanlon, K. Lee, J. N. Coleman, and G. S. Duesberg, "Transition metal dichalcogenide growth via close proximity precursor supply," *Scientific Reports*, vol. 4, p. 7374, 2014.

[208] Y.-H. Lee, X.-Q. Zhang, W. Zhang, M.-T. Chang, C.-T. Lin, K.-D. Chang, Y.-C. Yu, J. T.-W. Wang, C.-S. Chang, L.-J. Li, and T.-W. Lin, "Synthesis of large-area MoS_2 atomic layers with chemical vapor deposition," *Advanced Materials*, vol. 24, pp. 2320–2325, 3 2012.

[209] H. R. Gutiérrez, N. Perea-López, A. L. Elías, A. Berkdemir, B. Wang, R. Lv, F. López-Urías, V. H. Crespi, H. Terrones, and M. Terrones, "Extraordinary room-temperature photoluminescence in triangular WS_2 monolayers," *Nano Letters*, vol. 13, pp. 3447–3454, 12 2012.

[210] Y. Zhan, Z. Liu, S. Najmaei, P. M. Ajayan, and J. Lou, "Large-area vapor-phase growth and characterization of MoS_2 atomic layers on a SiO_2 substrate," *Small*, vol. 8, pp. 966–971, 2 2012.

[211] D. Hanlon, C. Backes, T. M. Higgins, M. Hughes, A. O'Neill, P. King, N. McEvoy, G. S. Duesberg, B. M. Sanchez, H. Pettersson, V. Nicolosi, and J. N. Coleman, "Production of molybdenum trioxide nanosheets by liquid exfoliation and their application in high-performance supercapacitors," *Chemistry of Materials*, vol. 26, pp. 1751–1763, 2 2014.

[212] R. F. Frindt, "Single crystals of MoS_2 several molecular layers thick," *Journal of Applied Physics*, vol. 37, pp. 1928–1929, 3 1966.

[213] Y. Huang, E. Sutter, N. N. Shi, J. Zheng, T. Yang, D. Englund, H.-J. Gao, and P. Sutter, "Reliable exfoliation of large-area high-quality flakes of graphene and other two-dimensional materials," *ACS Nano*, vol. 9, pp. 10612–10620, 11 2015.

[214] A. Castellanos-Gomez, N. Agraït, and G. Rubio-Bollinger, "Optical identification of atomically thin dichalcogenide crystals," *Applied Physics Letters*, vol. 96, p. 213116, 5 2010.

[215] M. M. Benameur, B. Radisavljevic, J. S. Héron, S. Sahoo, H. Berger, and A. Kis, "Visibility of dichalcogenide nanolayers," *Nanotechnology*, vol. 22, p. 125706, 2 2011.

[216] H. Li, G. Lu, Z. Yin, Q. He, H. Li, Q. Zhang, and H. Zhang, "Optical identification of single- and few-layer MoS_2 sheets," *Small*, vol. 8, pp. 682–686, 1 2012.

[217] "EBL process flowchart." `https://upload.wikimedia.org/wikipedia/commons/0/0e/Photolithography_process.png`. Accessed: 2019-08-02.

[218] A. H. N. V., "EUV lithography: status, future requirements and challenges." `https://www.euvlitho.com/2013/S2.pdf`, 2019. Accessed: 2019-06-27.

[219] Y.-Q. Bie, Y.-B. Zhou, Z.-M. Liao, K. Yan, S. Liu, Q. Zhao, S. Kumar, H.-C. Wu, G. S. Duesberg, G. L. Cross, *et al.*, "Site-specific transfer-printing of individual graphene microscale patterns to arbitrary surfaces," *Advanced Materials*, vol. 23, no. 34, pp. 3938–3943, 2011.

[220] P. Fischione, J. Ringnada, Y. Feng, T. Krekels, M. Hayies, H. Colijn, M. J. Mills, and J. Wiezorek, "The use of a cold gas plasma for the final processing of contamination-free TEM specimens," *MRS Online Proceedings Library Archive*, vol. 480, 1997.

[221] P. Eaton and P. West, *Atomic force microscopy*. Oxford University Press, 2010.

[222] Nanosurf, "Phase imaging mode." `https://www.nanosurf.com/en/how-afm-works/dynamic-modes`, 2019. Accessed: 2019-05-14.

[223] K. Kumagai and T. Sekiguchi, "Sharing of secondary electrons by in-lens and out-lens detector in low-voltage scanning electron microscope equipped with immersion lens," *Ultramicroscopy*, vol. 109, pp. 368–372, 3 2009.

[224] B. J. Griffin, "A comparison of conventional everhart-thornley style and in-lens secondary electron detectors—a further variable in scanning electron microscopy," *Scanning*, vol. 33, no. 3, pp. 162–173, 2011.

[225] Y. Zhou, D. S. Fox, P. Maguire, R. O'Connell, R. Masters, C. Rodenburg, H. Wu, M. Dapor, Y. Chen, and H. Zhang, "Quantitative secondary electron imaging for work function extraction at atomic level and layer identification of graphene," *Scientific Reports*, vol. 6, 2 2016.

[226] W. Zhou and Z. L. Wang, *Scanning microscopy for nanotechnology: techniques and applications*. Springer Science & Business Media, 2007.

[227] Wikipedia, "Electron microscope." https://en.wikipedia.org/wiki/Electron_microscope, 2019. Accessed: 2019-05-16.

[228] E. Laboratories;, "TEM/STEM." http://www.nanoscience.co.jp/knowledge/TEM/knowledge01.html, 2019. Accessed: 2019-05-19.

[229] Q. Zhang, Z. Shi, K. Yin, H. Dong, F. Xu, X. Peng, K. Yu, H. Zhang, C.-C. Chen, I. Valov, H. Zheng, and L. Sun, "Spring-like pseudoelectroelasticity of monocrystalline Cu_2S nanowire," *Nano Letters*, vol. 18, pp. 5070–5077, 7 2018.

[230] S. Yamashita, J. Kikkawa, K. Yanagisawa, T. Nagai, K. Ishizuka, and K. Kimoto, "Atomic number dependence of Z contrast in scanning transmission electron microscopy," *Scientific Reports*, vol. 8, 8 2018.

[231] T. C. Lovejoy, Q. M. Ramasse, M. Falke, A. Kaeppel, R. Terborg, R. Zan, N. Dellby, and O. L. Krivanek, "Single atom identification by energy dispersive X-ray spectroscopy," *Applied Physics Letters*, vol. 100, p. 154101, 4 2012.

[232] Wikipedia, "Raman spectroscopy." https://en.wikipedia.org/wiki/Raman_spectroscopy, 2019. Accessed: 2019-05-19.

[233] C. Lee, H. Yan, L. E. Brus, T. F. Heinz, J. Hone, and S. Ryu, "Anomalous lattice vibrations of single- and few-layer MoS_2," *ACS Nano*, vol. 4, pp. 2695–2700, 5 2010.

[234] X. Fan, D. J. Singh, and W. Zheng, "Valence band splitting on multilayer MoS_2: Mixing of spin–orbit coupling and interlayer coupling," *The Journal of Physical Chemistry Letters*, vol. 7, pp. 2175–2181, 5 2016.

[235] C.-H. Chang, X. Fan, S.-H. Lin, and J.-L. Kuo, "Orbital analysis of electronic structure and phonon dispersion in MoS_2, $MoSe_2$, WS_2, and WSe_2 monolayers under strain," *Physical Review B*, vol. 88, 11 2013.

[236] Y. Lin, X. Ling, L. Yu, S. Huang, A. L. Hsu, Y.-H. Lee, J. Kong, M. S. Dresselhaus, and T. Palacios, "Dielectric screening of excitons and trions in single-layer MoS_2," *Nano Letters*, vol. 14, pp. 5569–5576, 9 2014.

[237] F. Cadiz, S. Tricard, M. Gay, D. Lagarde, G. Wang, C. Robert, P. Renucci, B. Urbaszek, and X. Marie, "Well separated trion and neutral excitons on superacid treated MoS_2 monolayers," *Applied Physics Letters*, vol. 108, no. 25, p. 251106, 2016.

[238] E. J. Sie, A. J. Frenzel, Y.-H. Lee, J. Kong, and N. Gedik, "Intervalley biexcitons and many-body effects in monolayer MoS_2," *Physical Review B*, vol. 92, no. 12, p. 125417, 2015.

[239] S. Mouri, Y. Miyauchi, and K. Matsuda, "Tunable photoluminescence of monolayer MoS_2 via chemical doping," *Nano Letters*, vol. 13, no. 12, pp. 5944–5948, 2013.

[240] Y. Li, W. Liu, H. Xu, C. Zhang, L. Yang, W. Yue, and Y. Liu, "Abnormal high-temperature luminescence enhancement observed in monolayer MoS_2 flakes: thermo-driven transition from negatively charged trions to neutral excitons," *Journal of Materials Chemistry C*, vol. 4, no. 39, pp. 9187–9196, 2016.

[241] Wikipedia, "Energy-dispersive X-ray spectroscopy." `https://en.wikipedia.org/wiki/Energy-dispersive_X-ray_spectroscopy`, 2019. Accessed: 2019-05-16.

[242] M. A. Mutalib, M. Rahman, M. Othman, A. Ismail, and J. Jaafar, "Scanning electron microscopy (SEM) and energy-dispersive X-ray (EDX) spectroscopy," *Membrane Characterization*, pp. 161–179, 2017.

[243] D. B. Williams and C. B. Carter, *The transmission electron microscope*. Springer, 1996.

[244] Wikipedia, "Electron energy loss spectroscopy." `https://en.wikipedia.org/wiki/Electron_energy_loss_spectroscopy`, 2019. Accessed: 2019-05-17.

[245] F. Müller, "Photoelectron spectrometer." `https://jacobs.physik.uni-saarland.de/home/index.php?page=forschung/UHV-Lab-1`, 2019. Accessed: 2019-05-21.

[246] J.-G. Choi and L. Thompson, "XPS study of as-prepared and reduced molybdenum oxides," *Applied Surface Science*, vol. 93, no. 2, pp. 143–149, 1996.

[247] E. Coleman, S. Monaghan, F. Gity, M. Schmidt, J. Connolly, J. Lin, L. Walsh, K. Cherkaoui, K. O'Neill, N. McEvoy, *et al.*, "Large area growth of MoS_2 by chemical vapour deposition," in *Meeting Abstracts*, no. 16 in 2, pp. 708–708, The Electrochemical Society, 2018.

[248] H. Liu, A. T. Neal, and P. D. Ye, "Channel length scaling of MoS_2 MOSFETs," *ACS Nano*, vol. 6, no. 10, pp. 8563–8569, 2012.

[249] D. S. Schulman, A. J. Arnold, and S. Das, "Contact engineering for 2D materials and devices," *Chemical Society Reviews*, vol. 47, no. 9, pp. 3037–3058, 2018.

[250] S. Harrison, *Exploring and Exploiting Charge-Carrier Confinement in Semiconductor Nanostructures*. PhD thesis, Lancaster University, UK, 2016.

[251] H. Nan, Z. Wu, J. Jiang, A. Zafar, Y. You, and Z. Ni, "Improving the electrical performance of MoS_2 by mild oxygen plasma treatment," *Journal of Physics D: Applied Physics*, vol. 50, no. 15, p. 154001, 2017.

[252] W. Yang, Q.-Q. Sun, Y. Geng, L. Chen, P. Zhou, S.-J. Ding, and D. W. Zhang, "The integration of sub-10 nm gate oxide on MoS_2 with ultra low leakage and enhanced mobility," *Scientific Reports*, vol. 5, 7 2015.

[253] M.-Y. Ryu, H.-K. Jang, K. J. Lee, M. Piao, S.-P. Ko, M. Shin, J. Huh, and G.-T. Kim, "Triethanolamine doped multilayer MoS_2 field effect transistors," *Physical Chemistry Chemical Physics*, vol. 19, no. 20, pp. 13133–13139, 2017.

[254] W.-B. Zhang, Q. Qu, and K. Lai, "High-mobility transport anisotropy in few-layer MoO_3 and its origin," *ACS Applied Materials & Interfaces*, vol. 9, pp. 1702–1709, 1 2017.

[255] S. Balendhran, J. Deng, J. Z. Ou, S. Walia, J. Scott, J. Tang, K. L. Wang, M. R. Field, S. Russo, S. Zhuiykov, *et al.*, "Enhanced charge carrier mobility in two-dimensional high dielectric molybdenum oxide," *Advanced Materials*, vol. 25, no. 1, pp. 109–114, 2013.

[256] M. M. Alsaif, A. F. Chrimes, T. Daeneke, S. Balendhran, D. O. Bellisario, Y. Son, M. R. Field, W. Zhang, H. Nili, E. P. Nguyen, *et al.*, "High-performance field effect transistors using electronic inks of 2D molybdenum oxide nanoflakes," *Advanced Functional Materials*, vol. 26, no. 1, pp. 91–100, 2016.

[257] R. Dhall, M. R. Neupane, D. Wickramaratne, M. Mecklenburg, Z. Li, C. Moore, R. K. Lake, and S. Cronin, "Direct bandgap transition in many-layer MoS_2 by plasma-induced layer decoupling," *Advanced Materials*, vol. 27, no. 9, pp. 1573–1578, 2015.

[258] R. Rao, A. E. Islam, P. M. Campbell, E. M. Vogel, and B. Maruyama, "In situ thermal oxidation kinetics in few layer MoS_2," *2D Materials*, vol. 4, no. 2, p. 025058, 2017.

[259] Y. Guo and J. Robertson, "Origin of the high work function and high conductivity of MoO_3," *Applied Physics Letters*, vol. 105, p. 222110, 12 2014.

[260] S. Y. Lee, U. J. Kim, J. Chung, H. Nam, H. Y. Jeong, G. H. Han, H. Kim, H. M. Oh, H. Lee, H. Kim, Y.-G. Roh, J. Kim, S. W. Hwang, Y. Park, and Y. H. Lee, "Large work function modulation of monolayer MoS_2 by ambient gases," *ACS Nano*, vol. 10, pp. 6100–6107, 6 2016.

[261] T. N. Walter, F. Kwok, H. Simchi, H. M. Aldosari, and S. E. Mohney, "Oxidation and oxidative vapor-phase etching of few-layer MoS_2," *Journal of Vacuum Science & Technology B, Nanotechnology and Microelectronics: Materials, Processing, Measurement, and Phenomena*, vol. 35, no. 2, p. 021203, 2017.

[262] D. Kim, H. Du, T. Kim, S. Shin, S. Kim, M. Song, C. Lee, J. Lee, H. Cheong, D. H. Seo, and S. Seo, "The enhanced low resistance contacts and boosted mobility in two-dimensional p-type WSe_2 transistors through Ar^+ ion-beam generated surface defects," *AIP Advances*, vol. 6, p. 105307, 10 2016.

[263] H. Li, Q. Zhang, C. C. R. Yap, B. K. Tay, T. H. T. Edwin, A. Olivier, and D. Baillargeat, "From bulk to monolayer MoS_2: Evolution of Raman scattering," *Advanced Functional Materials*, vol. 22, pp. 1385–1390, 1 2012.

[264] N. Kang, H. P. Paudel, M. N. Leuenberger, L. Tetard, and S. I. Khondaker, "Photoluminescence quenching in single-layer MoS_2 via oxygen plasma treatment," *The Journal of Physical Chemistry C*, vol. 118, no. 36, pp. 21258–21263, 2014.

[265] A. T. Neal, R. Pachter, and S. Mou, "P-type conduction in two-dimensional MoS_2 via oxygen incorporation," *Applied Physics Letters*, vol. 110, no. 19, p. 193103, 2017.

[266] D. O. Scanlon, G. W. Watson, D. Payne, G. Atkinson, R. Egdell, and D. Law, "Theoretical and experimental study of the electronic structures of MoO_3 and MoO_2," *The Journal of Physical Chemistry C*, vol. 114, no. 10, pp. 4636–4645, 2010.

[267] P. J. Cumpson, "The Thickogram: a method for easy film thickness measurement in XPS," *Surface and Interface Analysis: An International Journal devoted to the development and application of techniques for the analysis of surfaces, interfaces and thin films*, vol. 29, no. 6, pp. 403–406, 2000.

[268] M. Baker, R. Gilmore, C. Lenardi, and W. Gissler, "XPS investigation of preferential sputtering of S from MoS_2 and determination of MoS_x stoichiometry from Mo and S peak positions," *Applied Surface Science*, vol. 150, no. 1-4, pp. 255–262, 1999.

[269] S. McDonnell, A. Azcatl, R. Addou, C. Gong, C. Battaglia, S. Chuang, K. Cho, A. Javey, and R. M. Wallace, "Hole contacts on transition metal dichalcogenides: Interface chemistry and band alignments," *ACS Nano*, vol. 8, pp. 6265–6272, 6 2014.

[270] S. Chuang, C. Battaglia, A. Azcatl, S. McDonnell, J. S. Kang, X. Yin, M. Tosun, R. Kapadia, H. Fang, R. M. Wallace, and A. Javey, "MoS_2 p-type transistors and diodes enabled by high work function MoO_x contacts," *Nano Letters*, vol. 14, pp. 1337–1342, 3 2014.

[271] J. Yang, S. Kim, W. Choi, S. H. Park, Y. Jung, M.-H. Cho, and H. Kim, "Improved growth behavior of atomic-layer-deposited high-k dielectrics on multilayer MoS_2 by oxygen plasma pretreatment," *ACS Applied Materials & Interfaces*, vol. 5, no. 11, pp. 4739–4744, 2013.

[272] L. Tao, X. Duan, C. Wang, X. Duan, and S. Wang, "Plasma-engineered MoS_2 thin-film as an efficient electrocatalyst for hydrogen evolution reaction," *Chemical Communications*, vol. 51, no. 35, pp. 7470–7473, 2015.

[273] J. Berkowitz, M. G. Inghram, and W. A. Chupka, "Polymeric gaseous species in the sublimation of molybdenum trioxide," *The Journal of Chemical Physics*, vol. 26, pp. 842–846, 4 1957.

[274] V. P. Zhdanov, "nm-sized metal particles on a semiconductor surface, Schottky model, etc.," *Surface Science*, vol. 512, no. 1-2, pp. L331–L334, 2002.

[275] S. Das and J. Appenzeller, "Where does the current flow in two-dimensional layered systems?," *Nano Letters*, vol. 13, no. 7, pp. 3396–3402, 2013.

[276] C. G. da Rocha, H. G. Manning, C. O'Callaghan, C. Ritter, A. T. Bellew, J. J. Boland, and M. S. Ferreira, "Ultimate conductivity performance in metallic nanowire networks," *Nanoscale*, vol. 7, no. 30, pp. 13011–13016, 2015.

[277] C. O'Callaghan, C. G. da Rocha, H. G. Manning, J. J. Boland, and M. S. Ferreira, "Effective medium theory for the conductivity of disordered metallic nanowire networks," *Physical Chemistry Chemical Physics*, vol. 18, no. 39, pp. 27564–27571, 2016.

[278] J. Fairfield, C. Rocha, C. O'Callaghan, M. Ferreira, and J. Boland, "Co-percolation to tune conductive behaviour in dynamical metallic nanowire networks," *Nanoscale*, vol. 8, no. 43, pp. 18516–18523, 2016.

[279] T. Gebele, "Site percolation threshold for square lattice," *Journal of Physics A: Mathematical and General*, vol. 17, no. 2, p. L51, 1984.

[280] M. J. Moody, A. Henning, T. Jurca, J. Y. Shang, H. Bergeron, I. Balla, J. N. Olding, E. A. Weiss, M. C. Hersam, T. L. Lohr, *et al.*, "Atomic layer deposition of molybdenum oxides with tunable stoichiometry enables controllable doping of MoS_2," *Chemistry of Materials*, 2018.

[281] B. W. Baugher, H. O. Churchill, Y. Yang, and P. Jarillo-Herrero, "Intrinsic electronic transport properties of high-quality monolayer and bilayer MoS_2," *Nano Letters*, vol. 13, no. 9, pp. 4212–4216, 2013.

[282] I. Filanovsky and A. Allam, "Mutual compensation of mobility and threshold voltage temperature effects with applications in CMOS circuits," *IEEE Transactions on Circuits and Systems I: Fundamental Theory and Applications*, vol. 48, no. 7, pp. 876–884, 2001.

[283] J. Xue, S. Huang, J.-Y. Wang, and H. Q. Xu, "Mott variable-range hopping transport in a MoS_2 nanoflake," *RSC Advances*, vol. 9, no. 31, pp. 17885–17890, 2019.

[284] S. Peng, Z. Jin, Y. Yao, L. Li, D. Zhang, J. Shi, X. Huang, J. Niu, Y. Zhang, and G. Yu, "Metal-contact-induced transition of electrical transport in monolayer MoS_2: From thermally activated to variable-range hopping," *Advanced Electronic Materials*, vol. 5, p. 1900042, 6 2019.

[285] J. Wang, Q. Yao, C.-W. Huang, X. Zou, L. Liao, S. Chen, Z. Fan, K. Zhang, W. Wu, X. Xiao, C. Jiang, and W.-W. Wu, "High mobility MoS_2 transistor with low schottky barrier contact by using atomic thick h-BN as a tunneling layer," *Advanced Materials*, vol. 28, pp. 8302–8308, 7 2016.

[286] B. R. Matis, N. Y. Garces, E. R. Cleveland, B. H. Houston, and J. W. Baldwin, "Electronic transport in bilayer MoS_2 encapsulated in HfO_2," *ACS Applied Materials & Interfaces*, vol. 9, pp. 27995–28001, 8 2017.

[287] A. Efros and B. I. Shklovskii, "Coulomb gap and low temperature conductivity of disordered systems," *Journal of Physics C: Solid State Physics*, vol. 8, no. 4, p. L49, 1975.

[288] O. Lopez-Sanchez, D. Lembke, M. Kayci, A. Radenovic, and A. Kis, "Ultrasensitive photodetectors based on monolayer MoS_2," *Nature Nanotechnology*, vol. 8, no. 7, pp. 497–501, 2013.

[289] X. Wang, Y. Cui, T. Li, M. Lei, J. Li, and Z. Wei, "Recent advances in the functional 2D photonic and optoelectronic devices," *Advanced Optical Materials*, vol. 7, no. 3, p. 1801274, 2019.

[290] X. Wang, P. Wang, J. Wang, W. Hu, X. Zhou, N. Guo, H. Huang, S. Sun, H. Shen, T. Lin, *et al.*, "Ultrasensitive and broadband MoS_2 photodetector driven by ferroelectrics," *Advanced Materials*, vol. 27, no. 42, pp. 6575–6581, 2015.

[291] A. E. Yore, K. K. Smithe, S. Jha, K. Ray, E. Pop, and A. Newaz, "Large array fabrication of high performance monolayer MoS_2 photodetectors," *Applied Physics Letters*, vol. 111, no. 4, p. 043110, 2017.

[292] H. Wang, C. Zhang, W. Chan, S. Tiwari, and F. Rana, "Ultrafast response of monolayer molybdenum disulfide photodetectors," *Nature Communications*, vol. 6, p. 8831, 2015.

[293] S. Lee, Y. Park, G. Yoo, and J. Heo, "Wavelength-selective enhancement of photo-responsivity in metal-gated multi-layer MoS_2 phototransistors," *Applied Physics Letters*, vol. 111, no. 22, p. 223106, 2017.

[294] S.-W. Wang, H. Medina, K.-B. Hong, C.-C. Wu, Y. Qu, A. Manikandan, T.-Y. Su, P.-T. Lee, Z.-Q. Huang, Z. Wang, *et al.*, "Thermally strained band gap engineering of transition metal dichalcogenide bilayers with enhanced light-matter interaction toward excellent photodetectors," *ACS Nano*, 2017.

[295] Y. Yang, N. Huo, and J. Li, "Sensitized monolayer MoS_2 phototransistors with ultrahigh responsivity," *Journal of Materials Chemistry C*, vol. 5, no. 44, pp. 11614–11619, 2017.

[296] G. Yoo, S. Hong, J. Heo, and S. Kim, "Enhanced photoresponsivity of multilayer MoS_2 transistors using high work function MoO_x overlayer," *Applied Physics Letters*, vol. 110, no. 5, p. 053112, 2017.

[297] D. Kufer, I. Nikitskiy, T. Lasanta, G. Navickaite, F. H. Koppens, and G. Konstantatos, "Hybrid 2D-0D MoS_2-PbS quantum dot photodetectors," *Advanced Materials*, vol. 27, no. 1, pp. 176–180, 2015.

[298] D. Kufer, T. Lasanta, M. Bernechea, F. H. Koppens, and G. Konstantatos, "Interface engineering in hybrid quantum dot-2D phototransistors," *ACS Photonics*, vol. 3, no. 7, pp. 1324–1330, 2016.

[299] J. J. Gough, N. McEvoy, M. O'Brien, A. P. Bell, D. McCloskey, J. B. Boland, J. N. Coleman, G. S. Duesberg, and A. L. Bradley, "Dependence of photocurrent enhancements in quantum dot (QD)-sensitized MoS_2 devices on MoS_2 film properties," *Advanced Functional Materials*, vol. 28, no. 13, p. 1706149, 2018.

[300] D.-H. Kang, M.-S. Kim, J. Shim, J. Jeon, H.-Y. Park, W.-S. Jung, H.-Y. Yu, C.-H. Pang, S. Lee, and J.-H. Park, "High-performance transition metal dichalcogenide photodetectors enhanced by self-assembled monolayer doping," *Advanced Functional Materials*, vol. 25, no. 27, pp. 4219–4227, 2015.

[301] Y. Huang, W. Zheng, Y. Qiu, and P. Hu, "Effects of organic molecules with different structures and absorption bandwidth on modulating photoresponse of MoS_2 photodetector," *ACS Applied Materials & Interfaces*, vol. 8, no. 35, pp. 23362–23370, 2016.

[302] S. H. Yu, Y. Lee, S. K. Jang, J. Kang, J. Jeon, C. Lee, J. Y. Lee, H. Kim, E. Hwang, S. Lee, *et al.*, "Dye-sensitized MoS_2 photodetector with enhanced spectral photoresponse," *ACS Nano*, vol. 8, no. 8, pp. 8285–8291, 2014.

[303] J. Miao, W. Hu, Y. Jing, W. Luo, L. Liao, A. Pan, S. Wu, J. Cheng, X. Chen, and W. Lu, "Surface plasmon-enhanced photodetection in few layer MoS_2 phototransistors with Au nanostructure arrays," *Small*, vol. 11, no. 20, pp. 2392–2398, 2015.

[304] W. Jing, N. Ding, L. Li, F. Jiang, X. Xiong, N. Liu, T. Zhai, and Y. Gao, "Ag nanoparticles modified large area monolayer MoS_2 phototransistors with high responsivity," *Optics Express*, vol. 25, no. 13, pp. 14565–14574, 2017.

[305] J. Jadwiszczak, Y. Zhou, and H. Zhang, "Low-temperature electrical conduction of plasma-treated bilayer MoS_2," *MRS Communications*, pp. 1–7, 2018.

[306] M. J. Park, K. Park, and H. Ko, "Near-infrared photodetector achieved by chemically-exfoliated multilayered MoS_2 flakes," *Applied Surface Science*, vol. 448, pp. 64–70, 2018.

[307] W. Zhang, J.-K. Huang, C.-H. Chen, Y.-H. Chang, Y.-J. Cheng, and L.-J. Li, "High-gain phototransistors based on a CVD MoS_2 monolayer," *Advanced Materials*, vol. 25, no. 25, pp. 3456–3461, 2013.

[308] C. Xie, C. Mak, X. Tao, and F. Yan, "Photodetectors based on two-dimensional layered materials beyond graphene," *Advanced Functional Materials*, vol. 27, no. 19, p. 1603886, 2017.

[309] J. Jadwiszczak, G. Li, C. P. Cullen, J. J. Wang, P. Maguire, G. S. Duesberg, J. G. Lunney, and H. Zhang, "Photoresponsivity enhancement in monolayer MoS_2 by rapid O_2:Ar plasma treatment," *Applied Physics Letters*, vol. 114, no. 9, p. 091103, 2019.

[310] C. Garcia, N. Pradhan, D. Rhodes, L. Balicas, and S. McGill, "Photogating and high gain in ReS_2 field-effect transistors," *Journal of Applied Physics*, vol. 124, no. 20, p. 204306, 2018.

[311] M. Massicotte, P. Schmidt, F. Vialla, K. G. Schaedler, A. Reserbat-Plantey, K. Watanabe, T. Taniguchi, K.-J. Tielrooij, and F. H. Koppens, "Picosecond photoresponse in van der Waals heterostructures," *Nature Nanotechnology*, vol. 11, no. 1, p. 42, 2016.

[312] C.-C. Wu, D. Jariwala, V. K. Sangwan, T. J. Marks, M. C. Hersam, and L. J. Lauhon, "Elucidating the photoresponse of ultrathin MoS_2 field-effect transistors by scanning photocurrent microscopy," *The Journal of Physical Chemistry Letters*, vol. 4, no. 15, pp. 2508–2513, 2013.

[313] B. E. Saleh and M. C. Teich, *Fundamentals of photonics*. John Wiley & Sons, 1991.

[314] D.-H. Kang, S. R. Pae, J. Shim, G. Yoo, J. Jeon, J. W. Leem, J. S. Yu, S. Lee, B. Shin, and J.-H. Park, "An ultrahigh-performance photodetector based on a perovskite–transition-metal-dichalcogenide hybrid structure," *Advanced Materials*, vol. 28, no. 35, pp. 7799–7806, 2016.

[315] J. He, Y. Yang, Y. He, C. Ge, Y. Zhao, L. Gao, and J. Tang, "Low noise and fast photoresponse of few-layered MoS_2 passivated by $MA_3Bi_2Br_9$," *ACS Photonics*, vol. 5, pp. 1877–1884, 3 2018.

[316] Y. Liang, S. Huang, R. Soklaski, and L. Yang, "Quasiparticle band-edge energy and band offsets of monolayer of molybdenum and tungsten chalcogenides," *Applied Physics Letters*, vol. 103, no. 4, p. 042106, 2013.

[317] Z. Zhang and J. T. Yates Jr, "Band bending in semiconductors: chemical and physical consequences at surfaces and interfaces," *Chemical Reviews*, vol. 112, no. 10, pp. 5520–5551, 2012.

[318] M. M. Furchi, D. K. Polyushkin, A. Pospischil, and T. Mueller, "Mechanisms of photoconductivity in atomically thin MoS_2," *Nano Letters*, vol. 14, no. 11, pp. 6165–6170, 2014.

[319] D. Kufer and G. Konstantatos, "Highly sensitive, encapsulated MoS_2 photodetector with gate controllable gain and speed," *Nano Letters*, vol. 15, no. 11, pp. 7307–7313, 2015.

[320] C. Chen, H. Qiao, S. Lin, C. M. Luk, Y. Liu, Z. Xu, J. Song, Y. Xue, D. Li, J. Yuan, *et al.*, "Highly responsive MoS_2 photodetectors enhanced by graphene quantum dots," *Scientific Reports*, vol. 5, p. 11830, 2015.

[321] J. F. Ziegler, M. D. Ziegler, and J. P. Biersack, *SRIM: the stopping and range of ions in matter*. Cadence Design Systems, 2008.

[322] P. Maguire, D. S. Fox, Y. Zhou, Q. Wang, M. O'Brien, J. Jadwiszczak, C. P. Cullen, J. McManus, S. Bateman, N. McEvoy, *et al.*, "Defect sizing, separation, and substrate effects in ion-irradiated monolayer two-dimensional materials," *Physical Review B*, vol. 98, no. 13, p. 134109, 2018.

[323] Z. Cheng, J. A. Cardenas, F. McGuire, and A. D. Franklin, "Modifying the Ni-MoS_2 contact interface using a broad-beam ion source," *IEEE Electron Device Letters*, vol. 37, no. 9, p. 512, 2016.

[324] Z. Cheng, H. Abuzaid, Y. Yu, F. Zhang, Y. Li, S. G. Noyce, N. X. Williams, Y.-C. Lin, J. L. Doherty, C. Tao, L. Cao, and A. D. Franklin, "Convergent ion beam alteration of 2D materials and metal-2D interfaces," *2D Materials*, vol. 6, p. 034005, 6 2019.

[325] G. Arutchelvan, C. J. L. de la Rosa, P. Matagne, S. Sutar, I. Radu, C. Huyghebaert, S. De Gendt, and M. Heyns, "From the metal to the channel: a study of carrier injection through the metal/2D MoS_2 interface," *Nanoscale*, vol. 9, no. 30, pp. 10869–10879, 2017.

[326] B. H. Moon, G. H. Han, H. Kim, H. Choi, J. J. Bae, J. Kim, Y. Jin, H. Y. Jeong, M.-K. Joo, Y. H. Lee, *et al.*, "Junction-structure-dependent Schottky barrier inhomogeneity and device ideality of monolayer MoS_2 field-effect transistors," *ACS Applied Materials & Interfaces*, vol. 9, no. 12, pp. 11240–11246, 2017.

[327] H.-J. Kim, D.-H. Kim, C.-Y. Jeong, J.-H. Lee, and H.-I. Kwon, "Determination of interface and bulk trap densities in high-mobility p-type WSe_2 thin-film transistors," *IEEE Electron Device Letters*, vol. 38, no. 4, pp. 481–484, 2017.

[328] H.-P. Komsa, S. Kurasch, O. Lehtinen, U. Kaiser, and A. V. Krasheninnikov, "From point to extended defects in two-dimensional MoS_2: Evolution of atomic structure under electron irradiation," *Physical Review B*, vol. 88, 7 2013.

[329] I. S. Kim, V. K. Sangwan, D. Jariwala, J. D. Wood, S. Park, K.-S. Chen, F. Shi, F. Ruiz-Zepeda, A. Ponce, M. Jose-Yacaman, *et al.*, "Influence of stoichiometry on the optical and electrical properties of chemical vapor deposition derived MoS_2," *ACS Nano*, vol. 8, no. 10, pp. 10551–10558, 2014.

[330] J. Shannon, "Control of Schottky barrier height using highly doped surface layers," *Solid-State Electronics*, vol. 19, no. 6, pp. 537–543, 1976.

[331] P. Hirsch, M. Kässens, M. Püttmann, Reimer, and L, "Contamination in a scanning electron microscope and the influence of specimen cooling," *Scanning*, vol. 16, no. 2, pp. 101–110, 1994.

[332] A. E. Vladár, M. T. Postek, and R. Vane, "Active monitoring and control of electron-beam-induced contamination," in *Metrology, Inspection, and Process Control for Microlithography XV*, vol. 4344, pp. 835–844, International Society for Optics and Photonics, 2001.

[333] W. Ding, D. Dikin, X. Chen, R. Piner, R. Ruoff, E. Zussman, X. Wang, and X. Li, "Mechanics of hydrogenated amorphous carbon deposits from electron-beam-induced deposition of a paraffin precursor," *Journal of Applied Physics*, vol. 98, no. 1, p. 014905, 2005.

[334] C. Soong, P. Woo, and D. Hoyle, "Contamination cleaning of TEM/SEM samples with the ZONE cleaner," *Microscopy Today*, vol. 20, no. 6, pp. 44–48, 2012.

[335] H. Wanzenboeck, P. Roediger, G. Hochleitner, E. Bertagnolli, and W. Buehler, "Novel method for cleaning a vacuum chamber from hydrocarbon contamination," *Journal of Vacuum Science & Technology A*, vol. 28, 2010.

[336] J. Wu, H. Li, Z. Yin, H. Li, J. Liu, X. Cao, Q. Zhang, and H. Zhang, "Layer thinning and etching of mechanically exfoliated MoS_2 nanosheets by thermal annealing in air," *Small*, vol. 9, pp. 3314–3319, 8 2013.

[337] Y. Yang, P. Sheridan, and W. Lu, "Complementary resistive switching in tantalum oxide-based resistive memory devices," *Applied Physics Letters*, vol. 100, p. 203112, 5 2012.

[338] G. Burr, R. Shelby, C. di Nolfo, J. Jang, R. Shenoy, P. Narayanan, K. Virwani, E. Giacometti, B. Kurdi, and H. Hwang, "Experimental demonstration and tolerancing of a large-scale neural network 165,000 synapses, using phase-change memory as the synaptic weight element," in *2014 IEEE International Electron Devices Meeting*, IEEE, 12 2014.

[339] N. Gong, T. Idé, S. Kim, I. Boybat, A. Sebastian, V. Narayanan, and T. Ando, "Signal and noise extraction from analog memory elements for neuromorphic computing," *Nature Communications*, vol. 9, 5 2018.

[340] D. Ielmini, F. Nardi, and S. Balatti, "Evidence for voltage-driven set/reset processes in bipolar switching RRAM," *IEEE Transactions on Electron Devices*, vol. 59, pp. 2049–2056, 8 2012.

[341] S. Shin, K. Kim, and S.-M. Kang, "Memristor applications for programmable analog ICs," *IEEE Transactions on Nanotechnology*, vol. 10, no. 2, pp. 266–274, 2011.

[342] A. A. Bessonov, M. N. Kirikova, D. I. Petukhov, M. Allen, T. Ryhänen, and M. J. A. Bailey, "Layered memristive and memcapacitive switches for printable electronics," *Nature Materials*, vol. 14, no. 2, pp. 199–204, 2014.

[343] Z. Yin, Z. Zeng, J. Liu, Q. He, P. Chen, and H. Zhang, "Memory devices using a mixture of MoS_2 and graphene oxide as the active layer," *Small*, vol. 9, no. 5, pp. 727–731, 2013.

[344] D. S. Chung, D. H. Lee, C. Yang, K. Hong, C. E. Park, J. W. Park, and S.-K. Kwon, "Origin of high mobility within an amorphous polymeric semiconductor: Space-charge-limited current and trap distribution," *Applied Physics Letters*, vol. 93, no. 3, p. 258, 2008.

[345] L. Wang, L. Wang, K.-W. Ang, A. V.-Y. Thean, and G. Liang, "A compact model for 2-D poly-MoS_2 FETs with resistive switching in postsynaptic simulation," *IEEE Transactions on Electron Devices*, vol. 66, pp. 4092–4100, 9 2019.

[346] D. Le, T. B. Rawal, and T. S. Rahman, "Single-layer MoS_2 with sulfur vacancies: Structure and catalytic application," *The Journal of Physical Chemistry C*, vol. 118, pp. 5346–5351, 3 2014.

[347] M. Prezioso, F. Merrikh-Bayat, B. D. Hoskins, G. C. Adam, K. K. Likharev, and D. B. Strukov, "Training and operation of an integrated neuromorphic network based on metal-oxide memristors," *Nature*, vol. 521, pp. 61–64, 5 2015.

[348] P. K. Chow, R. B. Jacobs-Gedrim, J. Gao, T.-M. Lu, B. Yu, H. Terrones, and N. Koratkar, "Defect-induced photoluminescence in monolayer semiconducting transition metal dichalcogenides," *ACS Nano*, vol. 9, no. 2, pp. 1520–1527, 2015.

[349] L. Li, R. Long, T. Bertolini, and O. V. Prezhdo, "Sulfur adatom and vacancy accelerate charge recombination in MoS_2 but by different mechanisms: Time-domain ab initio analysis," *Nano Letters*, vol. 17, pp. 7962–7967, 12 2017.

[350] H.-P. Komsa and A. V. Krasheninnikov, "Native defects in bulk and monolayer MoS_2 from first principles," *Physical Review B*, vol. 91, 3 2015.

[351] S. Urasaki and H. Kageshima, "First-principles study on charged vacancies in MoS_2," *Japanese Journal of Applied Physics*, vol. 57, p. 125202, 10 2018.

[352] M. G. Sensoy, D. Vinichenko, W. Chen, C. M. Friend, and E. Kaxiras, "Strain effects on the behavior of isolated and paired sulfur vacancy defects in monolayer MoS_2," *Physical Review B*, vol. 95, 1 2017.

[353] M.-H. Shang, H. Hou, J. Zheng, Z. Yang, J. Zhang, S. Wei, X. Duan, and W. Yang, "Elimination of S vacancy as the cause for the n-type behavior of MoS_2 from the first-principles perspective," *The Journal of Physical Chemistry Letters*, vol. 9, pp. 6032–6037, 9 2018.

[354] W. M. Parkin, A. Balan, L. Liang, P. M. Das, M. Lamparski, C. H. Naylor, J. A. Rodríguez-Manzo, A. T. C. Johnson, V. Meunier, and M. Drndić, "Raman shifts in electron-irradiated monolayer MoS_2," *ACS Nano*, vol. 10, no. 4, pp. 4134–4142, 2016.

[355] S. Tongay, J. Zhou, C. Ataca, J. Liu, J. S. Kang, T. S. Matthews, L. You, J. B. Li, J. C. Grossman, and J. Q. Wu, "Broad-range modulation of light emission in two-dimensional semiconductors by molecular physisorption gating," *Nano Letters*, vol. 13, no. 6, pp. 2831–2836, 2013.

[356] S. Tongay, J. Suh, C. Ataca, W. Fan, A. Luce, J. S. Kang, J. Liu, C. Ko, R. Raghunathanan, J. Zhou, F. Ogletree, J. Li, J. C. Grossman, and J. Wu, "Defects activated photoluminescence in two-dimensional semiconductors: interplay between bound, charged and free excitons," *Scientific Reports*, vol. 3, no. 1, 2013.

[357] H. Nan, Z. Wang, W. Wang, Z. Liang, Y. Lu, Q. Chen, D. He, P. Tan, F. Miao, X. Wang, *et al.*, "Strong photoluminescence enhancement of MoS_2 through defect engineering and oxygen bonding," *ACS Nano*, vol. 8, no. 6, pp. 5738–5745, 2014.

[358] A. Alharbi, D. Armstrong, S. Alharbi, and D. Shahrjerdi, "Physically unclonable cryptographic primitives by chemical vapor deposition of layered MoS_2," *ACS Nano*, vol. 11, pp. 12772–12779, 11 2017.

[359] H. Schmidt, S. Wang, L. Chu, M. Toh, R. Kumar, W. Zhao, A. Castro Neto, J. Martin, S. Adam, B. Özyilmaz, and E. Goki, "Transport properties of monolayer MoS_2 grown by chemical vapor deposition," *Nano Letters*, vol. 14, no. 4, pp. 1909–1913, 2014.

[360] X. Chen, Z. Wu, S. Xu, L. Wang, R. Huang, Y. Han, W. Ye, W. Xiong, T. Han, G. Long, Y. Wang, Y. He, Y. Cai, P. Sheng, and N. Wang, "Probing the electron states and metal-insulator transition mechanisms in molybdenum disulphide vertical heterostructures," *Nature Communications*, vol. 6, p. 6088, 2015.

[361] H. Bergeron, V. K. Sangwan, J. J. McMorrow, G. P. Campbell, I. Balla, X. Liu, M. J. Bedzyk, T. J. Marks, and M. C. Hersam, "Chemical vapor deposition of monolayer MoS_2 directly on ultrathin Al_2O_3 for low-power electronics," *Applied Physics Letters*, vol. 110, no. 5, p. 053101, 2017.

[362] K. Kaasbjerg, K. S. Thygesen, and K. W. Jacobsen, "Phonon-limited mobility inn-type single-layer MoS_2 from first principles," *Physical Review B*, vol. 85, 3 2012.

[363] K. Taniguchi, A. Matsumoto, H. Shimotani, and H. Takagi, "Electric-field-induced superconductivity at 9.4 K in a layered transition metal disulphide MoS_2," *Applied Physics Letters*, vol. 101, no. 4, p. 042603, 2012.

[364] D. Costanzo, S. Jo, H. Berger, and A. F. Morpurgo, "Gate-induced superconductivity in atomically thin MoS_2 crystals," *Nature Nanotechnology*, vol. 11, no. 4, p. 339, 2016.

[365] J. Lu, O. Zheliuk, I. Leermakers, N. F. Yuan, U. Zeitler, K. T. Law, and J. Ye, "Evidence for two-dimensional ising superconductivity in gated MoS_2," *Science*, vol. 350, no. 6266, pp. 1353–1357, 2015.

[366] H. Bae, S. Jun, C.-K. Kim, B.-K. Ju, and Y.-K. Choi, "Quantitative analysis of trap states through the behavior of the sulfur ions in MoS_2 FETs following high vacuum annealing," *Journal of Physics D: Applied Physics*, vol. 51, p. 105102, 2 2018.

[367] X. Fang, P. Wei, L. Wang, X. Wang, B. Chen, Q. He, Q. Yue, J. Zhang, W. Zhao, J. Wang, G. Lu, H. Zhang, W. Huang, X. Huang, and H. Li, "Transforming monolayer transition-metal dichalcogenide nanosheets into one-dimensional nanoscrolls with high photosensitivity," *ACS Applied Materials & Interfaces*, vol. 10, pp. 13011–13018, 3 2018.

[368] Microchem, "NANO PMMA and Copolymer." `http://microchem.com/pdf/PMMA_Data_Sheet.pdf`, 2019. Accessed: 2019-05-24.

Appendix A: Typical electron beam lithography recipe

1. Firstly, the chip containing the MoS_2 samples is cleaned by gentle ultrasonication in baths of acetone, IPA and de-ionised water - in that order. Each time, the sonication time is only a few seconds to avoid the scrolling up of MoS_2 flakes into nano-scrolls due to the varying rates of organic solvent evaporation from the MoS_2 surface [367], and to avoid the detachment of EBL markers from the substrate.

2. The polymer resist is then spun onto the chip. It is crucial that no impurities or air bubbles are present on the surface of the chip, as this will lead to an uneven final film and thus a non-uniform electron dose necessary for the scission of the polymer chains. The resist of choice for EBL in this thesis was PMMA A3 (*Microchem*). The number signifies the concentration of the polymer solids dissolved in the anisole carrier solvent. The spin speed of the chip, which is vacuum-held to the chuck, determines the final thickness of the resist, and it varies depending on this concentration. For PMMA A3 and the 3000 rpm spin speed utilised for 45 seconds, the final film thickness is $\sim$ 200 nm; as per manufacturer specifications [368].

3. Following this step, the chip is *baked* on a hotplate at a temperature of 130°C for 3 minutes. This ensures the evaporation of the remaining solvent and adheres the polymer to the chip.

4. The chip is loaded into the SEM for exposure. Once the stage is appropriately aligned and the planned pattern location is found, with minimal exposure to the film during imaging, the microscope is aligned by scanning four location markers nearby the designed pattern and flagging their centres. It is thus crucial that the desired samples are not too close together, as the scanned markers will be exposed and metallised, which could lead to shorting if this happens to be on a neighbouring electrode.

5. Each resist (and concentration) has a given exposure electron *dose* which is necessary to fully break the polymer bonds in the film, allowing for it to be developed. The dose is expressed in units of μAs cm^{-2}. For PMMA A3, the typical exposure dose is 200, which allows for the patterns to not be under-developed (not all of the polymer is fully removed) or over-developed (the opened areas extend past the shapes defined during electron beam exposure).

6. Metallisation of the developed patterns takes place in an electron beam evaporator instrument in CRANN (*Temescal FC2000*). Crucibles filled with small pellets of a given element are heated by a scanning electron beam and evaporated onto a spinning target, coating the sample with a thin layer of metal, whose thickness is monitored by the feedback from a vibrating crystal. In this thesis, titanium was used as an adhesion layer for the deposition of gold contacts. The Ti layer thickness used was usually 5 or 10 nm, while the Au thickness was usually 35, 40 or 80 nm on some devices.

7. Lift-off is performed by keeping the metal-coated chips in acetone overnight. A brief ultrasonication step (1-3 s) is sometimes necessary to fully detach the film from the substrate, followed by a wash in IPA, deionised H_2O and a nitrogen gas blow.

Appendix B: *Thickogram* calculation of MoO_3 on MoS_2

The assumed over-layer of α-MoO_3 has an IMFP of 2.413 nm, while the substrate of MoS_2 has an IMFP of 2.442 nm (values obtained from **NIST Electron Inelastic-Mean-Free-Path Database: Version 1.2**).

From [267]:

$$\frac{I_s}{S_s} = \exp\left(\frac{-t}{\lambda_s \cos\theta}\right) \tag{1}$$

and

$$\frac{I_o}{S_o} = \exp\left(\frac{-t}{\lambda_o \cos\theta}\right) \tag{2}$$

where the subscript o denotes the over-layer and the subscript s the substrate, t is the over-layer thickness, λ is the corresponding IMFP, I is the peak intensity divided by the sensitivity factor s for a given core level, and θ is the emission angle equal to 0° in our system.

However, s_o and s_s are the same, as we are looking at the same Mo 3d levels in both compounds. Hence, we can simplify to:

$$\frac{t}{\lambda_o \cos\theta} = \frac{I_o}{I_s} \tag{3}$$

This ratio of intensities is obtained from the XPS spectra fits of Mo 3d peaks in **Fig. 5.6(e)**.

The intensity ratio at 6 seconds is 4847/13714 = 0.35. Thus: 0.35· 2.413 nm = 0.853 nm = **61**% of effective bilayer of 2D MoO_3 (for MoO_3, b = 1.3855 nm [266]).

The intensity ratio at 10 seconds is 5665/9659 = 0.59. Thus: 0.59· 2.413 nm = 1.415 nm =**102**% of effective bilayer of 2D MoO_3.

Appendix C: Simulation of conductive networks

The following is based on the work of Dr. Colin O'Callaghan and Eamonn Weitz from the group of Prof. Mauro Ferreira (*School of Physics, TCD*). Largely informed by their publication on effective medium theory modelling of resistive networks from 2016 [277].

Kirchhoff's circuit laws and Ohm's laws can be combined to create a system of linear equations that can be used to calculate the sheet conductance of a network:

$$\mathcal{K}V_m = I \tag{4}$$

where V_m is the induced voltage at node m in the network and I is the current vector. Elements of the current vector are defined as $+i(-i)$; the current injection (extraction) nodes, i.e. the electrodes on the MoS_2 surface. All other values of I are 0. The Kirchhoff matrix $\mathcal{K}$ contains the inter-nodal connectivity and conductance information of the network. It is defined as:

$$(K)_{mn} = \begin{cases} -\Gamma_{mn} & \text{if } m \neq n \\ |\sum_{m=1,m\neq n}^{N}(K)_{mn}| & \text{if } m = n \end{cases} \tag{5}$$

where Γ_{mn} is the conductance of the connection between nodes m and n. If no connection exists between nodes m and n then the conductance between them is 0. The induced voltage vector V is calculated from (4) and is in turn used to calculate the sheet conductance of the network. During each iteration, when one of the conductors is updated, the Kirchhoff matrix is updated to account for the changed conductance value.

The network conductance Γ_N is calculated using the difference in induced potentials on the current injection/extraction nodes $V_{\text{in}}/V_{\text{out}}$:

$$\Gamma_N = \frac{i}{|V_{\text{in}} - V_{\text{out}}|} \tag{6}$$

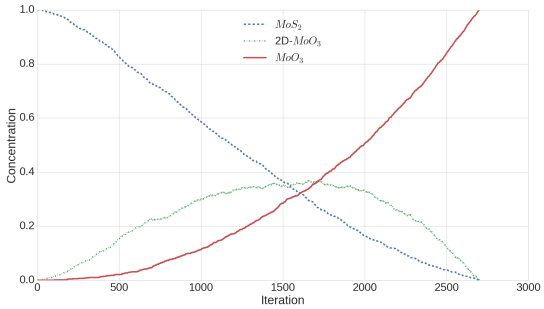

Figure 1: **Plot of the concentration of the three phases in the simulation as they change with iteration number.** A phase diagram can be created to reflect the changing of the transition rates between subsequent phases. The conversion probabilities used in the main manuscript were p_1 = 0.16 and p_2 = 0.20.

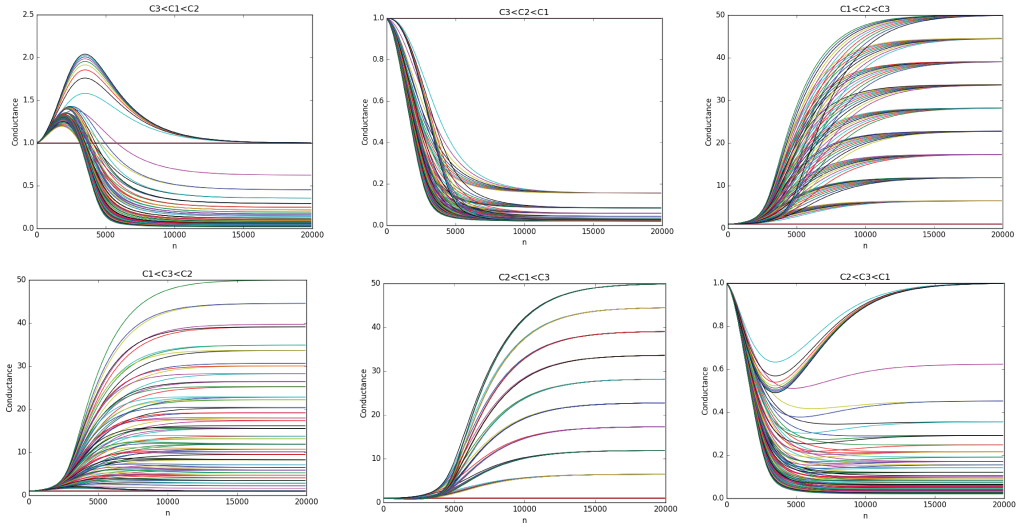

Figure 2: **Trial and error plots for different combinations of conductances between the 3 phases** $C1$**,** $C2$ **and** $C3$. A peak can only be observed when $C2$ is higher than $C1$ and $C3$.

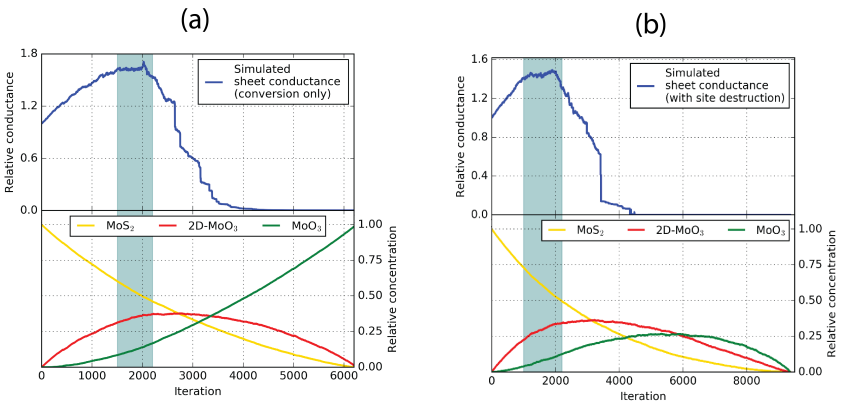

Figure 3: Example conductance plots and associated phase concentration charts generated for the cases of networks where sites **(a)** are not destroyed and where **(b)** all sites are eventually destroyed. Both networks show recovery peaks in the green shaded areas, but the drop to no conductance is more pronounced in the case of site destruction.

Appendix D: Defining the current polarity in our memtransistors

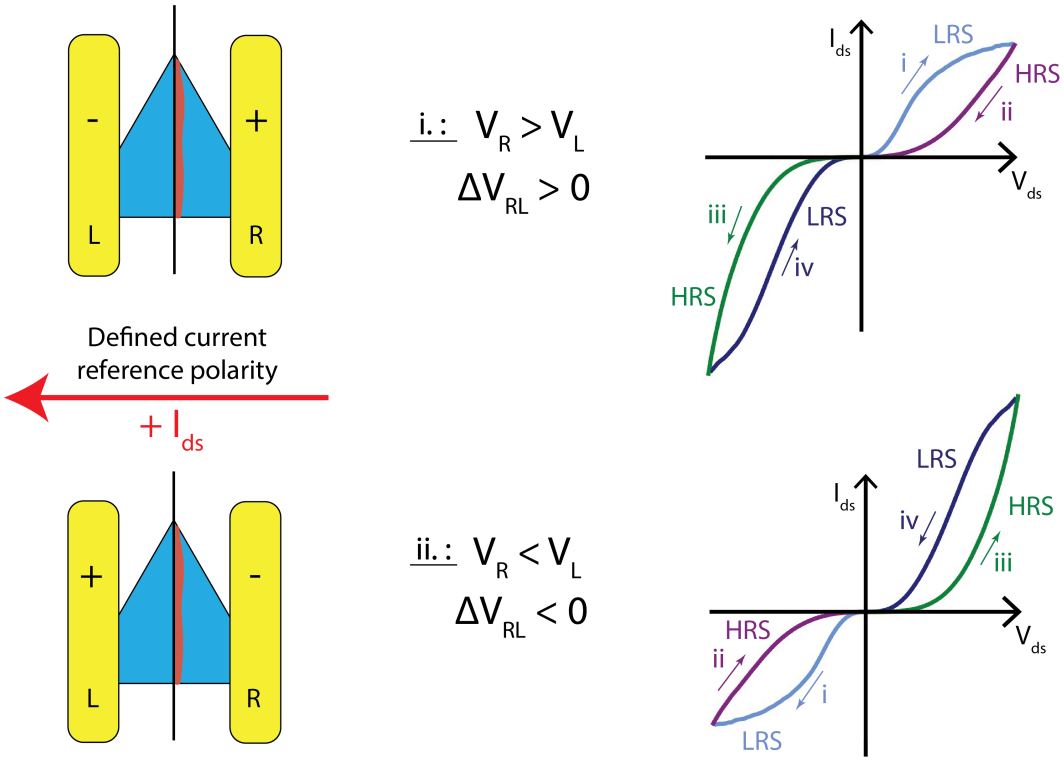

Figure 4: **Defining the current polarity in the MoS_2 memtransistor.** Sketch of an irradiated MoS_2 memtransistor device, with the skewed V_S distribution marked in red around the fissure region bisecting the FET channel. Electrodes are defined as *left* (*L*) and *right* (*R*). We consider two polarity cases: **i** and **ii**. The current polarity is defined with respect to the higher voltage electrode on the side of the V_S extension. Thus, the representative *I-V* curve shown for case **i** traces out positive I_{ds} when $\Delta V_{RL} > 0$. When the voltage polarity is swapped between *R* and *L*, a positive I_{ds} is recorded when $\Delta V_{RL} < 0$, as seen on the representative *I-V* loop for case **ii**.

Let us consider the two cases presented in **Fig. 4**. When the same memtransistor device is tested in two different ways, by changing the voltage polarity on the electrodes, we need to consider what effect this has on the recorded *I-V* sweep. We must define our current polarity with respect to the device asymmetry introduced by the ion beam. The two sketches in **Fig. 4** present the same memtransistor device with defined electrodes: *left* (*L*) and *right* (*R*). The irradiated fissure in this device is naturally asymmetric towards one side, as represented by the red colour spreading out of the fissure region towards the *R* electrode.

We want to link the switching dynamics with the device asymmetry - as such, this

passive sign convention is followed all the time to help interpret the data correctly. We can define the *positive* I_{ds} as flowing from the electrode with higher potential towards that with lower potential. Thus, we will obtain two cases:

i. when $\mathbf{V}_R > \mathbf{V}_L$ we obtain $\Delta\mathbf{V}_{\mathrm{RL}} > 0$. As we always start the SMU sweep in the positive quadrant of the *I-V* curve, we observe a positive I_{ds} for a positive V_{ds} and a negative I_{ds} for a negative V_{ds}. A representative sketch of the obtained *I-V* loop for case **i** is hence shown starting in LRS in the first quadrant of the sweep.

ii. when $\mathbf{V}_R < \mathbf{V}_L$ we obtain $\Delta\mathbf{V}_{\mathrm{RL}} < 0$. As we always start the SMU sweep by applying a positive V_{ds} we *must* detect a negative I_{ds} because $\Delta\mathrm{V}_{\mathrm{RL}} < 0$ and we have defined positive I_{ds} as flowing from high to low. Thus, the sequential parts of the obtained *I-V* loop will evolve as shown on the sketch for case **ii**.

If we do not account for this asymmetry in a physical scenario where $\Delta\mathrm{V}_{\mathrm{RL}} < 0$, we will be reflecting our true raw I_{ds} data through the origin every time we apply a positive voltage on the SMU. Hence, whenever we swap electrode polarities in this chapter on the same device, we need to reflect our raw I_{ds} data about the origin to recover the true picture of how the resistance states evolve with the applied bias (as necessitated by our ever unidirectional SMU sweep).